STRUCTURAL, MAGNETO-STATIC AND MAGNETO-DYNAMIC PROPERTIES OF Ni-Mn-Z AND Ni-Mn-X-Z (X = Cu, Fe, Co; Z = Sn, In) THIN FILMS

A thesis submitted

by

Rajkumar Modak

to

Indian Institute of Technology Guwahati

in

partial fulfillment of the requirement for the award of the degree of
Doctor of Philosophy in Physics

Department of Physics
Indian Institute of Technology Guwahati
Guwahati 781039, Assam, India

August 2018

STRUCTURAL, MAGNETO-STATIC AND MAGNETO-DYNAMIC PROPERTIES OF Ni-Mn-Z AND Ni-Mn-X-Z (X = Cu, Fe, Co; Z = Sn, In) THIN FILMS

A thesis submitted

by

Rajkumar Modak

to

Indian Institute of Technology Guwahati

in

partial fulfillment of the requirement for the award of the degree of
Doctor of Philosophy in Physics

Department of Physics
Indian Institute of Technology Guwahati
Guwahati 781 039, Assam, India

August 2018

STATEMENT

The work contained in the thesis entitled "***Structural, magneto-static and magneto-dynamic properties of Ni-Mn-Z and Ni-Mn-X-Z (X = Cu, Fe, Co; Z = Sn, In) thin films***" has been carried out by me under the supervision of Prof. A. Srinivasan, at the Department of Physics, Indian Institute of Technology Guwahati. This work has not been submitted elsewhere for the award of any degree.

Rajkumar Modak

9th August 2018

(Rajkumar Modak)
Roll No:136121019
Department of Physics
Indian Institute of Technology Guwahati
Guwahati – 781039
India

CERTIFICATE

It is certified that the work contained in the thesis entitled “***Structural, magneto-static and magneto-dynamic properties of Ni-Mn-Z and Ni-Mn-X-Z (X = Cu, Fe, Co; Z = Sn, In) thin films***” submitted by Rajkumar Modak (Roll No: 136121019), a Ph. D. student of the Department of Physics, Indian Institute of Technology Guwahati for the award of degree of Doctor of Philosophy has been carried out under the supervision of Prof. A. Srinivasan. This work has not been submitted elsewhere for the award of any degree.

9th August 2018

(Dr. A. Srinivasan)
Professor
Department of Physics
Indian Institute of Technology Guwahati
Guwahati – 781039
India.

Dedicated to

My beloved parents . . .

ACKNOWLEDGEMENTS

During almost five years of hard work and the innumerable help and support from the people around me made it possible to complete this thesis work.

First I express my deep sense of gratitude to my thesis supervisor Prof. A. Srinivasan for giving me the opportunity to work with him. During the course of my doctoral research I have not only learnt physics from him but also so many personal things. His knowledge, relevant ideas and energetic spirit have helped me to complete the thesis work successfully. I must acknowledge him for providing me unconditional freedom to work, think and express on whatever I have done in my research work by keeping faith on my abilities.

I am highly thankful to my doctoral committee members, Prof. S. Ravi (Chairman), Dr. S. Thota and Prof. P.S. Robi for their continuous academic guidance and monitoring my work progress and seminars during my Ph. D thesis work. Their valuable guidance and suggestions helped me to explore my objectives meaningfully and improve the quality of my thesis work.

I am thankful to Prof. Subhradip Ghosh, the current Head, Department of Physics, and former Heads, Prof. S. Basu and Prof. P. Poulose, for giving me the opportunity to work in the department and to use all the departmental facilities with full freedom.

I am very much grateful to Dr. M. Manivel Raja, DMRL, Hyderabad for his help in preparing alloy ingots. I am also thankful to all staff members of the Central Workshop, IIT Guwahati for their help in preparing sputtering targets from the alloy ingot.

I remain indebted to Prof. V. V. Srinivasu, Department of Physics, University of South Africa and Dr. P. Mandal and Dr. B. Samantaray, Saha Institute of Nuclear Physics, for their help with ferromagnetic resonance measurements.

I sincere thanks to Indian Institute of Technology Guwahati and the Ministry of Human Resource Development, Government of India, for a scholarship to pursue the research wotk without financial worry.

I express my sincere thanks to Dr. Sidananda Sarma, Scientific Officer in Department of Physics, for guiding me to operate various high precision instruments in the department. The Central instrument Facility provided by Indian Institute of Technology Guwahati and the high power powder XRD facility provided by DST, New Delhi, to the department through FIST program [SR/FST/PSII-020/2009] are acknowledged.

I am fortunate to have my lab seniors, Dr. Akhilesh Kr. Singh, Dr. Bhargab Deka, Dr. Nisha Shankhwar, Dr. P.C. Shyni, Dr. Tribedi Bora, Dr. T. Santosh, Dr. Bipul Deka, Dr. Bhagban Kisan, Dr. Ravikumar Patta Mr. Arnab Kumar Das and Mr. Anabil Gayen who helped me in various ways throughout my research work.

My lab mates, Bibhuti, Pratap, Camelia, Buddhadeb, Aneeta, Dolly, Manisha, Nitu and Anirban will always be remembered for the wonderful time we shared together. I am thankful to my friends Kamal, Soumya, Noor, Sanjib, Srikrishna, Pankaj, Deep and all other batch mates

I owe a lot to my beloved parents. My parents have encouraged me a lot to pursue my doctoral work. Without their infinite motivation and support I could not have finished my PhD work. Finally, my sincere thanks are due to all those have been helped me in whatever manner and brought me to this position, some of whom I may have inadvertently forgotten to mention in this acknowledgement.

Rajkumar Modak

PREFACE

Magnetic materials play an important role in technological development. They are extensively used in power transmission, communication, data storage, data read/write heads, medical diagnosis equipment, power conversion, etc. With the advent of new magnetic materials with several exciting and hitherto unknown properties, many new applications emerge. Heusler alloys which have the chemical formula X_2YZ (where X and Y are usually transition metals and Z is a *sp*-element) have amazed researchers with a plethora of novel physical properties since their discovery in 1903 by Frederic Heusler. Bulk form of these alloys has received considerable attention and several exciting phenomena have been observed in them such as ferromagnetic shape memory effect, magneto-caloric effect (MCE), giant magneto-resistance, spin polarization, superconductivity, thermoelectric effect, etc. Among these, MCE is the basis for magnetic refrigeration which is an emerging, low-carbon technology with a strong potential to be an environment friendly alternative to conventional vapour compression based refrigeration. However, the most popular room temperature magnetic refrigerants are rare earth element gadolinium and its compounds, which are very costly. Hence, the current demand is to develop rare earth free materials with giant MCE for this application. In this context, off-stoichiometric Heusler alloys with elemental composition of $Ni_{50}Mn_{25+x}Z_{25-x}$ (Z = Ga, In, Sn, Sb) have attracted immense attention due to the large MCE exhibited by them, low cost of production and relatively large abundance and availability. Several attempts have been made to understand the structural, magnetic and magneto-caloric properties of bulk $Ni_{50}Mn_{25+x}Z_{25-x}$ (Z = Ga, In, Sn, Sb) alloys and it has been found the MCE shown by these alloys is tunable over a wide temperature range which increases the operating temperature range of magnetic refrigerators made of these alloys. Since the current technological scenario is focused on micro- and nano-structured devices, one needs these alloys in thin film form with optimized properties. Moreover, thin films with high surface to volume ratio can facilitate faster heat transfer to the environment, which is a distinct advantage of magnetic cooling devices based on thin films. There are several theoretical and experimental studies which indicate that the physical properties of thin films are very different from their bulk counterparts. This has prompted several researchers to investigate the influence of parameters like deposition pressure, annealing temperature and time, surface roughness, film thickness on the microstructure and magnetic properties of these alloy thin films. Apart from MCE, these $Ni_{50}Mn_{25+x}Z_{25-x}$ (Z = Ga, In, Sn, Sb) alloy thin films are expected to exhibit geometry and microstructure dependent properties which are of immense interest from both basic scientific as well technological viewpoints. These films exhibiting soft ferromagnetism, in-plane magnetic anisotropy, high saturation magnetization and appropriate anisotropy field, find applications as microwave integrated circuits, spintronic and microelectronic device, cores in high-frequency inductors, wireless inductors, microwave noise filters, electromagnetic wave absorbers, etc. However these applications demand a clear understanding and control of parameters like magnetic anisotropy, magnetic exchange interactions, and intrinsic and extrinsic damping of these alloy films. A survey of the literature shows that Ni-Mn-Z based thin films alloys have not been well explored from these viewpoints. This served as the main motivation for exploring the properties of Ni-Mn-Z and Ni-Mn-X-Z (X = Cu, Fe, Co; Z = Sn, In) thin films prepared by dc magnetron sputtering on low-cost Si substrates in this thesis work. By varying the composition of the sputtering target, sputtering parameters and post deposition annealing conditions, off-stoichiometric Heusler alloy films with different crystal structures could be synthesized. Along with structural, magneto-static and magneto-caloric properties, magneto-dynamic properties of these films have also been investigated using ferromagnetic resonance (FMR) technique so as to evaluate parameters of relevance to high frequency device applications. Two FMR techniques, *viz*., broad-band micro-strip waveguide based FMR (MS-FMR) and cavity based FMR (C-FMR) operating at 9.4 GHz, were used to gather information about magnetic anisotropy, magnetic inhomogeneity and magnetization relaxation (or intrinsic and extrinsic damping) processes which define the applicability of these films for next generation devices.

The thesis consists of eight chapters. **Chapter 1** presents a brief introduction to the content of the thesis. A review of literature relevant to the thesis work and the motivation behind the thesis work are also included in this chapter. **Chapter 2** discusses the experimental techniques used in the present studies including the sample preparation methodologies. The basic principle and the theory behind the experiments, the experimental set up and the measurements/ methodologies leading to the determination of the physical properties are also discussed here.

In **chapter 3**, composition and thickness dependent physical properties of two series of off-stoichiometric Ni-Mn-Sn films are discussed. Series 1 consists of

$Ni_{48.14}Mn_{38.14}Sn_{13.72}$ films of 250 nm, 500 nm, 750 nm, 1000 nm and 1500 nm thickness. As-deposited amorphous films crystallized in austenite phase with high $L2_1$ order upon annealing at 823 K for 1 h. These austenite films exhibit ferromagnetic behavior with Curie temperature (T_C) close to room temperature. Martensite to austenite (M $\leftrightarrow$ A) structural phase transition was not observed in this series which may be due to low crystallite size (D ~ 10 - 15 nm). Magnetic entropy change (ΔS_M), which is a measure of MCE was calculated near T_C using Maxwell's relation and ($-\Delta S_M)_{max}$ of 0.81 J/kg.K was obtained at 306 K for a field change (dH) of 12 kOe for the 250 nm thick film. Series 2 films with thickness 360 nm, 500 nm, 700 nm and 1000 nm and composition $Ni_{53.4}Mn_{33.2}Sn_{13.4}$ annealed at 823 K for 1 h exhibited room temperature martensite phase with a modulated 14M structure. These weakly ferromagnetic films with D > 90 nm exhibit M $\leftrightarrow$ A transition, although the transition was spread over a wide temperature range. High T_C (~ 560 - 570 K) was observed for the first time in these films. FMR study performed using MS-FMR method on series 1 films reveals very low Gilbert damping constant (α) of 0.007, 0.0075 and 0.008 for the 500 nm, 1000 nm and 1500 nm thick films. High effective anisotropy constant (K_1 ~ 10^6 erg/cc) has been observed in the 1500 nm film. FMR study carried out using C-FMR method on series 2 films showed very low K_1 (~10^4 erg/cc) in the martensite Ni-Mn-Sn films, although α remained almost similar (~ 0.008).

In **chapter 4,** the effect of Co substituted martensite Ni-Mn-Sn films (series 2) with different thicknesses ranging between 360 to 1000 nm is presented. $Ni_{53.2}Mn_{29.2}Co_{7.0}Sn_{10.6}$ films with room temperature martensite phase exhibited ferromagnetism. Ni-Mn-Co-Sn films exhibited higher T_C (more than 300 K) than the ternary martensite films. Upon Co substitution, a 3.8, 2.3, 1.7 and 1.6 fold increase in ($-\Delta S_M)_{max}$ across T_C is achieved as compared to martensite Ni-Mn-Sn films of thickness 360 nm, 500 nm, 700 nm and 1000 nm, respectively. C-FMR study revealed for the first time very low K_1 (~ 10^4 erg/cc) and α of 0.0085 in the quaternary films.

Chapter 5 showcases the effect of fourth element X (= Cu, Fe, Co) substitution on the properties of 500 nm thick Ni–Mn–Sn films with austenite structure at room temperature. X atoms occupied the Sn-sublattice by replacing the Ni and/or Mn atoms without changing the austenite structure of the ternary film. The ternary Ni-Mn-Sn and Cu substituted alloy films exhibit almost similar room temperature ferromagnetic behavior, whereas the Fe and Co substituted alloy films show more softer loops with increased M_r/M_s ratio. Using FMR study a very low value of α (= 0.007) was found for the first time in Ni-Mn-Co-Sn film together with perpendicular anisotropy and easy axis along film plane. These films also do not show M ↔ A transition but high $-\Delta S_M$ (0.45–0.70 J/kg.K) was obtained near T_C (320-330 K).

Chapter 6 is devoted to investigations on Ni-Mn-In films in which Mn has been partially substituted by Co or Fe. Films with 1 and 3 at.% Fe and Co exhibited room temperature austenite phase after annealing at 823 K for 1 h. However, presence of 1 – 3 at.% Fe or Co atoms in Mn sites strongly affected the magnetic and magneto-caloric properties of the films. As much as 120 emu/cc increase in magnetization is achieved when 3% Fe or Co substituted in the ternary alloy film. $-\Delta S_M$ in the vicinity of T_C increased from 0.98 J/kg.K to 1.58 J/kg.K for the film with 3 at.% Fe and 1.23 J/kg.K for the film with 3 at.% Co, for dH of 18 kOe. These ΔS_M values are highest achieved in Ni-Mn-In thin films and comparable to values obtained in bulk Ni-Mn-In alloys. FMR study of these films revealed for the first time low α (= 0.008), which did not show significant variation with substitution of Fe or Co. Additionally, these films also exhibited high M_s, high perpendicular anisotropy and easy axis along film plane.

Chapter 7 discusses structural, magneto-static and magneto-dynamic properties of 500 nm thick $Ni_{53.7}Mn_{29.5}In_{16.8}$ and $Ni_{48.5}Mn_{29.6}Fe_{4.8}In_{17.1}$ films. Ni-Mn-In film annealed at 823 K and 973 K for 1 h exhibit room temperature martensite phase with very low magnetization whereas Ni-Mn-Fe-In films annealed at 823 K and 923 K for 1 h exhibit a mixed phase (martensite and austenite phases) at room temperature. FMR analysis of Ni-Mn-Fe-In films shows the presence of very low K_1 (~ 10^4 erg/cc) and moderately low α of 0.009 ± 0.001. Very low magnetic anisotropy of these films results in magnetic properties which are not dependent on film orientation. Moreover, the unique properties shown by Ni-Mn-Fe-In films are observed in films of all thicknesses ranging from 250 nm to 1000 nm.

Chapter 8 provides a summary of the results obtained in the thesis and briefly points out the scope for further work in these topics.

References and publications which have originated from this thesis work are listed at the end of the thesis.

CONTENTS

1. Introduction

2. Experimental Methodology and Models

3. Austenite and martensite Ni-Mn-Sn thin films

4. **Martensite Ni-Mn-Co-Sn thin films**

5. **Austenite Ni-Mn-Sn and Ni-Mn-X-Sn (X = Cu, Fe, Co) thin films**

6. **Austenite Ni-Mn-In and Ni-Mn-X-In (X = Fe, Co) thin films**

7. **Mixed phase Ni-Mn-In and Ni-Mn-Fe-In thin films**

8. **Conclusions and scope for future work**

Chapter 1

Introduction

The search for new materials exhibiting rich multifunctional properties has always been a priority for every materials researcher. In fact, past eras have been named after specific materials such as the primitive stone age, the early civilization time of bronze age, the industrialized iron age, the recent high technology silicon / polymer age and so on [HUMM98]. Magnetic materials have received considerable attention of mankind due to their interesting physical properties and wide applications in large scale. Continuous investigations on these materials have helped researchers to unravel exciting new physics and develop new technologies to make our life easier. Magnetic materials have evolved in times from bulk form to the nanostructures to cater to newer demands via novel technologies. Modern device-happy and data-centred world demands faster, better, cheaper and smaller (micro/nano) device technologies [CHOI15, SHUR00]. Magnetic thin films are the key elements of continued technological advances made in the field of solid state micro/nano electronics. Investigations on these 2-dimensional nanostructures have revealed many new areas of research in solid state physics and chemistry which are mainly based on their thickness, geometry and structure based properties [VOLK11, NALW02]. The extensive applications of thin films in diverse fields of electronics, optics, space science, aircrafts, defence and other industries have induced remarkable rise in research and development activities on thin film in recent years. Most of the functional materials are required in optimized thin film form for applications purpose [BANE12]. These investigations have led to numerous inventions in the forms of active devices and passive components such as piezo-electric devices, micro-miniaturized power supplies, sensor elements, microelectronic devices, microelectromechanical systems, recording/reading heads, magnetic sensors, gas sensors, complicated fast computer circuitry, micro actuators, micro transducers, etc. [KUAN08, GAOY03, TEIC15a, CONG10, PLAN09]. Among the magnetic materials known to mankind, Heusler alloys have amazed researchers since their discovery with their rich variety of magnetic behaviour and smart multifunctional properties. One can find diverse magnetic phenomena such as itinerant and localized magnetism, antiferromagnetism, helimagnetism, non-collinear magnetism in the same family of Heusler alloys. Recently, Heusler alloys have invoked considerable experimental and theoretical investigations due to novel properties such as ferromagnetic shape memory effect (FSME), giant magneto-caloric effect, giant magneto-resistance, half metallicity, superconductivity, thermoelectric effect, etc. [GRAF11, ZHUK16, FELS16, SRIV12,

DUBE12, GALA05, ONER07, ONER12, DURA18, CHEN13, TRIT01]. Within the large Heusler alloy family, off-stoichiometric Ni-Mn based bulk alloys have been found to exhibit extremely high magnetic field induced strain in the ferromagnetic martensite phase and giant MCE across the magneto-structural transition [FUJI00, SOZI13, TITO12, KREN07a, DUBE12]. Thin film form of these alloys are expected to exhibit geometry and microstructure dependent properties which are of immense interest from both basic scientific as well technological viewpoints. In this thesis work, multifunctional properties of off-stoichiometric Ni-Mn-based ternary and quaternary alloy thin films deposited on low cost Si (100) substrates have been investigated.

1.1 Full and half Heusler alloys

Our understanding of structure-property correlations in solid state materials changed considerably after the discovery of Heusler alloys by Friedrich Heusler, a German mining engineer and chemist in 1903. His discovery of room temperature ferromagnetism in Cu_2MnAl alloy containing no ferromagnetic element posed a challenge to both theorists and experimentalists [HEUS03]. The structure of the compound that Heusler prepared was unknown in 1903, although he realized that a chemical compound must have been formed. Later in 1934, Otto Heusler, son of F. Heusler [HEUS34], and Bradley [BRAD34] determined the crystal structure of Cu_2MnAl alloy and declared it to be an intermetallic alloy with chemical formula Cu_2MnAl. Since then, various research groups started investigating various other Heusler alloy compounds with Cu_2MnAl-like structure and a new class of materials with diversified properties was born in materials science community. These alloys are known as full Heusler alloys with general formula X_2YZ. The X and Y elements usually come from the transition metals group, whereas the Z component is a III-V group element. The full Heusler (X_2YZ) structure consists of four interpenetrating face centred cubic (fcc) sub-lattices, of which two are formed from the same (X) element. After Heusler's discovery, Nowotny and Juza published [NOWO51, NOWO50, JUZA48, JUZA68] the outcome of their study on a different group of materials consisting of main-group element compounds, which are now referred to as Nowotny-Juza phases. The connection between the Nowotny-Juza phases and the Heusler compounds was established by L. Castelliz, who first synthesized the Nowotny-Juza compound NiMnSb [CAST51, CAST52]. Nowotny-Juza phases are now referred to as half Heusler compounds have the chemical formula XYZ, in which one of the four fcc sub-lattices of the full Heusler alloy structure is empty. The family of Heusler compounds incorporates a large number of magnetic members exhibiting diverse magnetic phenomena like itinerant and localized magnetism, antiferromagnetism, helimagnetism, Pauli's paramagnetism or heavy fermionic behaviour [WEBS88, ZIEB01, PIER97, TOBO98, TOBO00, TOBO03, GILL09, GILL10].

At the stoichiometric composition, full Heusler alloys with general chemical formula X_2YZ crystallize in the stable cubic structure (represented by the point group $L2_1$ and space group $Fm\bar{3}m$) with Cu_2MnAl as the prototype compound [HEUS03, HEUS34, BRAD34]. This stable phase is also known as the austenite phase. Elements normally associated with X, Y and Z, are indicated in Figure 1.01. The X atoms form a primitive cubic sub-lattice and adjacent cubes of this X sub-lattice are filled alternatively by Y or Z atoms as depicted in Figure 1.02. The primitive cell of the $L2_1$ structure contains four atoms that form the base of an fcc primitive cell. This results in a lattice with $Fm\bar{3}m$ symmetry in which the Wyckoff positions 4a (0,0,0), 4b (½,½,½), and 8c (¼,¼,¼ and ¾,¾,¾) are occupied by Z, Y, and X atoms, respectively. The full Heusler structure is formed essentially from the ordered combination of two binary compounds XY and XZ. Both compounds may have CsCl-type crystal structures. For instance, CuMn and CuAl can yield Cu_2MnAl. In off-stoichiometric alloy compositions with $X_2Y_{1+x}Z_{1-x}$ structure, the excess Y generally occupy the Z sub-lattice site [UBAL17, SOKO12].

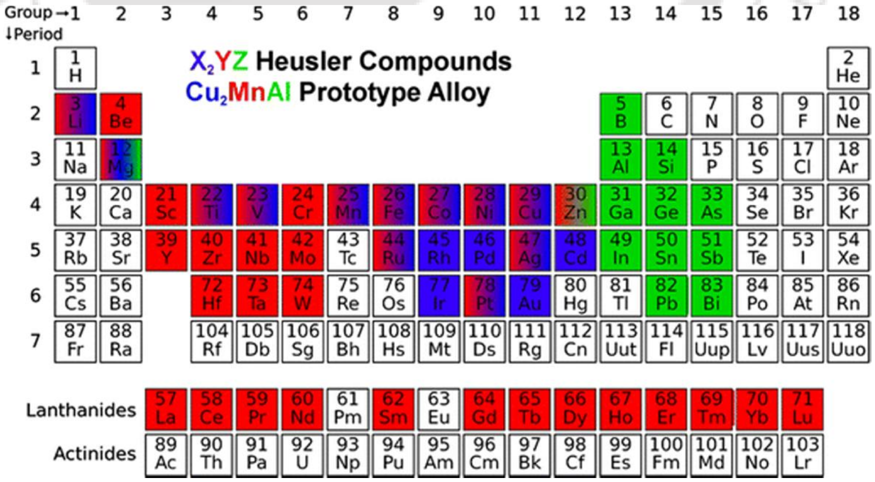

Figure 1.01: Periodic table indicating possible X, Y and Z elements in Heusler alloys.

Half Heusler alloys with general chemical formula of XYZ, crystallize in a non-centrosymmetric cubic structure (point group $C1_b$ and space group $F\bar{4}3m$). This is a ternary ordered variant of CaF_2 structure and can be derived from the tetrahedral ZnS-type structure by filling the octahedral lattice sites (*cf.* Figure 1.02). As mentioned earlier, $C1_b$ compounds with chemical formula of XYZ consist of three interpenetrating fcc sub-lattices, each of which are occupied by the X, Y and Z atoms [WATA76, GROO83]. The corresponding occupied Wyckoff positions are 4a (0,0,0), 4b (½,½,½), and 4c (¼,¼,¼). In other words, the $C1_b$ unit cell can be visualized as an $L2_1$ unit cell with one unoccupied sub-lattice (or one vacant 8c position).

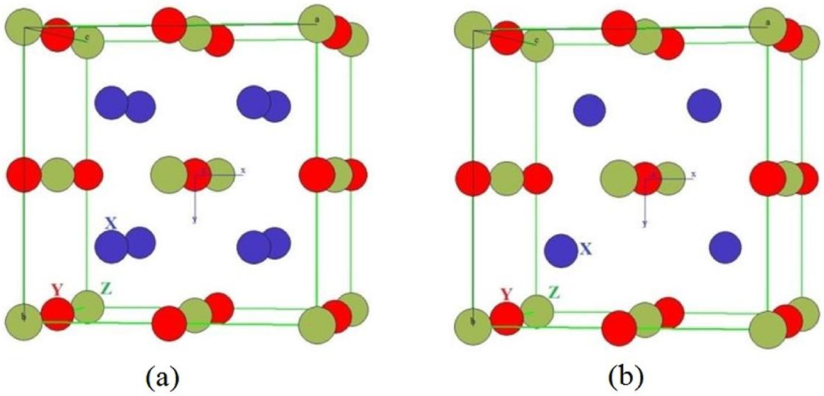

Figure 1.02: Unit cells of (a) full (X_2YZ) and (b) half (XYZ) Heusler compounds.

1.2 Disorders in Heusler alloy structure

During synthesis of Heusler alloys, it is often found that the alloy always does not form a completely (or 100%) ordered $L2_1$ austenite structure due to different types of possible disorders in the structure. The most prominent disorders in full Heusler alloy structure [WEBS69, BACO71, ZIEB01, HORN04, GRAF09] are shown in Figure 1.03. The most frequent type of disorder in a fully ordered $L2_1$ structure is the B2-type disorder which results in the CsCl-like structure shown in Figure 1.03(a). In a fully B2-type disordered structure, the Y and Z atoms are equally distributed in the unit cell and consequently the 4a and 4b positions become equivalent. As a consequence, the symmetry is reduced, resulting in $Pm\bar{3}m$ space group. Another common type of disorder found in full Heusler alloy is due to random distribution of X and Y atoms or X and Z atoms, known as DO_3-type disorder or BiF_3-like structure as depicted in Figure 1.03(b) belonging to $Fm\bar{3}m$ space group. Apart from these commonly found disorders, sometimes these alloys crystallize in a more complicated disordered phase with B32a and A2 disorders. The B32a type disorder occurs very rarely, when the X atoms which occupy one of the fcc sub-lattices are mixed with the Y atoms, whereas the X atoms on the second sub-lattice are mixed with the Z atoms. In this type of disorder, the alloy forms NaTl-like structure (space group $Fd\bar{3}m$) which is shown in Figure 1.03(c). It can be seen that in this case, the X atoms are placed at Wyckoff position 8a (0,0,0), while Y and Z are randomly distributed at 8b (½,½,½) position. In contrast to these partial atomic site disorders, if all Wyckoff positions become equivalent, then A2-type of complete disorder is obtained, resulting in W-like bcc structure with space group $Im\bar{3}m$ as illustrated in Figure 1.03(d)).

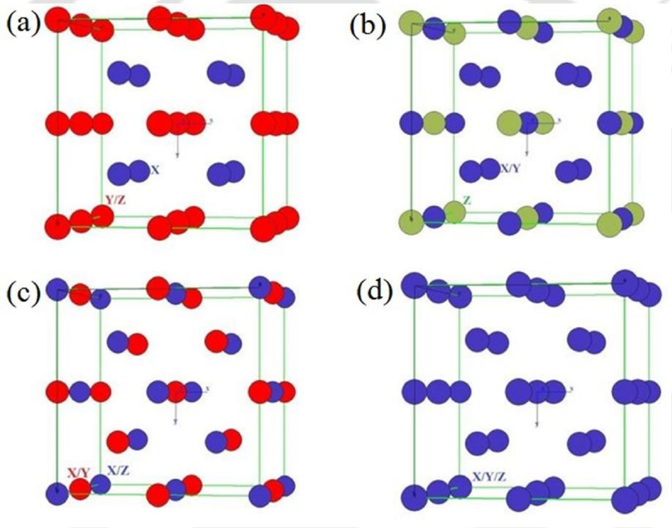

Figure 1.03: Changes in the atomic arrangement in the unit cell of full Heusler alloys due to (a) B2, (b) DO_3, (c) B32a and (d) A2-type disorders.

Properties of Heusler alloys are strongly dependent on the nature of atomic arrangement of the atoms within the unit cell. Band structure calculations show that even small amounts of disorder in the distribution of atoms on lattice sites induce distinct changes in their electronic structure, which in turn influence their magnetic and transport properties [MIUR04, PICO04, KAND07]. Therefore, a careful analysis of the crystal structure is essential to understand the structure-property correlation in Heusler compounds. Some of these disorders can be detected and estimated by analyzing X-ray diffraction (XRD) patterns of the alloys. For full Heusler compounds, we can divide all possible X-ray reflections (those allowed by the extinction rules for an fcc lattice) into three groups with three different structure factors [SZYT89], *viz*.,

1. h, k, l all odd → ((111), (311), (331), (333), (511), (531),...)

$$\text{or } F(111) = 4(f_y - f_z) \qquad 1.01$$

2. h + k + l = 2(2n − 1), n = 1, 2, . . . → ((200), (222), (420), (600), (442),...)

$$\text{or } F(200) = 4[2f_x - (f_y + f_z)] \qquad 1.02$$

3. h + k + l = 4n, n = 1, 2, . . . → ((220), (400), (422), (440), (620), (444),...)

$$\text{or } F(220) = 4[2f_x + f_y + f_z] \qquad 1.03$$

where f_x, f_y and f_z are average scattering amplitudes of the respective sub-lattices and h, k, l are the Miller indices of the crystal planes. The structure factor expressions given above are simplified forms obtained after neglecting the anomalous correction terms. The third group of reflections is independent of atomic disorder(s) in the four sub-lattices, making it a fundamental reflection. The other two groups of reflections depend on the type of disorder present. The first group vanishes if B2 disorder is present while the second group vanishes if A2 disorder is present in the alloy. However, it should be noted that some types of disorders such as DO_3 cannot be easily detected by XRD, especially when the scattering coefficients of the concerned 3d transition metals are nearly equal [BALK07]. The typical XRD pattern of a full Heusler alloy with $L2_1$ structure is shown in Figure 1.04. Here, the first there peaks (111), (200) and (220) are the characteristic peaks and analyzing these peak profiles can provide information about the structure and the atomic disorder(s) in the alloy.

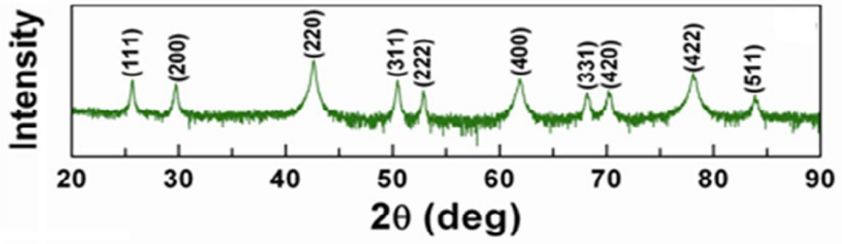

Figure 1.04: Typical XRD pattern of full Heusler alloy with $L2_1$ structure (with y-axis in log scale).

1.3 Structural phase transition in Heusler alloys

Apart from these disorders in the stable (cubic) austenite phase, several Heusler alloys including Ni-Mn-based alloys, exhibit a low symmetry crystal phase known as martensitic phase at low temperatures. Reversible transition of the alloy crystal structure from high symmetric (cubic) austenite (A) phase to low symmetry martensite (M) phase is known as martensitic transition (MT). Unlike atomic order-disorder transitions, MT is caused by non-diffusional cooperative movement of atoms in the crystal [NISH78]. MT usually takes place over a temperature range and is characterized by a thermal hysteresis behavior (a feature of first-order phase transition) between the A → M and M → A transitions. The characteristic temperatures, namely, martensite start (T_{Ms}) and martensite finish (T_{Mf}) temperatures during the cooling process, and austenite start, (T_{As}) and austenite finish (T_{Af}) temperatures during the heating process are indicated in Figure 1.05(a) [OTSU98]. In the forward MT, the formation of martensite phase progresses between T_{Ms} and T_{Mf}, and in the reverse transition, austenite phase formation progresses between T_{As} and T_{Af}. The martensite phase in Ni-Mn-based alloys may consist of any one of the low symmetric phases such as L1$_0$, 10M, 14M, *etc*. depending upon the alloy composition and constitution [PONS00,KREN05b, SUTO04].

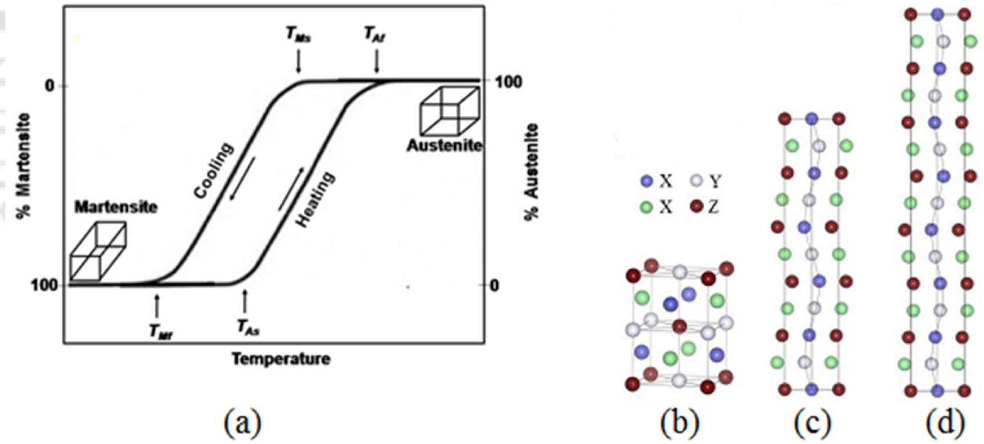

Figure 1.05: (a) Variation of phase fractions across the MT. Characteristic temperatures associated with the MT are indicated by vertical arrows. Possible martensite structures, viz., (b) non modulated tetragonal (L1$_0$), (c) modulated 10M, and (d) modulated 14M are also schematically depicted [OTSU98, ACET11, KUND17].

The structural stability of the martensite phase of Ni-Mn-Z (Z = Ga, Sn, In, Sb) alloys strongly depends on composition [ROTH54]. The martensitic structure, transformation temperatures and the Curie points can be systematized as a function of the average number of valence electrons per atom (*e/a* ratio) [PONS00, CHER99, JINX02]. *e/a* ratio for Ni_2MnGa (or $Ni_{50}Mn_{25}Ga_{25}$) alloy is estimated as follows:

$$\frac{e}{a} = \frac{(10 \times \text{at\% of Ni})+(7 \times \text{at\% of Mn})+(3 \times \text{at\% of Ga})}{(\text{at\% of Ni}+\text{at\% of Mn}+\text{at\% of Ga})} \tag{1.04}$$

$$= \frac{(10 \times 50)+(7 \times 25)+(3 \times 25)}{(50+25+25)} = \frac{750}{100} = 7.5 \tag{1.05}$$

Here, the value of 10 assigned for Ni represents the valence electrons in its outer electron shells ($3d^8 4s^2$). Similarly for Mn, the value 7 arises from $3d^5 4s^2$ and for Ga the value 3 comes from $4s^2 4p^1$. The relation between magnetic and structural phase transition temperatures of Ni-Mn-Z (Z = Sn, In) with *e/a* ratio is shown in Figure 1.06 [PLAN09]. It can be seen from the figures that the stable structure of both alloys transforms from cubic → 10 M → 14M → $L1_0$ as *e/a* ratio is increased.

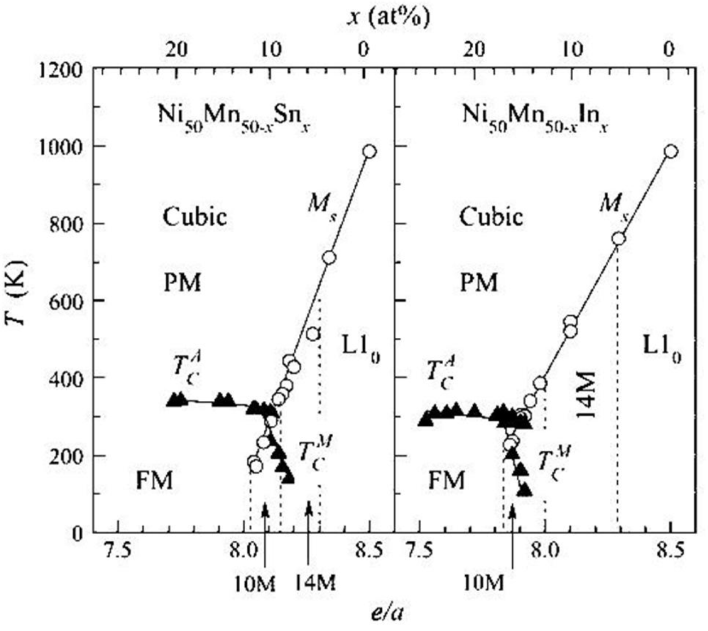

Figure 1.06: Magnetic and structural phase diagram of Ni-Mn-Z (Z = Sn, In) alloys. The triangles and circles correspond to the magnetic and martensite transformation temperatures, respectively [PLAN09].

1.4 Magnetic properties of Heusler alloys

Heusler alloys exhibit a variety of interesting magnetic properties. However, Heusler alloys with total valence electron number, $Z_t > 24$ order ferromagnetically and attain magnetic saturation under weak applied magnetic fields. Being ferromagnetic, these alloy compositions exhibit magnetic hysteresis (*M-H* loop) under the application of reversible magnetic field as displayed in Figure 1.07(a). By studying its hysteresis loop, we can get information about the magnetic properties of the alloy at a given temperature. The most important parameters of a ferromagnetic material are coercivity (H_c), saturation magnetization (M_s), retentivity (M_r) and hysteresis loop size. Understanding these parameters is very important to realize the potential of the magnetic material for a specified application. It has been observed that under certain conditions the *M-H* loop shifts from the origin as shown in Fig.1.07(b). This phenomenon is known as exchange bias (EB) effect. EB effect was first observed in Co/CoO core–shell nanoparticles in 1956 by Meiklejohn and Bean [MEIK56]. EB generally ascribed to unidirectional anisotropy induced by exchange interactions between the ferromagnetic and antiferromagnetic layers at their interfaces. At the interface, the ferromagnetic spins interact with interfacial antiferromagnetic moments and get pinned. This causes a shift in the magnetic hysteresis loop. Extra amount of energy is required to unpin the ferromagnetic spins, which gives us a measure of the EB field (H_{EB}). A schematic representation of EB behavior is represented in Figure 1.07. H_{EB} can be measured as,

$$H_{EB} = \frac{1}{2}|H_{c+} + H_{c-}| \tag{1.06}$$

where H_{c+} and H_{c-} are the coercivities during field up and field down modes, respectively, as illustrated in Figure 1.07.

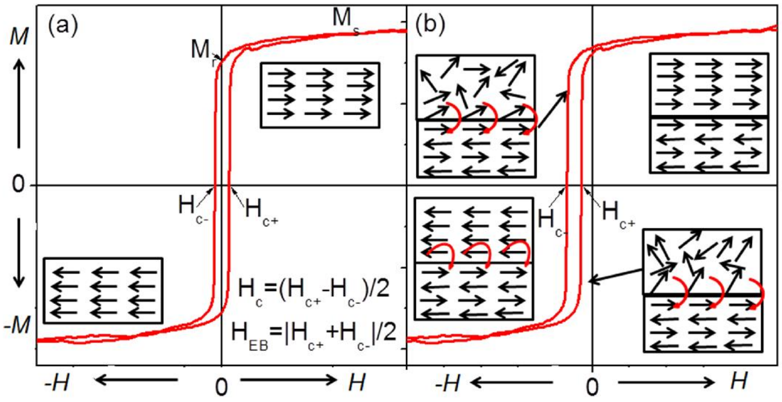

Figure 1.07: (a) Typical magnetic hysteresis loop of a soft ferromagnetic material (b) Typical magnetic hysteresis loop showing EB effect [FANY13].

The magnetism in most Ni-Mn based systems is believed to come from the interaction between the Mn atoms. The interaction of Mn atoms are indirect and is sensitive to both distance and percentage of X and Z elements. Although they are metals, these compounds have localized magnetic properties and are ideal model systems for studying the effects of both atomic disorder and changes in the electron concentration on magnetic properties. In order to understand the role of the 3d (X) and sp (Z) atoms on magnetic properties of Heusler alloys, extensive experiments have been performed. Inelastic neutron scattering study on Ni_2MnSn, Pd_2MnSn and Cu_2MnAl revealed that the interaction is long ranged and oscillatory in nature [NODA76, TAJI77]. In the austenite phase, the interaction among the Mn-Mn in regular site is ferromagnetic where as it is weakly antiferromagnetic for the Mn atoms sitting at Z position. The antiferromagnetic interaction is sensitive to distance and is enhanced at shorter interatomic distance [LAZP11, BROW06]. The interaction responsible for ferromagnetism is Ruderman-Kittel-Kasuya-Yoshida (RKKY) in nature, while the origin of antiferromagnetic interaction in Heusler alloys with excess Mn is still not very clear [PRIO13, BUCH08, PRIO11]. Monte Carlo simulations reveal that the antiferromagnetism is an outcome of RKKY interaction between Mn atoms [BUCH08]. On the other hand, some first principles study propose super-exchange interactions arising due to hybridization between Ni 3d and Mn 3d bands as the origin of antiferromagnetism in Ni-Mn based alloys [SASI04, SASI08].

1.4.1 Magnetic phase transitions

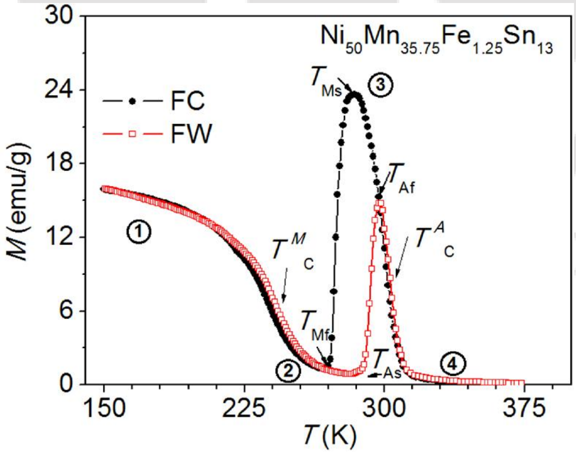

Figure 1.08: Typical thermomagnetic (M-T) behaviour of $Ni_{50}Mn_{35.75}Fe_{1.25}Sn_{13}$ alloy showing martensite to austenite transition [DASR13b].

Depending on composition, Ni-Mn based Heusler alloys can exist in four different magnetic states as a function of temperature. They are (1) lower symmetric martensite ferromagnetic/antiferromagnetic state with low magnetic moment, (2) martensite paramagnetic state, (3) austenite ferromagnetic state with high magnetic moment and (4) austenite paramagnetic state. Whenever the alloy transforms from one state to another as a function of temperature, the total magnetic moment of the alloy changes. The most prominent $\partial M/\partial T$ change is seen across MT when the martensite low moment ferromagnetic/paramagnetic state transforms to austenite high moment ferromagnetic phase. Large $\partial M/\partial T$ is also observed across austenite ferromagnetic to paramagnetic transition (second order pure magnetic transition), but this transition exhibits no thermal hysteresis. A typical thermo-magnetization (*M-T*) curve with all these phases is shown in Figure 1.08. The characteristic ($T_{Ms}, T_{Mf,}$ T_{As} and T_{Af}) temperature are also marked in the figure. The *M-T* curves were recorded with two distinct conditions, viz., measuring magnetisation with increasing temperature in the presence of magnetic field (FW), and measuring magnetization with decreasing temperature in the presence of magnetic field (FC). The hysteresis nature between FW and FC curves signify the presence of first order matensitic phase transition in the temperature range.

1.4.2 Magneto-caloric effect

The phenomenon related to the change in temperature a magnetic material upon application or removal of an external magnetic field is called the magneto-caloric effect (MCE). MCE is usually quantified in terms of the isothermal total entropy change (ΔS_{iso}) or the adiabatic temperature change (ΔT_{ad}) during the process. The relation between these two important MCE parameters can be understood in terms of thermodynamic relations. We start with the general thermodynamic potentials (internal energy *U* of the system, enthalpy *H*, Helmholtz free energy *F* and Gibbs free energy *G*) which are related to the magnetic as well as thermodynamic variables as follows [SWAL62, BAZA64, VONO74, TISH99, TISH03]:

$$U = U(S,V,M) \tag{1.07}$$

$$F = U - ST \tag{1.08}$$

$$\text{and } G = U - ST + PV - MH \tag{1.09}$$

where *P, V, T, S, H* and *M* are pressure, volume, absolute temperature, entropy, magnetic field and magnetization, respectively. Now, differential forms of *U*, *F* and *G* can be expressed as

$$dU = TdS - PdV + HdM \tag{1.10}$$

$$dF = -SdT - PdV + HdM \tag{1.11}$$

$$dG = VdP - SdT - MdH \tag{1.12}$$

Using the above equations, the variables *P, V, S, H* and *M* can be determined by the following equations of state:

$$P(T,H,V) = -\left(\frac{\partial F}{\partial V}\right)_{H,T} \tag{1.13}$$

$$V(T,H,P) = \left(\frac{\partial G}{\partial P}\right)_{H,T} \tag{1.14}$$

$$S(T,H,V) = -\left(\frac{\partial F}{\partial T}\right)_{H,V} \quad or \quad S(T,H,P) = -\left(\frac{\partial G}{\partial T}\right)_{H,P} \tag{1.15}$$

$$H(T,M,V) = \left(\frac{\partial F}{\partial M}\right)_{V,T} \tag{1.16}$$

$$M(T,H,P) = -\left(\frac{\partial G}{\partial H}\right)_{T,P} \tag{1.17}$$

From these equations of state, it is possible to derive the thermodynamic Maxwell relations,

$$\left(\frac{\partial S}{\partial H}\right)_{T,P} = \left(\frac{\partial M}{\partial T}\right)_{H,P} \tag{1.18}$$

$$\left(\frac{\partial S}{\partial P}\right)_{T,H} = -\left(\frac{\partial V}{\partial T}\right)_{H,P} \tag{1.19}$$

$$\left(\frac{\partial S}{\partial M}\right)_{T,P} = -\left(\frac{\partial H}{\partial T}\right)_{M,P} \tag{1.20}$$

Considering *S* as a function of *T, P* and *H*, the total differential of *S* can be written as,

$$dS = \left(\frac{\partial S}{\partial T}\right)_{H,P} dT + \left(\frac{\partial S}{\partial H}\right)_{T,P} dH + \left(\frac{\partial S}{\partial P}\right)_{T,H} dP \tag{1.21}$$

For an isothermal and isobaric process (for which $dT = 0$ and $dP = 0$),

$$dS = \left(\frac{\partial S}{\partial H}\right)_{T,P} dH \tag{1.22}$$

By integrating this equation, it is possible to obtain the finite isothermal entropy change for the change of magnetic field from H_i to H_f as,

$$\Delta S_M(H,T) = S_M(H_i,T) - S_M(H_f,T) = \int_{H_i}^{H_f} \left(\frac{\partial S}{\partial H}\right)_T dH \tag{1.23}$$

Using the Maxwell relation, $\left(\frac{\partial S}{\partial H}\right)_T = \left(\frac{\partial M}{\partial T}\right)_H$ 1.24

the isothermal entropy change can also be expressed as,

$$\Delta S_M = \int_{H_i}^{H_f} \left(\frac{\partial M}{\partial T}\right)_H dH \tag{1.25}$$

According to the second law of thermodynamics, the variation of *S* of a system is the infinitesimal transfer of heat (*δQ*) to a closed system driving a reversible process, divided by the equilibrium temperature (*T*) of the system i.e.

$$dS = \left(\frac{\delta Q}{T}\right) \tag{1.26}$$

Again, at constant parameter, *x,* the heat capacity C_x of a system is defined as,

$$C_x = \left(\frac{\delta Q}{dT}\right)_x \tag{1.27}$$

Since $\delta Q = T\mathrm{d}S$, C_x can also be expressed as,

$$C_x = T\left(\frac{\partial S}{\partial T}\right)_x \tag{1.28}$$

In terms of C_x, the total differential of *S* can be written as,

$$TdS = C_{H,P}dT + T\left(\frac{\partial S}{\partial H}\right)_{T,P} dH + T\left(\frac{\partial S}{\partial P}\right)_{T,H} dP \tag{1.29}$$

For an adiabatic and isobaric process (i.e., $T\mathrm{d}S = 0$ and $\mathrm{d}P = 0$), the finite temperature change is obtained by the integration of the Maxwell relations as,

$$\Delta T_{ad}\left(T,H\right) = -\int_{H_i}^{H_f} \frac{T}{C_H}\left(\frac{\partial M}{\partial T}\right)_H dH \tag{1.30}$$

Finally, it is possible to deduce that,

$$\Delta T_{ad} \approx -\frac{T}{C_H}\Delta S_M \tag{1.31}$$

Usually, in common magnetic materials (ferromagnetic and paramagnetic), *M* in a constant magnetic field decreases with increasing temperature i.e. $(\partial M/\partial T)_H < 0$. In such a case, $\Delta T_{ad} > 0$ and the $\Delta S_M < 0$ for a positive magnetic field change ΔH. Such a process is named as direct (or conventional) MCE, while the reversed condition is referred to as inverse MCE [TEGU02, ZHAN04, KREN05a, RANK09]. Since ΔS_M is proportional to both $(\partial M/\partial T)_H$ and ΔH, larger absolute values of $(\partial M/\partial T)_H$ and ΔH give rise to larger MCE.

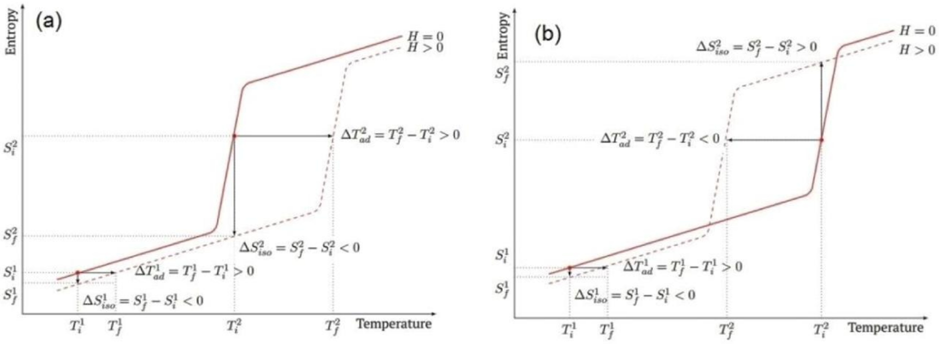

Figure 1.09: Schematic representation of (a) conventional MCE and (b) inverse MCE [TITO14].

To understand the MCE qualitatively, let us consider a schematic representation of the temperature dependence of the total entropy $S_{\text{total}}(T)$ of the system close to the transition as shown in Figure 1.09. The solid line denotes the zero-field temperature dependence of the total entropy $S_{\text{total}}(T)$ at $H_i = 0$, and the dashed line denotes the temperature dependence of the total entropy in an external field $S_{\text{total}}(T)$ at $H_{\text{f}} = H_0$. Figure 1.09(a) represents the case of $S_{\text{total}}(T)$ in the vicinity of a second order (e.g. ferromagnetic (FM) ↔ paramagnetic (PM)) transition. It can be noticed that $S_{\text{total}}(T)$ for $H_{\text{i}} = 0$ lies higher than that for $H > 0$ in the whole temperature interval, since the main contribution to the total entropy comes from the magnetic entropy ($S_{\text{total}} \approx S_{\text{magn}}$), and applying a magnetic field lowers it. Applying a magnetic field adiabatically at T_i^2 leads to a positive temperature change, $\Delta T_{ad}^2 = T_f^2 - T_i^2$, whereas applying a magnetic field isothermally leads to a negative entropy change, $\Delta S_{iso}^2 = S_f^2 - S_i^2$, resulting in conventional MCE.

Similarly, Figure 1.09(b) shows the case of $S_{\text{total}}(T)$ in the vicinity of a first order phase transition. Below and above the transition, $S_{\text{total}}(T)$ for $H_{\text{i}} = 0$ lies higher than that for $H > 0$. This results in a positive adiabatic temperature change. $\Delta T_{ad}^1 = T_f^1 - T_i^1 > 0$, and a negative isothermal entropy change, $\Delta S^1 = S_f^1 - S_i^1 < 0$, upon applying a magnetic field. During the transformation, both magnetic and lattice entropies change, and the applied field stabilize the state with higher saturation magnetization. This results in a positive total entropy change on applying a magnetic field [$\Delta S_{\text{latt}} > \Delta S_{\text{magn}}$, $S_{\text{total}}(T)$ at $H = H_0 > S_{\text{total}}(T)$ at $H = 0$] and leads to a negative adiabatic temperature change, $\Delta T_{ad}^{1} = T_f^1 - T_i^1 < 0$, and a positive isothermal entropy change, $\Delta S^1 = S_f^1 - S_i^1 > 0$. Hence, this results in the inverse MCE.

From these schematic considerations of MCE in the vicinity of the thermodynamic transition, it can be understood that both temperature and entropy changes are substantially larger in the vicinity of the transition so that the transition temperature is the most favorable working temperature for MCE applications. ΔS_M associated with first order phase transition (FOPT) is generally large but it is confined to a narrow temperature region of a few Kelvin. On the other hand, ΔS_M near the second order phase transition (SOPT) is smaller but extends over a wider temperature range. Moreover, FOPT inherently suffers from a large hysteresis effect during thermal cycling, which is not found in SOPT. Hence, SOPT is considered to have no thermal hysteresis so that the adiabatic temperature changes on applying and removing the field are equal [PHAN12].

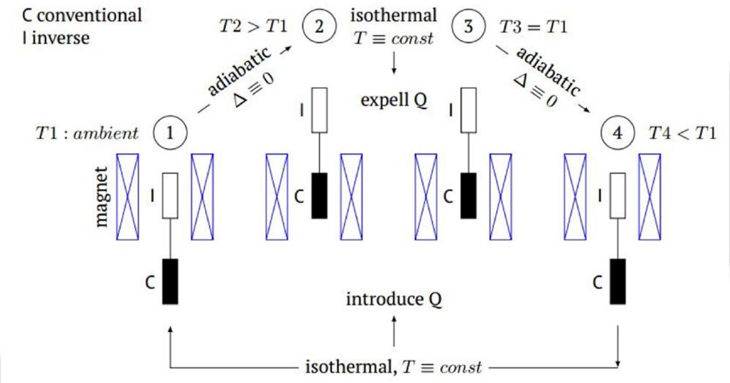

Figure 1.10: A refrigeration cycle using conventional and inverse MCE elements simultaneously. Adopted from [TITO12].

Materials showing phase transition and MCE find wide applications. One of the most popular applications is magnetic refrigeration based on MCE. Magnetic refrigeration is an emerging low carbon technology with a strong potential to be an environment friendly alternative to conventional vapour compression based refrigeration. The history of MCE and refrigeration can be traced back to Warburg's pioneering work on Fe in 1881 [WARB81]. Later in 1933, Giauque and MacDougall [GIAU33] successfully demonstrated a magnetic refrigerator to cool down to sub-Kelvin temperatures. The research on magnetic refrigeration came in focus in 1976 when Brown [BROW76] designed the first magnetic refrigerator operating at room temperature. Gadolinium, the best known rare earth element mostly used as magnetic refrigerant is very costly. Hence, the current demand is in the development of rare earth free materials with giant MCE. Ni-Mn based Heusler alloys showing both inverse and conventional MCE yield large adiabatic temperature changes. These can be used for magnetic refrigeration with enhanced cooling power as proposed by Titov *et al.* [TITO12], shown in Figure 1.10.

However the efficacy of a magneto-caloric material as a magnetic refrigerant is defined in terms of its refrigerant capacity (*RC*). It is a measure of the amount of heat that can be transferred between hot and cold reservoirs in an ideal refrigeration cycle. If there are two different magnetic refrigerants which differ only in their *RC* value, then the one with higher *RC* is expected to perform better because of its capability to transport larger amounts of heat in a real cycle [PECH01]. *RC* can be estimated by integrating ΔS_M with respect to temperature over the full width at half maximum (FWHM) of $\Delta S_M(T)$ curve [PECH01, SHAR07a, BING09]. Mathematically, *RC* can be expressed as,

$$RC = \int_{T_1}^{T_2} \Delta S_M \left(T, H\right) dT \qquad 1.32$$

The lower (T_1) and upper (T_2) limits of the FWHM represent the cold and hot temperatures, making them the analogues of the sink and source temperatures in the conventional refrigeration cycle. So, while considering an MCE material, one should also consider its *RC* value and full width at half maximum (FWHM) of $\Delta S_M\,(T)$ curve as these entities play an important role in defining the efficiency and working limit of a magnetic refrigerator.

Apart from refrigeration technology the MCE find its application to convert heat energy to electricity as demonstrated by Srivastava *et al.* [SRIV01]. They have demonstrated a device using $Ni_{45}Co_5Mn_{40}Sn_{10}$ alloy which was able to produce output peak voltage of about 0.6 mV. The working principle of the device is based on magnetic moment change across phase transition and Faraday's law of electromagnetic induction. The detailed operation of the device can be found in literature [SRIV01].

1.5 Magnetization Dynamics

Ferromagnetism in a material can be understood by the presence of a spontaneous magnetization which is produced by a parallel alignment of spins / magnetization vectors. Under the application of external magnetic field the magnetization vectors in ferromagnetic materials align along the applied field following a helical path. The dynamics of a spin can be described mathematically by an equation of motion. The equation of motion can be derived from quantum mechanics [KAUF06, MILT02]. The commutation of spin observable $\boldsymbol{S}$ ($S\vec{n}$, where $\vec{\text{n}}$ is unit vector alon S) with the Hamiltonian operator (H) gives the time evolution of $\boldsymbol{S}$.

$$i\hbar\frac{d}{dt}\langle\boldsymbol{S}\rangle=[\boldsymbol{S},H] \qquad 1.33$$

The interaction of $\boldsymbol{S}$ with the magnetic induction vector $\boldsymbol{B}$ ($B\vec{n}$, where $\vec{\text{n}}$ is unit vector alon B) can be written as,

$$\text{H}=-\frac{\text{g}\mu_{\text{B}}}{\hbar}\boldsymbol{S}.\boldsymbol{B} \qquad 1.34$$

Using commutation rule for spin operators [KAUF06],

$$\left[S_i,S_j\right]=i\hbar\varepsilon_{ijk}S_k \qquad 1.35$$

and using Eqn. 1.34, we can write,

$$[\boldsymbol{S},\text{H}]=\text{ig}\mu_{\text{B}}(\boldsymbol{S}\times\boldsymbol{B}) \qquad 1.36$$

Substituting Eqn 1.36 in 1.33 we get,

$$\frac{d}{dt}\langle\boldsymbol{S}\rangle=\frac{g\mu_B}{\hbar}(\boldsymbol{S}\times\boldsymbol{B}) \qquad 1.37$$

The above equation of motion is for a single spin. In the macro spin model, the magnetization $\boldsymbol{M}$ is supposed to be uniform throughout the sample (where $\boldsymbol{M}=M\vec{n}$, M is the magnitude of total magnetic moment as used in previous sections and $\vec{n}$ is the direction of magnetization. So here after, whenever direction is involved to define magnetization $\boldsymbol{M}$ will be used, otherwise M will be used). The relation between $\boldsymbol{S}$ and $\boldsymbol{M}$ can be written as,

$$\boldsymbol{M}=\frac{g\mu_B}{\hbar}\langle\boldsymbol{S}\rangle \qquad 1.38$$

Therefore, equation of motion of magnetization in the presence of an external magnetic field $\boldsymbol{H}$ ($H\vec{n}$, where $\vec{\text{n}}$ is unit vector alon H) will be,

$$\frac{d\boldsymbol{M}}{dt}=-\frac{g\mu_B}{\hbar}(\boldsymbol{M}\times\boldsymbol{H}) \qquad 1.39$$

$$\text{or} \quad \frac{d\boldsymbol{M}}{dt}=-\gamma(\boldsymbol{M}\times\boldsymbol{H}) \qquad 1.40$$

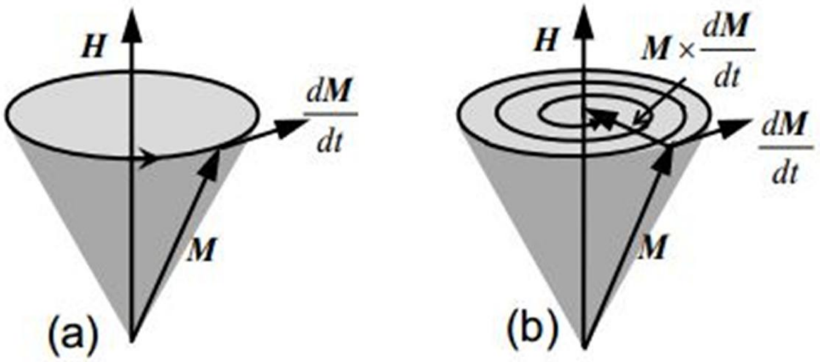

Figure 1.11: Precession of magnetization vector (M) around magnetic field (H) (a) in the absence of damping, and (b) in the presence of a damping.

The above equation is called the Landau-Lifshitz equation (without damping), where $\gamma = \frac{g\mu_B}{\hbar}$, is the gyromagnetic ratio. The above equation can be generalized by replacing $\boldsymbol{H}$ by $\boldsymbol{H}_{\text{eff}}$. This equation implies that the tip of the magnetization vector precesses around the effective magnetic field in a circular orbit as shown in Figure 1.11(a) for infinitely long time with an angular frequency, $\omega = \gamma H_{\text{eff}}$. Practically, the precession amplitude of magnetization decreases with time and the tip of the magnetization vector executes a spiral path (Figure 1.11(b)). Therefore, a damping or relaxation term (R) should be added with the Landau-Lifshitz equation [GURE96].

$$\frac{d\boldsymbol{M}}{dt} = -\gamma\left(\boldsymbol{M} \times \boldsymbol{H}_{eff}\right) + R\left(\boldsymbol{M}, \boldsymbol{H}_{eff}\right) \qquad 1.41$$

Landau and Lifshitz proposed [LAND35],

$$R = -\frac{\lambda}{M_s^2}\boldsymbol{M} \times \left(\boldsymbol{M} \times \boldsymbol{H}_{eff}\right) \qquad 1.42$$

and Gilbert suggested [GILB55, GILB04]

$$R = \frac{\alpha}{M_s}\left(\boldsymbol{M} \times \frac{d\boldsymbol{M}}{dt}\right) \qquad 1.43$$

Using the above expression, the equation of motion of magnetization vector in presence of damping can be expressed as,

$$\frac{d\boldsymbol{M}}{dt} = -\gamma\left(\boldsymbol{M} \times \boldsymbol{H}_{eff}\right) + \frac{\alpha}{M_s}\left(\boldsymbol{M} \times \frac{d\boldsymbol{M}}{dt}\right) \qquad 1.44$$

Eqn. 1.44 is known as Landau-Lifshitz-Gilbert (LLG) equation [LAND35, GILB55]. Here, $\boldsymbol{H}_{eff}$ is the effective magnetic field acting on $\boldsymbol{M}$. The symbol γ represents the gyromagnetic ratio and is defined in terms of Lande's g factor, Bohr magneton (μ_B) and reduced Planck constant ($\hbar$) as $\gamma = g\mu_B/\hbar$. The factor G ($= \gamma\alpha M_s$) is related to the intrinsic relaxation rate of the material and the Gilbert damping constant (α). α is a very important parameter for a material from application point of view. $\alpha << 1$ for transition metals, which ensures that the magnetization precesses a number of times around the effective field before coming to the equilibrium position. The values of α for Ni, Fe, Co, permalloy and Ni_2MnSn Heusler alloy are 0.064, 0.0019, 0.011, 0.008, and 0.0075, respectively [OOGA06, TRUD10, SCHE06, DUBO11].

Ferromagnetic resonance (FMR) is a simple and handy technique to investigate the magnetization dynamics of ferromagnetic materials. In a typical FMR experiment, the sample is placed in a strong static magnetic field and subjected to the radiation of an electromagnetic wave at microwave frequency. Now, if a varying force perpendicular to $\boldsymbol{H}$ is applied over the magnetic moment (like a radio frequency electromagnetic signal), it can make it precess about the equilibrium direction. Besides, if this force has a frequency similar to the precessional frequency of $\boldsymbol{M}$, maximum energy would be absorbed by the ferromagnetic sample. This is when ferromagnetic resonance occurs and all magnetic moments will be oscillating in phase. By studying the resonance condition, one can infer about the magneto-dynamics in the sample. The FMR technique depends on the geometry of the sample at hand, thus it allows a three dimensional analysis of samples. FMR is an excellent tool to investigate the magnetic properties of 2-dimensional magnetic materials like ferromagnetic thin films.

1.6 Overview of literature on Ni-Mn-based alloy

Off-stoichiometric Ni-Mn-Z (Z = Sn, In, Ga, Sb) Heusler alloys exhibiting large MCE [DUJZ07, ALIE10, KHAN07a, BHOB07] and multifunctional properties like magnetic shape memory effect [KAIN07], large magnetoresistance [YUSL06], piezoresistance [PORC12], barocaloric effect [MANO10], and exchange bias [PATH09a] have great application potential. Off-stoichiometric Ni-Mn-Z alloys exhibit two phase transitions, namely, M↔A transformation and ferromagnetic (FM) to paramagnetic (PM) transition. Large positive and negative ΔS_m occurs across these two transitions known as inverse MCE and direct MCE, respectively. During the last decade, several research groups have synthesized and investigated these off-stoichometric $Ni_{50}Mn_{50-x}Z_x$ (Z = Sn, In, Sb) alloys in bulk form. They found that Ni-Mn-Sn [KREN05a, PHAN12], Ni-Mn-In [HANZ06, KREN07b, SHAR07b, BHOB07] and Ni-Mn-Sb [DUJZ07, KHAN07a, FENG09] exhibit large inverse MCE across the first order (M↔A) phase transition. Phan *et al*. obtained $(\Delta S_M)_{max}$ of 22 J/kg.K at 255 K for a field change (ΔH) of 50 kOe in $Ni_{50}Mn_{37}Sn_{13}$ ribbon [PHAN12]. Bhobe *et al*. [BHOB07] observed $(\Delta S_M)_{max}$ of 25 J/kg.K for dH of 50 kOe at 301 K in $Ni_{50}Mn_{35}In_{15}$ alloy. In $Ni_{49}Mn_{39}Sb_{12}$ alloy, $(\Delta S_M)_{max}$ value of 6.15 J/kg.K was recorded by Feng *et al*. [FENG09] for 10 kOe field change at 279 K. Addition of extra elements is a classical way to modify the properties of a given alloy [WANG01, IMAN06, PHAN07, PONS08, BARI11, SURE11]. So, addition of a fourth element can be an effective way to change the magnetic and structural properties of ternary full Heusler (X_2YZ) and off-stoichiometric Heusler alloys. Additional elements like Co, Si, Fe, Cu, etc., in ternary $Ni_{50}Mn_{50-x}Z_x$ Heusler alloy provide a means to enhance the MCE as well as tailor the MT [DASR13a, HANZ08, GAOB09a, PATH10, FENG11, GHOS13]. Chen *et al*. achieved $(\Delta S_M)_{max}$ value of 32.4 J/kg.K for 50 kOe field change at 273 K by adding Co in $Ni_{48}Co_2Mn_{38}Sn_{12}$ alloy [CHEN15]. Das *et al*. [DASR13a] observed large $(\Delta S_M)_{max}$ value of 31.3 J/kg.K for 18 kOe magnetic field change at 278 K in $Ni_{50.69}Mn_{33.83}In_{14.07}Si_{1.41}$ alloy. Feng *et al.* were able to increase $(\Delta S_M)_{max}$ up to 9.38 J/kg.K for 50 kOe field change at 291 K in $Ni_{48}Cu_1Mn_{39}Sb_{12}$ alloy [FENG11]. Substitution of Co ($Ni_{43}Mn_{43}Co_3Sn_{11}$) [GAOB09a] and Cu ($Ni_{50}Mn_{33}Cu_2Sn_{15}$) [GAOB09b]· has yielded ΔS_M of 33 J/kg.K at 188 K and 13.5 J/kg.K at ~206 K, respectively, for dH of 50 kOe. ΔT_{ad} of −1.5 K and −1.99 K have been achieved at MT for dH ~ 18 kOe in Ge and Al substituted $Ni_{50}Mn_{35}In_{15}$ alloy, respectively [KAZA11]. $(\Delta S_M)_{max}$ of 124 J/kg.K and RC of 158 J/kg have been recorded in $Ni_{50}Mn_{35}In_{12}Si_3$ alloy at 239 K for ΔH of 50 kOe [PATH08].

Apart from the MCE, exchange bias (EB) effects have also been reported in Ni-Mn-Sn and Ni-Mn-In alloys [PATH09a, LIZJ07, KHAN07b]. In $Ni_{50}Mn_{35}In_{15-y}Si_y$ alloys ($0 < y < 4$), the EB field increased with Si substitution and maximum EB field of ~ 170 Oe was observed for the alloy with y = 4 at 5 K when field cooled with 50 kOe field [PATH09b]. These studies suggest that these Heusler alloys have potential application as actuators, magnetic cooling and hybrid systems. It was shown that

Heusler alloy films exhibit FSME can be used as microfluidic valves, micro-pumps and micro-grippers [WINZ04].

Current technological scenario is focused on micro structured devices. In order to incorporate the advantage of Heusler alloys in microstructured devices, thin film form of these alloys have to be prepared, characterized and optimized. Theoretical and experimental studies suggest that the MT as well as the microstructure may change significantly in thin film form of these alloys [DUNA11, MALY09]. For magnetic cooling devices, thin films offer the advantage of higher specific cooling power (SCP) due to their large surface to volume ratio [NIEM10]. Higher SCR ensures faster heat transfer in practical application. A general knowledge of influence reduced dimensionality on the MT is required for all these applications. Investigations on MT behavior in Heusler alloy thin films have shown a broader transition region and a shift in MT temperature. The broadening of the transition as well as a reduced transition temperature can be caused by constraints emanating from the substrate [ROYT98] and/or confinement of the nucleus and size scale effects on the mean free path of transformation dislocations [MALY09]. An increase in the transition temperature can also be attributed to stress induced by lattice mismatch between substrate and film [DUNA11].

Some of the important questions which need attention are

1. Can all the bulk properties be replicated in thin films?
2. What is the effect of reduced dimensionality on the M ↔ A transition?
3. How do the key MCE parameters (ΔS_m, RC and $T_{operating}$) vary in thin films?
4. What other applications can these thin films cater to?

Limited amount of investigations pertaining to the above questions have been done on Ni-Mn-Z alloy thin films in recent years which reveal many interesting features in thin films which are quite different from their bulk counterparts. A systematic study by Vishnoi *et al.* [VISH11, VISH10a] on thickness and annealing temperature dependence of polycrystalline Ni-Mn-Sn films grown on Si show that the MT is suppressed in films with thickness below 410 nm and an increase in transition temperature was observed with increase in film thickness. Vishnoi *et al.* [VISH10b] have also looked at the composition dependence of MT temperature in Ni-Mn-Sn film. Yuzuak *et al.* [YUZU13] obtained $(\Delta S_M)_{max}$ of 1.6 J/kg.K for 10 kOe field change along with RC value of 36.5 J/kg at 271 K for 200 nm thick $Ni_{51.6}Mn_{32.9}Sn_{15.5}$ film on MgO

(001) substrate. Sokolov *et al*. [SOKO13] found a thermal hysteresis of 8 K in $Ni_{50}Mn_{35}In_{15}$ film grown on MgO (100) with MT at 315 K. Neiman *et al*. [NIEM10] reported $(\Delta S_M)_{max}$ of 8.8 J/kg.K for field change 90 kOe at MT (353 K) for 300 nm thick $Ni_{48}Co_5Mn_{35}In_{12}$ film on MgO (001) substrate with 20 nm Cr buffer layer. Klaer *et al*. [KLAE13] also observed MT in 300 nm $Ni_{48}Co_5Mn_{35}In_{12}$ film on MgO(100). Akkera *et al.* [AKKE17] found ΔS_M of 7.0 mJ/cm^3.K at 302 K and RC of 39.2 mJ/cm^3 in $Ni_{51.1}Mn_{34.9}In_{9.5}Cr_{4.5}$ film for an applied field of 20 kOe. Apart from these interesting MCE properties, 2-dimensional Ni_2MnZ alloys are expected to exhibit geometry and microstructure dependent properties which are of great relevance not only for basic scientific interests but also for next generation microdevice applications. Singh *et al.* [SING14] studied strain mediated coupling in PZT/Ni-Mn-In/Si thin film heterostructure for potential microelectromechanical systems. Chao Jing *et al.* [JING15] observed EB in epitaxial $Ni_{50}Mn_{35}In_{15}$ films on MgO(001) substrate. Sokolov *et al.* [SOKO13] found MT in 10 nm thick $Ni_{50}Mn_{35}In_{15}$ film on MgO single crystal substrate. Niemann *et al.* [NIEM10] demonstrated magnetically induced austenite phase transition in epitaxially grown metamagnetic Ni-Co-Mn-In films on MgO (001). Crouïgneau *et al.* [CROU15] revealed that MT is very sensitive to annealing temperature in free standing $Ni_{45}Co_5Mn_{36.5}In_{13.5}$ film. Teichert *et al.* [TEIC15a] demonstrated that Ni-Mn-Sn films can be used to induce unidirectional anisotropy in CoFeB/MgO/CoFeB magnetic tunnel junctions. Point contact Andreev reflection studies [JOHN96] on Ni_2MnIn film grown on Si (100) substrate have established maximum spin polarization of 54% in this spintronic material. These results open up various possibilities for these alloys to be applied in spintronic and microelectronic device such as current-induced magnetization switching devices, magnetic random access memories, magnetic oscillators, magnetic sensors etc. [TEIC15a, BERN12, SATO13]. However, a complete investigation of magnetic quality, magnetic homogeneity, magnetic anisotropy and intrinsic damping characteristics of Ni-Mn-Sn thin films is required to fully evaluate their potential for such magneto-electronic applications. Magnetic relaxation processes plays a vital role in enhancing the efficiency and reducing the power consumption in spintronic and microelectronic devices [ZUTI04]. Hence, understanding magnetic relaxation processes in these nanoscale devices has become one of the most interesting challenges in magnetism to date.

1.7 Motivation and objectives of current work

The above review of the literature reveals that Ni-Mn-Z Heusler alloys exhibit rich physical phenomena of technological importance. Due to MT, these materials display several interesting multifunctional properties. MCE is well investigated in bulk Ni–Mn-Z (Z = Sn, In, Ga, Sb) alloys [ZHAN16, DASR11, DASR13a, NAYA09] and it has been found that Ni-Mn-Z has a great potential to be good refrigerant material near room temperature. But information on Ni-Mn-Z thin films is scarce and the underlying physical questions related to the magnitude and type of MCE in these thin films still remain unanswered. Some of the literature on Ni-Mn-Z thin films show the suppression and broadening of MT [VISH10b, VISH11, AUGE12, BEHL13, CROU15], whereas some others show clear existence of MT [YUZU13, SOKO13, AKKE17, NIEM10]. But, these reports do not give sufficient information to evaluate the potential of Ni-Mn-Z thin films as room temperature magnetic refrigerants. So, this thesis work is aimed at investigating the MCE in Ni-Mn-Sn and Ni-Mn-In thin films around room temperature for magnetic refrigerant application. Effect of substitution of elements like Co, Fe, Cu in Ni-Mn-Sn and Ni-Mn-In alloys on the properties of these alloy films would also be investigated to find out means to enhance the desired properties of the ternary alloys.

Realizing the fact that these Ni-Mn-based thin films alloys have not been explored fully and these 2-dimensional thin films may show several more interesting properties, our research extended to explore other physical phenomena in the films. Some of these films show room temperature soft ferromagnetic behavior. This could be exploited for fabricating magneto-electrical devices. However, proper estimation and control of parameters like magnetic anisotropy, magnetic exchange interactions, and intrinsic and extrinsic damping are necessary since these properties determine the efficiency and power consumption in spintronic and microelectronic devices [ZUTI04]. Exploiting the advantage of FMR technique in the measurement of amplitude, dynamics, and anisotropy of magnetization vector M and individual spins, dynamic properties of Ni-Mn-X-Sn (X=Cu/Fe/Co) and Ni-Mn-Y-In (Y=Fe/Co) thin films would be investigated in this thesis for the first time.

Chapter 2

Experimental Methodology and Models

In this chapter, the experimental techniques used in the current investigations are discussed together with the relevant theory associated with these techniques. Specific instruments used and the different measurement methodologies employed are also presented. Experimental data and results presented in chapters 3, 4, 5, 6 and 7 are based on the experimental procedures outlined in this chapter.

2.1 Preparation and processing of samples

2.1.1 Sputtering target preparation

2.1.1.1 Arc melting

Arc melting is widely used for melting metals to form alloys of desired compositions. In this process, the constituent metals of the desired alloy are melted by heating *via* an electric arc struck between a tungsten electrode and the metals placed in a depression (crucible) in the copper hearth. In vacuum arc melting, the chamber is evacuated to the base vacuum and then purged with argon gas. Melting is performed under residual argon atmosphere. A sharp tungsten needle is used as electrode (anode) to strike an electric arc between the anode and the cathode (copper hearth). Heat generated by the electric arc melts the metals placed in the crucible to form the alloy ingot. Repeated melting of the alloy ingot is done to improve the homogeneity of the alloy composition. A schematic diagram of an arc melting furnace is presented in Figure 2.01.

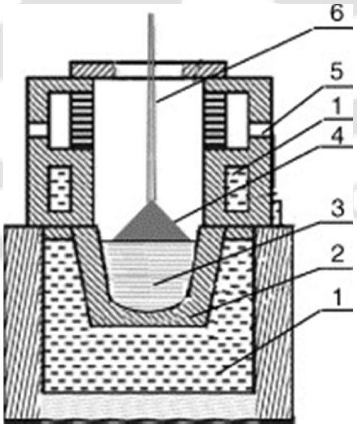

Figure 2.01: Schematic diagram of an arc melting furnace. (1) circulating water to cool the hearth, (2) copper hearth (cathode), (3) compacted metal blend, (4) electric arc between electrodes, (5) gas inlet valve (6) water cooled tungsten tip (anode) [QIND06].

Ni-Mn-Z (Z = Sn, In) alloy ingots were prepared by taking appropriately weighed quantities of high purity Ni (99.99%), Mn (99.95%), Sn (99.99%) and In (99.99%) pieces in a large capacity vacuum arc melting furnace available at Defence Metallurgical Research Laboratory, Hyderabad. 3 inch diameter ingot of a few millimeters thickness was cast after following the procedures outlined above. Figure 2.02(a) shows the irregularly shaped arc melted ingot of Ni_2MnIn alloy.

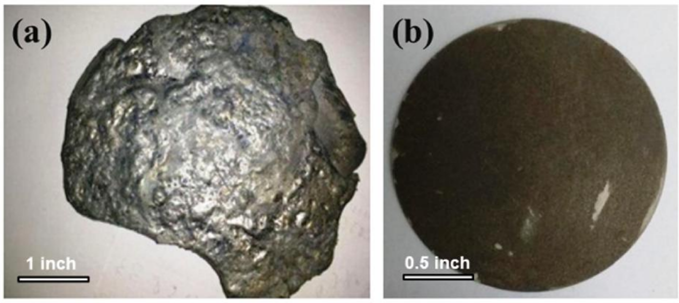

Figure 2.02: (a) Ingot prepared by arc melting. (b) Sputtering target of 2 inch diameter.

2.1.1.2 Electrical discharge machining

The irregularly shaped ingot has to be shaped into 2 or 1 inch diameter discs with 1 mm thickness and a smooth surface to serve as sputtering target in 2 or 1 inch magnetron gun. Wire electrical discharge machining is very simple and high-precision method for cutting almost any electrically conducting material in a very controlled way. Modern electrical discharge machining (EDM) is based on the basic principle known as electro-discharge erosion. In 1770, Joseph Preistly noticed that electrical discharges remove material from the electrodes during his experiments [KRAR03]. Later in 1960s, researchers in the Soviet Union invented wire EDM as a method for cutting steel to make tools [DULE71]. A thin, electrically charged EDM wire held between upper and lower mechanical guides forms one electrode, while the material being cut (work piece) forms the second electrode. Electrical discharge between the wire and the work piece creates sparks that rapidly cut away the material. A continuous flow of deionized water on the work piece and wire ensures removal of heat generated during cutting [TODD94]. As the charged wire never makes physical contact with the work piece, there are no cutting forces involved, making it possible to manufacture extremely small and delicate parts. Parts that require levels of accuracy and intricacy that traditional machining cannot achieve can be easily produced *via* wire EDM.

The randomly shaped ingots obtained by arc melting were then cut into 1 inch and 2 inch diameter discs of 1 mm thickness using a wire EDM unit (CNC wire cut EDM, DK7720) available at the Central Workshop, IIT Guwahati. These sliced discs were used as sputtering target for thin film fabrication. Figure 2.02(b) shows a typical sputtering target obtained by wire EDM.

2.1.2 Thin film fabrication

2.1.2.1 DC magnetron sputtering

The ejection of atoms from the cathode surface by bombarding high energy positive ions of noble gases (mostly argon) at a reduced gas pressure under high direct current (DC) voltage is known sputtering [OHRI92, WAGE94, SESH02]. In 1852, Sir W. R. Grove discovered surface coatings generated in a valve (vacuum tube) under a glow discharge [WAGE94]. Though this phenomenon was called as spluttering by Sir W. Thomson, it was soon renamed as sputtering. This process involves a momentum transfer between the impinging positive ions and the cathode surface atoms as shown in Figure 2.03(a), as a result of which physical removal of atoms from the cathode occurs.

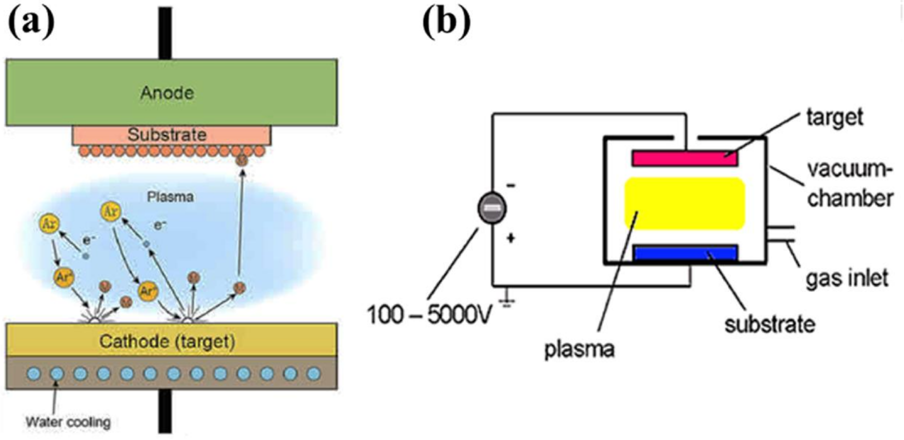

Figure 2.03: Schematic diagram of the (a) sputtering process and (b) the experimental arrangement for DC sputtering.

The sputter deposition process consists of three consecutive steps, namely, ejection of atoms from a source, transport of the atoms to the substrate, and condensation of the atoms on the substrate. Different types of sputtering processes such as DC, radio-frequency (RF), DC magnetron and reactive sputtering are widely used for thin film deposition. In this thesis work, DC magnetron sputtering has been used for preparing the thin films. Figure 2.03 depicts a typical arrangement used for DC sputtering. In this case, the target and substrate holder face each other in the vacuum chamber separated by a distance ranging from a few centimeters to few tens of centimeters. The target is connected to the negative output of a DC power supply and acts as the cathode. The electrically conducting substrate holder acts as the anode. After creating an argon atmosphere (pressure ~0.1−10 Pa), the gas discharge is ignited by applying a DC voltage. The ionized Ar^+ ions are now accelerated toward the target (due to negative bias voltage) and sputter atoms from the target. These ejected atoms subsequently get deposited on the substrate. At low pressures, the mean free path between collisions is large, the ionization efficiency is low and self-sustained discharges cannot be maintained below a few Pa pressure. As the pressure is increased at a fixed applied DC voltage, the electron mean free path decreases. So, more ions are generated and a larger current flows. If the pressure is too high, the sputtered atoms undergo increased collisional scattering resulting in low deposition rate. The deposition rate is proportional to the (a) power consumed, (b) square of the current density, and (c) reciprocal of spacing between the electrodes. DC sputtering works with all types of target materials which are conductive in nature.

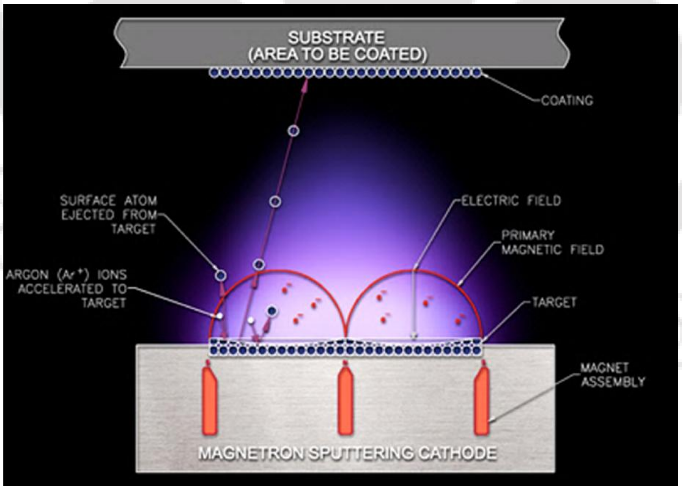

Figure 2.04: Schematic presentation of magnetron sputtering gun assembly [HTTP1].

However, DC sputtering suffers from two major drawbacks as compared to conventional evaporation, *viz*., (i) low deposition rate, and (ii) high thermal load on the substrate due to bombardment of secondary electrons. In order to increase the deposition rate and to control the thermal load, magnetron sputtering as described below in Figure 2.04 is utilized for the deposition of thin films.

In DC magnetron sputtering, electrons ideally do not even reach the anode but are trapped near the target, thereby enhancing the ionization efficiency. This is accomplished by employing a magnetic field oriented parallel to the target and perpendicular to the electric field. Practically, this is achieved by placing bar magnets behind the target as shown in Figure 2.04. The magnetic field lines emanate first normal to the target and then bend with a component parallel to the target surface and finally return to the magnet, to complete the magnetic circuit. Electrons emitted from the cathode are initially accelerated toward the anode, but execute a helical motion when they enter the region with parallel magnetic field. Therefore, they are bent in an orbit back to the target. Chief advantages of this technique are (1) increased sputtering rates (~ 5 - 10 times) due to high plasma density around target, (2) low discharge voltages of 300 to 1000 V due to the reduced plasma impedance resulting from high plasma density, and (3) low thermal load on the substrate due to deflection of secondary electrons by the magnetic field.

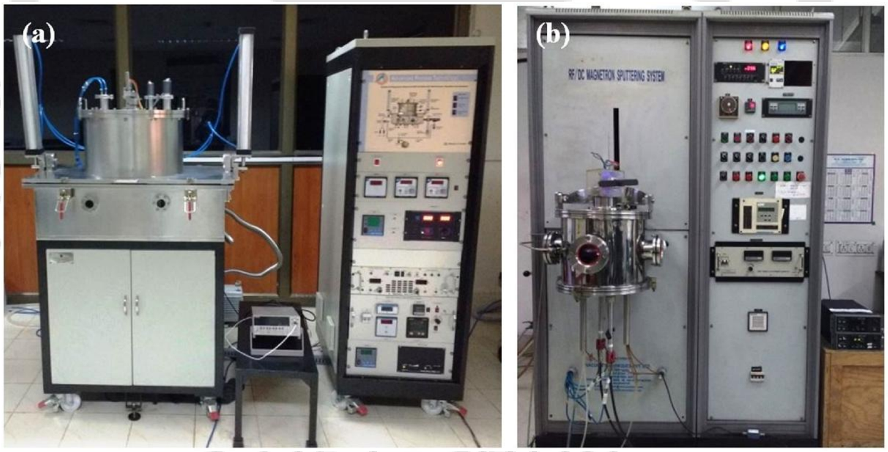

Figure 2.05: (a,b) Photographs of two DC magnetron sputtering systems used in this work.

Figure 2.05 depicts two magnetron sputtering systems used in this thesis work for fabricating thin films. The system (a) made by Advanced Process Technology, India, is equipped with two sets of three confocal DC/RF magnetron guns. This system is equipped with a combination of turbo molecular pump and rotary pump for creating vacuum. The substrates are loaded on the rotating substrate holder. This system was used to deposit thin films at high deposition pressure from 1 inch and 2 inch diameter targets described in chapters 3 (series 2), 4 and 7. On the other hand, the system (b) made by Vacuum Techniques, India, was used to deposit films at low deposition pressure from 2 inch targets as described later in chapters 3 (series 1), 5 and 6. This system is equipped with a combination of diffusion pump and rotary pump for creating vacuum. Before deposition, the chamber was evacuated to high vacuum (< 10^{-4} Pa) in both the systems. After stabilizing a constant argon gas pressure in the chamber, a constant DC power was applied to initiate the sputtering process. The deposition of the films on Si(100) substrates was carried out after stabilizing the argon ion plasma and sputter cleaning the target surface.

2.1.2.2 Film thickness optimization

In order to obtain thin films of different thicknesses, it is essential to understand the deposition rate of the film deposited under different sputtering conditions. Deposition rate of the films was calibrated using a surface profilometer (Vecco, Dektak-150) illustrated in Figure 2.06(a). Stylus profilers are versatile measurement tools for studying surface topography. Their primary function is to measure film thickness by scanning step heights and trench depths. Stylus profilers rely on a small diameter stylus moving along a surface either by movement of the stylus or movement of the surface of interest. A true stylus profiler moves linearly to obtain the measurement. As the stylus encounters surface features, the stylus moves vertically to measure various surface features, such as deposited film and irregularities. To monitor the thickness of the deposited films, a fine line is drawn along one edge on top of the cleaned substrate using a permanent marker. Subsequently, the deposition is done under controlled sputtering environment (constant Ar gas pressure, DC power and target to substrate distance, etc.) on the substrate for a given time at ambient temperature. After the completion of the deposition, the film is cleaned through sonication in acetone. After sonication, the film deposited on the substrate would reveal a clear step at the edge where the ink has been dissolved by treatment in acetone. The step height is evaluated using a stylus scan profile recorded using the surface profiler as displayed in Figure 2.06(b). The average deposition rate is then calculated by dividing the average thickness measured at various locations on the substrate with deposition time. In order to confirm the reproducibility of the results, more films were made under the same sputtering conditions and analysed using the profilometer. Similar procedure was followed for all the films prepared under different sputtering conditions.

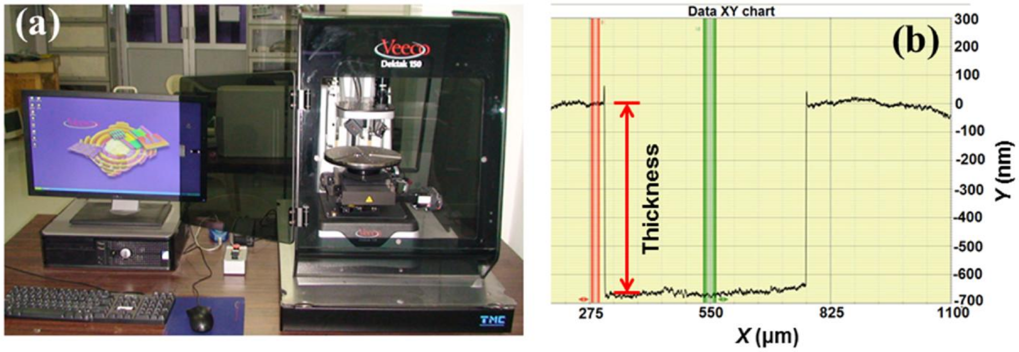

Figure 2.06: (a) Photograph of Vecco-Dektak 150 surface profilometer (b) Typical scan profile near the step. Red arrow indicates the step height or film theickness..

2.1.3 Post deposition processing

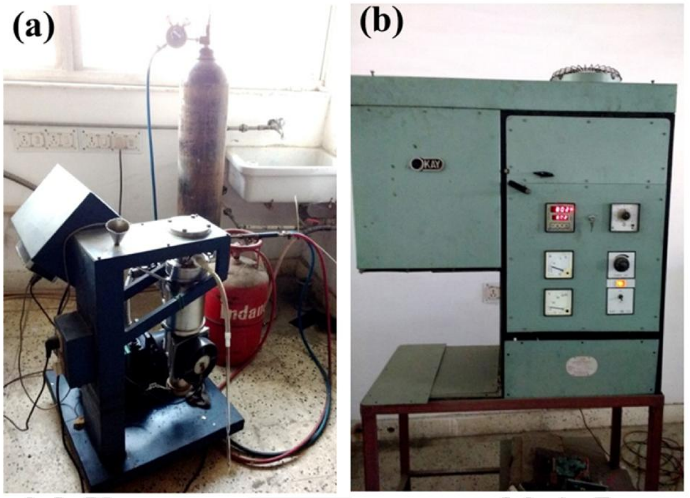

Figure 2.07: Photographs of (a) ampoule sealing setup, and (b) raising hearth furnace.

As-deposited thin films were subjected to heat treatment under different conditions depending upon the need. Since the metallic alloy films cannot be heated in air, the following procedure was followed: As-deposited films were taken in fused silica ampoules and pumped down to 10^{-3} Pa using an oil diffusion and rotary pump combination (Make: Vacuum Techniques, India) shown in Figure 2.07(a). The evacuated ampoules were then sealed in the pinched region with a neutral oxygenliquid petroleum gas flame and detached from the fused silica tube. The vacuum sealed ampoules containing the samples were placed inside a raising hearth electric furnace (Make: OKAY, India, Model: 70T-4) depicted in Figure 2.07(b), and heated to optimised annealing temperatures. The furnace with MoS_2 heating elements is equipped with a PID temperature controller and programmer for precise control of temperatures up to 1973 K. The ampoules were heated to the required annealing temperature, held at this temperature for the required time and allowed to cool down to room temperature by switching off the furnace.

2.2 Characterization of samples

2.2.1 X-ray Diffraction

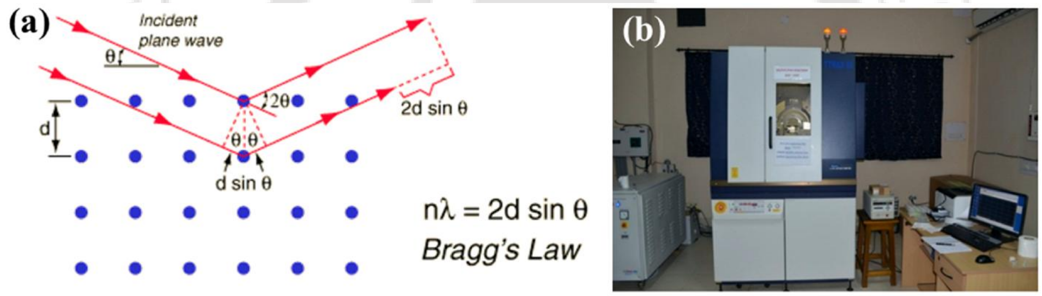

Figure 2.08: (a) Diffraction geometry of X-rays from a set of crystal planes with inter-planar distance d. (b) Photograph of Rigaku TTRAX III 18 kW powder X-ray diffractometer.

In a typical powder X-ray diffractometer, the X-ray source and the detector move by equal angular displacement at every step. This arrangement is known as θ-2θ geometry or Bragg-Brentano geometry (*c.f.* Fig 2.09 (a)). This configuration ensures that a high intensity beam diffracted from any particular set of crystalline planes of the sample reaches the detector. However, characterization of thin films using the conventional symmetrical Bragg Brentano configuration (θ-2θ) has several disadvantages. For example, X-rays with large incident glancing angles will penetrate a few to several micrometers inside the film. So, for thin films the beam penetration depth may be much more than the film thickness. In such a case, the experiment will produce weak signals from film and intense signal from substrate. The situation would be worse in case of single crystal substrates and in the case of multi-layer film stacks. To overcome this difficulty, a modified geometry is used for thin films known as grazing incidence XRD

(GI-XRD). In this geometry, the incidence angle is fixed at a small value (exceeding the critical angle of total reflection, typically, ~1° - 3°;) and the angle between the incident beam and the diffracted beam (2θ) is varied by moving only the detector arm. Thus, the incident beam is confined on the sample surface of interest, giving its true diffraction pattern, while the signal from the substrate is drastically reduced due to the small angle of incidence. All measurements made in this this work were carried out in GI-XRD mode with 1° grazing incidence angle, acceleration voltage of 50 kV and tube current of 180 mA.

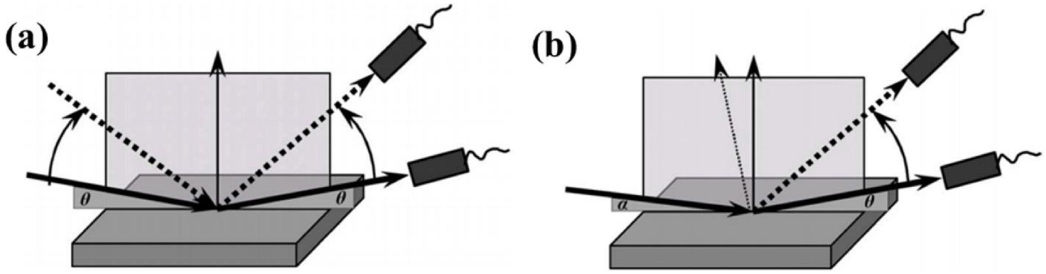

Figure 2.09: (a) Symmetric θ-2θ, and (b) asymmetric grazing incidence XRD geometries [BOUR12].

Structural parameters such as lattice constants (*a, b, c*), average crystallite size (*D*), lattice strain (ε) present in the crystallites have been estimated by a careful analysis of the XRD patterns. As discussed in chapter 1, Heusler alloys exhibit two crystal phases, namely, a (i) high symmetric austenite (cubic $L2_1$ in ordered structures), and (ii) low symmetric martensite (modulated structures, 14M orthorhombic supercells [BROW02] for present films). Figure 2.10(a,b) show typical XRD patterns for these two phases. To evaluate the lattice constants for of films with these structures, the following formulae have been used.

$$\frac{1}{d^2} = \frac{h^2 + k^2 + l^2}{a^2} \text{ (for } L2_1 \text{ structure)} \qquad 2.01$$

$$\frac{1}{d^2} = \frac{h^2}{a^2} + \frac{k^2}{b^2} + \frac{l^2}{c^2} \text{ (for 14M structure)} \qquad 2.02$$

where *d* is the inter-planer spacing defined by the Bragg's law [CULL01],

$$2d\sin\theta = n\lambda \qquad 2.03$$

and *a,b,c* are lattice constants along X,Y and Z-axis of the crystal.

Average crystallite (grain) size *D* can be estimated by Schërrer's equation [ROBE79],

$$D = \frac{k\lambda}{\beta \cos\theta} \qquad 2.04$$

Froom the broadening of the Bragg peaks, Here, β is the full width at half maximum (FWHM) of the Bragg peak, k is a constant, λ is the incident wavelength and θ is the diffraction angle. Eq, 2.04 attributes the entire broadening mechanism to crystallite sie reduction. Williamson-Hall (W-H) method [WILL53] defines the FWHM in terms of both reduction in crystallite size and microstrain (ε) present in crystallite as,

$$\beta = \frac{k\lambda}{D\cos\theta} + 4\varepsilon \tan\theta \qquad 2.05$$

Though W-H method is considered superior to Schërrer's for estimating D (and ε), the former is applicable only in case of structures with many XRD peaks such as 14M.

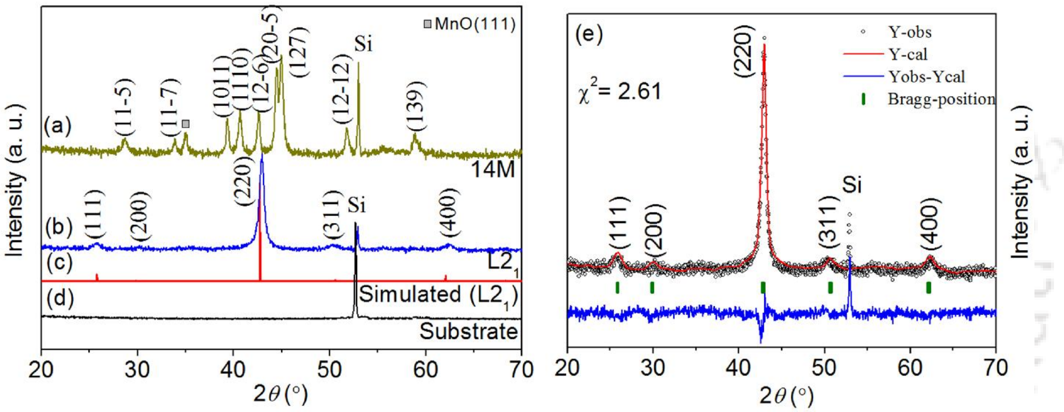

Figure 2.10: XRD patterns of Ni-Mn-Sn film with (a) martensite 14M, and (b) austenite L2$_1$ structures. (c) Simulated L2$_1$ structure. (d) XRD pattern of Si(100) substrate. (e) Output of Rietveld refinement performed on L2$_1$ pattern shown in (b).

As mention in chapter 1, some amount of atomic disorder is always found in the ordered L2$_1$ alloys. By comparing the experimentally found XRD pattern and theoritically simulated XRD patterns, the percentage of L2$_1$ and B2 order in the Heusler alloy film can be estimated using the following relationships proposed by Webster and Ziebeck [WEBS73] and subsequently modified by Takamura *et. al.* [TAKA09]:

$$(I_{200}/I_{220})_{exp} = S_{B2}^{2}\ (I_{200}/I_{220})_{th} \qquad 2.06$$

$$(I_{111}/I_{220})_{exp} = \left[S_{L2_1}\left(\frac{3-S_{B2}}{2}\right)\right]^2 (I_{111}/I_{220})_{th} \qquad 2.07$$

where the I_{hkl}s refer to the intensity of the Bragg peak designated by its Miller indices (hkl) and the suffixes 'exp' and 'th' represent experimentally obtained and theoretically simulated intensity values, respectively. S_{B2} and S_{L2_1} correspond to the degree of B2 and $L2_1$ ordering, respectively. Figure 2.10(b,c) shows XRD patterns experimentally recorded and simulated using CaRIne Crystallography 3.1^{TM} software for annealed $Ni_{48.84}Mn_{37.96}Sn_{13.20}$ film deposited on Si(100) substrate [MODA16]. The above analysis shows 82% $L2_1$ ordering (S_{L2_1}) along with 98% B2 ordering (S_{B2}) in the film.

FullProf software package was used to perform Rietveld refinement of experimental XRD pattern [RODR01, RODR93] to refine the crystal structures and extract crystallographic parameters from recorded XRD patterns. In simple terms, the Rietveld refinement procedure involves comparison of a simulated XRD pattern of the unit cell corresponding to the sample with the experimental data by a least squares procedure. Hence, it not only provides better estimate of the lattice constants but also provides other structural information such as bond angles, bond lengths, etc. The quality of refinements can be confirmed from the value of reduced chi-square (χ^2) found in the refinement process. χ^2 above 10 are not acceptable. Details about refinement using FullProf and refine parameters can be found elsewhere [ANIN01]. Figure 2.10(e) represent the typical refined pattern of 823 K annealed $Ni_{48.84}Mn_{37.96}Sn_{13.20}$ film. In the figure, open circles represent the experimental diffraction data (Y_{obs}) and the solid line corresponds to the fit obtained by Rietveld refinement method (Y_{cal}). The difference data (Y_{obs}-Y_{cal}) and χ^2 values indicate the goodness of the fit.

2.2.2 Energy dispersive X-ray analysis

As discussed in the introduction section, the properties of Heusler alloys are strongly dependent on the composition of the alloy. During deposition of different sets of thin films, the deposition conditions have been varied which in turn would influence the stoichiometry of the deposited thin films. Hence, compositional analysis of the films is very important for understanding the properties of these thin films. A field emission scanning electron microscope (FESEM, Sigma Zeiss, Germany) equipped with energy dispersive spectroscopy (EDS) attachment (Oxford) has been used to confirm the elemental composition. A snap shot of the FESEM used in the present study is shown in Figure 2.11.

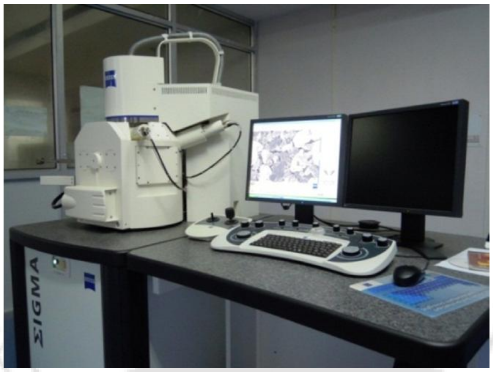

Figure 2.11: Pictorial view of the FESEM (Sigma Zeiss) used in the studies.

In an FESEM, electrons are emitted from a field emission source under ultra-low vacuum. The field emission source is usually tungsten filament (cathode) with a sharp tip which is placed in a large electrical potential gradient. The significance of the extremely thin and sharp tip (~10 - 100 nm) is to concentrate the electric field to an extreme level so that the work function of the material is lowered and electrons can leave the cathode easily. After emission, the electrons are accelerated by applying an accelerating potential (0.5 - 50 kV) between the cathode and the anode. This voltage combined with the beam diameter determines the resolution of the image. As the voltage increases, better point-to-point resolution can be obtained. Because of the smaller size of the electron source, the beam produced by this emitter is about 1000 times smaller than that in a standard scanning electron microscope (SEM), which markedly improves the image resolution. The beam is collimated by electromagnetic condenser lenses, focused by an objective lens and scanned across the surface of the sample by electromagnetic deflection coils. As the electrons interact with the sample, they produce secondary electrons, backscattered electrons and characteristic X-rays. These signals are collected by one or more detectors to form images which are then displayed on the computer screen to provide different structural information.

The primary imaging method is by collecting the scattered secondary electrons [HTTP4]. In this method, the detector converts the scattered secondary electrons into an image to display on the computer screen. In this mode, the images are in grayscale as the electrons detected here have energies beyond the light spectrum. The backscattered electrons also provide the same information as secondary electron. However, in backscattered mode, the image has real grayscale contrast as elements with higher atomic number will absorb more electrons than an element with a lower atomic number, resulting in high atomic number element appearing grayer than the lighter one. The characteristic X-rays are the beams which provide information about the composition of the specimen being used.

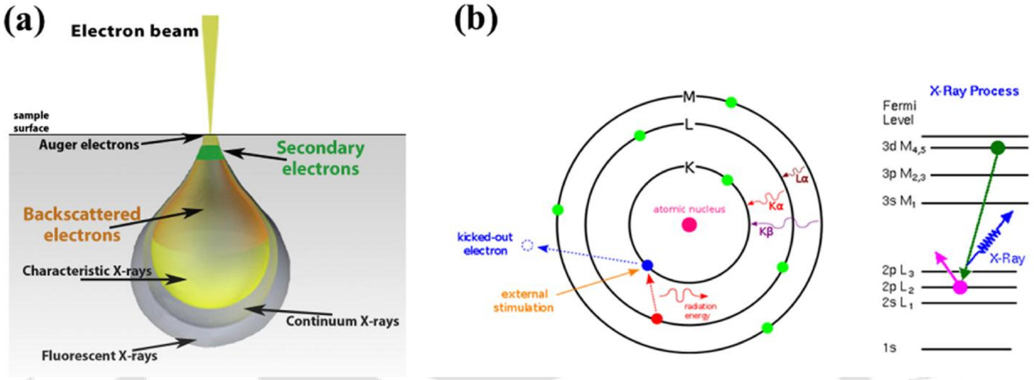

Figure 2.12: (a) Electrons and photons emanating from tear-shaped interaction volume during electron beam impingement on specimen surface [HTTP2]. (b) Characteristic X-ray emission mechanism from an atom during electron-atom interaction [HTTP3].

During EDS analysis, the specimen is bombarded with an electron beam inside the SEM. The electrons colliding with the specimen knock off some of the electrons from the inner shells of the atoms, as shown in Figure 2.12(b). A position vacated by an ejected inner shell electron is eventually occupied by a higher energy electron from an outer shell. To be able to do so, the transferring outer electron must give up some of its energy by emitting an X-ray. The amount of energy released by the transferring electron depends on which shell it is transferring from, as well as which shell it is transferring to. Furthermore, the atom of every element releases X-ray with unique amounts of energy during the transferring process. Thus, by measuring the amounts of energy present in the X-ray being released by a specimen during electron beam bombardment, the identity of the atom from which the X-ray was emitted can be established. The output of an EDS experiment is an EDS spectrum, which is just a plot of how frequently an X-ray is received for each energy level. An EDS spectrum normally displays peaks corresponding to the energy levels for which most X-rays had been received. Each of these peaks is unique to an atom, and therefore corresponds to a single element. The higher the intensity of the peak in a spectrum, the more is the concentration of the element is in the specimen. In the present work, as-deposited and annealed films are directly mounted on an adhesive carbon tape stuck on the FESEM stub and characterized after the customary gold coating at the top.

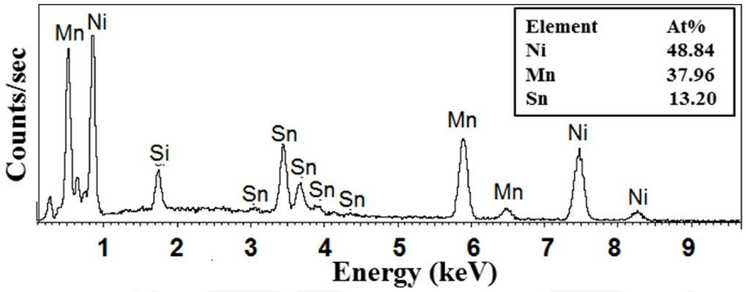

Figure 2.13: EDS pattern of a Ni-Mn-Sn thin film sample with elemental composition map in atomic percentage.

2.2.3 Atomic force microscopy

Scanning Probe Microscopy (SPM) is a powerful non-destructive technique to analyse the surface atomic morphology of thin films. SPM involves scanning the surface of a sample with a very fine probe (tip) and monitoring the strength of interaction between the atoms at the tip and the surface. The interaction between the atoms in the sharp probe tip and the film surface provides 3D topographic image of the atomic arrangement on the film surface. Scanning tunnelling microscope (STM) and atomic force microscope (AFM) are two popular SPM techniques. STM involves study of tunnelling of electrons between the microscope's scanning tip and the sample through a thin air barrier. The tunnelling current is used to image the atoms on the sample surface and infer the nature of atoms involved in the interaction. Unfortunately, this technique is limited to electrically conducting or semiconducting samples. In contrast, AFM generates images based on the modulation of inter-atomic forces and hence does not require the sample to be electrically conducting. AFM also involves scanning the tip across the sample surface. The fine tip is generally made of silicon or silicon nitride with typical radius of curvature 3 to 15 nm.

The working principle of an AFM is illustrated schematically in Figure 2.14(a). Here, the tip is brought to very close to the surface and van der Waals forces act between the tip and sample surface causing the tip to move closer to the sample surface. As the tip bends towards the sample, the laser beam bouncing off the bent cantilever, suffers a deflection which is recorded by the position-sensitive photodiode detector. The difference between laser light intensities falling on the four quadrants of the photodetector provides a good measure of the shift in the beam. The detector signal so generated is sent to the computer control feedback loop, which tries to keep the cantilever deflection constant by maintaining the distance between the sample and the cantilever constant (in what is known as the constant z mode). This is done by moving the piezoelectric scanner at each (x, y) position in the z-direction by adjusting the voltage applied to it. The signals from the position-sensitive photodiode detector are processed by the data processor and converted as raw data. It is crucial to adjust the tip of the cantilever, prior to the scanning a sample, in such a way that the reflected laser from the back of the cantilever falls at centre of position-sensitive photodiode detector, which can be confirmed by null voltage reading. The surface morphology of ternary Ni-Mn-Z and quaternary Ni-Mn-X-Z (X = Cu/Fe/Co, Z = Sn,In) thin films was imaged using the Agilent, 5500 series and Bruker, Innova series atomic force microscopes. The samples were scanned over 2 × 2 μm^2 area at multiple places on the sample so that reasonably good estimates of dimensions are obtained. The data were processed and analysed using open source software WSxM [HORC07] to obtain the average (R_{av}) and root mean square (R_{rms}) surface roughness values.

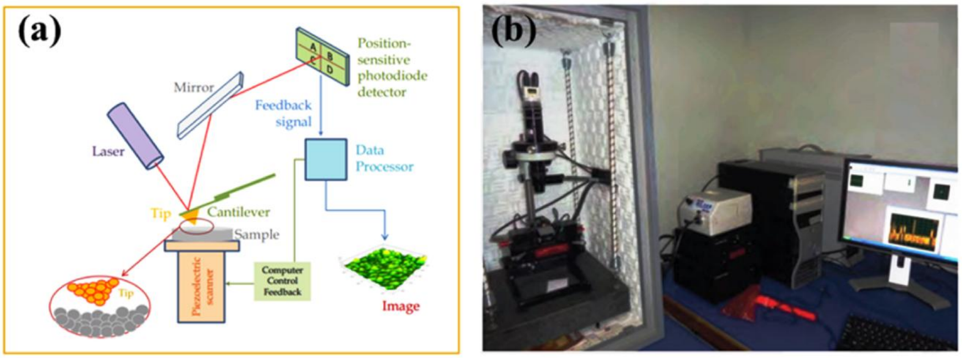

Figure 2.14: (a) Schematic diagram of an Atomic Force Microscopy. (b) Agilent, 5500 series Atomic Force Microscopy used in the current studies.

2.2.4 Vibrating sample magnetometer

Vibrating Sample Magnetometer (VSM) is a sensitive and versatile instrument to measure the net dipole moment of a material exposed to a magnetic field [SVOB04, CZIC06]. Using VSM, the magnetic moment of the material can be determined either as a function of magnetic field (*M-H* curve) at a particular temperature or as a function of temperature (*M-T* curve) at a particular magnetic field (H = 0 or H_i). The basic principle used in VSM to measure magnetization is the Faraday's laws of electromagnetic induction. VSM was first designed at the Lincoln laboratories, MIT, USA, by Simon Fonerin in 1959 [FONE59]. Since then, many modifications have been made to improve the sensitivity of the instrument, but the underlying principle remains the same [SMIT56].

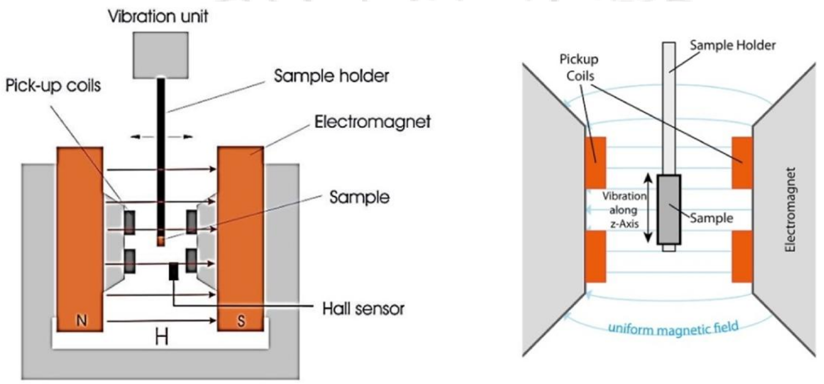

Figure 2.15: Schematic block diagram of modern VSM system [MCEL94, RAFI15].

Figure 2.15 displays the schematic diagram of a modern VSM. VSM consists of a (a) vibration exciter and sample holder, (b) water cooled electromagnet and power supply, (c) Hall probe, (d) pair of pick-up coils, (e) lock-in amplifier, (f) control panel, and (g) computer interface. The sample to be studied is placed inside a uniform magnetic field and set into sinusoidal vibration at a constant frequency using the vibration exciter. Due to the vibration of a magnetic sample, the flux inside the pick-up coils changes, resulting in an induced electromotive force due to electromagnetic induction. The induced voltage is measured by a lock-in amplifier using the piezoelectric vibration frequency signal as reference voltage. The induced voltage signal has amplitude proportional to the magnetic moment of the sample, the vibrating amplitude and the vibration frequency. Through the use of lock-in amplifier and feedback techniques, only that portion of the signal arising from the magnetic moment is picked up and is converted into direct read-out in the unit of magnetization (e.g. emu) on a digital panel meter. Raw experimental data is also stored in the computer memory.

Interactive software permits programming of field, temperature and time steps and plotting of desired quantities.

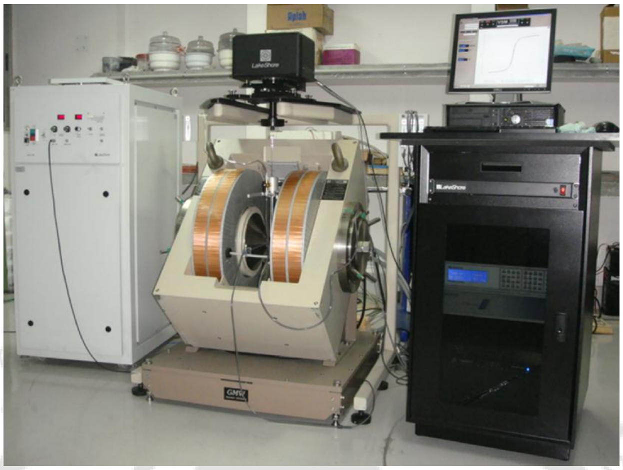

Figure 2.16: Photograph of VSM (Lakeshore 7410) used in the present investigations.

In this study, a Lakeshore 7410 VSM (*cf.* Figure 2.16) was used to characterize ambient and temperature dependent magnetic properties of thin films in the temperature range of 20 K – 310 K and 300 K – 1000 K using a closed cycle refrigerator and high temperature oven, respectively. The thin film samples were cut into ~5 mm (L) × 8 mm (W) size and firmly placed at the lower end of the fused silica sample rod using a piece of teflon tape. Magnetization data corresponding to the teflon tape is subtracted from the raw data prior to further analysis. The orientation of the film plane with respect to applied field was adjusted using a goniometer assembly for in-plane or out of plane measurements on thin films. Prior to the magnetic measurements, a calibration procedure was carried out using standard Ni sphere sample to standardise the magnitude of the measured magnetic moment. The measurement sequence is programmed as per the user's choice using the software (IDEASVSM) provided with the instrument such that the program starts either from the maximum field or from the zero applied field. The sequence is made with the intent to collect optimum number of data points, so that the extracted magnetic parameters (saturation magnetization, remenance magnetization, coercivity, etc.) carry minimum error. The magnetic field is increased automatically in user-defined steps for measuring *M-H* loops. Similarly, for high temperature *M-T* measurements, a high temperature oven attachment capable of providing a controlled heating/cooling of the sample from room temperature to 1000 K was used. For *M–T* measurements, the film was loaded in a high temperature sustainable holder (ceramic holder or quartz rod) after a calibration run using standard Ni sample. The oven was purged with nitrogen gas to avoid oxidization of the sample at high temperatures. Magnetization was recorded at different temperatures at a constant in-plane applied magnetic field. The heating rate and *M-T* sequences were programmed using the IDEASVSM software.

Prior to evaluating the magnetic entropy change (ΔS_M) during phase transition, initial *M-H* isotherms were recorded at different temperatures across the transition temperature. ΔS_M was estimated subsequently by integrating the *M-H* isotherms according to the Maxwell thermodynamic equation [PECH99],

$$\Delta S_M = \int_0^H \left(\frac{\partial M}{\partial T}\right)_H dH \tag{2.08}$$

where *M*, *H* and *T* are magnetization, magnetic field and temperature, respectively. In the present study, magnetization measurements were made at discrete temperature intervals. Hence ΔS_m was evaluated using the summation,

$$\Delta S_M(T,H) = \sum_i \frac{M_{i+1}(T_{i+1},H)-M_i(T_i,H)}{T_{i+1}-T_i}\Delta H \tag{2.09}$$

Another important property known as refrigeration capacity (RC) which represents the efficiency of a MCE material has also been evaluated using the relation [PECH01],

$$RC = \int_{T_1}^{T_2} \Delta S_M(\mathrm{T})_\mathrm{H}\, dT \tag{2.10}$$

It should be noted that since the alloys are in thin film form, the ΔS_M and RC values are evaluated in units of erg/cc.K and erg/cc (in CGS) unit. In order to facilitate comparison with bulk materials, these values are also represented in J/kg.K and J/kg units. For this, average alloy density was estimated using the additive rule,

$$\rho_{alloy} = a_X\rho_X + a_Y\rho_Y + a_Z\rho_Z, \tag{2.11}$$

where a_X, a_Y and a_Z are wt.% and ρ_X, ρ_Y and ρ_Z are bulk density of X,Y and Z alloys.

2.2.5 Ferromagnetic resonance spectroscopy

Ferromagnetic resonance (FMR) spectroscopy is a very powerful tool to evaluate the functional properties of a ferromagnetic material by analysing the dynamic response of the magnetic moment of the material at microwave frequencies. FMR spectra can be recorded in two modes, viz., ‘field swept’ mode where the microwave frequency is kept fixed and the external applied field is swept to record the spectra, and 'frequency swept' mode in which the applied field is kept fixed and the frequency of microwave signal is varied in order to record the spectra. In this this work, 'field swept' FMR technique was used. Again, two types of field swept FMR setups have been used in this thesis work, viz., a micro strip-line based homemade setup and a cavity based electron spin resonance spectrometer based setup. Brief outlines of these two techniques are given below.

2.2.5.1 Micro strip-line based FMR spectrometer

The micro strip-line based FMR (MS-FMR) was first developed in the 1960s [PATT68]. It consists of a combination of a metal strip of a few micrometers width which acts as the signal line (known as micro strip-line) and a parallel ground plane of infinite width. The two metallic planes are separated by a layer called the substrate made from a microwave dielectric material. A schematic diagram of a MS-FMR experimental setup is shown in Figure 2.17. Using MS-FMR setup, one can measure the microwave absorption spectrum at different microwave frequencies (few MHz to several GHz range) [HARW11, SHAW13, NAKA13] and also as a function of angle between applied external magnetic field and the sample (thin film) plane at desired frequencies. With these features, the MS-FMR technique can be used for evaluating material parameters such as the Gilbert or intrinsic damping constant (α), g-factor, magnetic anisotropy, inhomogeneities, etc. more accurately due to simpler data analysis as compared to other techniques employing measurements at a single microwave frequency.

The experimental setup used consisted of a home built micro strip-line coupled to a vector network analyzer (VNA, Model PNA-X, N-5242A) and Schottky diode detector (Agilent 8473D). The strip-line, which also serves as the sample holder is mounted between the pole pieces of an electromagnet. The magnetic thin film sample is placed on the micro strip-line with the film side facing the strip-line such that at zero degree ($\theta_H = 90^o$), the long axis of the film lies along the applied field direction. The coordinate system used is illustrated in Figure 2.19(a). The frequency of the microwave signal is selected using the VNA with the microwave power maintained at an optimum value (typically, ~5 dBm). Magnetic field modulation and lock-in detection techniques are employed to record the first derivative absorption spectrum as a function of applied magnetic field (*H*) for the desired frequency/angular settings. Using this setup, the FMR spectrum for a film can be recorded for different frequencies ranging from 2 GHz to 18 GHz with an interval of 0.5 GHz and also for different angles of applied field with respect to the film plane starting from in-plane to out-of-plane configuration for a fixed frequency. The resonance field (H_r) and linewidth of the spectrum (ΔH) have been extracted and fitted with appropriate formula to evaluate the desired magneto-dynamic parameters. The detailed discussion on the analysis of FMR data is presented in section 2.2.5.3. Despite several advantages, the MS-FMR also has some limitations. MS-FMR is very sensitive to the quality of the strip-line and coupling of the signal with the detector, which have to be optimized properly. Moreover, proper subtraction of background signal is also necessary to obtain good data. Due to these constraints, the homemade setup described above was unable to yield good FMR data for thin films with low magnetic moment.

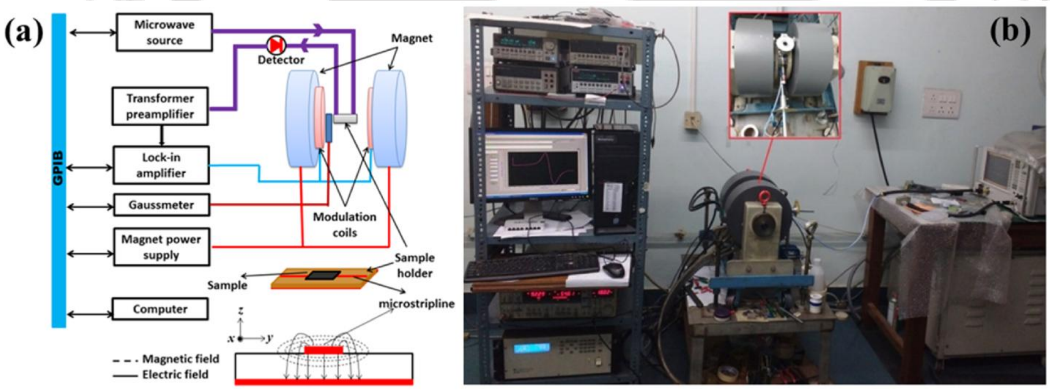

Figure 2.17: (a) Block diagram and (b) photograph of the MS-FMR setup.

2.2.5.2 Electron Spin resonance spectrometer based FMR measurement

To record FMR spectra of thin films with low magnetic moment, electron spin resonance (ESR) spectrometers (Models - Bruker EMX EPR and JEOL JES-FA200) operating at 9.44 GHz with a frequency modulation of 100 kHz have been used. Schematic diagram of a typical ESR setup is shown in Figure 2.18(a). To measure the microwave absorption spectra as a function of film orientation with respect to the applied field, a sample rotation assembly was designed for the ESR spectrometer. Thin film samples were firmly tethered to the flat tail of a fused silica sample rod such that at $\theta_H = 90°$, the long axis of the film lies along applied field direction. The sample rod, which could be manually placed in angular positions about a vertical axis, is inserted into the microwave cavity of the ESR spectrometer to record absorption spectrum as a function of applied magnetic field.

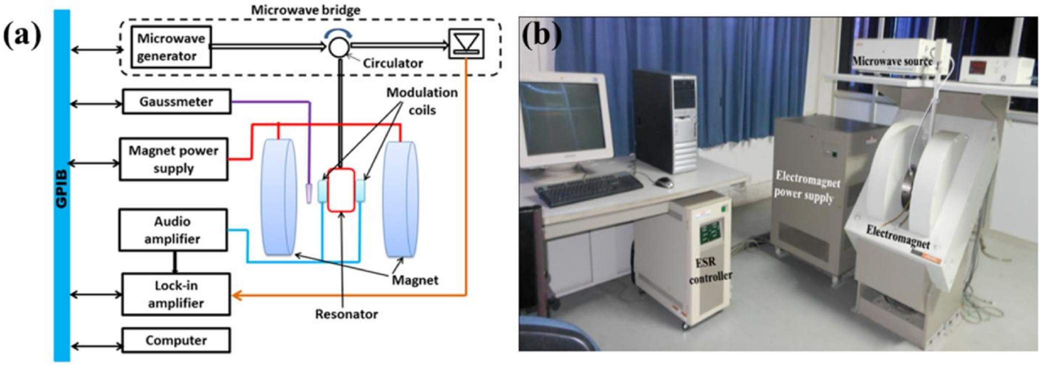

Figure 2.18: (a) Block diagram and (b) photograph of ESR spectrometer (JEOL JES-FA200) used in the studies.

Since the cavity FMR (C-FMR) methodology is based on commercial ESR setup with a high Q factor resonant cavity, the sensitivity of the instrument is very high as compared to the home built MS-FMR unit. Automatic phase tuning available with the commercial instrument ensures proper recording of the absorption signal with good frequency and field stabilities. Further, analysis of C-FMR data is simplified due to the microwave field uniformity over the sample and the absence of microwave electric currents in the sample [MAKS15]. So, FMR spectra of samples with low magnetic moments can also be captured and analysed with this technique.

2.2.5.3 Analysis of FMR spectra

The total energy of an electron in a ferromagnetic material under the influence of an external magnetic field is an important entity in the analysis of FMR spectra. For a ferromagnetic thin film having both in-plane and out-of-plane (perpendicular) anisotropy, the total magnetic free energy per unit volume can be expressed as [JOHN96, MODA17],

$$\begin{aligned} E = -M_s H\left[\sin\theta_H \sin\theta_M \cos\left(\varphi_M - \varphi_H\right) + \cos\theta_H \cos\theta_M\right] + 2\pi M_s^2 \cos^2\theta_M \\ + K_u \sin^2\theta_M \sin^2\varphi_M - K_1 \cos^2\theta_M \end{aligned} \tag{2.12}$$

where the first term corresponds to Zeeman energy and the second term represents the dipolar demagnetization energy. The third term refers to in-plane anisotropy and the fourth term implies effective perpendicular magnetic anisotropy energy. K_u is the in-plane anisotropy constant and K_1 is the out-of-plane anisotropy constant, which also includes other first-order (intrinsic) anisotropy energy contributions except the shape anisotropy.

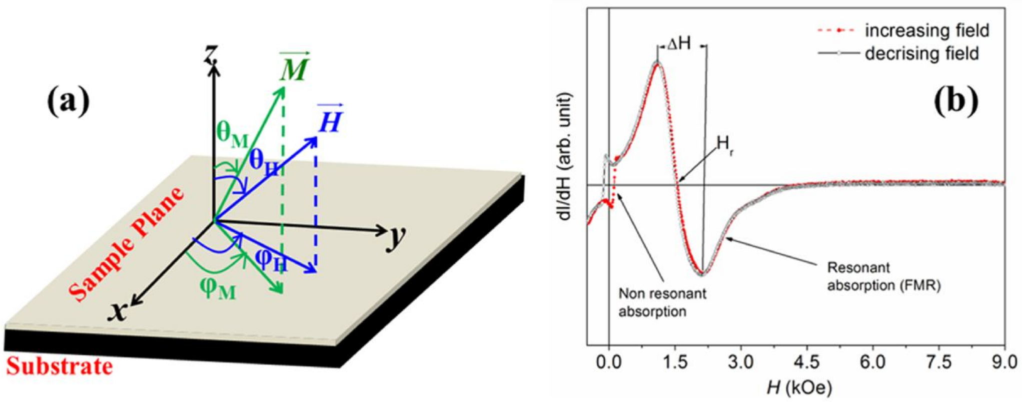

Figure 2.19: (a) Spherical coordinate geometry used in FMR analysis. (b) Typical FMR spectra recorded for Ni-Mn-Sn film at $\theta_H = 90°$ using C-FMR technique.

The coordinate system used in this treatment is illustrated in Figure 2.19(a). Here, φ_H (φ_M) is the in-plane angle between H (M) and x-axis, and θ_H (θ_M) is the polar angle between H (M) and z-axis. At resonance, the resonance frequency (f_r) of the uniform precession mode of the electron can be expressed in terms of the energy density using Smit-Beljers formula [SUHL55, ACHE03] as,

$$f_r^2 = \left(\frac{\gamma}{2\pi}\right)^2 \frac{1}{M_S^2 \sin^2\theta_M}\left[\frac{\partial^2 E}{\partial\theta_M^2}\frac{\partial^2 E}{\partial\varphi_M^2} - \left(\frac{\partial^2 E}{\partial\theta_M \partial\varphi_M}\right)^2\right] \qquad 2.13$$

By substituting the energy derivatives and imposing boundary conditions, one can arrive at simplified equations at resonance. Thus, in the case of angular variation measurement at $\varphi_H = 0$, Eqn. 2.13 reduces to

$$f_r = \left(\frac{\gamma}{2\pi}\right)\sqrt{\begin{matrix}\left(H\cos(\theta_M - \theta_H) - 4\pi M_{eff}\cos^2\theta_M + H_u\right) \\ \left(H\cos(\theta_M - \theta_H) - 4\pi M_{eff}\cos 2\theta_M\right)\end{matrix}} \qquad 2.14$$

where $4\pi M_{eff}$ ($= 4\pi M_s - 2K_1/M_s$) is called the effective magnetization. H_u ($= 2K_u/M_s$) is the in-plane anisotropy where K_u is the in-plane anisotropy constant. While reducing Eqn. 2.14, the energy minimum condition, viz.,

$$\left.\frac{\partial E}{\partial\theta_M}\right|_{\varphi_M = \varphi_H = 0} = 0 \qquad 2.15$$

or

$$-M_sH\left[\sin\theta_H\cos\theta_M-\cos\theta_H\sin\theta_M\right]=2\pi M_s^2\sin 2\theta_M-K_1\sin 2\theta_M \qquad 2.16$$

was used, resulting in

$$H=\frac{1}{2}\left(4\pi M_s-\frac{2K_1}{M_s}\right)\frac{\sin 2\theta_M}{\left[\cos\theta_H\sin\theta_M-\sin\theta_H\cos\theta_M\right]} \qquad 2.17$$

Solving Eqn. 2.14 and 2.17 numerically, one can obtain the typical variation of FMR resonance field (H_r) with θ_H. Numerical fitting of experimentally measured H_r versus θ_H data to Eqn. 2.14 and 2.17 yields various parameters like Landé g-factor (g), effective magnetization ($4\pi M_{eff}$) and also a visual estimate of anisotropy present in the system. The perpendicular anisotropy constant (K_1) can be extracted from the $4\pi M_{eff}$ by substituting the saturation magnetisation (M_s) of the sample measured using a VSM. K_u can be determined from FMR spectra recorded as a function of φ_H in in-plane orientation. Now, for in-plane angular variation (φ_H) with in-plane easy axis (θ_M=90 °), the boundary conditions are $\theta_M = \theta_H = 90°$. Energy minimization using these conditions yield,

$$\left.\frac{\partial E}{\partial\varphi_M}\right|_{\theta_M=\theta_H=90}=M_sH\sin\left(\varphi_M-\varphi_H\right)+K_u\sin 2\varphi_M=0 \qquad 2.18$$

Or,

$$H=\frac{2K_u}{M_s}\frac{\sin\varphi_M\cos\varphi_M}{\sin\left(\varphi_H-\varphi_M\right)} \qquad 2.19$$

Using these, Eqn. 2.13 can be reduced as

$$f_r=\left(\frac{\gamma}{2\pi}\right)\sqrt{\begin{matrix}\left(H\cos\left(\varphi_M-\varphi_H\right)+\left(4\pi M_s-\frac{2K_1}{M_s}\right)+\frac{2K_u}{M_s}\cos^2\varphi_M\right)\\ \left(H\cos\left(\varphi_M-\varphi_H\right)+\frac{2K_u}{M_s}\cos 2\varphi_M\right)\end{matrix}} \qquad 2.20$$

When $4\pi M_s \gg H_u$, where $H_u = 2K_u/M_s$, the expression for in-plane H_r (from the Eqns. 2.20 and 2.19) can be simplified to [LEEH08, SIHU07, GUOX14],

$$H_r=H_0-H_u\cos 2\varphi_H \qquad 2.21$$

This gives a maximum resonance field shift, $\delta H_r = 2H_u$ and a mean value of the FMR field, and $H_0 \sim (2\pi f_r/\gamma)^2/4\pi M_s$. Thus, H_0 helps in determining the magnetization of a given sample directly from FMR measurement. H_u can be obtained by fitting in-plane angular dependence of H_r using Eqn. 2.11.

On the other hand, if in-plane anisotropy (H_u) is absent in the sample, then the energy equation becomes,

$$\begin{aligned} E = &-M_s H\left[\sin\theta_H \sin\theta_M \cos\left(\varphi_M - \varphi_H\right) + \cos\theta_H \cos\theta_M\right] \\ &+ 2\pi M_s^2 \cos^2\theta_M - K_1 \cos^2\theta_M \end{aligned} \qquad 2.22$$

Then, Eqn. 2.14 and 2.17 can be written as

$$f_r = \left(\frac{\gamma}{2\pi}\right)\sqrt{\begin{array}{l}\left(H\cos\left(\theta_M - \theta_H\right) - 4\pi M_{eff}\cos^2\theta_M\right) \\ \left(H\cos\left(\theta_M - \theta_H\right) - 4\pi M_{eff}\cos 2\theta_M\right)\end{array}} \qquad 2.23$$

$$H = \frac{1}{2}\left(4\pi M_s - \frac{2K_1}{M_s}\right)\frac{\sin 2\theta_M}{\left[\cos\theta_H \sin\theta_M - \sin\theta_H \cos\theta_M\right]} \qquad 2.24$$

Apart from estimating anisotropy, FMR spectra can be used to understand the spin relaxation mechanism under the influence of an external magnetic field. The FMR linewidth (ΔH) provides a clear picture of the magnetic quality, magnetic interaction, homogeneity, defeats present in the material and also permit to estimate an important parameter, viz., the Gilbert damping constant (α). These properties determine the efficiency and power consumption in spintronic and microelectronic devices [ZUTI04]. The total peak-to-peak linewidth (ΔH) has contributions from different sources of damping which can be expressed as [MIZU02, YILG07, KURE13, LIND09],

$$\Delta H = \Delta H_0 + \Delta H_\alpha + \Delta H_{2mag} + \Delta H_{\Delta\theta_H} \qquad 2.25$$

where ΔH_0 is the frequency independent inhomogeneity contribution to the peak-to-peak linewidth and is related to the thermal history of the sample, lattice mismatch, etc. ΔH_α represents the intrinsic part of the Gilbert damping, which is due to the spin orbital coupling that relaxes the precessional energy into the lattice and dissipates it in the form of thermal energy. $\Delta H_{2\text{-mag}}$ arises from 2-magnon scattering and $\Delta H_{\Delta\theta_H}$ is associated with inhomogeneous broadening due to spatial variation of the magnetic properties (magnetization and magnetic anisotropy) in the measured volume. The linewidth broadening due to Gilbert damping (ΔH_α) can be expressed as

$$\Delta H_\alpha = \frac{1}{\sqrt{3}} \frac{1}{\left|\frac{\partial \omega}{\partial H_r}\right|} \frac{\alpha\gamma}{M_s} \left(\frac{\partial^2 E}{\partial \theta_M^2} + \frac{1}{\sin^2\theta_M} \frac{\partial^2 E}{\partial \varphi_M^2} \right) \tag{2.26}$$

This expression has been further modified by Lindner *et al.* [LIND09] as

$$\Delta H_\alpha = \frac{2}{\sqrt{3}} \frac{\alpha\omega}{\gamma\Xi} \tag{2.27}$$

where Ξ is the dragging function which is the consequence of magnetic anisotropy fields acting on the magnetization vector and is of the form,

$$\Xi = \cos(\theta_H - \theta_M) - \frac{3H_x + H_y}{H_y(H_x + H_y)} H_0 \sin^2(\theta_H - \theta_M) \tag{2.28}$$

where
$$\begin{aligned} H_x &= H_0 \cos(\theta_H - \theta_M) - 4\pi \mathrm{M}_{eff} \cos^2\theta_M \\ H_y &= H_0 \cos(\theta_H - \theta_M) - 4\pi \mathrm{M}_{eff} \cos 2\theta_M \end{aligned} \tag{2.29}$$

The 2-magnon scattering which transfers magnetic energy from uniform precession to degenerate spin wave states can be expressed as [KURE13, SPAR64, ARIA99, KRIV07],

$$\Delta H_{2-mag} = \sum_i \frac{\Gamma_i^{pr} f_i(\varphi_H)}{\gamma\Phi} \sin^{-1}\sqrt{\frac{\sqrt{\left((\omega)^2 + (\omega_0/2)^2\right)} - \omega_0/2}{\sqrt{\left((\omega)^2 + (\omega_0/2)^2\right)} + \omega_0/2}} \tag{2.30}$$

where ω_0 $(= \gamma 4\pi M_{eff})$ and the other terms can be simplified and expressed as [KURE13],

$$\Gamma_i^{pr} = \Gamma_i^0 \Phi\Psi\left(\theta - \frac{\pi}{4}\right) \frac{dH_r(\theta_H)}{d\omega(\theta_H)} \Big/ \frac{dH_r(\theta_H = 0)}{d\omega(\theta_H = 0)} \tag{2.31}$$

Here, Φ is a field dragging function which is defined as,

$$\Phi = \left(\frac{d\omega^2}{dH}\right) \Big/ \left(\gamma^2 H_x H_y\right) \tag{2.32}$$

The inhomogeneous broadening ($\Delta H_{\Delta\theta_H}$) is expressed as [KURE13],

$$\Delta H_{\Delta\theta_H} = \frac{1}{\sqrt{3}} \left(\left|\frac{\partial H}{\partial \theta_H}\right|_r \Delta\theta_H \right) \tag{2.33}$$

Substituting Eqns. 2.27, 2.30, 2.33 in 2.25 and fitting the experimentally obtained ΔH with Eqn. 2.25, one can extract the Gilbert damping constant (α) and other important information as discussed previously.

In the case of frequency variation FMR spectrum recorded for in-plane configuration, the solution for f dependence of H_r can be expressed as [ACHE03],

$$f_r = \frac{\gamma}{2\pi}\left[H_r\left(4\pi M_{eff} + H_r\right)\right]^{1/2} \tag{2.34}$$

where $4\pi M_{eff} = 4\pi M_s - 2K_1/M_s$.

Frequency dependence of total linewidth in planar orientation can be expressed as [ACHE03, ARIA99],

$$\Delta H\left(f\right) = \Delta H_0 + \Delta H_G\left(= \frac{2}{\sqrt{3}}\frac{\alpha}{\gamma}f\right) + \Delta H_{2M}\left(= \Gamma \sin^{-1}\sqrt{\frac{\sqrt{f^2 + \left(\frac{f_0}{2}\right)^2} - \frac{f_0}{2}}{\sqrt{f^2 + \left(\frac{f_0}{2}\right)^2} + \frac{f_0}{2}}}\right) \tag{2.35}$$

Here, the first term (i.e., ΔH_0) is the inhomogeneous residual linewidth at zero frequency. The second term refers to Gilbert damping contribution, where α is the Gilbert damping constant. The third term represents the 2-magnon scattering contribution to the total linewidth arising out of the inhomogeneity and defects in the magnetic nanostructure [ARIA99]. Here, Γ determines the strength of the magnon scattering and $f_0 = \gamma(4\pi M_s - 2K_1/M_s)$. All FMR spectra analyses presented in this thesis are based on these formulae. A typical example of use of this formalism can be found in the next sub-section.

2.2.5.4 MS-FMR versus C-FMR

To compare the two well-known FMR techniques, off-stoichiometric Ni-Mn-Sn alloy films with thickness of 250 nm, 500 nm and 1000 nm deposited by DC magnetron sputtering technique on Si (100) substrates were used. The target to substrate distance was 50 mm. All films were deposited under Ar gas pressure of 0.5 Pa using an input DC power of 15 W. As-sputtered films were annealed *ex situ* at 823 K for 1 h under residual Ar pressure of 10^{-3} Pa. XRD and VSM studies confirmed that the films have a single phase austenite structure with room temperature ferromagnetism [MODA16]. These films with different values of magnetic moment have been used to understand the limitations of the two FMR methods. Typical FMR spectra recorded for Ni-Mn-Sn films using C-FMR and MS-FMR techniques at 9.44 GHz along the directions $\theta_H = 0^o$ and 90^o are shown in Figure 2.20 [MODA18a].

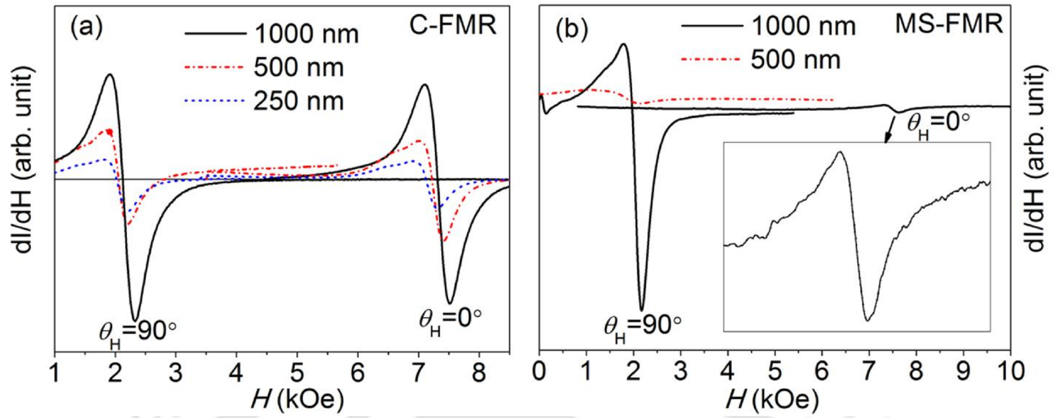

Figure 2.20: In-plane ($\theta_H = 90°$) and out-of-plane ($\theta_H = 0°$) FMR spectra of Ni-Mn-Sn films of different thicknesses recorded at 9.44 GHz by (a) C-FMR, and (b) MS-FMR techniques. The coordinate system used is the same as defined in Figure 2.19(a).

From the figures, it is evident that one can record good FMR spectra for film thicknesses down to 250 nm for films with magnetic moment ~ 180 emu/cc and sample dimensions 2 × 2 mm^2 using C-FMR technique. However, the home built MS-FMR's capability is limited to 500 nm thick film. Also, in the case of C-FMR, in-plane ($\theta_H = 90^o$) and out-of-plane ($\theta_H = 0^o$) spectra are of nearly of similar intensity, but the intensity decreased drastically for out-of-plane orientation in the case of MS-FMR spectra. A shift in resonance field (H_r) between $\varphi_H = 0^o$ and $\varphi_H = 90^o$ spectra which signifies the presence of uniaxial anisotropy in the film can also be noticed in both sets of spectra. FMR spectra has been recorded from $\varphi_H = 0^o$ to $\varphi_H = 360^o$ at intervals of 10^o in order to visualize the direction of uniaxial anisotropy. It was found that the film has easy axis along its long axis (i.e., at $\varphi_H = 0^o$) and hard axis along its short axis (i.e., at $\varphi_H = 90^o$). The symbols in Figure 2.21(a) represent the H_r variation with φ_H. Figure 2.21(b) depicts the H_r variation with θ_H for both the techniques. The solid lines in Figure 2.21(a) and (b) represent φ_H and θ_H dependences of H_r calculated according to Eqn. 2.20 and 2.14. The calculated curves fit well with the experimental data for the sample from which g-factor of 2.1, $4\pi M_{eff}$ = 3135 Oe , K_1 = -9.0×10^4 erg/cc and $K_u = 1.6 \times 10^4$ erg/cc were estimated from C-FMR data with the corresponding values being

$4\pi M_{eff}$ = 3198 Oe , K_1 = -9.5 × 10^4 erg/cc and K_u = 1.4 × 10^4 erg/cc from MS-FMR data.

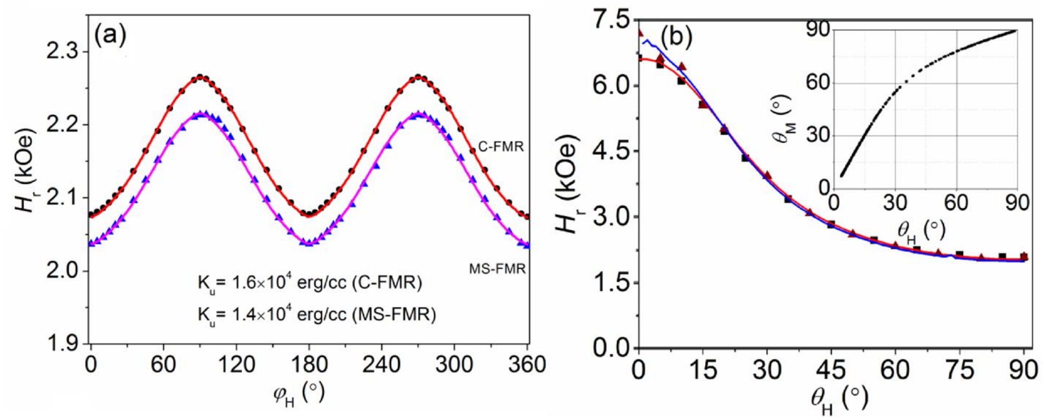

Figure 2.21: (a) Experimental data (symbols) and numerically fitted (solid lines) curves for in plane φ_H variation of H_r for 1000 nm Ni-Mn-Sn film (b) Variation of FMR resonance field (H_r) with θ_H from spectra obtained by C-FMR and MS-FMR. Inset shows the corresponding θ_M value for each θ_H for 1000 nm film.

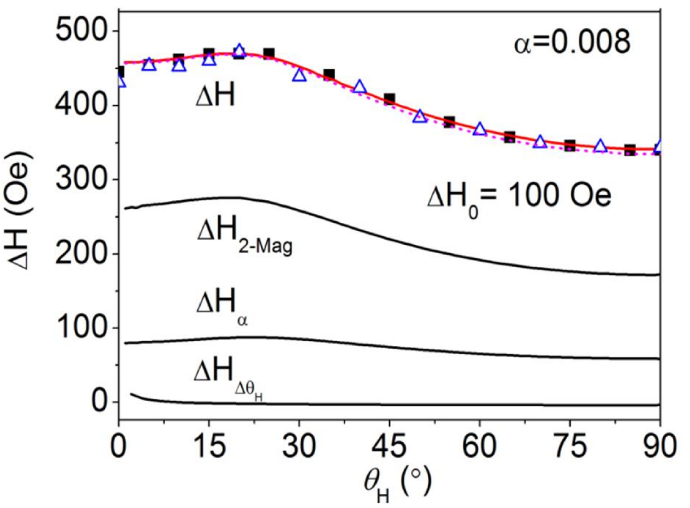

Figure 2.22: Angular dependence of total linewidth (ΔH) for both C-FMR and MS-FMR data along with the individual contributions ($\Delta H_{2\text{-}mag}$, ΔH_α and $\Delta H_{\Delta\theta}$).

A plot depicting ΔH versus θ_H data recorded for 1000 nm Ni-Mn-Sn film and its fit to Eqn. 2.25 is shown in Figure 2.22. A significant broadening of linewidth is caused by the intrinsic damping part ΔH_α and the external 2-magnon scattering term $\Delta H_{2\text{-Mag}}$. The best fitted parameters give us the Gilbert damping constant (α) of 0.008.

From the above comparative study of the two FMR techniques, it was found that for samples exhibiting reasonable magnetic moment (i.e., $M \geq 1$ memu for a 4 × 6 mm^2 sized sample), both the techniques yield similar results. However, good FMR data could not be recorded for lower thickness films (say, 250 nm and low thickness) which have low magnetic moment using MS-FMR technique due to its lower sensitivity. A survey of the literature shows that both MS-FMR [DURR15, HUSA16, BELM15] and C-FMR [ISOG15, DUTO16, JIAN17, GOLU17] techniques have been extensively used to study the magneto-dynamic properties of magnetic materials. Since MS-FMR permits measurement of FMR spectra as functions of both angular orientation with respect to field and a broad range of frequencies, this technique certainly yields a more reliable value for α and other magneto-dynamic parameters. But the limitations of this home built technique have already been pointed out. In this regard, the C-FMR methodology based on commercial ESR setup offers some advantages when low moment films are involved [MAKS15]. In this thesis work, MS-FMR has been used for series 1 films in chapter 3. Rest of the films has been characterized using C-FMR, since MS-FMR set-up accessible to us was unable to provide analyzable FMR spectra for low moment samples. For, the same reason, ultra-low thickness films were not taken up for study in this thesis work although such films could be prepared using the sputtering systems available with us.

Chapter 3

Austenite and Martensite Ni-Mn-Sn thin films

As seen in literature, off-stoichiometric Ni-Mn-Sn Heusler compounds are recognized as potential materials for technological developments due to their multifunctional properties like magneto-caloric effect, magnetoresistance, magnetic shape memory effect *etc.* [KREN05a, CZAJ16, PAND17, DUBO12b, TURA16]. These alloys have been well studied in the bulk form towards the understanding and tailoring their properties as a function of composition, particle size *etc*. [HANZ07, AYDO16, GHOS14, BUCH11, MUTH10]. However, very limited information is available on Ni-Mn-Sn thin films. Since these thin films are expected to exhibit geometry and microstructure dependent properties, composition and thickness dependent studies on Ni-Mn-Sn thin films may yield several interesting results which may find new applications. Hence, this chapter is devoted to investigate the structural, magneto-static, magneto-caloric and magneto-dynamic properties of Ni-Mn-Sn films deposited on low cost Si (100) substrates.

3.1 Sample preparation and processing

Off-stoichiometric Mn-rich Ni-Mn-Sn films were deposited on Si (100) substrate by DC magnetron sputtering from 2 inch diameter and 1 mm thick $Ni_{50}Mn_{37}Sn_{13}$ alloy target. Before deposition, the substrates were thoroughly cleaned in an ultrasonic bath with boiling acetone. The sputtering chamber was evacuated to a base pressure of $<10^{-4}$ Pa. Two series of films have been deposited under different deposition conditions from the same target. The first series of films with thickness of 250 nm, 500 nm, 750 nm, 1000 nm and 1500 nm (series 1) were deposited under a working pressure of 0.5 Pa and DC power of 15 W using the system shown in Figure 2.05(b). The films of different thicknesses were deposited by varying only the deposition time while keeping all other conditions identical. The compositions of the films were verified using EDS analysis and only a very minor variation in composition was found with film thickness. Overall compositions for the films are $Ni_{48.2}Mn_{38.2}Sn_{13.6}$, $Ni_{48.1}Mn_{38.1}Sn_{13.8}$, $Ni_{48.3}Mn_{38.2}Sn_{13.5}$, $Ni_{48.3}Mn_{38.4}Sn_{13.3}$ and $Ni_{48.2}Mn_{38.1}Sn_{13.7}$ for 250 nm, 500nm, 750 nm, 1000nm, and 1500 nm, respectively. The as-deposited films were then annealed *ex situ* under vacuum. To optimize the annealing temperature, as-deposited 250 nm thick film was vacuum annealed at different temperatures for 1 h each. Films of other thicknesses were all annealed *ex situ* at the optimized temperature of 823 K under residual Ar gas pressure of 10^{-3} Pa for 1 h. The second series of films of thickness 360 nm, 500 nm, 700 nm and 1000 nm (series 2) were deposited under a working pressure of 1.8 Pa and DC power to 70 W using the sputtering system shown in the Figure 2.05(a). During deposition, the substrates were rotated at 15 rpm to ensure uniform deposition. The films of different thicknesses were deposited by varying the deposition time only, while keeping all other deposition conditions identical. The compositions of the films were evaluated using EDS analysis and found to be $Ni_{53.4}Mn_{33.2}Sn_{13.4}$. As-deposited films were annealed *ex situ* at 823 K under residual Ar gas pressure of 10^{-3} Pa for 1 h.

3.2 Structure and morphology

Figure 3.01 shows the room temperature XRD patterns of 250 nm thick film (series 1) annealed at different temperatures. From the data, it is evident that the as-deposited films are amorphous in nature. Upon annealing at 573 K, the amorphous films begin to crystallize. The XRD peak at $2\theta = 42.85°$ indicates the formation of A2 structure and the super-lattice peaks at $2\theta = 25.78°$ and 29.87° signify the onset of $L2_1$ order in the films. Degree of $L2_1$ ordering increases with increasing annealing temperature, as seen from the development of the two super-lattice peaks with increasing annealing temperature. In order to understand the influence of annealing temperature on the degree of structural order in this alloy films, a simple analysis using Eqns. 2.06 and 2.07 was carried out. Degree of $L2_1$ ordering factor (S_{L2_1}) and B2 ordering factor (S_{B2}) for the 250 nm film annealed under different temperature is listed in Table 3.01.

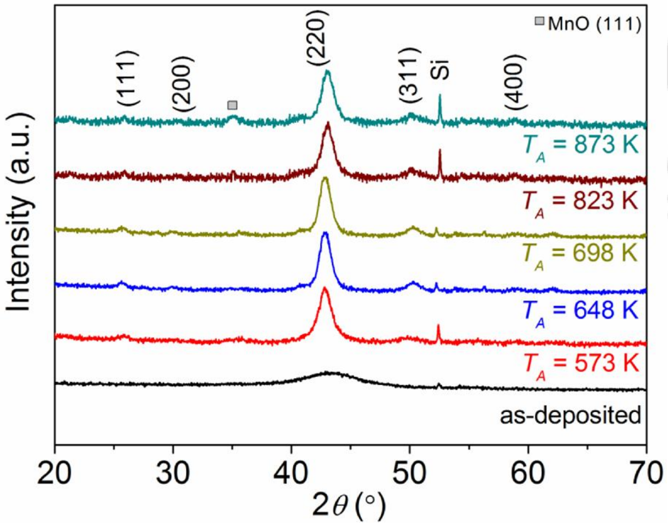

Figure 3.01: Room temperature XRD patterns of as-deposited and vacuum annealed 250 nm thick Ni-Mn-Sn films (series 1).

Table 3.01: Structural and magnetic properties of as-deposited and annealed 250 nm thick Ni-Mn-Sn films

Annealing Temp. (K)	% of B2 order (S_{B2})	% of $L2_1$ order (S_{L2_1})	M@5kOe (emu/cc)	M_r (emu/cc)
As-deposited	-	-	-	-
573	-	-	102	5.4
648	93	80	144	20.3
698	95	82	150	21.4
823	98	86	158	36.5
873	98	87	159	36.7

From Table 3.01, it is clear that the degree of $L2_1$ order improves with an increase in annealing temperature due to improvement in crystallinity of the phase. Annealing at 823 K for 1 h provides the desired crystalline ordering in the films. Beyond 823 K, the film surface starts deforming and no further improvement in structural ordering is observed. Hence, the annealing temperature is fixed at 823 K for the rest of the films. All films in series 1 were annealed at 823 K for 1 h under vacuum. Room temperature XRD pattern of films of all thickness are shown in Figure 3.02. From the figure it is evident that the films exhibit austenite phase with $L2_1$ ordering at room temperature. The degree of B2 and $L2_1$ ordering evaluated for these films using Eqns. 2.06 and 2.07 are listed in Table 3.02. Rietveld refinement was performed on the XRD patterns by considering a $L2_1$ unit cell for Ni-Mn-Sn alloy compositions. While considering the unit cell, excess Mn atoms in the alloy were assumed to occupy Sn position as predicted by other researchers [UBAL17, SOKO12]. The refined pattern for all the films are shown in Figure 3.02. The low χ^2 value and difference pattern between observed and refined data (Y_{obs}-Y_{cal}) confirms the good fitting obtained for the unit cell. Rietveld fitting was done for all the films and lattice parameters extracted from the fits are listed in Table 3.02. The average crystallite (grain) size (*D*) of the films calculated using the most intense (220) peak and Schërrer's equation (Eqn. 2.04) are listed in Table 3.02. From the table, it is can be seen that the lattice parameter does not vary much with film thickness. However, *D* increases with increasing film thickness, since higher thickness facilitates grain growth by offering more space for the same.

Table 3.02: Structural and morphological parameters of 823 K annealed Ni-Mn-Sn films of different thickness.

Thickness (nm)	% of B2 order (S_{B2})	% of $L2_1$ order (S_{L2_1})	*a* (nm)	*D* (±0.3) (nm)	$R_{av.}$ (nm)	$R_{r.m.s.}$ (nm)
250	98	86	0.596	8.1	1.44	1.78
500	97	84	0.595	7.3	1.53	1.92
750	97	84	0.597	7.2	1.38	1.69
1000	98	82	0.596	12.4	1.82	1.91
1500	98	82	0.597	12.7	1.67	2.12

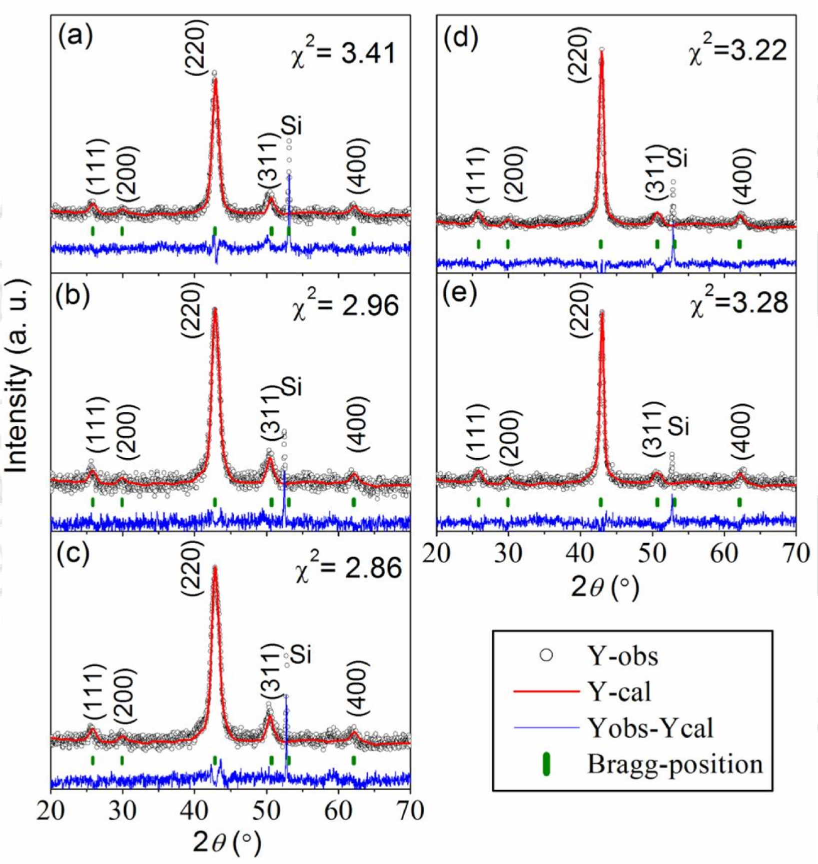

Figure 3.02: (a) XRD patterns of 823 K annealed Ni-Mn-Sn films (series 1) of thickness (a) 250 nm, (b) 500 nm, (c) 750 nm, (d) 1000 nm and (e) 1500 nm.

Figure 3.03 shows the room temperature XRD patterns of Ni-Mn-Sn (series 2) films after annealing at 823 K for 1 h. It is obvious from the XRD patterns that all the annealed films exhibit martensite phase at room temperature with modulated 14M structure [PLAN09, KREN05b, RANJ06]. The phase diagram of $Ni_{50}Mn_{50-x}Sn_x$ alloy [PLAN09] shows that the 14M phase can be stabilized in this ternary alloy system when the *e*/*a* (valence electrons per atom) ratio is between 8.15 and 8.30. Hence, room temperature 14M martensite phase and M ↔ A transition are expected in these films. Apart from the martensite peaks, an extra weak peak can be observed at $2\theta = 35.33°$ which corresponds to manganese oxide (MnO, space group 225). This MnO peak was not present in the amorphous as-deposited films. Hence, a small amount (3 to 4%) of MnO phase appears to have formed during the *ex situ* annealing process despite our effort to maintain an inert atmosphere. Formation of MnO on the surface has been reported during annealing of Mn based alloys because of the high reactivity of Mn at high temperatures [GEBE09, JETT12]. Since the Néel temperature of MnO is 116 K, it is paramagnetic at room temperature [KITT05]. In view of these facts, the small amount of MnO present on the surface of the films may slightly alter the composition of the martensite phase. Though it is difficult to estimate the change in composition, one expects the e/*a* of the martensite phase to vary by not more than ±0.08. Hence, this may not seriously affect the magnetic and mechanical properties of these films. The lattice constants of the films were calculated using the most intense (1 2 7), (2 0 -5), (1 1 10) peaks and the relation 2.02. Lattice parameters of the films are listed in Table 3.03. The average crystallite size (*D*) and the lattice strain (ε) present in the films estimated from the XRD data using the Williamson-Hall relation (Eqn. 2.05) are listed in Table 3.03.

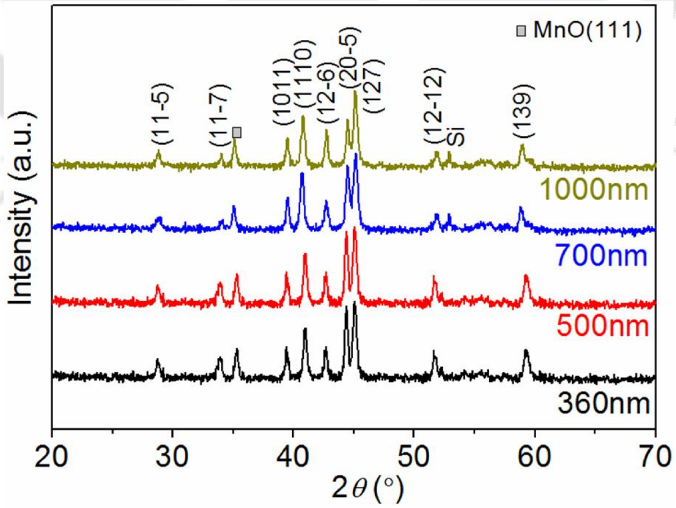

Figure 3.03: XRD patterns of $Ni_{53.4}Mn_{33.2}Sn_{13.4}$ alloy thin films (series 2) with different thicknesses annealed at 823 K.

It is evident that thicker films facilitate larger growth of grains in the polycrystalline films. The strain in all the annealed films was almost the same when annealed at 823 K. The stable martensite phase at room temperature in Ni-Mn-Sn offers the possibility to study this little explored phase in this ternary alloy films. Comparison between the films with room temperature austenite phase (series 1) and martensite phase (series 2) shows that the martensite films have larger crystallite size (almost 10 times higher for 1000 nm film) as compared to austenite films. This may be due to the relative ease of grain growth in the low symmetry films.

Table 3.03: Structural and morphological parameters of 823 K annealed Ni-Mn-Sn films (series 2) with 14M modulated martensite structure.

Thickness (*t*) (nm)	**Lattice constant**			***D* (±3) (nm)**	**ε (0.1) (× 10^{-3})**	**$R_{av.}$ (nm)**	**$R_{r.m.s.}$ (nm)**
	***a* (nm)**	***b* (nm)**	***c* (nm)**				
360	0.436	0.541	2.889	67	4.9	5.14	6.62
500	0.435	0.541	2.926	96	4.8	5.42	6.82
700	0.434	0.541	2.927	103	4.8	5.84	7.05
1000	0.434	0.541	2.927	121	5.0	5.34	6.52

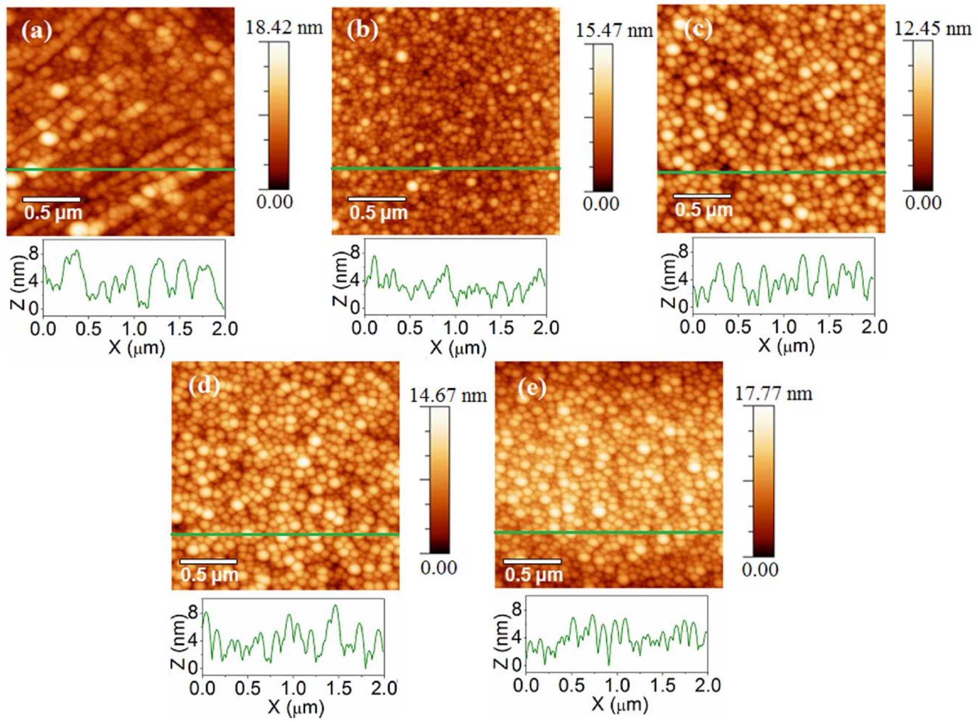

Figure 3.04: Atomic force micrographs of austenite Ni-Mn-Sn alloy thin films (series 1) of (a) 250 nm, (b) 500 nm, (c) 750 nm, (d) 1000 nm and (e) 1500 nm thickness.

Surface morphology of the series 1 and series 2 films was mapped over 2 × 2 μm^2 scan areas using AFM. AFM image of 823 K annealed austenite Ni-Mn-Sn (series 1) films are shown in Figure 3.04(a-e). The average (R_{av}) and r.m.s. ($R_{r.m.s}$) surface roughness of the films was found to be 1.44 and 1.78 nm, 1.53 and 1.92 nm, 1.38 and 1.69 nm, 1.52 and 1.91 nm and 1.67 and 2.12 nm for 250 nm, 500 nm, 750 nm, 1000 nm and 1500 nm, respectively. Similarly Figure 3.05 (a-d) shows the AFM image of 823 K annealed martensite Ni-Mn-Sn (series 2) films. These films exhibit average ($R_{av.}$) and r.m.s. ($R_{r.m.s.}$) surface roughness of 5.14 and 6.62 nm, 5.42 and 6.82 nm, 5.84 and 7.05 nm and 5.34 and 6.52 nm for 360 nm, 500 nm, 700 nm and 1000 nm films, respectively. In comparison with austenite films (series 1), martensite films (series 2) processed under the same conditions have higher surface roughness.

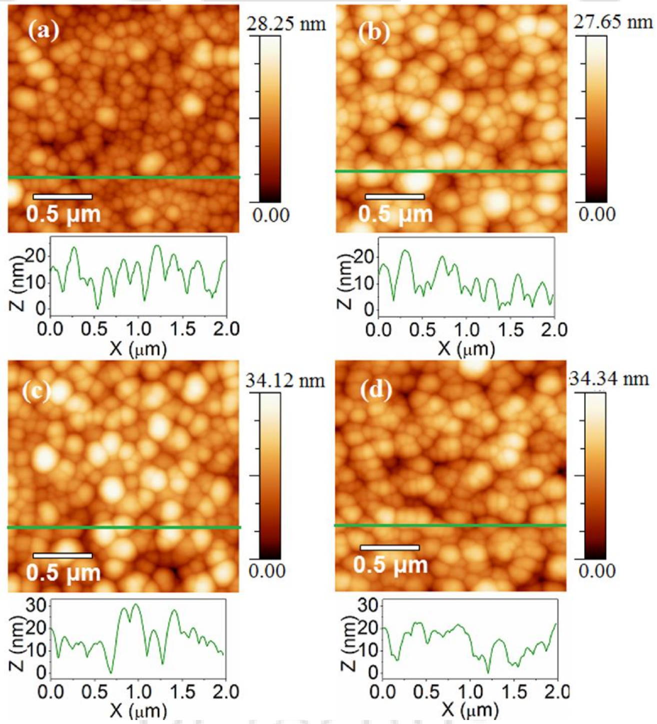

Figure 3.05: Atomic force micrograph of martensite Ni-Mn-Sn alloy thin films (series 2) with thicknesses (a) 360 nm, (b) 500 nm, (c) 700 nm and (d) 1000 nm.

3.3 Magneto-static properties

Figure 3.06 illustrates the field dependence of magnetization (*M-H* curves) of as-deposited and annealed 250 nm (series 1) films. As-deposited film is paramagnetic in nature which can be associated with the amorphous structure of the film. Upon annealing at 573 K, the film starts to become ferromagnetic which can be correlated with the nucleation and growth of a crystalline phase. The film annealed at 648 K is fully ferromagnetic. Upon increasing the annealing temperature up to 823 K, the film becomes magnetically softer along with improved $L2_1$ order. Films annealed above 823 K do not show much variation in magnetic property. From the figure, it is clear that films annealed at 823 K and 873 K show almost similar *M-H* loop. The gradual increment of retentivity (M_r) value with increasing annealing temperature also confirms the improvement of soft magnetic property.

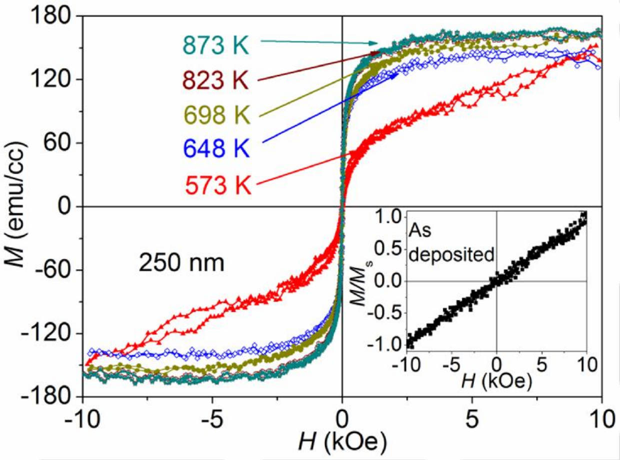

Figure 3.06: Room temperature *M-H* curves of 250 nm Ni-Mn-Sn film (series 1) annealed at different temperatures.

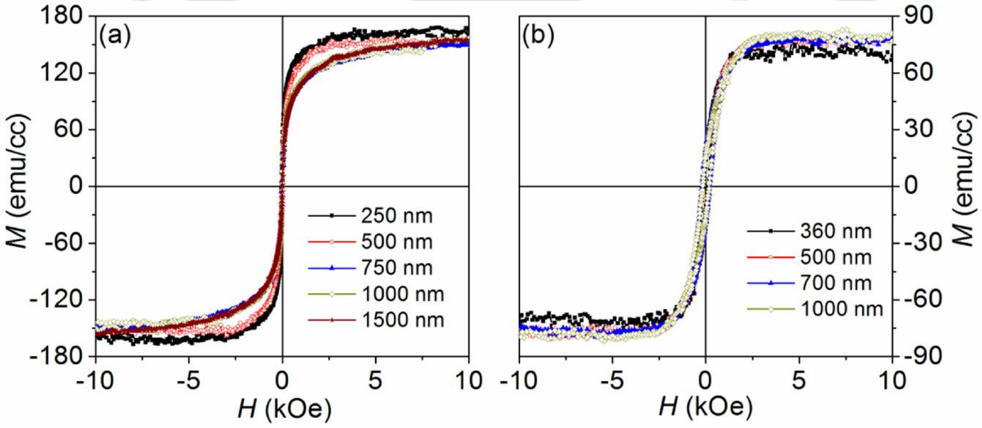

Figure 3.07: (a) Room temperature *M-H* loops for austenite (series 1) films of different thickness annealed at 823 K (b) Room temperature *M-H* loops of martensite (series 2) annealed films.

Room temperature *M-H* loops of all series 1 films with thicknesses of 250 nm, 500 nm, 750 nm, 1000 nm and 1500 nm annealed at 823 K are shown in Figure 3.07(a). From the figure, it is clear that all the films show room temperature ferromagnetic behavior with low thickness films exhibiting softer magnetic loop. The decrease in the soft magnetic properties for a fixed applied field direction may be attributed to the change in magnetic domain patterns with increase in film thickness [ANNA11]. Saturation magnetization of 250 nm, 500 nm, 750 nm, 1000 nm and 1500 nm thick films are found to be 158 emu/cc, 155 emu/cc, 149 emu/cc, 150 emu/cc and 152 emu/cc, respectively. Figure 3.07(b) represents the room temperature *M-H* loops of series 2 films annealed at 823 K. All these films exhibit room temperature ferromagnetism, but the magnetic moment is very low (almost half) of films in series 1. The saturation magnetization of these films are found to be 73 emu/cc, 74 emu/cc, 76 emu/cc and 81 emu/cc for 360 nm, 500 nm, 700 nm and 1000 nm films, respectively. The decrease in magnetic moment can be related with the structures of the films like series 1 film has austenite cubic phase whereas series 2 films has martensite phase. For the Ni-Mn-Z based Heusler alloy films, the magnetic moment is usually low for the martensite phase as compared to the austenite phase [TANC17, AKSO09]. Magnetization of the films remains nearly the same as the thickness is varied up to 1000 nm.

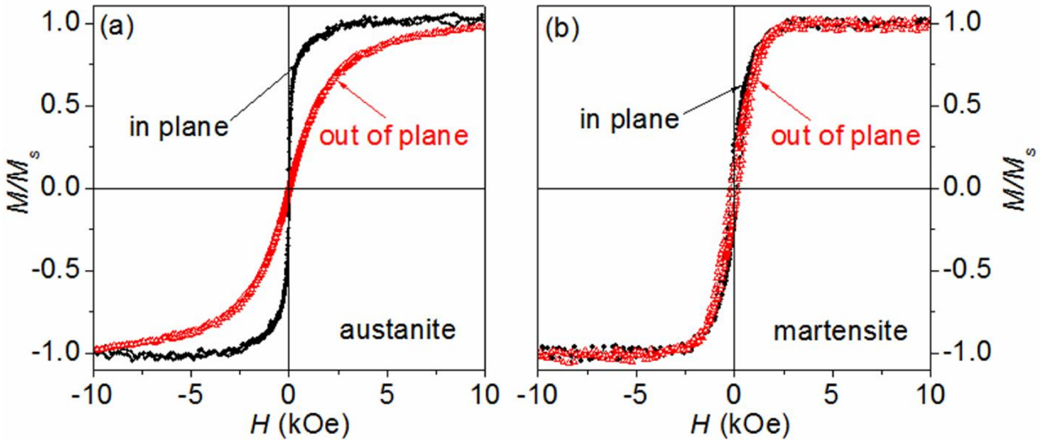

Figure 3.08: (a) *M-H* loop of 250 nm austenite Ni-Mn-Sn film (series 1) with in-plane and out-of-plane orientations. (b) In-plane and out-of-plane *M-H* loop of 360 nm martensite Ni-Mn-Sn film (series 2).

Figure 3.08 (a) shows the *M-H* loop along in-plane and out-of-plane directions for the 250 nm thick film annealed at 823 K from which it is clear that the easy axis is along the in-plane direction. The reduction in the soft magnetic properties with applied field direction could be attributed to the presence of magnetic anisotropy in a film which has easy axis along its plane [OHAN00]. Similar behavior is observed for films of all thicknesses (series 1). Similarly, Figure 3.08 (b) shows in-plane and out-of-plane *M-H* loops for 360 nm martensite film (series 2). The same trend is followed by films of different thickness. The *M-H* loops recorded with applied magnetic field along film plane and perpendicular to the film plane show is completely different behaviour for the two series of films. In the case of series 1 films there is a huge difference between in-plane and out-of-plane *M-H* loop shapes signifying large perpendicular anisotropy in the films. But in the case of the martensite (series 2) films, the two loops show almost similar shape which implies very low magnetic anisotropy in the films. This is a very interesting behaviour observed for the first time in Ni-Mn-Sn films. This observation is a consequence of the room temperature martensite phase in series 2 films.

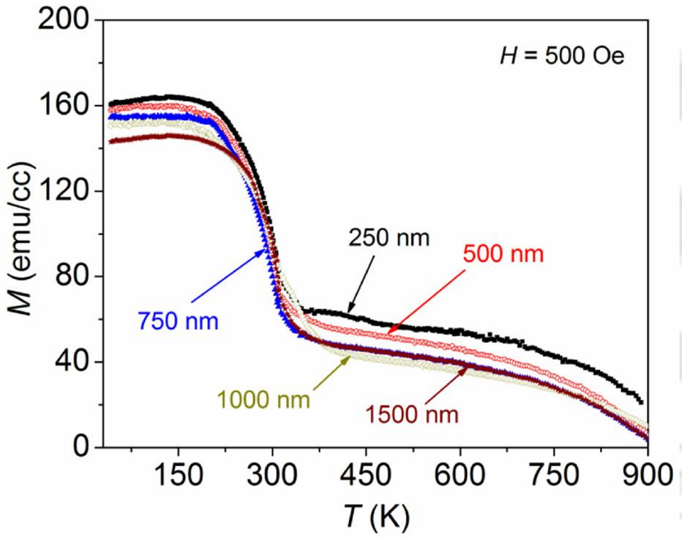

Figure 3.09: Thermo-magnetization (*M-T*) curves of austenite Ni-Mn-Sn films (series 1) recorded with a field of 500 Oe.

Temperature dependence of magnetization (*M-T* curves) for austenite Ni-Mn-Sn films of different thicknesses (series 1) under an applied field of 500 Oe is depicted in Figure 3.09. The *M-T* curves recorded in the temperature range of 30 K to 900 K did not show any evidence of first order martensite to austenite (M ↔ A) phase transition in these films. However, a second order magnetic transition near room temperature corresponding to austenite Curie temperature (T_C) is observed. The absence of M ↔ A in these films may be due to low crystallite (grain) size in these films. Similarly, Figure 3.10 shows the temperature dependence of magnetization (*M-T*) of martensite Ni-Mn-Sn thin films (series 2). *M-T* data recorded during heating and cooling cycle under applied field of 500 Oe are designated as field warmed (FW) and field cooled (FC) curves, respectively. It is evident from the figure that the FC and FW curves obtained for 360 nm Ni-Mn-Sn film superpose on each other well. However, a thermal hysteresis, characteristic of the M ↔ A transition can be observed in the FC and FW data of the 500 nm, 700 nm and 1000 nm films as depicted in the inset of Figure 3.10.

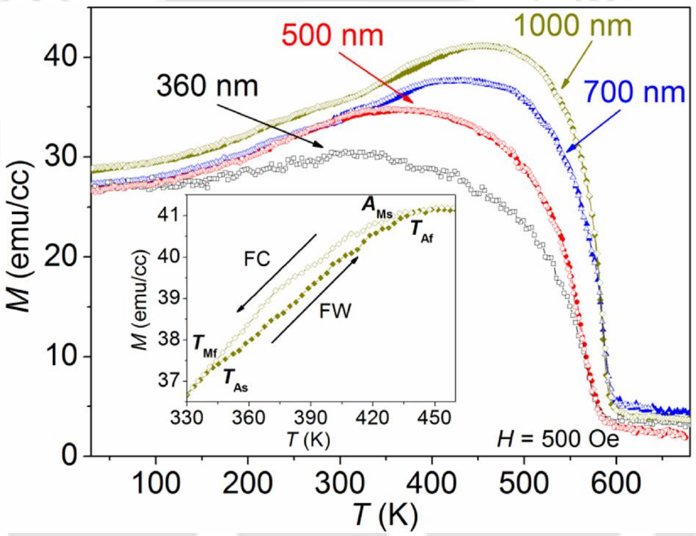

Figure 3.10: Thermo-magnetization (*M-T*) curves of martensite Ni-Mn-Sn films (series 2) recorded under an applied field of 500 Oe in FW (filled symbol) and FC (open symbol) modes. Inset shows an enlarged view of a part of the *M-T* data of the 1000 nm film exhibiting a weak thermal hysteresis. T_{As}, T_{Af}, T_{Ms} and T_{Mf} are the austenite start, austenite finish, martensite start and martensite finish temperatures.

Since no thermal hysteresis is observed in the FC and FW data of the 360 nm thick film, there is no signature of the martensitic transition in this film despite the fact that the film exhibits martensite structure at room temperature. It is worthy to point out here that Vishnoi *et al.* [VISH11] also observed such suppression of M ↔ A transition in Ni-Mn-Sn films with thickness less than 410 nm. In contrast, a weak thermal hysteresis is observed in the temperature range of 295 - 360 K, 335 - 400 K and 340 - 445 K in the case of 500 nm, 700 nm and 1000 nm films, respectively. Apart from confirming the observation of the elusive M ↔ A transition in Ni-Mn-Sn films, the present results also confirm the fact that the martensitic transition is dependent on film thickness as pointed out earlier [VISH11, TEIC15b]. A look at Table 3.03 would reveal that Ni-Mn-Sn films with $D > 90$ nm exhibit the martensitic transition which in turn indicates a minimum film thickness required to observe the martensitic transition. From the *M-T* curves, it is evident that all the films have high T_C. A slight increase in T_C is also observed as the thickness of the films is varied from 360 nm to 1000 nm film which may be due to the variation in structural factors or minor deviation in overall composition of the films with thickness.

3.4 Magneto-caloric properties

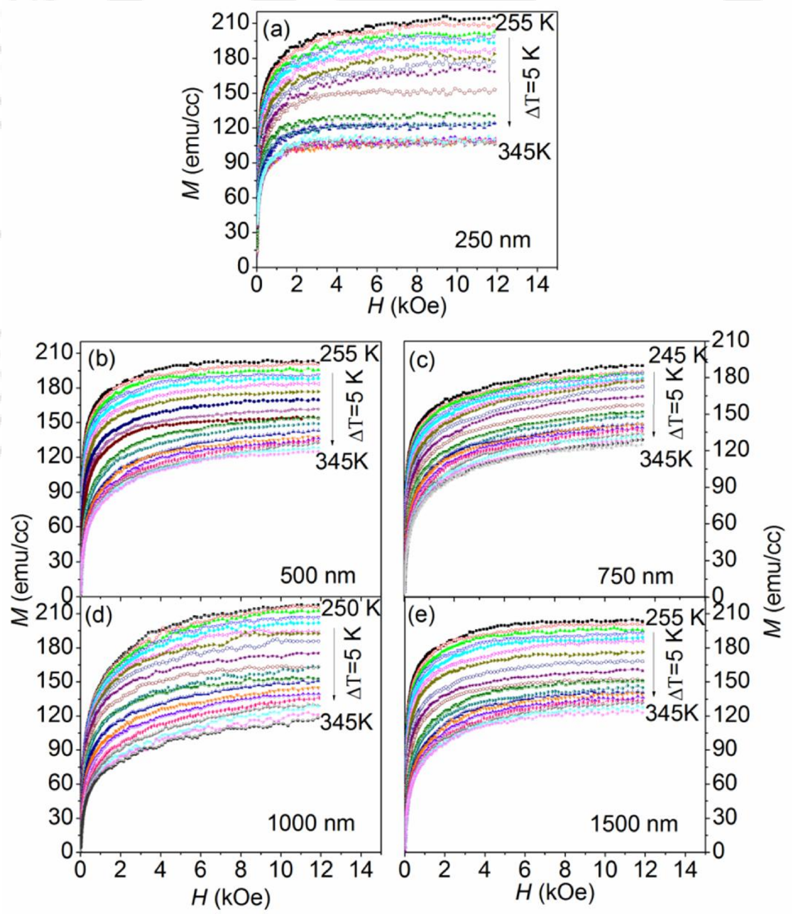

Figure 3.11: Initial *M-H* isotherms for austenite films (series 1) of different thickness recorded at discrete temperature interval across T_C.

From the *M*-*T* data of series 1 (Figure 3.09) and series 2 (Figure 3.10) films, it is evident that series 1 films exhibit only one second-order magnetic phase transition (SOPT) whereas series 2 films poses two phase transitions, one being the SOPT and the other being the first-order structural M ↔ A phase transformation (FOPT). ΔS_M is expected at both FOPT and SOPT. ΔS_M associated with FOPT is generally large (for bulk alloys) but it is confined to a narrow temperature region of a few Kelvin. ΔS_M near SOPT is small but extends over a wider temperature range. Moreover, FOPT inherently suffers from a large hysteresis effect during thermal cycling, which is not found in SOPT [PHAN12]. Since the magnetic moment change associated with the M ↔ A transition (FOPT) is very small and is extended over a large temperature range in series 2 films, the ΔS_M associated with this transition is very small to be estimated. Hence, the focus is on the conventional MCE around the SOPT which is more prominent. ΔS_M for d*H* of 0 to *H* has been estimated by integrating the *M*-*H* isotherms according the Maxwell thermodynamic equation [PECH99] as described in chapter 2 (Eqns. 2.08 & 2.09).

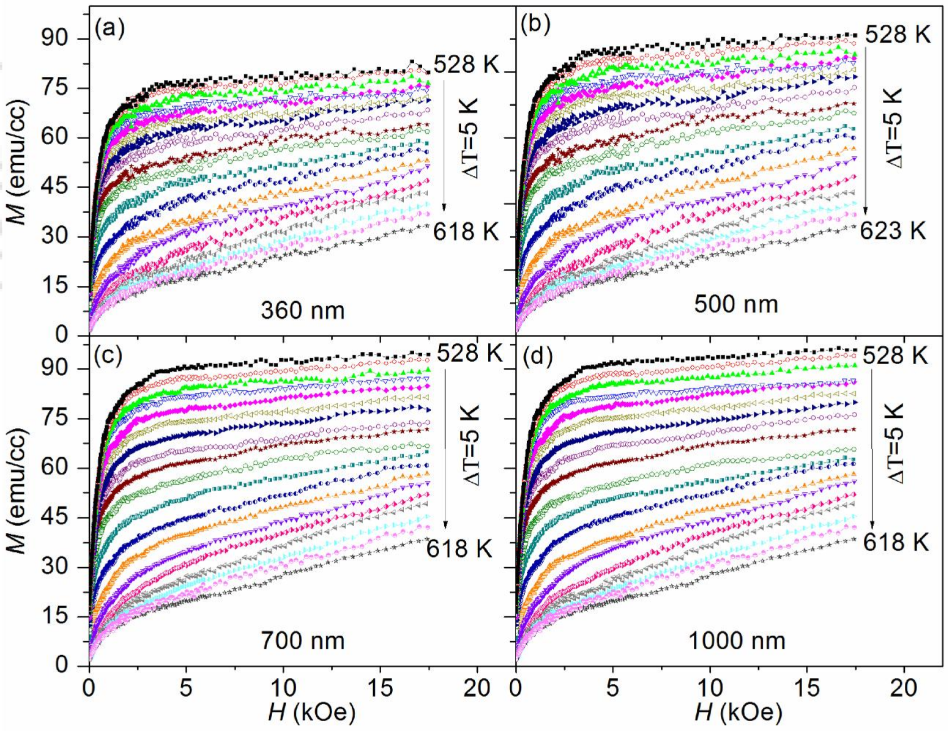

Figure 3.12: Initial *M*-*H* isotherms for martensite films (series 2) of different thickness recorded at discrete temperature interval across T_C.

Isothermal initial magnetization curves were recorded for all the films at discrete intervals of T as shown in Figure 3.11 and Figure 3.12. ΔS_M was calculated from this initial M-H curves using Eqn. 2.09 for all the austenite (series 1) and martensite (series 2) films close to T_C. The corresponding $\Delta S_M(T)$ plots are shown in Figure 3.13. $(\Delta S_M)_{max}$ associated with the SOPT for the Ni-Mn-Sn films are represented in Table 3.04. From Figure 3.13, it is clear that series 1 films shows higher ΔS_M as compared to series 2 films, which can be substantiated on the basis of high moment and larger $\partial M/_{\partial T}$ exhibited by series 1 films across T_C. Similarly, the gradual increase of ΔS_M with increase in thickness for series 2 films can be correlated with the increasing $\partial M/_{\partial T}$ due to the proximity of the M ↔ A phase transformation in higher thickness films. $(\Delta S_M)_{max}$ is found to increase with increasing applied field for all the field as shown by data in Figure 3.14.

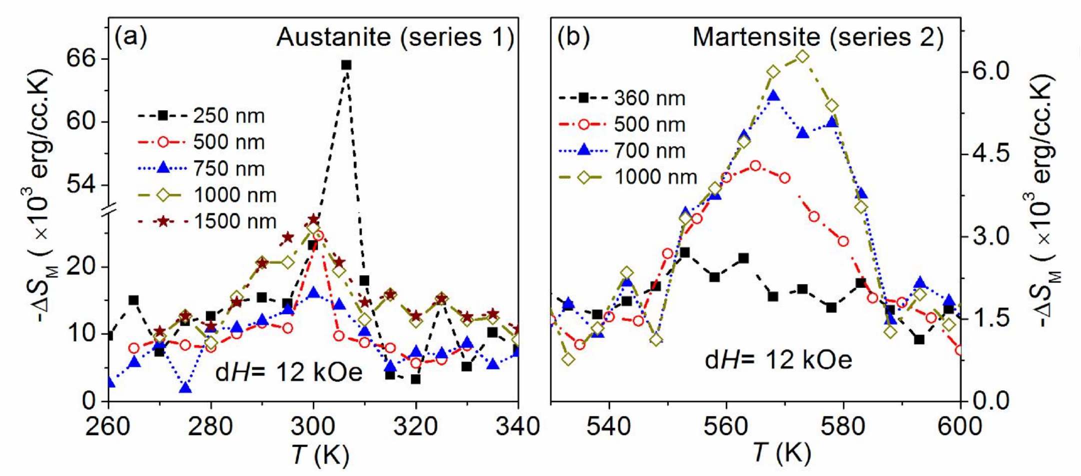

Figure 3.13: Magnetic entropy change ($-\Delta S_M$) estimated for across T_C (a) austenite (series 1) (b) martensite (series 2) Ni-Mn-Sn films for dH of 12 kOe.

The efficiency of a MCE material is expressed in terms of the refrigeration capacity (RC) which can be evaluated using Eqn. 2.10. RC calculated for all the films from the respective $\Delta S_M(T)$ curve using Eqn. 2.10 are tabulated in Table 3.04. From the table it is clear that although the ΔS_M values are much lower for martensite (series 2) films as compared to austenite (series 1) films, their RC values are comparable. This is related to the higher FWHM of $\Delta S_M(T)$ curves of the martensite (series 2) films.

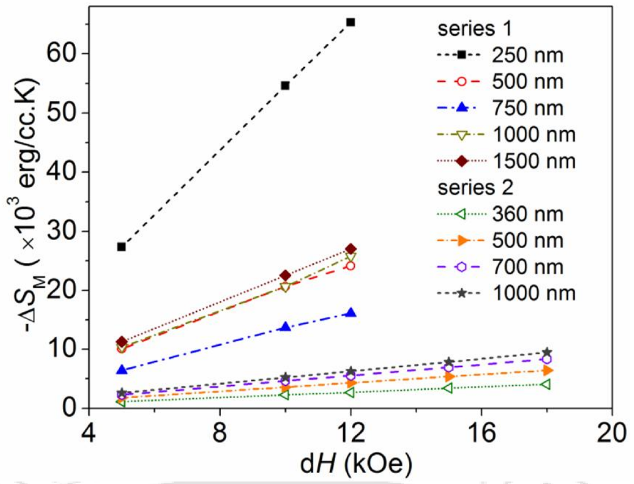

Figure 3.14: Veriation of $(-\Delta S_M)_{\max}$ with applied magnetic field change (dH).

Table 3.04: Magneto-caloric parameters for Ni-Mn-Sn films estimated for an applied field change (dH) of 12 kOe.

Film	(t) (nm)	T_C (±1) (K)	$(-\Delta S_M)_{\max}$(±0.8) $\times 10^3$ erg/cc.K	RC (±8) $\times 10^3$ erg/cc	$(\Delta S_M)_{\max}$ (±0.01)J/kg.K	RC(±0.1) J/kg
$L2_1$	250	306	65.3	451	0.81	5.6
$L2_1$	500	296	24.1	217	0.30	2.7
$L2_1$	750	301	16.1	515	0.21	6.4
$L2_1$	1000	301	25.8	741	0.32	9.2
$L2_1$	1500	302	27.0	845	0.34	10.5
14M	360	557	2.7	97	0.03	1.2
14M	500	562	4.3	146	0.05	1.8
14M	700	569	5.5	195	0.07	2.4
14M	1000	570	6.3	203	0.08	2.5

3.5 Magneto-dynamic properties

Magnetic anisotropy is one of the key factors which help in ascertaining the functional capability of the material. FMR is one of the best experimental techniques for estimating the magnetic anisotropy in ferromagnetic thin films, which is otherwise quite difficult to estimate. In order to understand the functional capability of these Heusler alloy films, the static and magneto-dynamic properties of the annealed Ni-Mn-Sn films (series 1) of thickness 500 nm, 1000 nm and 1500 nm were studied using MS-

FMR technique. The FMR spectra of the films were recorded by varying the applied field (*H*) along the plane of the film at a constant microwave frequency. Typical FMR spectra obtained for the films in in-plane orientation for different frequencies are shown in Figure 3.15. The spectra were recorded for microwave frequencies ranging from 2 to 18 GHz at an interval of 0.5 GHz. The frequency (*f*) dependences of resonance field (H_r) and linewidth (ΔH) of the FMR spectra were extracted for all the annealed films of different thicknesses and analysed with appropriate equations as discussed in chapter 2.

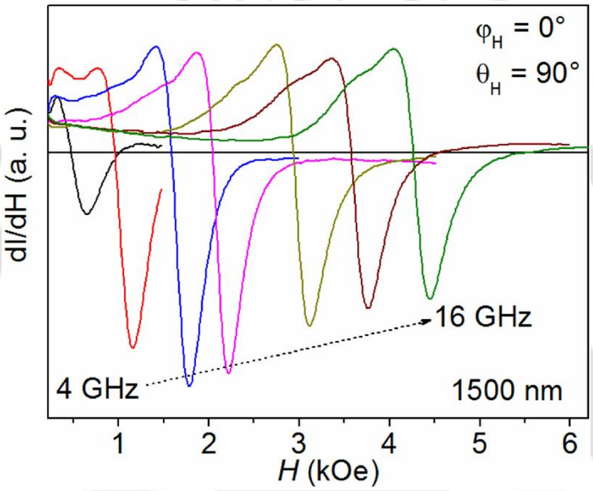

Figure 3.15: Typical MS-FMR spectra for 1500 nm austenite Ni-Mn-Sn film recorded at different frequencies with magnetic field applied along the long axis of film plane.

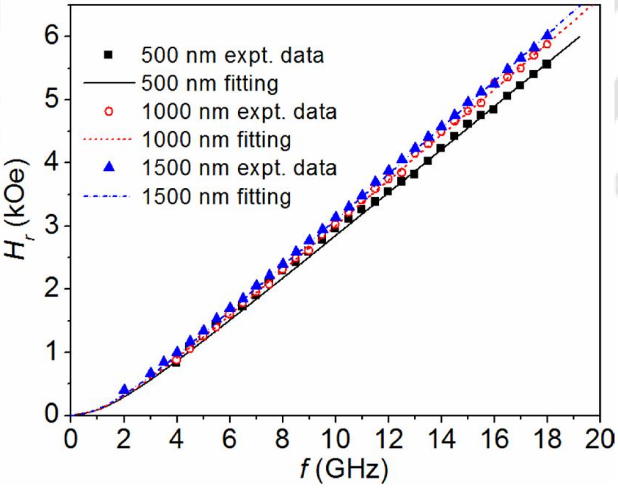

Figure 3.16: Variation of resonance field (H_r) with microwave frequency (*f*) corresponding to the annealed films with different thicknesses (in-plane orientation). Experimental data are shown as symbols and the sold lines represent fits to Eqn. 2.34.

Experimental data pertaining to the variation of H_r with f have been fitted to Eqn. 2.34 and the best fits are shown as solid lines in Figure 3.16. The good fit to the data obtained is evident from the figure and from the fits, γ of 2.95 MHz/Oe and *g*-factor of 2.1 were estimated. In order to study the relaxation of magnetization in the films, the linewidth (ΔH) was measured from FMR spectrum recorded at each frequency. f dependence of ΔH along the easy axis of magnetization is depicted in Figure 3.17 as open symbols. f dependence of ΔH data in in-plane film orientation has been fitted to Eqn. 2.35 and the fitted values are expressed as lines in Figure 3.17. ΔH along the easy axis of magnetization estimated numerically is shown as solid line in Figure 3.17.

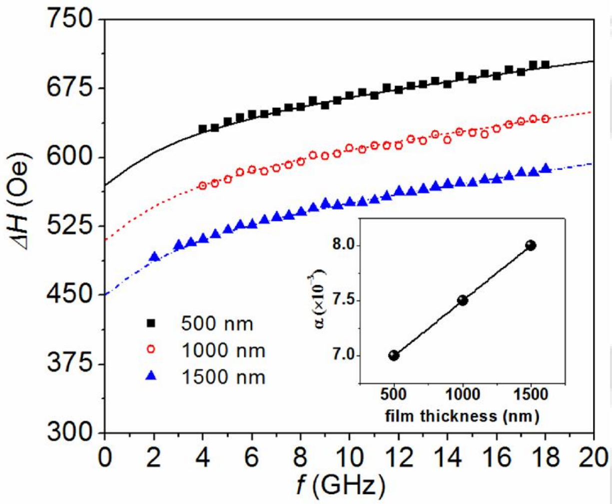

Figure 3.17: Variation of resonance linewidth (ΔH) with microwave frequency (f) corresponding to the annealed films with different thicknesses (in-plane orientation). Experimental data are shown as symbols and the solid lines represent fit to Eqn. 2.35. Inset shows the variation of Gilbert damping constant (α) with film thickness.

It is evident from the Figure 3.17 that the numerically evaluated values are in good agreement with the experimental data. From the analysis of the FMR spectra of films of different thicknesses, it is found that the Gilbert damping constant decreases with thickness (*c.f.* inset in Figure 3.17). This result is consistent with some previously reported results [CHEN07]. However, it has to be noted that there is a slight variation in the composition of the three films which could be due to small variations in sputtering parameters arising due to variation in the time duration of sputtering required to deposit the three different thicknesses. This minor composition variation might have also contributed to the observed variation in Gilbert damping constant in the three films. It has to be pointed that despite these factors, the value of $\alpha = 0.007$ obtained for the 500 nm thick film with overall composition of $Ni_{48.14}Mn_{38.14}Sn_{13.72}$ is the lowest ever reported value for any Ni-Mn-Sn film [DUBO11, DUBO12a]. From the figure, it is observed that ΔH follows a nonlinear variation with f. The reason behind this can be understood from the nonlinear variation of 2-magnon scattering (*c.f.* Figure 3.18). 2-magnon scattering contribution shows steep nonlinear slopes at low frequencies and a saturation behavior at extremely high frequencies. The individual contributions to the total linewidth for 500 nm film are shown in Figure 3.18.

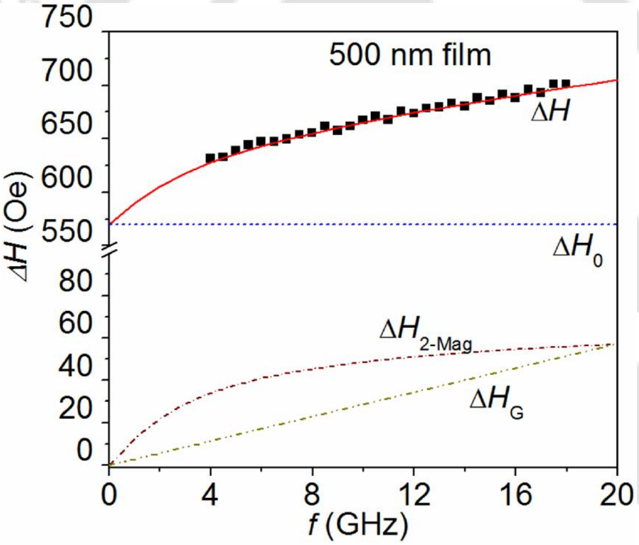

Figure 3.18: Frequency dependence of individual contributions to linewidth (ΔH) of 500 nm thick annealed film.

From the frequency variation FMR spectra analysis, we found that these films have high magnetic anisotropy and there are various external contributions to the total linewidth. Angular variation FMR spectra can provide a good visualization of the magnetic anisotropy in these films. Moreover, angular variation linewidth analysis can prove one with more explicit information about 2-magnon scattering and other external contributions. For this, FMR spectra were recorded at various angular positions of the film with respect to the field direction. Such a study gives us not only information about the perpendicular magnetic anisotropy but also about the contributions of external factors on the intrinsic linewidth (damping mechanism) of the material. Here, only out-of-plane measurements recorded on the 1500 nm thick film is presented since this sample gave the best MS-FMR signal. As the magnetic and structural properties of the films do not vary much with thickness, the results of the present analysis can be extended to all the films with lower thicknesses of the same series. Figure 3.19 shows the FMR spectra recorded from $\theta_H = 0°$ to 90° for the 1500 nm thick film. The spectra were recorded at three different microwave frequencies of 10, 12 and 14 GHz.

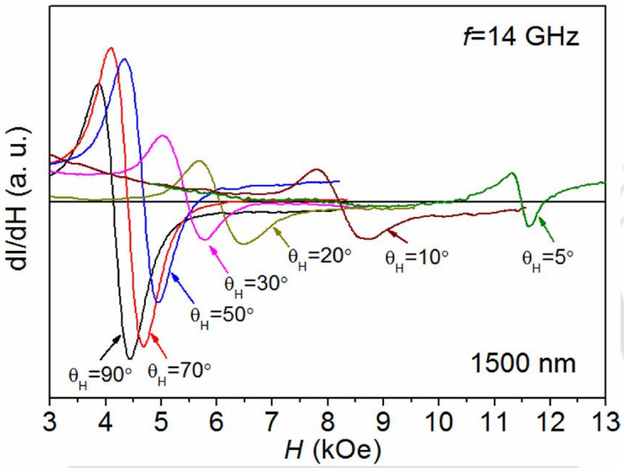

Figure 3.19: MS-FMR spectra of 1500 nm thick austenite Ni-Mn-Sn film recorded at different film orientation with magnetic field at 14 GHz microwave frequency.

H_r as a function of θ_H was then numerically calculated using Eqn. 2.23 and the interpolated values of θ_M are shown as lines in Figure 3.20 along with experimental data (symbols). The numerically calculated values yielded a good fit to experimental data. During fitting, the equilibrium angle of magnetization θ_M was numerically estimated for each value of θ_H at different f values and the same is depicted in the inset of Figure 3.20. From the numerical fitted equations, the effective anisotropy constant (K_1) to be $-9.0 \pm 0.5 \times 10^5$ erg/cc by substituting the M_s value obtained from VSM studies in $4\pi M_{\text{eff}}$. $K_1 < 0$ implies that the films have an in-plane easy axis [JOHN96]. Easy axis of magnetisation is determined from the expression, $-2\pi M_S^2 + K_1$, where K_1 represents other first-order (intrinsic) anisotropy energy contributions except the shape anisotropy. In this case, one of the major components in K_1 could be magneto-elastic anisotropy ($K_{me} \propto \lambda\sigma$), where σ is the stress which is related to the strain (ε) through the elastic modulus E (or $\sigma = E\varepsilon$) and λ is the magnetostriction constant, which depends on the orientation and can be positive or negative [JOHN96]. K_{me} can develop from the strain induced in the films by various sources such as thermal strain associated with differences in thermal expansion coefficients of the constituent metals during annealing, intrinsic strain due to high deposition rate or strain due to lattice parameter mismatch of the alloy with Si (100) substrate. If $-2\pi M_s^2 + K_1$ is negative, the film will have in-plane easy axis. On the other hand, if $-2\pi M_s^2 + K_1$ is positive, the films will have out-of-plane easy axis. In the present cae, K_1 is negative, which signifies in-plane easy axis in these films.

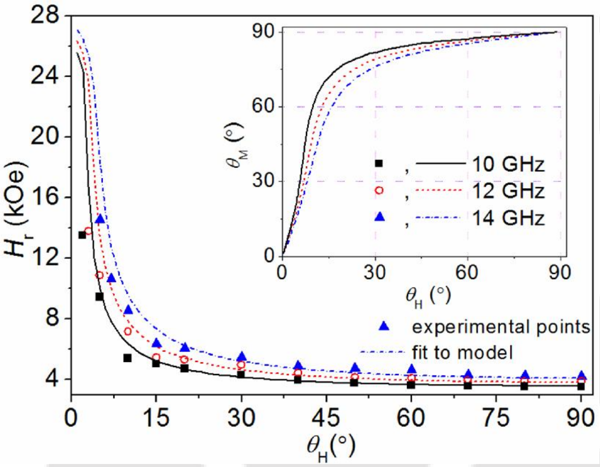

Figure 3.20: Angular dependence (θ_H) of resonance field (H_r) at different microwave frequencies for the 1500 nm thick film. Experimental data are shown as symbols and the solid lines represent fits to Eqn. 2.23. Inset shows variation of equilibrium angle of magnetization (θ_M)with applied field direction (θ_H) in out-of-plane configuration at different frequencies.

Finally, magnetic relaxation dynamics in the film was analyzed from the angular dependence of ΔH at different frequencies. This analysis gives information about Gilbert damping constant (α). Information about the quality of the film can also be understood from the external linewidth contributions. θ_H dependence of ΔH at different frequencies was estimated numerically using the Eqn. 2.25. The curves obtained by the above numerical model fitted very well to the experimental data (*c.f.* Figure 3.21). The independent contributions to magnetic damping from different sources are shown in Figure 3.22. The 2-magnon symmetry contribution was found to be 0.12 and the anisotropy dispersion constant $\Delta\theta_H$ was estimated to be 0.005°. The estimated parameters are in good agreement with those reported earlier [SAMA15, KURE13].

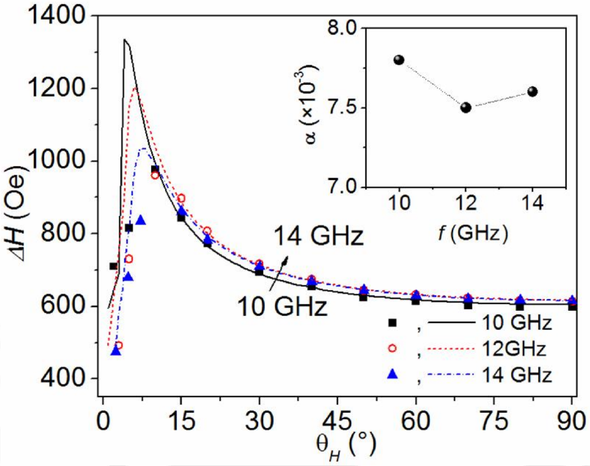

Figure 3.21: Variation of Δ*H* with out-of-plane angle θ_H at different frequencies. Experimental data are shown as symbols and the solid lines represent fits to Eqn. 2.25. Inset in figure shows the frequency dependence of Gilbert damping parameter.

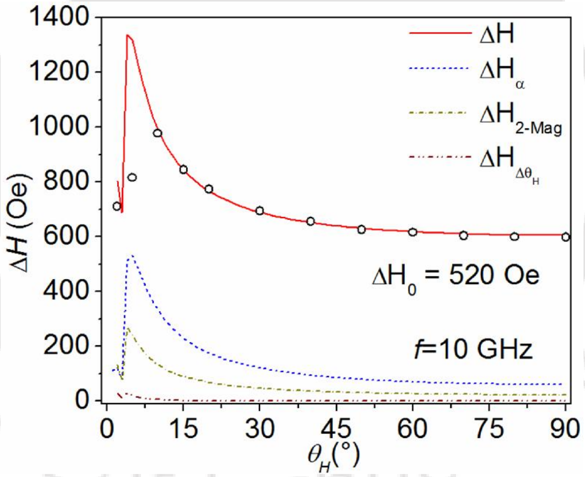

Figure 3.22: θ_H dependence of individual contributions ($\Delta H_{2\text{-}mag}$, ΔH_α and $\Delta H_{\Delta\theta}$) to ΔH at a frequency of 10 GHz.

In the present linewidth analysis, a significant contribution from 2-magnon scattering was noticed which may be due to the anisotropic distribution of scattering centers within the sample arising due to the structural defects present in the film. Similar observations have been made by Dubowik *et. al.* [DUBO11] in Ni_2MnSn

epitaxial films deposited by magnetron sputtering on MgO (100) substrates. For their 30 nm thick Ni_2MnSn film, the Gilbert contribution was found to be seven times smaller than the 2-magnon contribution which is primarily assumed to originate from high surface roughness. But for their 100 nm thick film, the Gilbert contribution and 2-magnon contributions were found to be comparable. The origin of the 2-magnon scattering was explained in terms of voids or other defects present inside the bulk of the thicker films. In the present case, the films were deposited on Si (100) substrate followed by *ex situ* annealing at 823 K. High temperature annealing induces higher surface roughness in the films. Being off-stoichiometric, the possibility of lattice defects is more in these films. Both these factors significantly can increase the 2-magnon contribution. The combined effect of these factors can result in a large increase in the 2-magnon contribution as observed in the present films as compared to their 100 nm thick epitaxial N_2MnSn film. In addition, Krivosik *et. al.*[KRIV07] showed that the density of states for degenerate magnons increases in thicker films. Hence, for the 1500 nm film, the magnon scattering contribution is much higher than that of the Gilbert contribution. Variation of α with frequency is shown as inset in Figure 3.21. The Gilbert damping parameter (α) was observed to be very low (average value of 0.0076) and was found to vary from 0.0075 to 0.0078 in the frequency interval of 10 to 14 GHz. This value of α is comparable to the value obtained from our ΔH *versus* f data. It may be noted that *ab initio* calculations [YEMK10] have pointed out that Ni-Mn-Sn alloy does not exhibit an energy gap in the spin-down band at the Fermi level. This lack of half-metallic character has seriously limited the application of Ni-Mn-Sn alloys. Discovery of very low Gilbert damping coefficient along with the possibility of getting lower damping constant by decreasing film thickness in these alloys in the work is certain to open up new applications for these alloys. Further, the present study also reveals the possibility of improving spin transfer torque based device performance by optimizing the operational frequency in the same type of material.

To understand the dynamic magnetic properties of Ni-Mn-Sn films in the martensite phase, FMR measurements of series 2 films have been done using C-FMR technique. Room temperature FMR spectra were recorded as a function of film orientation with respect to applied magnetic field using an electron spin resonance (ESR) spectrometer (Jeol JES-FA200) operating at 9.44 GHz with a modulation of 100 kHz. The resonance field exported from the spectrum is represented in Figure 3.23. The θ_H dependence resonance field (H_r) been analyzed using Eqn. 2.23 and shown as lines in Figure 3.23. From the figure, it is clear that with angle, the resonance field shift is very less, signifying that the film has very low effective anisotropy. The anisotropy value (K_1) for these films are found ~10^4 erg/cc which is very low as compared to austenite Ni-Mn-Sn films with K_1 ~ 10^6 erg/cc. Similar behavior is observed in films of all thicknesses. The magneto-dynamic parameters for the martensite films are presented in Table 3.05. This is the first observation of such very low M_{eff} and K_1 in Ni-Mn-Sn based films. The very low effective magnetization and anisotropy for these films may be the consequence of martensite phase of the films.

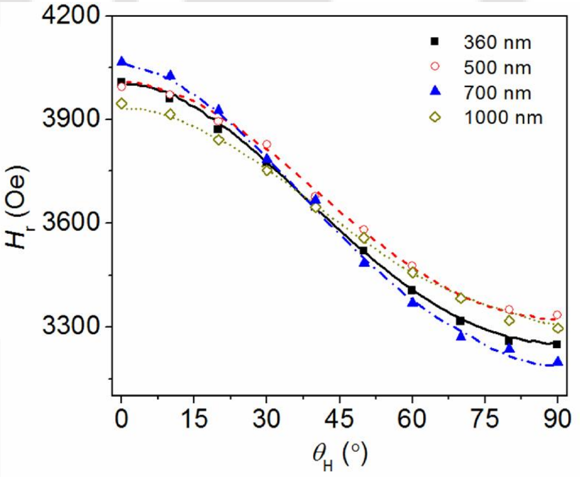

Figure 3.23: θ_H variation of resonance field (H_r) corresponding to martensite Ni-Mn-Sn (series 2) films of different thicknesses. Experimental data are shown as symbols and the solid lines represent fits to Eqn. 2.23.

Table 3.05: Magneto-dynamic parameters for martensite(series 2) Ni-Mn-Sn films

Thickness (nm)	$4\pi M_{eff}$ (±5) (Oe)	K_1 (±0.2) (×10^4 erg/cc)	g	ΔH_0	α (±0.0002)
360	849	2.5	2.10	220	0.0082
500	849	3.0	2.10	180	0.0082
700	876	3.0	2.10	120	0.0082
1000	949	2.8	2.10	100	0.0082

Magnetic relaxation dynamics in the martensite thin films was analyzed from the angular dependence of ΔH. ΔH verus θ_H data was fitted numerically to Eqn. 2.25.

The fitted curves are represented as lines in Figure 3.24 along with experimental data points represented as symbols. From the figure, it can be seen that numerically modeled curves yielded a good fit to the experimental data. The independent contributions of magnetic damping from various sources along with the phenomenological Gilbert damping contribution to the total linewidth are also shown in Figure 3.25 for all the films. The individual contributions to the total linewidth have been estimated using Eqn. 2.25 and it was found that there is a large contribution from the 2-magnon scattering term (*c.f.* Figure 3.25). The origin of this may be attributed to the high surface roughness induced in the films due to the high temperature annealing treatment and the presence of lower symmetry martensite phase. The decrease in ΔH with increasing thickness is due to decrease in ΔH_0 as other terms remained similar. The magneto-dynamic parameters obtained from the fitting are listed in Table 3.05.

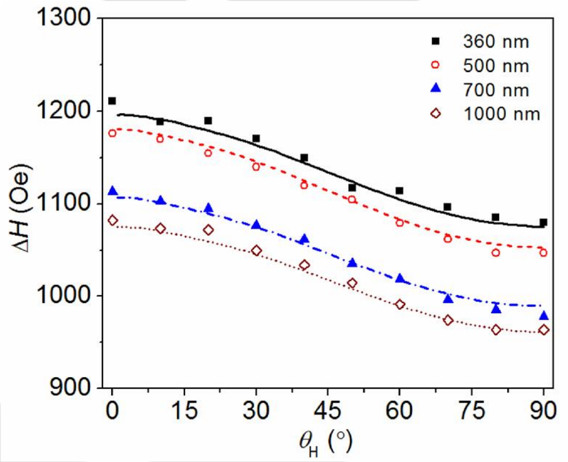

Figure 3.24: θ_H variation of FMR linewidth ΔH for martensite Ni-Mn-Sn (series 2) films of different thicknesses. Experimental data are shown as symbols and the solid lines represent fits to Eqn. 2.25.

In the studies, magneto-dynamic properties of martensite Ni-Mn-Sn films are revealed for the first time. Very low magnetic anisotropy of these films results in magnetic properties which are almost independent of film orientation. Such films are expected to have a large number of stable states as compared to the two stable states in conventional magnetic films with high anisotropy. This unusual property may lead to possible applications in memory storage and logical devices in computer circuitry [JOHN58, KEFA70, SLAU02].

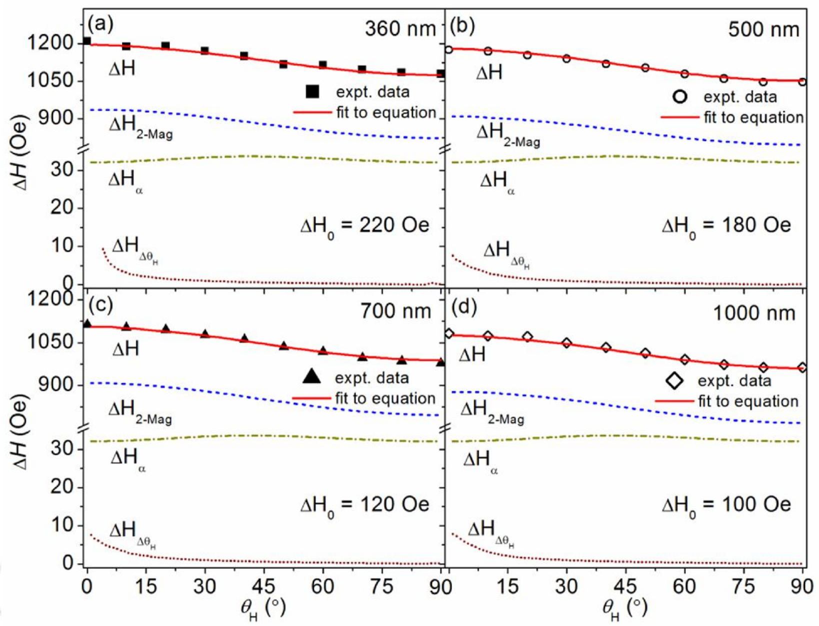

Figure 3.25: Angular dependence of individual contributions ($\Delta H_{2\text{-}mag}$, ΔH_{α} and $\Delta H_{\Delta\theta}$) to ΔH estimated for martensite Ni-Mn-Sn (series 2) films of different thickness.

3.6 Summary

Effects of composition and thickness on the structural, magneto-static, magneto-dynamic and magneto-caloric properties of Mn-rich Ni-Mn-Sn ferromagnetic Heusler alloy thin films sputter deposited on Si (100) substrates at ambient temperature have been investigated. Salient outcome of these investigations are listed below:

- All as-deposited films were amorphous in nature. Series 1 films annealed at 823 K exhibited room temperature cubic structure with space group $Fm\bar{3}m$ (space group 225) with high degree of $L2_1$ ordering, but series 2 films annealed at 823 K exhibited room temperature martensite phase with modulated 14M structure.
- Magnetic study disclosed paramagnetic nature of as-deposited films and room temperature ferromagnetism in the annealed films. High T_C (~ 550 K) with stable room temperature martensite ferromagnetic phase has been reported for first time in series 2 Ni-Mn-Sn films. Higher thickness martensite Ni-Mn-Sn films with $D > 90$ nm exhibited weak signature of martensitic transition.
- In-plane and out-of-plane *M-H* loops revealed films with room temperature austenite phase (series 1) has in-plane easy axis with large out-of-plane

magnetic anisotropy. But, series 2 films with room temperature martensite phase have very low magnetic anisotropy.

- MS-FMR spectra analysis revealed low Gilbert damping constant (α) and high effective perpendicular anisotropy (K_1) in austenite Ni-Mn-Sn films (series 1). Lowest α value of 0.0070 was observed in 500 nm thick film.
- C-FMR spectra analysis unveiled low α and very low K_1 in martensite Ni-Mn-Sn (series 2) films.
- Maximum magnetic entropy change ($(-\Delta S_M)_{\max}$) of 65.3×10^3 erg/cc.K (or 0.81 J/kg.K) was obtained at $T_C = 306$ K for a field change of 12 kOe in 250 nm thick austenite (series 1) film.

The above results reveal the potential of austenite (series 1) Ni-Mn-Sn films for fabricating efficient high density magnetic recording hard disks, magnetic random access memories, magnetic oscillators and magnetic sensors. Investigations on martensite Ni-Mn-Sn films (series 2) performed for the first time, indicates very low magnetic anisotropy of these films which may lead to possible applications in multistate memory storage and logical devices in computer circuitry [JOHN58, KEFA70, SLAU02].

Chapter 4

Martensite Ni-Mn-Co-Sn thin films

In chapter 3, Ni-Mn-Sn films of two different compositions exhibited two different ferromagnetic crystal phases at room temperature. One of them is cubic austenite phase with $L2_1$ ordering with low Curie temperature and other is modulated martensite phase with high Curie temperature. First time investigations on martensite Ni-Mn-Sn films revealed some unique properties of these alloys like room temperature ferromagnetism, very low magnetic anisotropy, low Gilbert damping constant etc. which has opened up new applications for these alloys. It has been observed that small amounts of substitution of Ni or Mn by Co in Ni-Mn-Z alloys (where Z = Ga, In, Sn, or Sb) improves the magnetic properties of these alloys [KAIN06, YUSY07a, NAYA09, YUSY07b, HANZ10]. Researchers have found various interesting properties in Ni-Mn-Co-Sn films such as large exchange bias effect and room temperature martensitic phase in epitaxially grown Ni-Co-Mn-Sn film on MgO (100) substrate [MACH13], Golub *et. al.* [GOLU17] performed magnetic resonance study on $Ni_{46.0}Mn_{36.8}Sn_{11.4}Co_{5.8}$ epitaxial thin films deposited on MgO(001) substrate to understand the antiferromagnetic coupling between martensitic twin variants. These interesting studies served as motivation to investigate the effect of Co substitution in martensite Ni-Mn-Sn films. This chapter discusses structural, magneto-static and magneto-dynamic studies carried out on martensite Ni-Mn-Co-Sn films sputter deposited on Si (100) substrates.

4.1 Sample preparation and processing

Ni-Mn-Co-Sn films with thicknesses of 360 nm, 500 nm, 700 nm and 1000 nm were deposited on Si (100) substrate by DC magnetron sputtering from a 2 inch diameter and 1 mm thick $Ni_{50}Mn_{37}Sn_{13}$ alloy target after optimizing working (Ar) gas pressure to 1.8 Pa and dc power to 70 W (the same condition as used to deposit martensite Ni-Mn-Sn (series 2) films in chapter 3). Cobalt (Co) was introduced in the films by symmetrically placed 2 × 2 mm^2 Co chips on the Ni-Mn-Sn target. Before deposition, the sputtering chamber was evacuated to a base pressure better than 10^{-4} Pa. During deposition, the substrate holder was rotated at 15 rpm to ensure uniform deposition. The compositions of the films were evaluated using EDS analysis and found to be $Ni_{53.2}Mn_{29.2}Co_{7.0}Sn_{10.6}$ with corresponding *e/a* ratio of 8.41. The films of different thicknesses were deposited by varying deposition time only, while keeping other deposition conditions identical. The composition variation with film thickness was very less which limited the *e/a* variation to ±0.04. As-deposited films were annealed *ex situ* at 823 K under residual Ar gas pressure of 10^{-3} Pa for 1 h. Thickness of the films were verified using a surface profiler which also indicated < 5 nm variation in thickness over the film surface. The annealed films were taken for further investigations.

4.2 Structure and morphology

Room temperature XRD patterns of annealed Ni-Mn-Co-Sn films are shown in Figure 4.01. From the XRD patterns, it is evident that all the annealed Ni-Mn-Co-Sn films exhibit martensite phase which can be indexed to a modulated 14M phase just as in the case of the ternary Ni-Mn-Sn (series 2) films. Apart from the martensite peaks, an extra weak peak can be observed at $2\theta = 35.33°$ which corresponds to MnO (space group 225). The MnO peak was also present in the Ni-Mn-Sn films and was discussed elaborately in chapter 3. As discussed there, the small amount of MnO present on the surface of the films may slightly alter the composition of the Ni-Mn-Co-Sn films, but would not affect their properties significantly. Lattice parameters of the films calculated using the (1 2 7), (2 0 -5), (1 1 10) peaks and relation 2.02 are listed in Table 4.01. The average crystallite size (D) and the lattice strain (ε) present in the films were also estimated from the XRD data using the Williamson-Hall relation (Eqn. 2.05) and the same are listed in Table 4.01. The Table shows that these films have larger D than the ternary films. Here too, D increased with increase in film thickness. ε did not vary with thickness and its value was similar to one observed the ternary films in chapter 3.

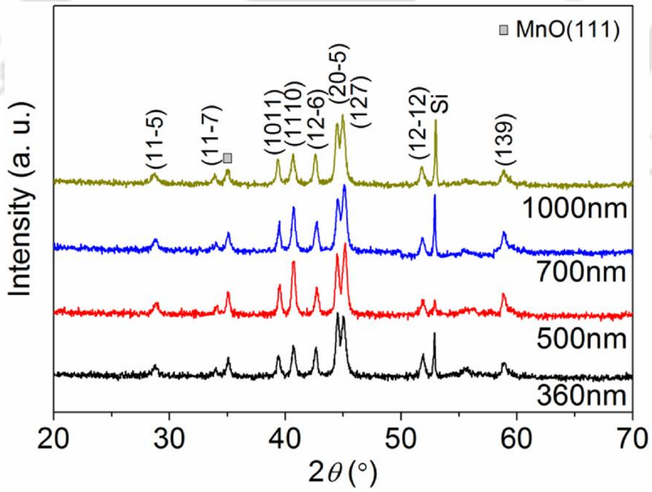

Figure 4.01: Room temperature XRD patterns of annealed Ni-Mn-Co-Sn alloy thin films of different thicknesses.

Table 4.01: Structural and morphological parameters of annealed Ni-Mn-Co-Sn films

Thickness (*t*) (±5) (nm)	**Lattice parameters**			**D (±3) (nm)**	**ε (±0.1) ($\times 10^{-3}$)**	**$R_{av.}$ (nm)**	**$R_{r.m.s.}$ (nm)**
	***a* (nm)**	***b* (nm)**	***c* (nm)**				
360	0.433	0.541	2.926	92	4.8	5.64	7.14
500	0.433	0.540	2.926	98	4.8	5.73	6.97
700	0.433	0.540	2.926	105	4.8	5.52	6.75
1000	0.433	0.540	2.926	124	4.6	5.87	7.13

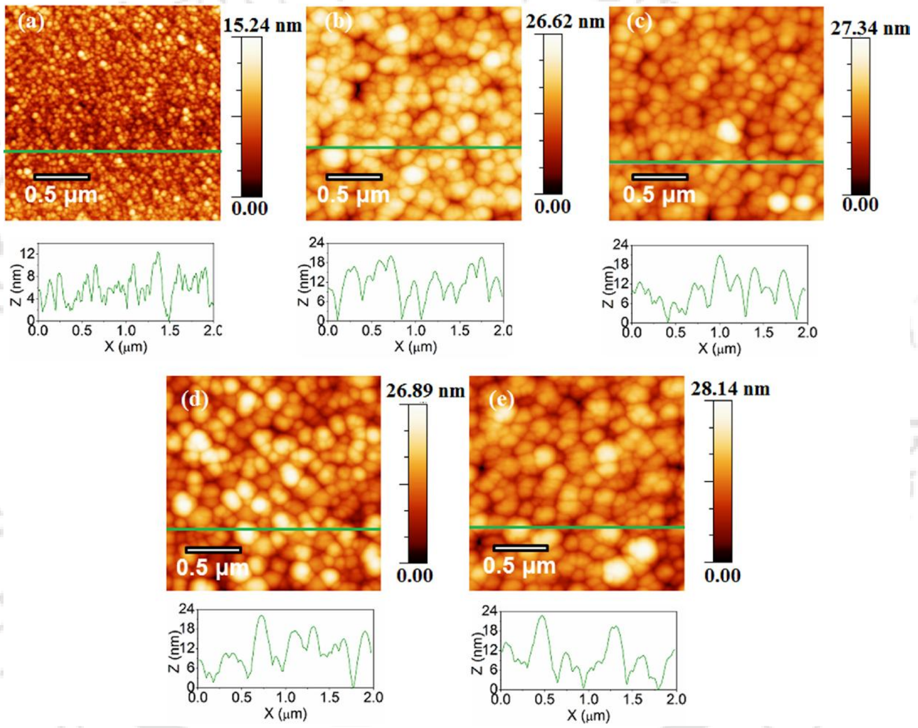

Figure 4.02: Atomic force micrographs of (a) as deposited (360 nm) and annealed (b) 360 nm, (c) 500 nm, (d) 700 nm and (e) 1000 nm thick Ni-Mn-Co-Sn films.

Figure 4.02 (a-e) show the AFM images of as-deposited (360 nm) and 823 K annealed martensite Ni-Mn-Co-Sn films of different thicknesses. Average ($R_{av.}$) and r.m.s. ($R_{r.m.s.}$) surface roughnesses of 2.11 and 2.62 nm, 5.64 and 7.14 nm, 5.73 and 6.97 nm, 5.52 and 6.75 nm and 5.87 and 7.13 nm were found for as-deposited (360 nm) and annealed 360 nm, 500 nm, 700 nm and 1000 nm films, respectively. The effect of annealing can be visualized by comparing the micrographs of as deposited (360 nm) and annealed Ni-Mn-Co-Sn films shown in Figure 4.02(a,b). An increase in the crystallite size and surface roughness is evident upon annealing from the two micrographs, indicating that the post-deposition annealing treatment increases the surface roughness. The structural parameters estimated are summarised in Table 4.01.

4.3 Magneto-static properties

Variation of magnetization of annealed Ni-Mn-Co-Sn films with applied field (*M-H* curves) is shown in Figure 4.03. Room temperature *M-H* curves (not shown) of all the as-deposited films exhibited paramagnetic behaviour just as the ternary Ni-Mn-Sn films due to the amorphous structure. It is clear from the figure that the films annealed at 823 K exhibit ferromagnetic behaviour at room temperature. With increasing film thickness, a small upswing in magnetic moment is also observed in the Ni-Mn-Co-Sn films which can be related to the improvement in crystallite size with increasing film thickness. The saturation magnetization (M_s) of these films are found to be 84 emu/cc, 90 emu/cc, 90 emu/cc and 96 emu/cc for 360 nm, 500 nm, 700 nm and 1000 nm films, respectively. A small upswing in magnetic moment is also found with Co substitution in Ni-Mn-Sn films. *M-H* loops recorded with in-plane and out-of-plane film orientations reveal that the films have easy magnetization along film plane. Further, the close similarity between two loop shapes signifies magnetic homogeneity in the films. This unique property found in martensite Ni-Mn-Sn films (series 2) is also present in the Ni-Mn-Co-Sn films. This suggests that the magnetic homogeneity observed in these films is a direct consequence of the room temperature martensite phase in these films.

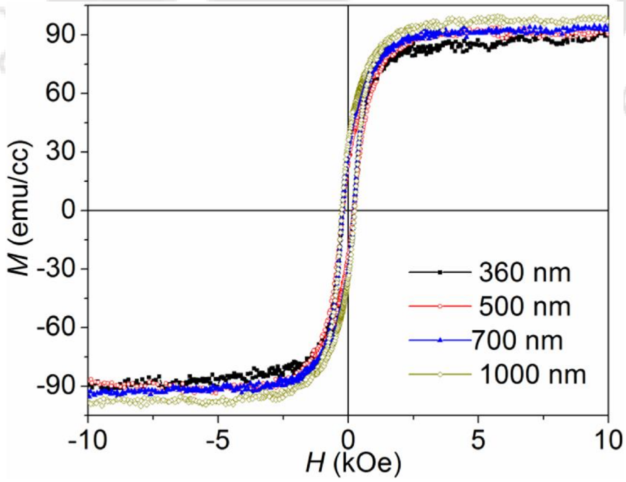

Figure 4.03: Room temperature *M-H* curves 823 K annealed Ni-Mn-Co-Sn alloy thin films with different thicknesses.

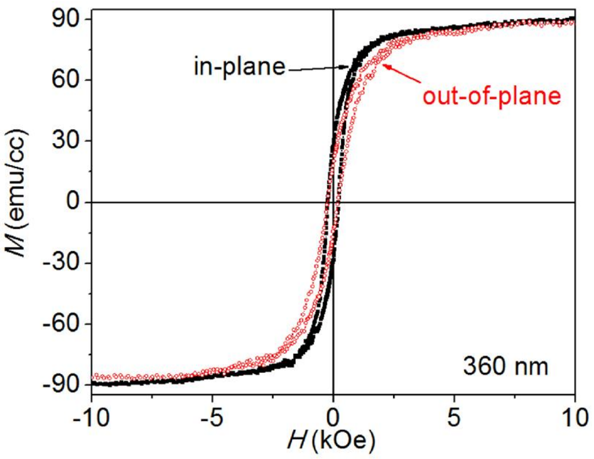

Figure 4.04: Room temperature M-H curves of 360 nm Ni-Mn-Co-Sn alloy thin film with in-plane and out-of-plane orientations.

Figure 4.05 shows the themo-magnetization (M-T) curves of the annealed Ni-Mn-Co-Sn films of all thicknesses. M-T data recorded during heating and cooling cycles under an applied field of 500 Oe are designated as field warmed (FW) and field cooled (FC) curves, respectively. It is evident from the M-T data that the reversible martensite to austenite (M $\leftrightarrow$ A) transition observed in martensite Ni-Mn-Sn films is absent in Ni-Mn-Co-Sn films. On the other hand, an irreversible transition near 600 K whose origin is not known is observed in the Co substituted films. This irreversible transition is observed only in the FW curve of the virgin sample and not in the subsequent thermal cycles. This suggests that there may be some minor structural rearrangement occurring in the film in an irreversible manner at this temperature. Since there is no record of such a feature in the literature, it is difficult to conclude on the origin of this feature in the M-T curves of the Co substituted films. From the M-T curves, it is evident that all the films have high Curie temperature (T_C). A slight increase in T_C is also observed as the thickness of the films is varied from 360 nm to 1000 nm film which may be due to the variation in structural factors or minor deviation in overall composition of the films with thickness. As compared to martensite Ni-Mn-Sn films, almost 300 K higher shift in T_C is noticed in the quaternary films as an effect of Co substitution. This increase in T_C is consistent with the increase in e/a ratio for Ni-Mn-Co-Sn films with respect to the ternary films. High T_C observed for the first time in Ni-Mn-Co-Sn alloy permits the possibility of stabilizing the low temperature ferromagnetic martensite phase at higher temperatures apart from providing better stability to the room temperature properties.

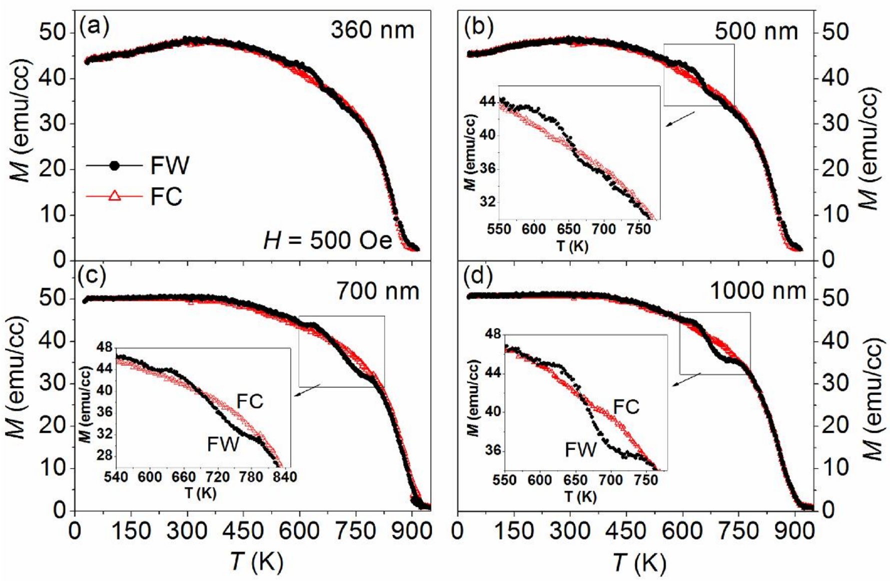

Figure 4.05: Thermo-magnetization curves of annealed (a) 360 nm, (b) 500 nm, (c) 700 nm and (d) 1000 nm Ni-Mn-Co-Sn films recorded under 500 Oe in FW and FC modes. Insets show an enlarged view of the irreversible transition region.

4.4 Magneto-caloric properties

From the *M*-*T* data, it is evident that although these films exhibit room temperature martensite phase, no first-order M ↔ A structural phase transformation (FOPT) is observed in these films. However, a second-order magnetic phase transition (SOPT) is observed at very high temperatures in all the films. ΔS_M across the SOPT has been evaluated using Maxwell thermodynamic equation (Eqns. 2.08 & 2.09). Isothermal initial *M–H* curves for all the films were recorded at discrete intervals of T (*c.f.* Figure 4.06) across T_C and ΔS_M was calculated from this data using Eqn. 2.09. Figure 4.07 shows the $\Delta S_M(T)$ curves of the films for dH = 18 kOe. $(\Delta S_M)_{max}$ values associated with the SOPT of these films are listed in Table 4.02. From the table it is clear that upon Co substitution in Mn/Sn sites, a 3.8, 2.3, 1.7 and 1.6 fold increase in $(\Delta S_M)_{max}$ is achieved as compared to martensite Ni-Mn-Sn films in 360 nm, 500 nm, 700 nm and 1000 nm thick films, respectively. $(\Delta S_M)_{max}$ evaluated for different dH is shown in Figure 4.08.

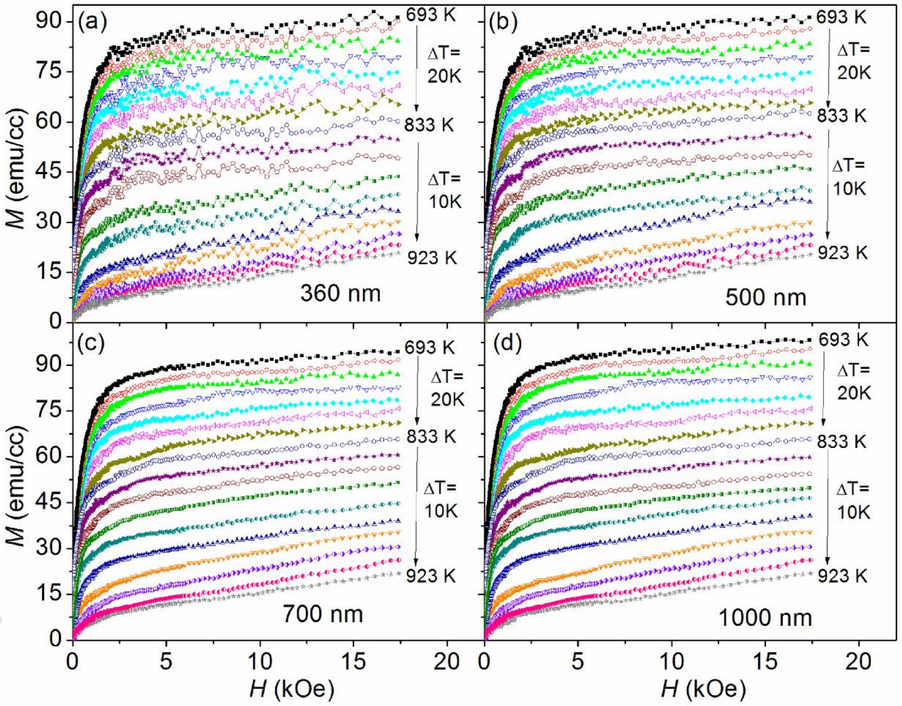

Figure 4.06: Initial *M-H* isotherms recorded for Ni-Mn-Co-Sn films of different thickness at discrete temperature interval across T_C.

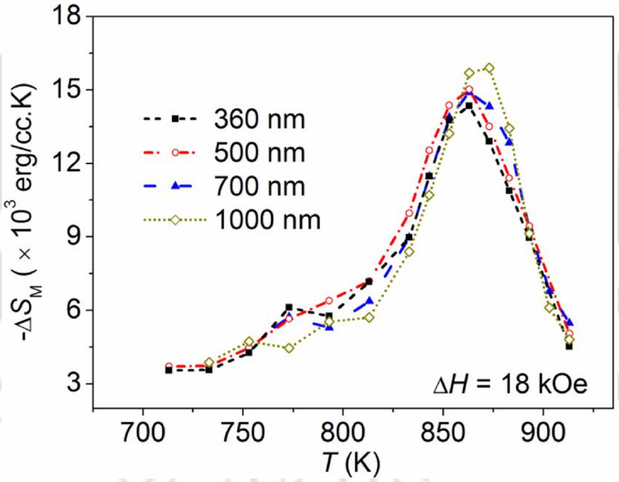

Figure 4.07: Variation of magnetic entropy change (ΔS_M) with temperature (T) for Ni-Mn-Co-Sn films of different thicknesses for dH of 18 kOe across T_C.

The refrigeration capacity (RC) of the films has been evaluated using Eqn. 2.10 from the respective $\Delta S_M(T)$ curve shown in Figure 4.07. The evaluated RC values are listed in Table 4.02. From the table it is clear that along with an increase in $(\Delta S_M)_{max}$, *RC* of the films are also increases remarkably with Co substitution in the ternary alloy film. A maximum (8.9 fold) increase in RC is observed for the 360 nm film with Ni-

Mn-Co-Sn film as compared to the martensite Ni-Mn-Sn film of the same thickness. The reason for this increase in the MCE parameters upon Co substitution is due to increase in the magnetic moment and the broadening of the SOPT. While the former increases $(\Delta S_M)_{max}$, the latter increases RC.

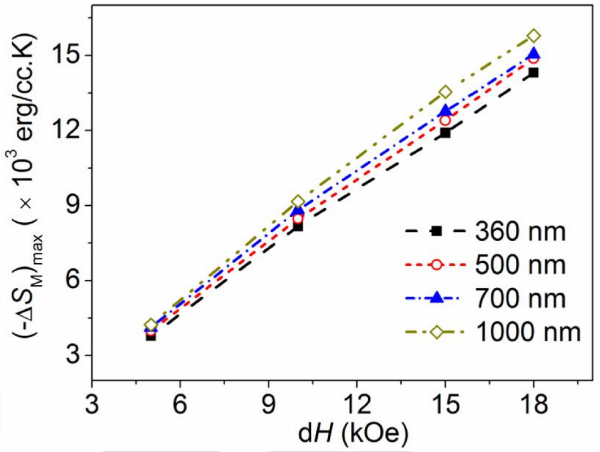

Figure 4.08: Variation of $(\Delta S_M)_{max}$ with dH for various Ni-Mn-Co-Sn films.

Table 4.02: Magneto-caloric parameters of Ni-Mn-Co-Sn films estimated for an applied field change (d*H*) of 18 kOe near T_C.

t (nm)	T_C (±1) (K)	$(-\Delta S_M)_{max}$ (±0.8) (×10^3 erg/cc.K)	RC (±8) (×10^3 erg/cc)	$(-\Delta S_M)_{max}$ (±0.01) (J/kg.K)	RC (±0.1) (J/kg)
360	860	13.2	643	0.16	7.8
500	862	14.9	707	0.18	8.5
700	863	14.9	754	0.18	9.1
1000	866	15.7	774	0.19	9.4

Materials showing large MCE can be used as refrigerants in environment friendly magnetic refrigerators. Though magnetic refrigerants are being primarily developed for room temperature refrigeration, several industrial and military applications require multi-stage refrigerators which can cool from high temperature in a stage by stage manner [KITA10]. In a multistage refrigerator system, the lower operating temperature of the previous stage behaves as the upper operating temperature for the next stage and so on. Such systems operate with magnetic refrigerants with a range of high operating temperatures. Ni-Mn-Co-Sn thin films exhibiting reasonable MCE parameters and composition dependent operating temperature may find use in such applications. These materials with no thermal hysteresis and high dM/dT at T_C can also be used for industrial waste energy harvesting [SRIV11].

4.5 Magneto-dynamic properties

To evaluate the room temperature magnetization dynamics, microwave absorption spectra were recorded as a function of film orientation with respect to applied magnetic field using an electron spin resonance (ESR) spectrometer (Jeol, JES-FA200) operating at 9.44 GHz with a modulation of 100 kHz. Samples of ~4 mm × 4 mm dimension firmly tethered to the flat tail of a quartz rod could be positioned with 1º angular precision inside the cavity of the spectrometer. Figure 4.09 shows the typical spectra recorded for the 360 nm thick Ni-Mn-Co-Sn film. From the spectrum it is clear that with angular variation, the resonance field (H_r) shift is very less, which signifies very low effective anisotropy in the film. Similar behavior is observed for all the film thicknesses. To evaluate the effective anisotropy quantitatively and other relevant magneto-dynamic parameters, H_r and resonance linewidth (ΔH) obtained from the FMR spectra were analyzed using Eqns. 2.23 and 2.25.

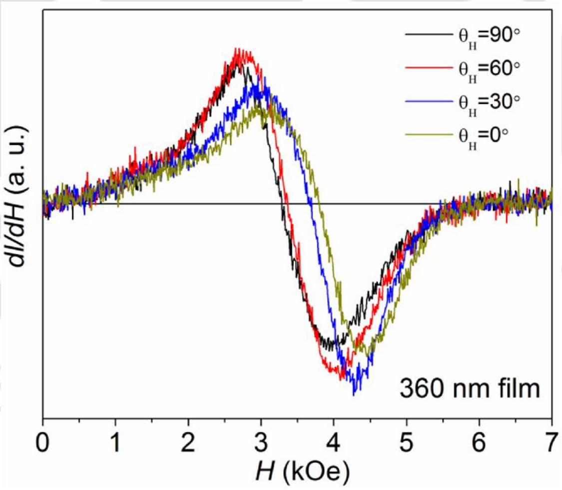

Figure 4.09: Room temperature FMR spectra for 360 nm Ni-Mn-Co-Sn film recorded at different film orientations with respect to the applied magnetic field direction.

Figure 4.10 depicts the θ_H dependence of H_r for all the films. The experimental data is represented as symbols and best fits to Eqn. 2.23 as solid lines in Figure 4.10. The numerically calculated values yielded a good fit to the experimental data. The effective magnetization ($4\pi M_{\mathrm{eff}}$) and effective perpendicular anisotropy (K_1) extracted from the analysis of H_r versus θ_H data and are listed in Table 4.03. The K_1 values found for these films are very low (~10^4 erg/cc), similar to the values obtained for martensite Ni-Mn-Sn (series 2) films discussed in chapter 3. Very low magnetic anisotropy of these films results in magnetic properties which are almost independent of film orientation. Such films are expected to have a large number of stable states as compared to the two stable states in conventional magnetic films with high anisotropy. From the analysis it is clear that the low anisotropy exhibited by the martensite Ni-Mn-Sn films is not altered upon the current Co substitution.

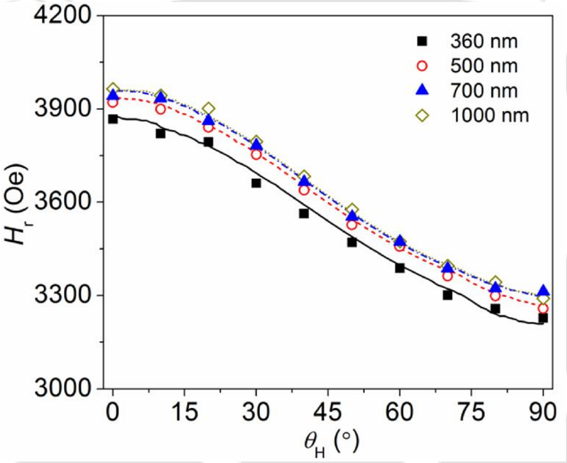

Figure 4.10: θ_H variation of resonance field (H_r) for Ni-Mn-Co-Sn films of different thicknesses. Solid lines represent best fits of experimental data (symbols) to Eqn. 2.23.

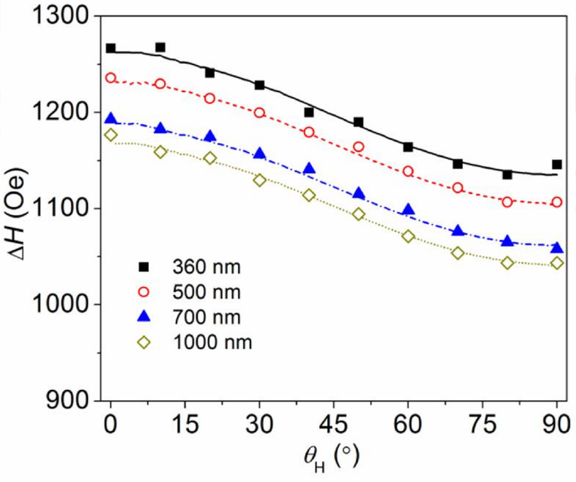

Figure 4.11: θ_H variation of FMR linewidth ΔH for Ni-Mn-Co-Sn films of different thicknesses. The solid lines represent fits of experimental data (symbols) to Eqn. 2.25.

Magnetic relaxation dynamics in the quaternary thin films was investigated using the angular dependence of ΔH. θ_H dependence of ΔH was estimated numerically using Eqn. 2.25 and the same is depicted as solid lines in Fig. 4.11 along with experimental data points represented as scattered points. From the figure it can be seen that numerically modeled curves yielded a good fit to the experimental data. In the present analysis, the individual contributions to the total linewidth have been estimated using Eqn. 2.25. The independent contributions of magnetic damping from different sources to the total ΔH are also shown in Figure 4.12 for all the films. From the figure it is clear that the major contributions to ΔH are from θ_H dependent $\Delta H_{2\text{-mag}}$ (~ 76% at $\theta_H = 90°$) and θ_H independent ΔH_0 (~ 20% for 360 nm films to 12% for 1000 nm film at $\theta_H = 90°$). So, the small decrease in ΔH with thickness is due to the decrease in the ΔH_0 term. All the magneto-dynamic parameters found for these films are summarized in Table 4.03. The Gilbert damping factor (α) was estimated from Eqn. 2.25 and a low α value of 0.0085 has been obtained. It has to be pointed out that this study is the first of its kind on Ni-Mn-Co-Sn films. The observed α value in the present Ni-Mn-Co-Sn films is reasonably low and in good agreement with those reported for other Ni-Mn-based Heusler alloy films (~0.0070-0.0075) [MODA16, DUBO11].

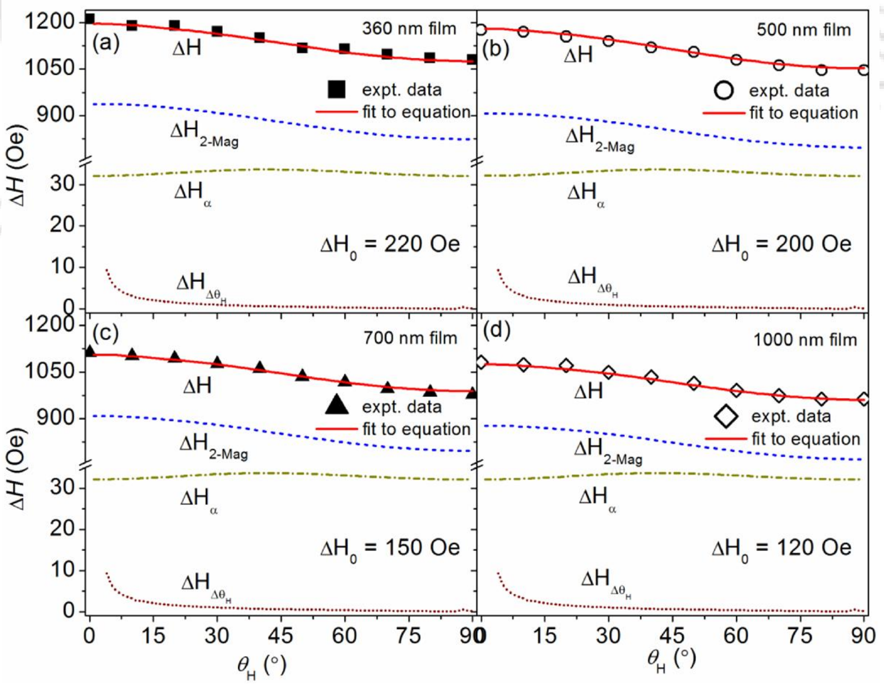

Figure 4.12: Angular dependence of individual contributions ($\Delta H_{2\text{-}mag}$, ΔH_α and $\Delta H_{\Delta\theta}$) to to total linewidth ΔH fit to Eqn. 2.25 for Ni-Mn-Co-Sn films of different thickness.

Table 4.03: Magneto-dynamic parameters for Ni-Mn-Co-Sn films

t (nm)	$4\pi M_{\mathrm{eff}}$ (±5) (Oe)	K_1(±0.2) (×10^4 erg/cc)	g	ΔH_0 (Oe)	α (±0.0005)
360	948	4.5	2.10	220	0.0085
500	1020	5.0	2.10	200	0.0085
700	1020	5.0	2.10	150	0.0085
1000	1091	5.5	2.10	120	0.0085

4.6 Summary

Structural, magneto-static, magneto-caloric and magneto-dynamic properties of Ni-Mn-Co-Sn films deposited on Si (100) substrate have been investigated in this chapter. Some of the exciting results found in this analysis are mentioned below.

- $Ni_{53.2}Mn_{29.2}Co_{7.0}Sn_{10.6}$ films annealed at 823 K exhibited room temperature martensite phase and ferromagnetism.
- Annealed Ni-Mn-Co-Sn films exhibited higher T_C (more than 300 K) than the ternary martensite Ni-Mn-Sn films (series 2 in previous chapter).
- Upon Co substitution, a 3.8, 2.3, 1.7 and 1.6 fold increase in $(-\Delta S_M)_{max}$ across T_C is achieved as compared to martensite Ni-Mn-Sn films of thickness 360 nm, 500 nm, 700 nm and 1000 nm, respectively.
- C-FMR study revealed for the first time very low K_1 (~ 10^4 erg/cc) and α of 0.0085 in the quaternary Ni-Mn-Co-Sn films.

Chapter 5

Austenite Ni-Mn-Sn and Ni-Mn-X-Sn (X = Cu, Fe, Co) thin films

In chapter 4, it was observed that Co substitution in martensite Ni-Mn-Sn films improved their magnetic properties significantly. This is in accordance with the reports in the literature which suggest that appropriate substitution of a fourth element in ternary Ni-Mn-Sn alloys can enhance their functional properties [KAIN06, YUSY07a, NAYA09, YUSY07b, HANZ10]. After reviewing these earlier works, it is clear that substitution of other elements in austenite Ni-Mn-Sn films will also impact their physical properties and may help in obtaining films with better properties. Hence, this chapter is devoted to a study of substitution of the fourth element X (= Cu, Fe, Co) on the physical and functional properties of Ni-Mn-Sn alloy films.

5.1 Sample preparation and processing

Ni-Mn-Sn and Ni-Mn-X-Sn (X = Cu, Fe, Co) films of thickness 500 nm were deposited on Si (100) substrate from a 2 inch diameter and 1 mm thick $Ni_{50}Mn_{37}Sn_{13}$ alloy target using the DC magnetron sputtering system shown in Figure 2.05(b). Optimized values of working (Ar) gas pressure (0.6 Pa) and DC power (10 W) were maintained throughout the deposition process. The fourth element (X) was introduced in the films by symmetrically placed 2×2 mm^2 X chips on the Ni-Mn-Sn target. Before deposition, the sputtering chamber was evacuated to a base pressure better than 10^{-4} Pa. As-deposited films were annealed *ex situ* at 823 K under residual Ar gas pressure of 10^{-3} Pa for 1 h. Surface profiler measurements showed that the thickness variation was < 5 nm over the film surface. Composition of the films was evaluated using an energy dispersive X-ray spectroscopy unit attached to a field emission scanning electron microscope and found to be $Ni_{58.1}Mn_{34.4}Sn_{7.5}$ (T1), $Ni_{57.5}Mn_{33.6}Cu_{1.4}Sn_{7.5}$ (Cu1), $Ni_{56.0}Mn_{33.1}Cu_{3.4}Sn_{7.5}$ (Cu2), $Ni_{57.5}Mn_{33.9}Fe_{1.0}Sn_{7.6}$ (Fe1), $Ni_{55.9}Mn_{33.4}Fe_{3.6}Sn_{7.4}$ (Fe2), $Ni_{57.1}Mn_{33.9}Co_{1.5}Sn_{7.5}$ (Co1), $Ni_{55.7}Mn_{33.0}Co_{3.8}Sn_{7.4}$ (Co2).

5.2 Structure and morphology

Room temperature XRD patterns of all the annealed films are shown in Figure 5.01. The as-deposited films were amorphous in nature (XRD patterns not shown here). After vacuum annealing at 823 K for 1 h, the amorphous films crystallized and the corresponding XRD patterns consisted of five Bragg peaks emanating from reflections from the cubic lattice planes. Presence of (111) and (200) super-lattice peaks in the XRD patterns confirmed the formation of single phase austenite structure with $L2_1$

ordering (space group $Fm\bar{3}m$) in the films (*cf.* Fig. 5.01). The degree of B2 and $L2_1$ ordering in the films evaluated using Eqns. 2.06 and 2.07 are listed in Table 5.01. It has been observed that all the films show > 82 % cubic $L2_1$ ordering which signifies good amount crystalline order in these off-stoichiometric Ni-Mn-based alloys.

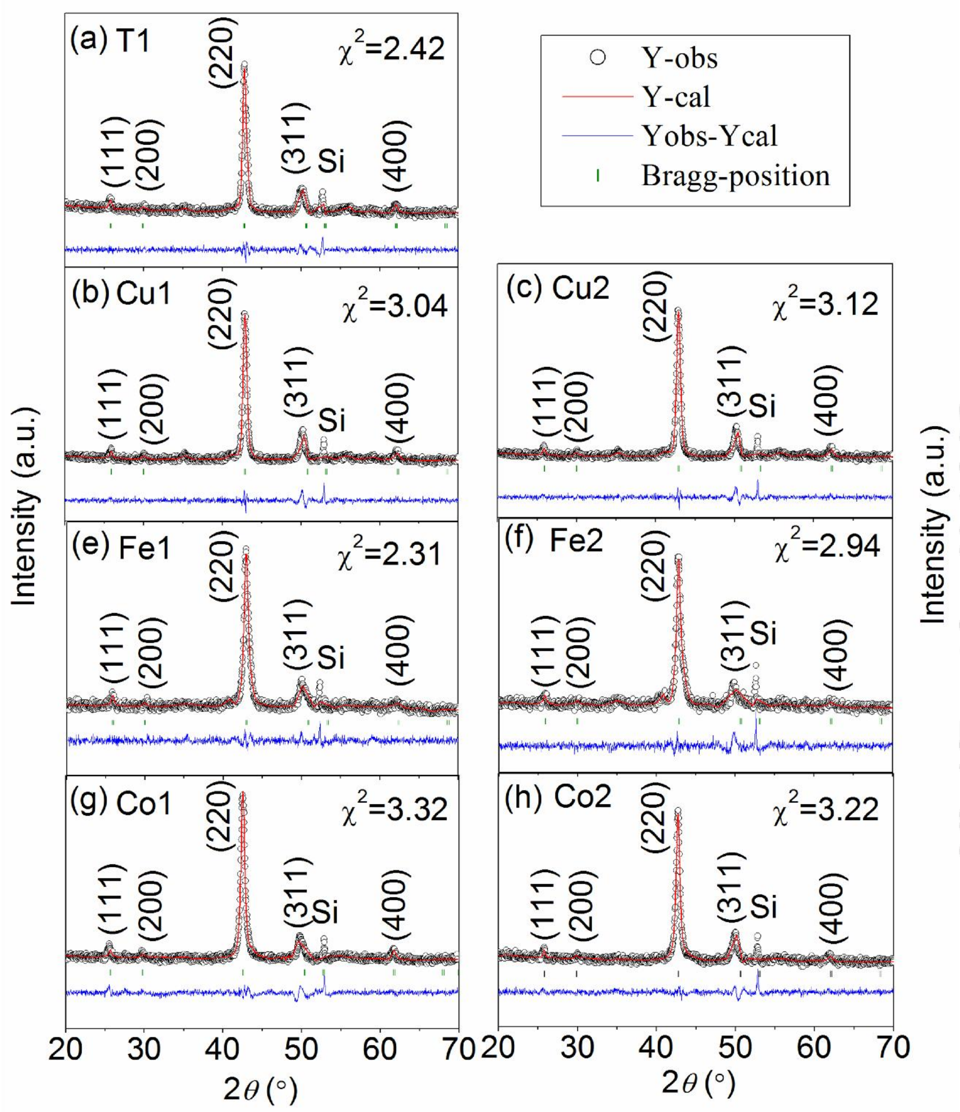

Figure 5.01: Rietveld refined room temperature XRD patterns of annealed ternary and quaternary films.

To evaluate the structural parameters in a more reliable way, the XRD data were refined using Rietveld method by presuming a $L2_1$ unit cell. In the stoichiometric Ni_2MnSn compound with $L2_1$ structure belonging to $Fm\bar{3}m$ space group, the Ni, Mn and Sn atoms occupy the Wyckoff positions 8c (1/4, 1/4, 1/4), 4b (1/2, 1/2, 1/2) and 4a

(0, 0, 0), respectively, as shown in Figure 5.02(a). In the case of off-stoichiometric $Ni_{58.1}Mn_{34.4}Sn_{7.5}$ alloy film, the excess Mn and Ni atoms are presumed to occupy the Sn-sublattice (*c.f.* Figure 5.02(b)) as pointed out earlier [UBAL17, SOKO12]. The refinement performed using the 'FullProf' open source software [RODR93, RODR01] confirmed the validity of the assumption by yielding good fits to the experimental data (*c.f.* Figure 5.01(a)). The goodness of the fit from which the crystallographic parameters of the films were extracted can be inferred from the quality of the difference data (Y_{obs}-Y_{cal}) and χ^2 value obtained. In the case of the quaternary films, the fourth element (X = Cu. Fe, Co) atoms are assumed to occupy the Sn-sublattice by replacing the Ni and/or Mn atoms in those sites. Typical unit cell for the $Ni_{55.7}Mn_{33.0}Co_{3.8}Sn_{7.4}$ (Co2) is shown in Figure 5.02(c). The unit cell has been modified accordingly for all the different compositions of the films. The refined patterns for all the films are shown in Figure 5.01(a-h). In the figure, open black circles represent the experimental diffraction data and the solid red line corresponds to the fit obtained by Rietveld refinement method. The optimized lattice constants of the films found from the refinement are listed in Table 5.01.

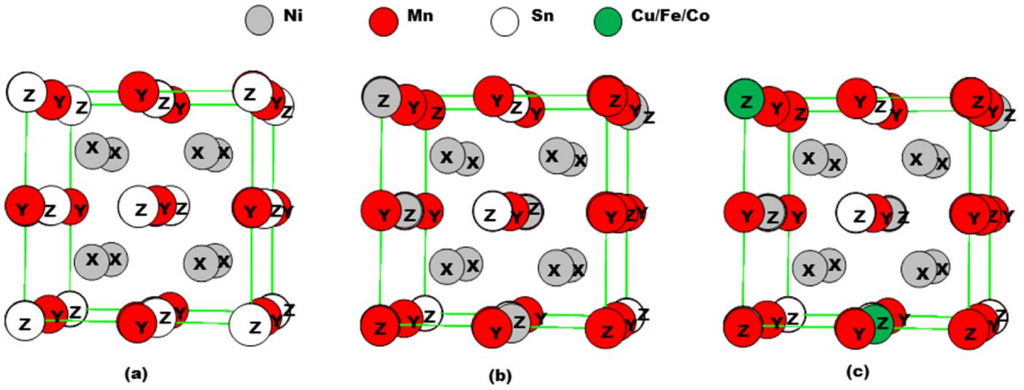

Figure 5.02: Schematic representation of different unit cells of Ni–Mn–Sn alloys used for Rietveld refinement. (a) X_2YZ (*e.g.*, $Ni_{50}Mn_{25}Sn_{25}$), (b) off-stoichiometric X_2YZ (*e.g.*, $Ni_{58.1}Mn_{34.4}Sn_{7.5}$), (c) X_2YZ with X/Y substitution (*e.g.*, $Ni_{55.7}Mn_{33.0}Co_{3.8}Sn_{7.4}$).

The average crystallite (grain) size (*D*) of the films has been estimated using the most intense (220) peak and Schërrer's equation (Eqn. 2.04). The lattice parameter (*a*) evaluated from the Rietveld refinement procedure and the estimated *D* values are tabulated in Table 5.01. It is evident from the table that incorporation of a small percentage ($1 < X < 4$) of X (X = Cu, Fe, Co) atoms has not changed the lattice constant or the average grain size in the films in a significant manner.

Table 5.01: Structural and morphological parameters of 823 K annealed Ni-Mn-Sn and Ni-Mn-X-Sn (X = Cu, Fe, Co) films.

Film	% of B2 order (S_{B2})	% of L2$_1$ order (S_{L2_1})	*a* (nm)	*D* (±0.3) (nm)	$R_{av.}$ (nm)	$R_{r.m.s.}$ (nm)
T1	98	84	0.599	14.4	1.05	1.39
Cu1	97	82	0.598	14.3	1.56	2.01
Cu2	98	83	0.598	14.6	1.42	1.92
Fe1	97	83	0.597	15.0	1.35	1.75
Fe2	98	85	0.597	14.7	1.39	1.80
Co1	98	84	0.601	14.3	1.37	1.69
Co2	98	83	0.598	14.6	1.40	1.77

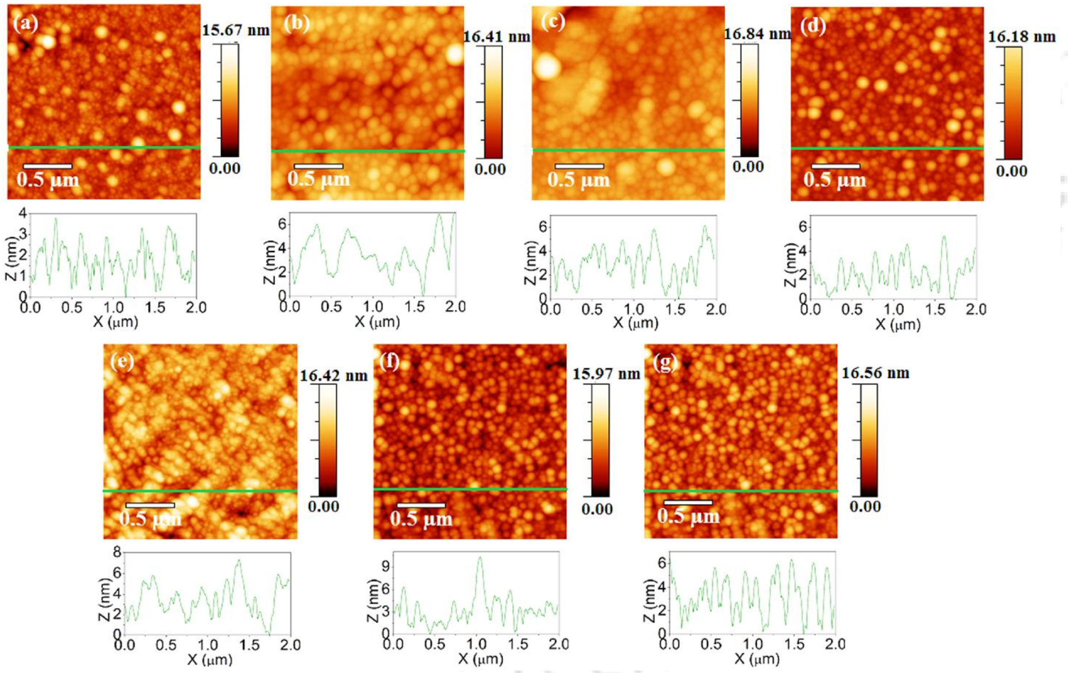

Figure 5.03: Atomic force micrographs of annealed (a) T1, (b) Cu1, (c) Cu2, (d) Fe1, (e) Fe2, (f) Co1 and (g) Co2 films scanned over 2 × 2 µm^2 area.

Surface morphology of the films was mapped over 2×2 µm^2 scan area using an AFM. The average ($R_{av.}$) and r.m.s. ($R_{r.m.s.}$) surface roughness of the films evaluated from the AFM data were found to be 1.05 and 1.39, 1.56 and 2.01, 1.42 and 1.92, 1.35 and 1.75, 1.39 and 1.80, 1.37 and 1.69 and 1.40 and 1.77 nm for T1, Cu1, Cu2, Fe1, Fe2, Co1 and Co2 films, respectively. Hence, the surface roughnesses of the films are less than 2 nm. It may be noted that a slight increase in $R_{av.}$ and $R_{r.m.s}$ are found upon substitution of the fourth element. Figure 5.03 (a-g) shows the AFM images of all the annealed films.

5.3 Magneto-static properties

Room temperature magnetic properties of both as-deposited and annealed Ni-Mn-X-Sn thin films were studied using the VSM with an applied field cycle of ±10 kOe. The room temperature isothermal magnetization as a function of applied field (*M-H* curves) of all the as-deposited films exhibited paramagnetic behaviour (not shown here) which can be attributed to the amorphous or poor-crystalline nature of the films. However upon annealing, ferromagnetic order is induced in the films with the formation of a single phase polycrystalline structure. It is well known that the magnetism in these materials is strongly related to the microstructure, atomic structure and the exchange interaction between the magnetic elements present in the alloy [SOKO17, XUYX18]. The black and red curves in Figure 5.04 represent in-plane and out-of-plane *M-H* loops. It is evident from the figure that it is easy to magnetize the films along the film plane, or in other words, the films have easy magnetization axis along their plane. A finite loop area found in out-of-plane *M-H* loops of some films may be due to some perpendicular domains present in these films. The Co2 film shows a flat, hard magnetic loop along the out-of-plane direction which confirms that all the domains in this film are aligned along the film plane. The in-plane and out-of-plane *M-H* loops also indicate the presence of magnetic anisotropy in the films. Though no significant change in saturation magnetization is observed upon Cu/Fe/Co substitution (*cf.* Table 5.02), the *M-H* loop shape of the films changed noticeably with orientation. This may be due to change in the exchange interaction between the atoms in the unit cell induced by the substituent (X) element since exchange coupling depends on the type of atoms and the distance between them [SOKO17, XUYX18]. A careful look at the *M-H* loops (*cf.* Figure 5.04(f)) and Table 5.02 would reveal that the ternary (T1) and 1.4 at.% (Cu1) and 3.4 at.% Cu (Cu2) substituted quaternary alloy films exhibit almost similar magnetic behaviour. But, substitution of small amounts of magnetic element Fe/Co significantly modifies the *M-H* loop shape by changing the M_r/M_s ratio (defining the softness of a ferromagnetic material) and coercively (H_c). With 1.0 at.% Fe substitution (Fe1), the M_r/M_s ratio of the film increased from 0.48 to 0.53 H_c value to decreased to 94 Oe from 100 Oe. So, Fe substitution enhances the soft magnetic property of the film. The M_r/M_s ratio further increased to 0.60 and H_c decreased to 70 Oe when 3.6 at.% Fe (Fe2) is substituted in the ternary alloy film. The effect is more prominent for Co substitution. 1.5 at.% Co substitution (Co1) enhances the M_r/M_s ratio to 0.70 and decreased H_c to 48 Oe. Similarly, for 3.8 at.% Co substitution (Co2), M_r/M_s ratio increases to 0.75 and H_c decreases to 38 Oe. This comparison reveals that the presence of small amounts of non-magnetic (X) element in the unit cell of Ni-Mn-Sn alloy does not contribute much to the magnetic behavior of the alloy. However, the same amount of magnetic X (= Fe/Co) element in the unit cell is capable of considerably modifying the M-H loop of the alloy film.

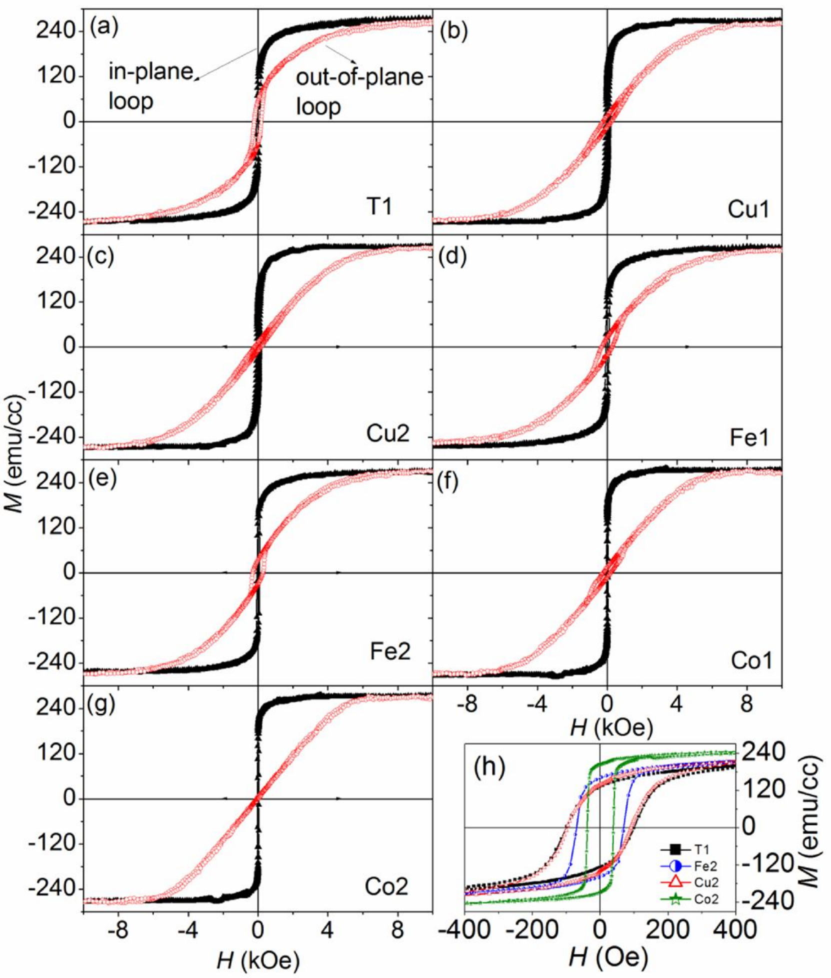

Figure 5.04: (a-g) Room temperature in-plane and out-of-plane M-H loops for all the annealed films. (h) Enlarged view of in-plane M-H loops of all the films.

Table 5.02: Magneto-static parameters of annealed Ni-Mn-Sn and Ni-Mn-X-Sn (X = Cu, Fe, Co) films

Film	M_s (emu/cc)	M_r/M_s	H_c (Oe)
T1	272	0.48	100
Cu1	260	0.50	95
Cu2	265	0.52	94
Fe1	258	0.53	94
Fe2	268	0.60	70
Co1	269	0.70	48
Co2	270	0.75	38

Temperature dependent magnetization (*M-T*) curves recorded for annealed Ni-Mn-Sn and Ni-Mn-X-Sn (X = Cu, Fe, Co) films are displayed in Figure 5.05. The *M-T* data of all the films were recorded during warming cycle (FW mode) under the application of 100 Oe field in the temperature region between 30 K and 750 K. From the *M-T* data, it is evident that these austenite films too do not show any FOPT corresponding to the M↔A transformation just like the austenite Ni-Mn-Sn films discussed in chapter 3. However, the second-order ferromagnetic to paramagnetic phase transition (SOPT) is observed near room temperature in all the films. The Curie temperature (T_C) does not vary much with X element substitution, which is an interesting feature observed in these films.

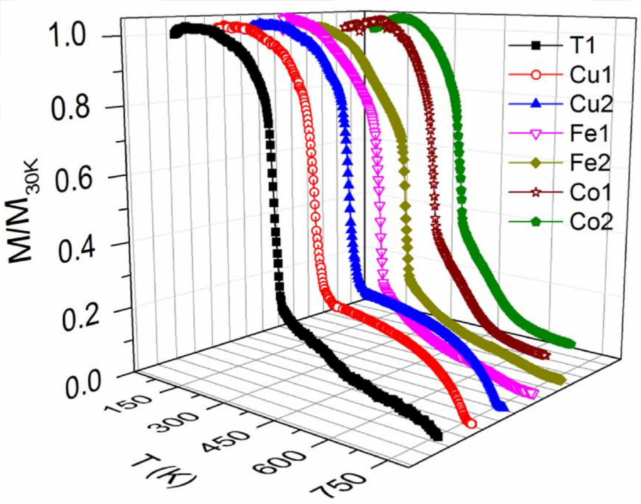

Figure 5.05: *M-T* curves of all the films recorded under FW mode with 100 Oe applied magnetic field.

5.4 Magneto-caloric properties

Since these films show only SOPT, one can expect only direct MCE at T_C in these films. ΔS_M for a field change (dH) from 0 to H has been estimated in the thin films by integrating the M-H isotherms according to the Maxwell thermodynamic relation as described in chapter 2 (Eqns. 2.08 & 2.09). Accordingly, isothermal initial magnetization curves were recorded for all the films at discrete intervals of T across T_C.

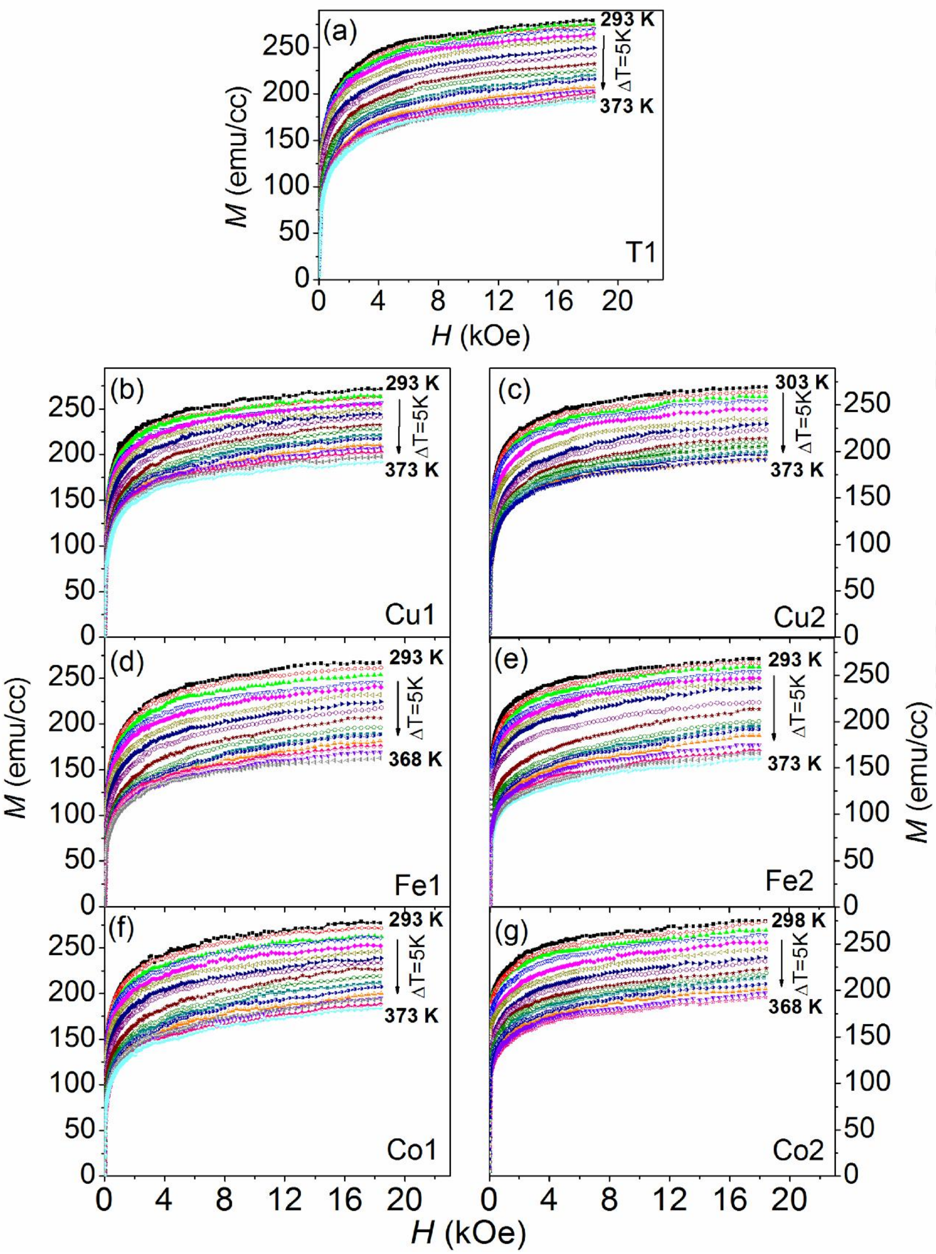

Figure 5.06: Initial magnetization curves recorded around T_C for all the films up to maximum field of 18 kOe.

Figure 5.06(a-g) shows the isothermal initial M–H curves recorded for all the films during cooling cycle in the temperature region close to the magnetic transition (T_C). ΔS_M has been calculated for dH of 18 kOe for all the films using Eqn. 2.09. The calculated ΔS_M values across the magnetic transition (T_C) for all the films are shown in Figure 5.07 as $\Delta S_M(T)$ curves. It is observed that with Cu/Co substitution, $(\Delta S_M)_{max}$ value remained in the range of 36.7−39.7 ($\times 10^3$ erg/cc.K) or 0.44−0.48 (J/kg.K). However, with Fe substitution, an increase in $(\Delta S_M)_{max}$ is observed. For 1.0 at.% Fe substitution (Fe1), $(\Delta S_M)_{max}$ of 48.6 × 10^3 erg/cc.K (or 0.59 J/kg.K) is observed which further increased to 56.6 $\times 10^3$ erg/cc.K (or 0.69 J/kg.K) for 3.6 at.% Fe substitution (Fe2). Apart from increasing ΔS_M, Fe substitution also shifts the peak position of $\Delta S_M(T)$ curves to lower temperature (approaching room temperature). $(\Delta S_M)_{max}$ for all the films are found to increase with increasing dH as depicted in Figure 5.08, which is according to expectations.

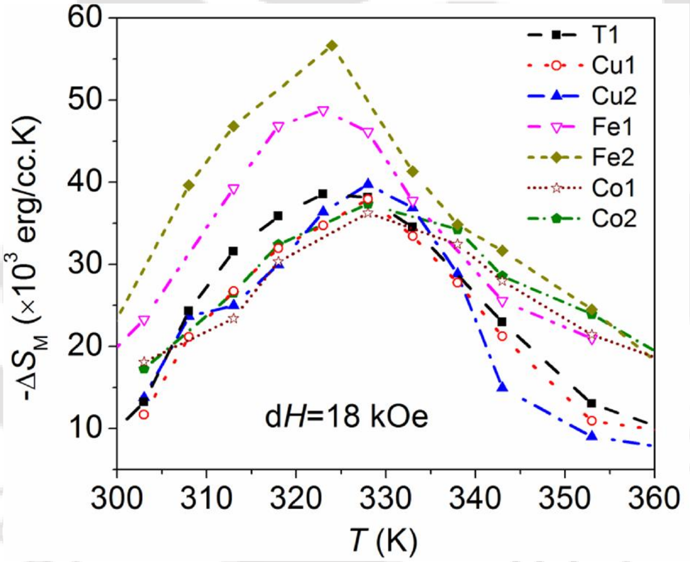

Figure 5.07: Temperature dependence of ΔS_M of T1, Cu1, Cu2, Fe1, Fe2, Co1 and Co2 films obtained for dH of 18 kOe.

Refrigeration capacity (RC) calculated for all the films from the respective $\Delta S_M(T)$ curve using Eqn. 2.10 are listed in Table 5.03. From Figure 5.07 and Table 5.03, it is clear that although $(\Delta S_M)_{max}$ of these films are comparatively low as compared to Ni-Mn-Sn (series 1) films, the large FWHM of $\Delta S_M(T)$ curves (~ 40−50 K) of Fe/Co substituted films yields larger RC value. Hence, the RC values for these films are more than double the value of the ternary films discussed in chapter 3. Since larger RC provides higher operational stability for the magnetic refrigerants, these quaternary films have an advantage over the ternary films.

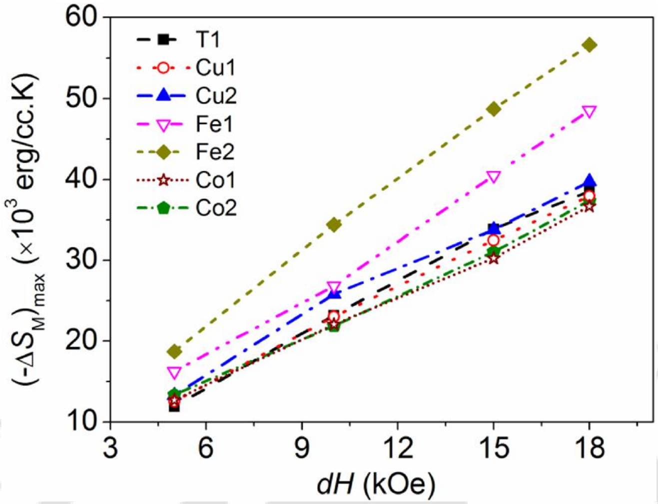

Figure 5.08: Variation of $(\Delta S_M)_{max}$ as function of applied field change (dH).

Table 5.03: Magneto-caloric parameters for Ni-Mn-Sn and Ni-Mn-X-Sn (X = Cu, Fe, Co) films estimated for an applied field change (dH) of 18 kOe near T_C.

Film	T_C (±1) (K)	$(-\Delta S_m)_{max}$ (±0.4) ($\times 10^3$ erg/cc.K)	RC (±6) ($\times 10^3$ erg/cc)	$(-\Delta S_M)_{max}$ (±0.01)(J/kg.K)	RC (±0.1) (J/kg)
T1	328	38.5	1499	0.47	18.3
Cu1	333	37.9	1400	0.46	17.0
Cu2	335	39.7	1311	0.48	15.8
Fe1	329	48.6	1847	0.59	22.4
Fe2	326	56.6	2498	0.69	30.4
Co1	330	36.7	1948	0.44	23.3
Co2	329	37.4	2054	0.45	24.7

Very less information is available in the literature on MCE in Ni-Mn-Sn films. Yüzüak *et. al.* reported (ΔS_M) of 1.6 J/kg.K and RC of 36.5 J/kg for dH of 10 kOe [YUZU13] around FOPT (MT~256 K) in 200 nm thick epitaxial Ni-Mn-Sn film deposited on MgO (100) substrate. Although the current Fe2 film shows lower ΔS_M (as expected since FOPT gives higher ΔS_M than SOPT) and lower RC value, its operating temperature is from 302 K to 347 K whereas, Yüzüak *et. al.'s* sample can operate only well below the room temperature. Moreover, their sample requires epitaxial growth and costly MgO substrates. ΔS_M obtained for the current alloy films are also comparable to the value of 1 J/kg.K obtained in bulk $Ni_{50}Mn_{37}Sn_{13}$ alloy alloy for dH of 12 kOe across T_C [KREN05a]. This comparison brings out the potential application of the current quaternary films in mesoscopic magnetic cooling devices.

5.5 Magneto-dynamic properties

Room temperature FMR spectra of the films were recorded at different polar angles (θ_H) with applied magnetic field oriented along the film plane (θ_H =90º) to out of plane (θ_H =0º) directions using C-FMR technique described in chapter 2. In Figure 5.09, typical C-FMR spectra recorded at the X-band frequency of 9.44 GHz for Co2 film at various polar angles are shown as a typical example. The FMR signal is found to shift from high field (for θ_H = 0º) to lower field (for θ_H = 90º) with polar angles (similar to the FMR spectra of austenite Ni-Mn-Sn series 1 films discussed in chapter 3) which signifies the presence of uniaxial anisotropy in the film. It can be noticed from the FMR spectrum depicted in Figure 5.09 that the film exhibits two absorption signals, one at low magnetic field which is the non-resonant low field absorption (LFMA) [GOLO12, MONT05, MONT06, BHAT87] and the other at higher field which is the well-known uniform precision mode of spins (or the resonant FMR signal). Though LFMA has been observed for the first time in Heusler alloy thin films, it will not be investigated further in this thesis work since this thesis work will focus only on the resonant FMR signal related to magneto-dynamic property of these films.

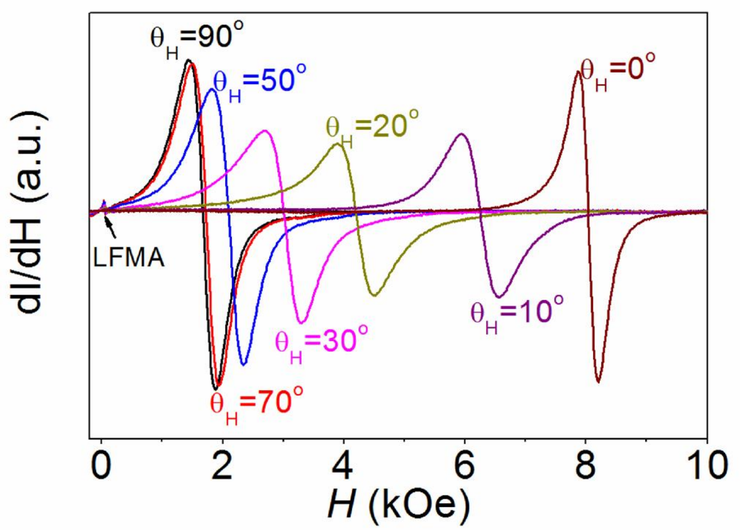

Figure 5.09: Typical FMR spectra of Co2 (given as example) film recorded as a function of applied magnetic field for various film orientations (*i.e.*, θ_H = 90º to 0º).

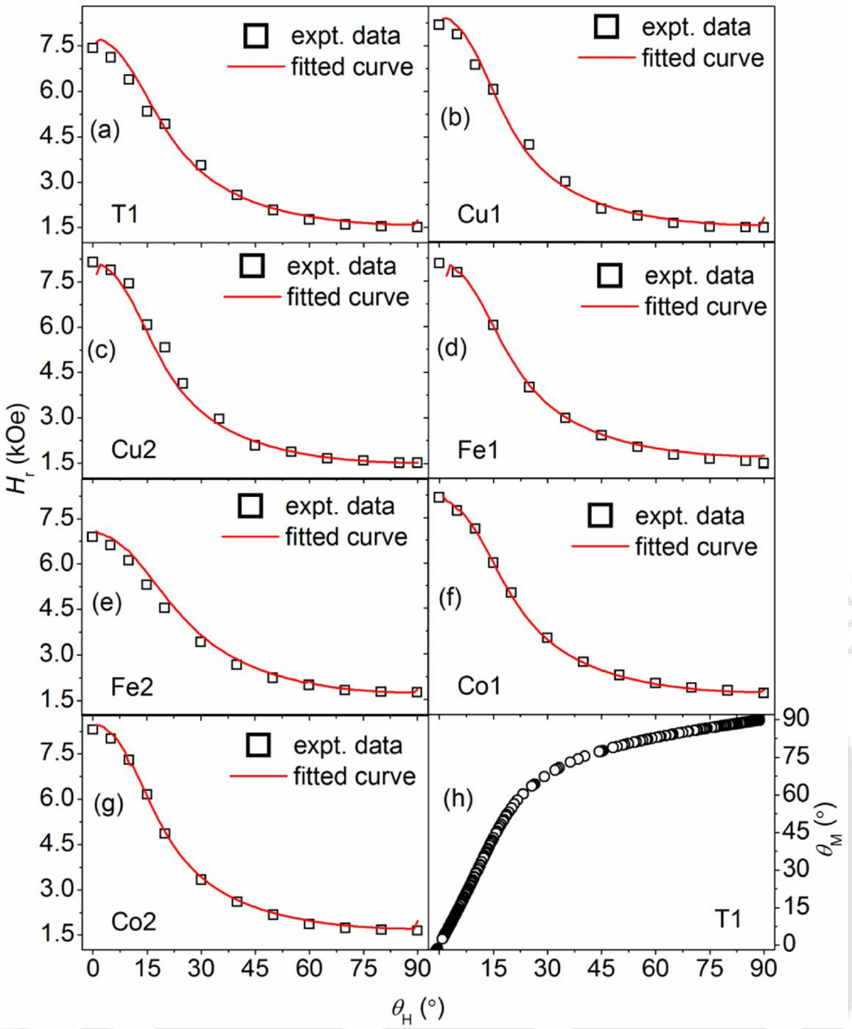

Figure 5.10: (a-g) Polar angle (θ_H) dependence of resonance field recorded at 9.44 GHz for the films. Experimental data are shown as scattered points and the solid lines represent fits to Eqn. 2.23.(h) Typical relation between θ_M and θ_H (Data corresponding to T1 film is shown as an example).

The collected FMR data were analyzed by numerical fitting using Eqn. 2.23. The numerical fitting of Eqn. 2.23 to the experimental data recorded from in-plane (90º) to out-of-plane (0º) orientations of the film with respect to the applied magnetic field yields an estimate of the perpendicular effective magnetic anisotropy (K_1) of the films. Figure 5.10 represents the variation of resonance field (H_r) with θ_H. The experimental data are represented as scattered points and the fit to Eqn. 2.23 are represented as continuous line. From the plot, it is clear that the magnetization easy axis is along the film plane which is in accordance with the magneto-static (VSM) result.

The effective magnetization term ($4\pi M_{\mathrm{eff}}$) was evaluated from H_r versus θ_H data by fitting the same to Eqn. 2.23. Perpendicular effective anisotropy (K_1) has been extracted from the $4\pi M_{\mathrm{eff}}$ variation and the same are shown in Table 5.04. The anisotropy values found for these films are in moderate range (~10^5 erg/cc) and the negative sign of K_1 confirms in-plane easy magnetization in these films. The g values varied slightly with X (Cu, Fe, Co) substitution.

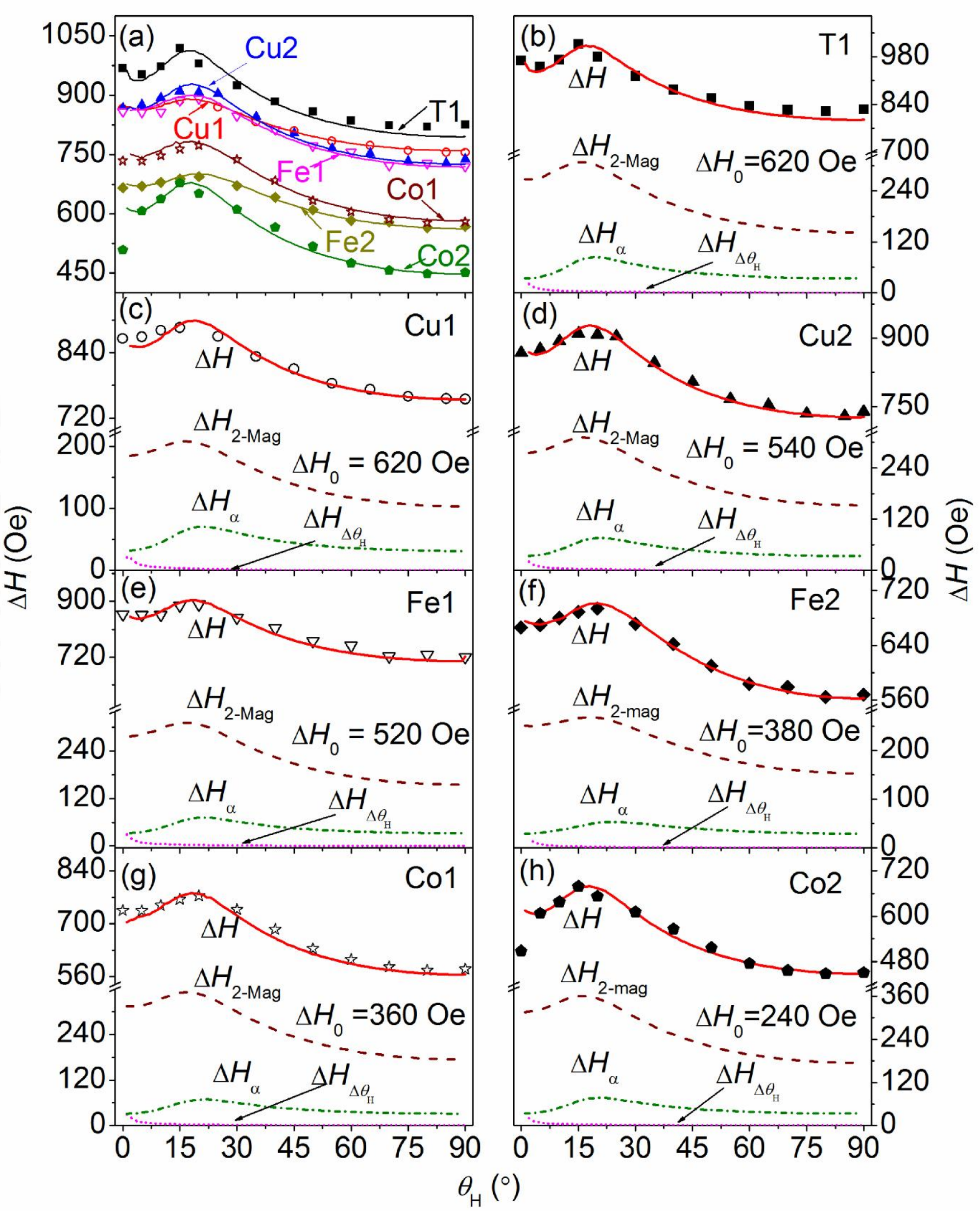

Figure 5.11: FMR linewidth (ΔH) recorded as a function of θ_H at 9.44 GHz for (a) all the films, (b-h) each film along with estimated individual contributions of ΔH. Experimental data are shown as symbols and the solid lines represent fits to Eqn. 2.25.

ΔH versus θ_H data was numerical fit to Eqn. 2.25 is shown in Figure 5.11. It can be seen that the numerically modeled curves yield a good fit to the experimental data. Upon substituting the fourth element (X), the resonance linewidth varied with different substituents as dictated by their magneto-static properties. For Cu1 (1.4 at.%) and Cu2 (3.4 at.%) films, ΔH decreases by a very less amount (from 833 Oe for T1 to 755 Oe for Cu1 and 730 Oe for Cu2 at $\theta_H = 90^o$). But with Fe/Co substitution, the linewidth decreases significantly. With 1.0 at.% Fe substitution (Fe1), ΔH decreases to 724 Oe (at $\theta_H = 90^o$) which further reduces to 566 Oe (at $\theta_H = 90^o$) for 3.6 at.% Fe substitution (Fe2). The effect is more pronounced for Co substitution. For 1.5 at.% Co substitution (Co1), ΔH reduces to 580 Oe (at $\theta_H = 90^o$) and with 3.8 at.% Co substitution (Co2), the lowest ΔH of 451 Oe (at $\theta_H = 90^o$) is observed. A correlation between the M-H loop shape and the FMR linewidth can also be found. It is observed that as M_r/M_s ratio or squareness increases, ΔH decreases. Values of α extracted from the Gilbert contribution are listed in Table 5.04. From the table, it can be seen that 3.8 at.% Co substituted film ($Ni_{55.7}Mn_{33.0}Co_{3.8}Sn_{7.4}$) exhibits the lowest α value of 0.0070. In comparison, the lowest α value reported for Ni-Mn based system in the literature is 0.0075 for Ni-Mn-Sn film on MgO [DUBO11]. From the above analysis, it can be seen that Co substitution in $Ni_{58.1}Mn_{34.4}Sn_{7.5}$ films significantly improves the magneto-dynamic response of the films.

Table 5.04: Magneto-dynamic parameters for Ni-Mn-Sn and Ni-Mn-X-Sn (X=Cu, Fe, Co) films

Alloy	ΔH (Oe) at $\theta_H = 90^o$	ΔH_0 (Oe)	$4\pi M_{eff}$ (±20) (Oe)	g	K_1 (±0.2) ($\times 10^5$ erg/cc)	α (±0.0002)
T1	833	620	4504	2.10	-1.5	0.0080
Cu1	755	620	4874	2.10	-2.0	0.0080
Cu2	730	540	4819	2.10	-2.0	0.0080
Fe1	724	520	4682	2.08	-2.0	0.0082
Fe2	566	380	3965	2.05	-0.8	0.0075
Co1	580	360	4688	2.08	-1.8	0.0080
Co2	451	240	4895	2.05	-1.9	0.0070

The independent contributions of magnetic damping from different sources are shown in Figure 5.11 (b-h) for all the films. From the figure, it is clear that three crucial factors contribute to the observed linewidth. These are Gilbert damping term (ΔH_α) which is an internal property of the material, 2-magnon scattering term ($\Delta H_{2\text{-mag}}$) and ΔH_0 term which depends on various extrinsic parameters related to the material nature. It can be noticed that a significant amount of 2-magnon scattering contribution is present in the ΔH, and $\Delta H_{2\text{-mag}}$ is higher than the ΔH_α contribution. Large $\Delta H_{2\text{-mag}}$ is due to the large scattering of the spin waves by bulk and/or surface inhomogeneities present in the film [KRIV07]. The ΔH_α contribution to total ΔH is ~ 4.0 % in T1, ~4.1 % in Cu1, ~4.5 % in Cu2, ~4.0 % in Fe1, ~5.9 % in Fe2, ~5.4 % in Co1 and ~7.1 % in Co2 at $\theta_H = 90°$. ΔH_α contribution in these films is very less which may be a drawback for these films. However, the external factors contributing to the total linewidth which depend on the film quality can be controlled by improving film quality further.

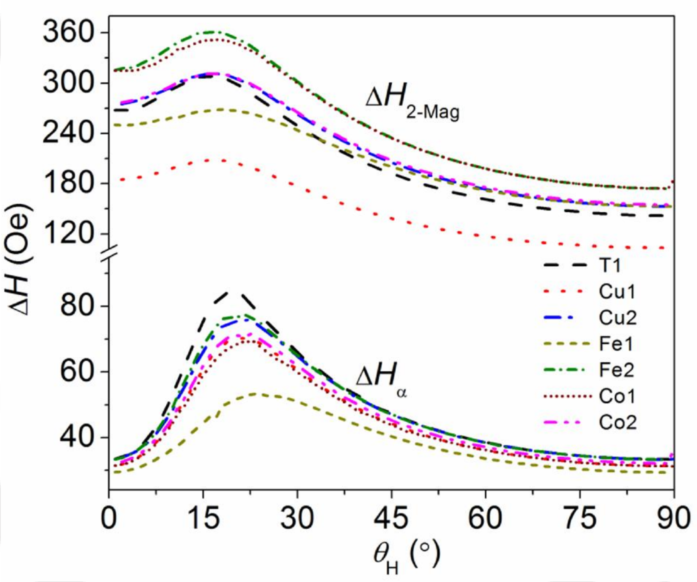

Figure 5.12: Angular dependence of two important ($\Delta H_{2\text{-}mag}$, ΔH_α) contributions to ΔH.

In order to understand the role of X element substitution in reducing various linewidth components of the total linewidth ΔH, a comparative analysis of three major contributions was carried out. ΔH_0 is θ_H independent and hence has a constant value. ΔH_0 contribution in each film is mentioned in Figure 5.11 (b-h). 1.4 at.% Cu in Cu1 does not change ΔH_0 from the ternary (T1) film value. However, 3.4 at.% Cu in Cu2 film reduces ΔH_0 from 620 Oe to 520 Oe. Magnetic X elements have a significant impact on ΔH_0, with the maximum reduction in ΔH_0 being achieved by 3.8 at.% Co substitution in Co2 film. Figure 5.12 shows the other two major contributions ($\Delta H_{2\text{-mag}}$

and ΔH_{α}) which exhibit a θ_H dependence, for all the films. It is evident from the figure that $\Delta H_{2\text{-mag}}$ variation among the films is much more than ΔH_{α} variation. Let us consider these contributions at any one orientation of the film, say at $\theta_H = 90^o$. At this orientation, the ΔH_{α} contribution in the films varies by merely 4 Oe. Apart from this low variation of ΔH_{α} among the different films, its overall contribution to ΔH is < 8% in these films. However, $\Delta H_{2\text{-mag}}$ varies from 103 Oe to 175 Oe with change in X element and its concentration. Cu1 film has the least contribution from $\Delta H_{2\text{-mag}}$ to ΔH. This comparison bring forth these conclusions: Each X element has a different influence on each of the three contributions. In the case of $\Delta H_{2\text{-mag}}$ and ΔH_{α}, increasing the concentration of X increases these contributions, whereas, ΔH_0 decreases with increase in the concentration of each X. ΔH_0 contribution to the total ΔH of T1, Cu1, Cu2, Fe1, Fe2, Co1 and Co2 are 620 Oe, 620 Oe, 540 Oe, 520 Oe, 380 Oe, 360 Oe, and 240 Oe, respectively which are around 74.4, 82.1, 73.9, 71.8, 67.1, 62.1 and 53.2 % of total ΔH. Hence, ΔH_0 contribution to the total ΔH is so strongly dominating in these films. In such a situation, the X element which reduces this component drastically, (such as Co in this case), would be most successful in reducing the total ΔH. Hence, Co substitution yields the best magneto-dynamic response in these films. Since ΔH_0 is related to film quality, improving the film quality can further reduce this contribution which may lead to films with excellent magneto-dynamic response. This analysis also shows that the film quality of the ternary austenite Ni-Mn-Sn film improves with fourth element substitution.

5.6 Summary

A systematic investigation of structural, magneto-static, magneto-caloric and magneto-dynamic properties of Cu/Fe/Co substituted Ni–Mn–Sn films deposited on Si (100) substrate has been carried out. The salient features of the studies conducted on the films are as follows:

- Structural investigations show the successful growth of Ni-Mn-Sn films with high $L2_1$ order on low cost Si substrate upon heat treatment at 823 K for 1 h.
- The effect of fourth element X (= Cu, Fe, Co) substitution on the properties of 500 nm thick Ni–Mn–Sn films with austenite structure has been investigated.
- X atoms occupied the Sn-sublattice by replacing the Ni and/or Mn atoms without changing the austenite structure of the ternary film.

- The films show room temperature ferromagnetism. Ternary Ni-Mn-Sn and Cu substituted alloy films exhibit almost similar room temperature ferromagnetic behavior, whereas the Fe and Co substituted alloy films show softer *M-H* loops with increased M_r/M_s ratio.
- Thermomagnetic investigations do not indicate M ↔ A transition in these films. Less variation in T_C is observed with X (= Cu, Fe, Co) substitution in the films.
- Moderately high $(-\Delta S_M)_{max}$ of 56.6×10^3 erg/cc (= 0.69 J/kg.K) with RC of 2498×10^3 erg/cc (= 30.4 J/kg) is obtained for $Ni_{55.9}Mn_{33.4}Fe_{3.6}Sn_{7.4}$ film (Fe2).
- Very low value of α (= 0.007) was found for the first time in $Ni_{55.7}Mn_{33.0}Co_{3.8}Sn_{7.4}$ film together with perpendicular anisotropy and easy axis along film plane.
- Analysis of major contributions to FMR linewidth in these films shows the role of the X element, the dominating contribution and means to improve the magneto-dynamic response of the films further.

The present study reveals that the functional properties of Ni-Mn-Sn films can be improved with substitution of appropriate fourth element. For example, $Ni_{55.9}Mn_{33.4}Fe_{3.6}Sn_{7.4}$ film with high ΔS_M and RC can be useful for micro/nano magnetic cooling technology or energy conversion device. Similarly, soft ferromagnetic $Ni_{55.7}Mn_{33.0}Co_{3.8}Sn_{7.4}$ film with low Gilbert damping, high magnetization can be a potential material for fabricating efficient high density magnetic recording hard disks, magnetic random access memories, magnetic oscillator, magnetic sensors *etc*. after proper optimization.

Chapter 6

Austenite Ni-Mn-In and Ni-Mn-X-In (X = Co, Fe) thin films

In bulk form, Ni-Mn-In based alloys show better magneto-caloric properties as compared to Ni-Mn-Sn alloy. However, thin films of Ni-Mn-In have not received so much attention despite the fact that thin films with larger surface area are expected to possess higher cooling efficiency. Recently, Singh *et al.* [SING14] studied strain mediated coupling in PZT/Ni-Mn-In/Si thin film hetero-structure. Harish *et al.* [AKKE17] found ΔS_M of 70 × 10^3 erg/cc.K at 302 K and RC of 392 × 10^3 erg/cc in $Ni_{51.1}Mn_{34.9}In_{9.5}Cr_{4.5}$ film for dH of 20 kOe. Jing *et al.* [JING15] observed EB in epitaxial $Ni_{50}Mn_{35}In_{15}$ films deposited on MgO (001) substrate indicating interfacial spin interaction between FM and AFM clusters. Sokolov *et al.* [SOKO13] found martensite transition in 10 nm $Ni_{50}Mn_{35}In_{15}$ film deposited on single crystal MgO substrate. Niemann *et al.* [NIEM10] demonstrated magnetically induced austenite phase in epitaxial metamagnetic Ni–Co–Mn–In films grown on MgO(001). Crouïgneau *et al.* [CROU15] pointed out that the martensite transition is very sensitive to annealing temperature in freestanding $Ni_{45}Co_5Mn_{36.5}In_{13.5}$ film. But these results do not give much information related to the potential of Ni-Mn-In thin films as magnetic refrigerant. Besides that, Ni-Mn-In alloy based thin films stand out as promising candidates for fabricating magneto-electronic devices (MED) due to their multi-functional properties and half metallic character. Recently, strain mediated coupling of Ni-Mn-In and lead zirconium titanate layers has been reported [SING14] which may open up application in microelectromechanical systems. However, practical application of these Heusler alloy films requires a clear understanding of their structural and magnetic properties. In this chapter, structural, magnetic, magneto-caloric and magneto-dynamic properties of Ni-Mn-In and Ni-Mn-X-In (X = Fe, Co) films on Si (100) substrate have been studied.

6.1 Sample preparation and processing

Off-stoichiometric Ni-Mn-In and Ni-Mn-X-In (X = Fe, Co) alloy films of thickness 500 ± 5 nm each were deposited on Si (100) substrate by DC magnetron sputtering using the system shown in Figure 2.05(b) from a $Ni_{48}Mn_{39}In_{13}$ alloy target under working (Ar) gas pressure of 0.6 Pa and applied electrical power of 10 W. The fourth element (X) was introduced in the films by symmetrically placed 2 × 2 mm^2 X chips on the Ni-Mn-In target. Before deposition, the sputtering chamber was evacuated to a base pressure better than 10^{-4} Pa. As-deposited films were annealed *ex situ* at 823 K under residual Ar gas pressure of 10^{-3} Pa for 1 h. Thickness of the films was confirmed with a surface profiler and the variation in thickness was found to be < 5 nm over the entire film surface. The overall composition of the films was evaluated by EDS analysis to be $Ni_{49.2}Mn_{39.7}In_{11.1}$ (T1), $Ni_{49.1}Mn_{38.7}Fe_{1.1}In_{11.1}$ (Fe1), $Ni_{49.1}Mn_{36.9}Fe_{2.9}In_{11.1}$ (Fe2), $Ni_{49.0}Mn_{38.8}Co_{1.0}In_{11.2}$ (Co1) and $Ni_{49.0}Mn_{36.8}Co_{3.0}In_{11.2}$ (Co2). It is evident that Co has been substituted for Mn in all the quaternary films. The corresponding valence electron to atom (*e*/*a*) ratio of films T1, Fe1, Fe2, Co1 and Co2 are 8.02, 8.04, 8.09, 8.04 and 8.08, respectively. These annealed films were used for subsequent studies.

6.2 Structure and morphology

The XRD patterns of Ni-Mn-In and Ni-Mn-X-In (X = Fe, Co) films recorded in the range of $20^{o} \leq 2\theta \leq 70^{o}$ are shown in Figure 6.01. XRD patterns of all the annealed Ni-Mn-In and Ni-Mn-X-In (X = Fe, Co) films exhibit austenite phase at room temperature and all the Bragg peaks could be indexed to a cubic $L2_1$ unit cell. The presence of (111) and (200) super-lattice peaks in all the patterns confirms the presence of $L2_1$ order in the austenite phase (space group $Fm\overline{3}m$). The degree of B2 and $L2_1$ ordering in these films have been evaluated using Eqn. 2.06 and 2.07 and listed in Table 6.01. It is observed that the films exhibited 83 - 85 % $L2_1$ ordering. Rietveld refinement of the XRD data was performed using an $L2_1$ (cubic) unit cell (space group: $Fm\overline{3}m$). While constructing the unit cell, the same atomic occupancy presumed for the Ni-Mn-Sn systems was used. So, Ni atoms occupy the X site, Mn atoms occupy the Y site and the excess Mn and In atoms occupy the Z site in the unit cell [UBAL17, SOKO12]. The unit cell for $Ni_{49.2}Mn_{39.7}In_{11.1}$ (T1) film is shown in Figure 6.02(a). For the X (Fe,Co) substituted alloys, the fourth element (X) atoms are assumed to occupy the Z-sublattice by replacing the Mn atoms in those sites (*c.f.* Figure 6.02(b)). The modified unit cell for $Ni_{49.0}Mn_{36.8}Co_{3.0}In_{11.2}$ is also shown in Figure 6.02(b). The unit cell has been modified accordingly for other substitution percentages. Rietveld refinement confirms that the sample is of single phase (austenite, cubic) structure at room temperature.

The refined patterns are shown in Figure 6.01(a-e). In the figure, open black circles represent the experimental diffraction data and the solid red line corresponds to the fit obtained by Rietveld refinement method using the ‘FullProf’ open source software [RODR93, RODR01]. The goodness of the fit from which the crystallographic parameters of the films were extracted can be inferred from the difference data (blue solid line) and χ^2 values provided in the figures. The optimized lattice constants of the films found from the refinement are listed in Table 6.01. From the table, it is clear that small amount (~1, 3 %) Fe/Co substitution does not alter the crystal structure but merely induces a small change in the lattice constant with respect to the ternary Ni-Mn-In alloy film. The average crystallite (grain) size (*D*) of the films has been calculated using the most intense (220) peak and Schërrer's equation (Eqn. 2.04) and listed in Table 6.01. It is observed that with 1 and 3 % Fe substitution, the *D* variation is extremely small (15.7 nm for T1 to 16.8 nm for Fe2). But with Co substitution, a relatively larger increase in *D* is found (from 15.7 nm for T1 to 18.9 nm for Co2).

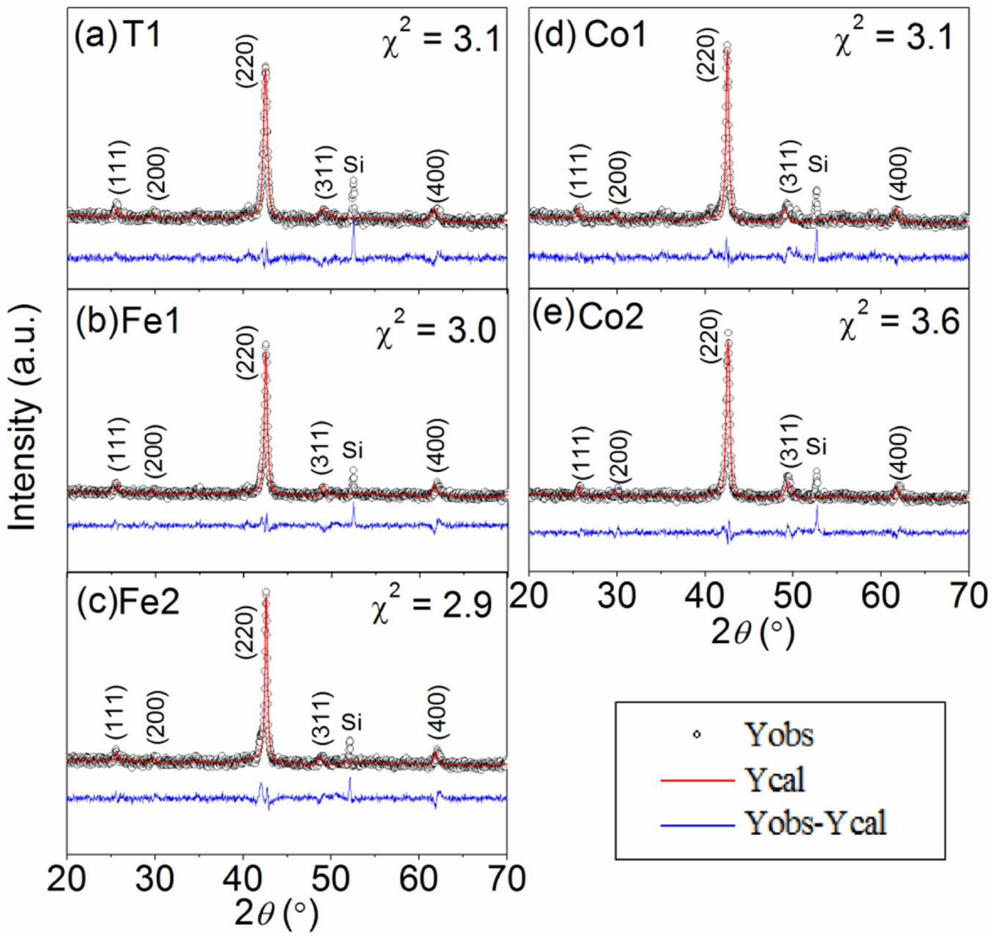

Figure 6.01: Rietvield refined XRD patterns of annealed (a) ternary T1, and quaternary (b) Fe1, (c) Fe2, (d) Co1 and (e) Co2 films.

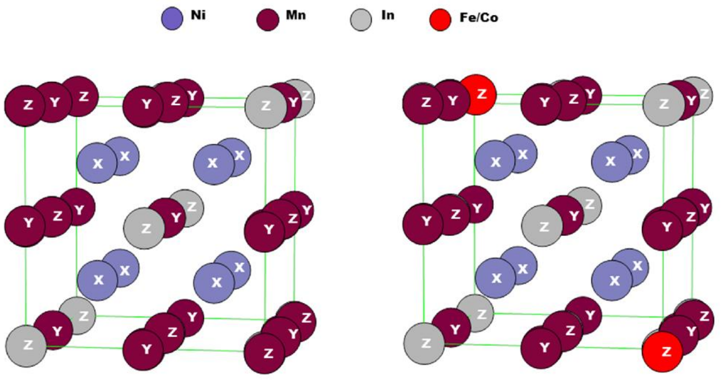

(a) (b)

Figure 6.02: Schematic representation of off-stoichiometric (a) $Ni_{49.2}Mn_{39.7}In_{11.1}$, and (b) $Ni_{49.0}Mn_{36.8}Co_{3.0}In_{11.2}$ unit cells used in Rietveld refinement. Unit cells of X_2YZ have been modified to obtain these unit cells.

Table 6.01: Structural, morphological and magneto-static parameters of 823 K annealed Ni-Mn-In and Ni-Mn-X-In (X = Fe, Co) films.

Film	% of B2 order (S_{B2})	% of $L2_1$ order (S_{L2_1})	a (nm)	D (±0.3) (nm)	$R_{av.}$ (nm)	$R_{r.m.s.}$ (nm)	M_s (emu/cc)
T1	98	83	0.598	15.7	1.65	1.97	183
Fe1	97	84	0.596	16.2	1.72	2.10	260
Fe2	98	85	0.595	16.8	2.12	2.61	308
Co1	98	84	0.600	17.8	1.55	1.77	220
Co2	98	84	0.601	18.9	2.31	2.80	304

The surface morphology of the films was evaluated using AFM as described in chapter 2. Fig. 6.03(a-e) illustrates the morphological patterns of T1, Fe1, Fe2, Co1 and Co2 films. The average (R_a) and root mean square ($R_{r.m.s.}$) roughness of T1, Fe1, Fe2, Co1 and Co2 films are 1.65 and 1.97 nm, 1.72 and 2.10 nm, 2.12 and 2.61 nm, 1.55 and 1.77 nm and 2.31 and 2.80 nm, respectively. It can be noticed that Ni-Mn-In film has uniform small grains with smoother surface. Upon Fe/Co substitution, the grain size as well as surface roughness increases. This is consistent with the results obtained for the Ni-Mn-X-Sn films and may be related to the way X atoms are introduced during the sputtering process (as X chips stacked symmetrically on the ternary target).

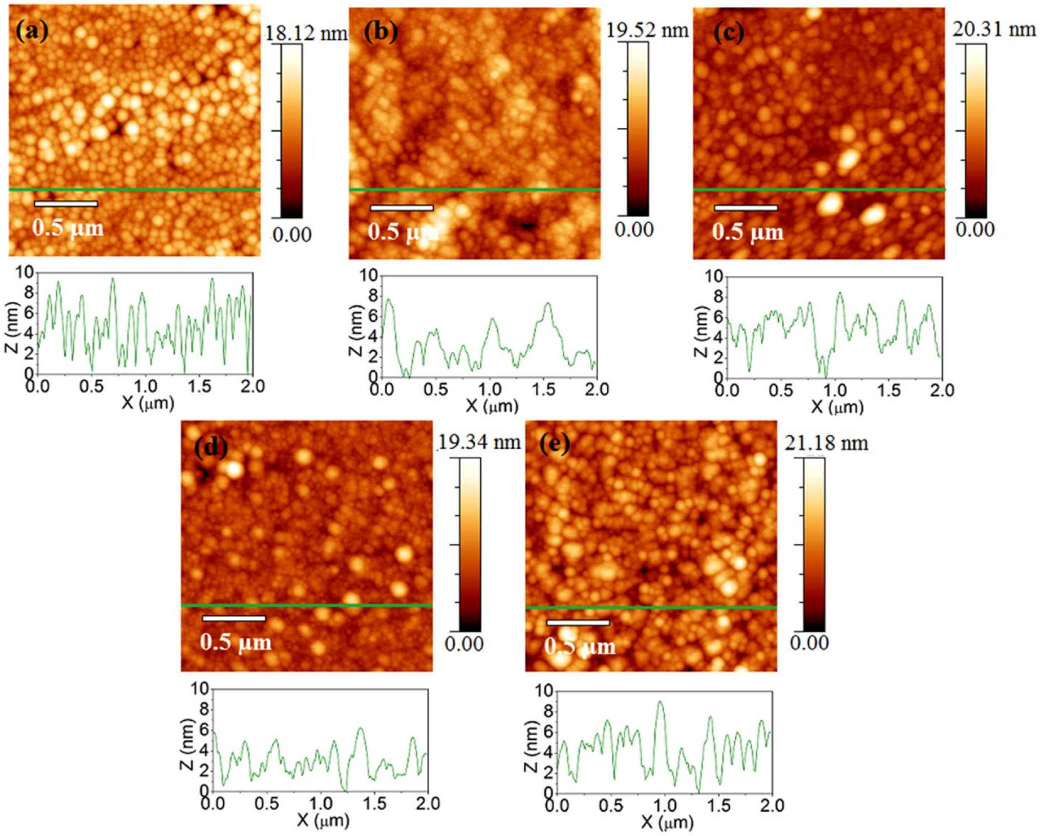

Figure 6.03: Atomic force micrographs of annealed (a) ternary T1, and quaternary (b) Fe1, (c) Fe2, (d) Co1 and (e) Co2 alloy films scanned over 2 × 2 μm^2 area.

6.3 Magneto-static properties

Variation of magnetization of annealed Ni-Mn-In and Ni-Mn-X-In (X = Fe, Co) films as a function of applied field (*M-H* curves) recorded at room temperature are shown in Fig. 6.04. As deposited films exhibited paramagnetic nature due to poor crystallinity, similar to other films discussed in the previous chapters. These *M-H* curves are not shown here as they do not provide any new information. But upon annealing at 823 K, these films showed ferromagnetic behavior at room temperature. Figure 6.01 and Table 6.01, show that the annealed films show high degree of $L2_1$ order which provides the reason for the room temperature ferromagnetism in the annealed films. With the introduction of small amounts of the magnetic X element (Fe or Co) in the place of Mn in Ni-Mn-In film, its magnetization increases significantly as depicted in Figure 6.04 and Table 6.01.

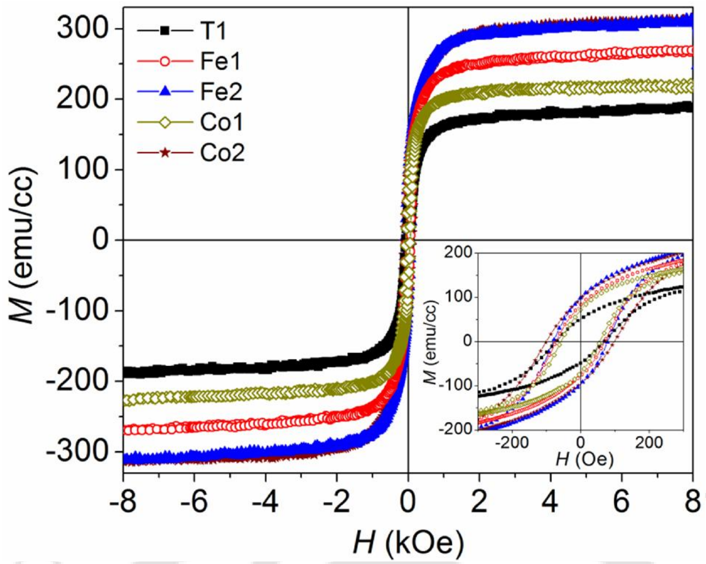

Figure 6.04: Room temperature *M-H* loops of Ni-Mn-In and Ni-Mn-X-In films with in-plane orientation. Inset shows enlarged view of *M-H* loops close to origin.

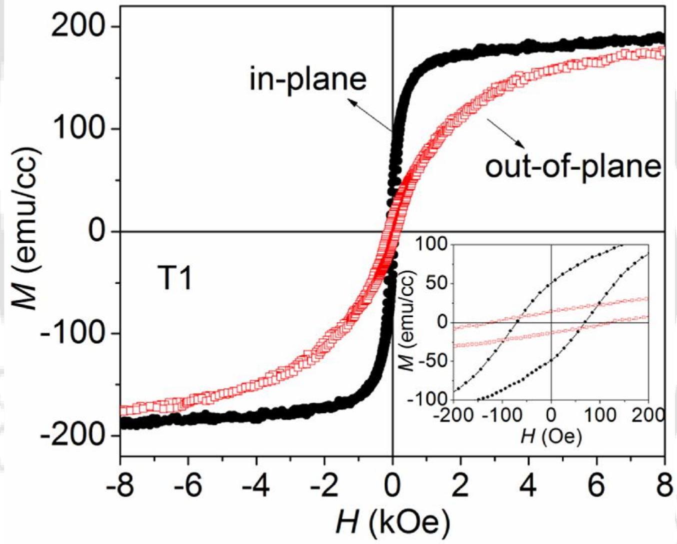

Figure 6.05: Room temperature *M-H* loops of T1 film in in-plane and out-of-plane orientations. Inset shows enlarged view of the loops close to origin.

Substitution of 1.1 at.% Fe for Mn increased the saturation magnetization (M_s) of the film from 183 emu/cc to 260 emu/cc which further increased to 308 emu/cc for 2.9 at.% Fe substitution. Similarly, with 1.0 at.% Co substitution, M_s increased up to 220 emu/cc which further increased to 304 emu/cc for 3.0 at.% Co substitution. It should be mentioned here that although small amounts of Fe/Co substitution do not change the crystal structure of Ni-Mn-In alloy film, a significant change in magnetic properties is observed. The in-plane and out-of-plane *M-H* loops indicate that the easy axis of magnetization of T1 film is along the film plane (*c.f.* Figure 6.05). It is observed that in-plane loops exhibit very high retentivity and soft magnetic nature, whereas out-of-plane loops exhibit very low retentivity. A similar trend is found in all the films.

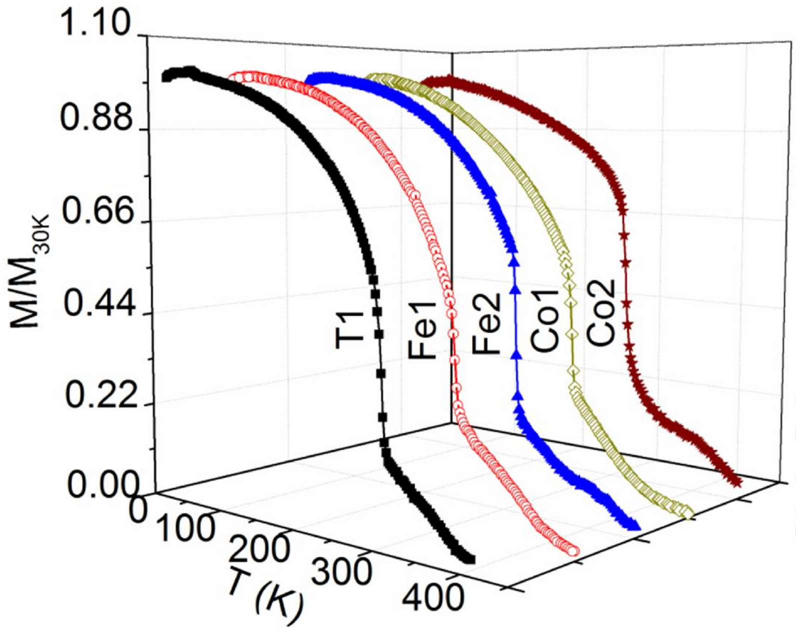

Figure 6.06: *M-T* curves for all the films recorded under FW mode with 100 Oe applied magnetic field.

Figure 6.06 shows the temperature dependence of magnetization (*M-T* curve) of the annealed Ni-Mn-In and Ni-Mn-X-In (X=Fe,Co) films. The *M-T* data of all the films were recorded during warming cycle (FW mode) under the application of constant magnetic field of 100 Oe in the temperature region between 30 K and 450 K. The Curie temperature (T_C) of the films was evaluated from the first derivative of *M-T* curves. T_C for Ni-Mn-In film is 309 K. It is observed that with Fe substitution in the Ni-Mn-In system, T_C shifts to higher temperatures (317 K for 1.1 at.% Fe and 318 K for 2.9 at.% Fe substituted films). A similar trend is also found for Co substitution also but the shift is smaller as compared to Fe substitution (i.e, 314 K for 1.0 at.% Co and 315 K for 3.0 at.% Co substituted films). These T_C shifts are in accordance with the increase in the *e*/*a* ratio with X atom substitution. From the *M-T* data, it is evident that these austenite films do not show any first order structural phase transition (FOPT) corresponding to the M↔A transformation. However, the second-order ferromagnetic to paramagnetic phase transition (SOPT) is observed near room temperature (*c.f.* Figure 6.06).

6.4 Magneto-caloric properties

As seen from the *M-T* data, austenite Ni-Mn-In and Ni-Mn-X-In films exhibit only SOPT only as seen in the case of austenite Ni-Mn-Sn and Ni-Mn-X-Sn films in the previous chapter. Hence, only direct MCE can be expected in these films across T_C. To evaluate the same, initial *M-H* isotherms at discrete temperature intervals have been recorded for all the films across T_C. ΔS_M for a reasonable magnetic field change of dH (0 to H) has been estimated using the relation 2.09 from these curves. Figure 6.07(a-e) shows the isothermal initial *M–H* curves recorded for all the films in the temperature region close to T_C.

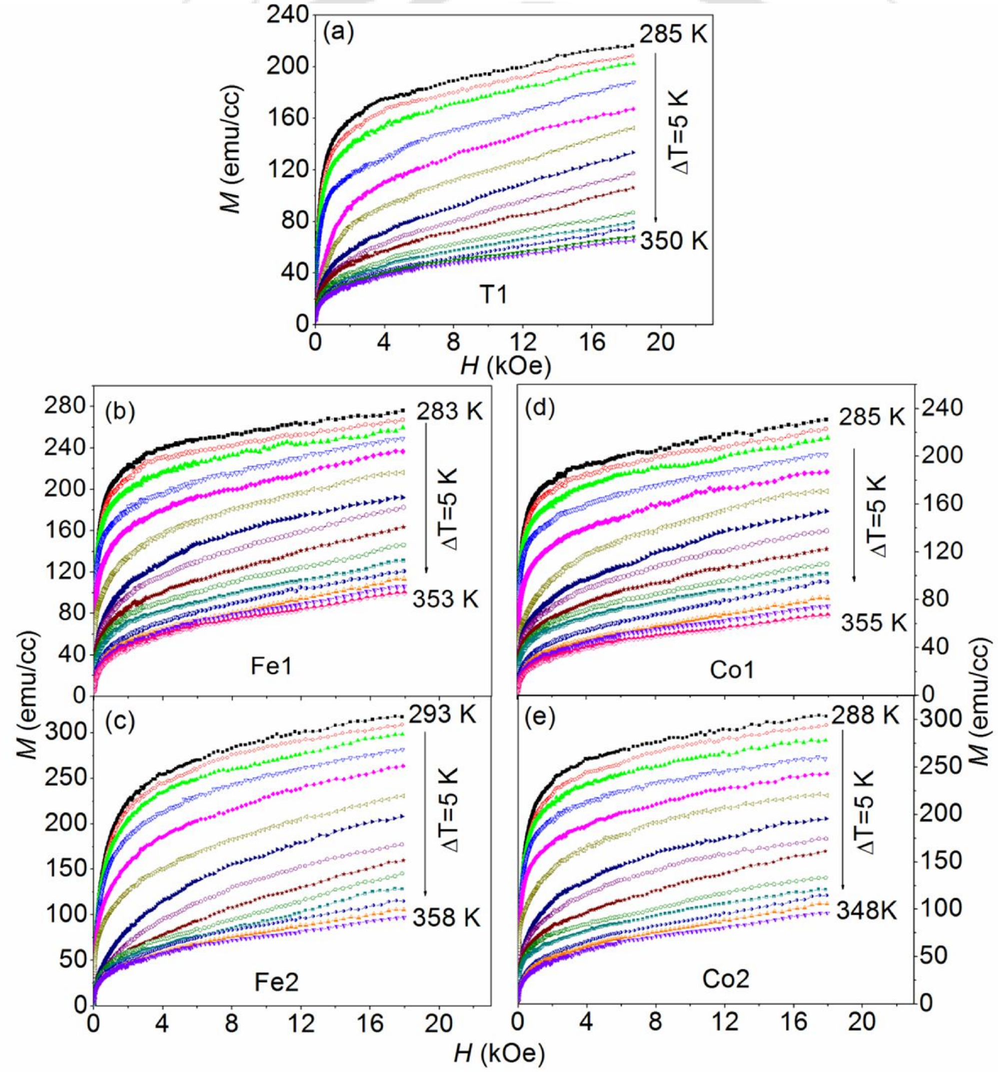

Figure 6.07: Initial magnetization curves recorded for applied field of 18 kOe around T_C for all the films.

Figure 6.08 displays the $\Delta S_M(T)$ curves for all the films for dH = 18 kOe calculated from the initial M-H isotherms depicted in Figure 6.07. The maximum ΔS_M value estimated for 18 kOe field change has been listed in Table 6.02. From Figure 6.08, it is observed that $Ni_{49.2}Mn_{39.7}In_{11.1}$ film shows a maximum ΔS_M value ($(\Delta S_M)_{max}$) of 79.3 × 10^3 erg/cc (or 0.98 J/kg.K) and the $\Delta S_M(T)$ curve shows a broader full width half maxima (FWHM) over the temperature region of 294 K to 322 K. With 1.1 at.% Fe substitution in the film, $(\Delta S_M)_{max}$ value increases to 95.5 × 10^3 erg/cc (or 1.18 J/kg.K) and shifts to higher temperature (since T_C shifts to higher temperature). The FWHM for the film spreads over 25 K (300 K to 325 K). For 2.9 at.% Fe substitution, the $(\Delta S_M)_{max}$ value further increases to 127.9 × 10^3 erg/cc (or 1.58 J/kg.K) with FWHM ranging from 302 K to 328 K. Co substitution also shows similar behavior with lower magnitude. 1.0 at.% Co substitution increases the $(\Delta S_M)_{max}$ value to 88.3 × 10^3 erg/cc (or 1.09 J/kg.K) with a shift of 5 K towards high temperature. The FWHM for 1.0 at.% Co substituted film is in the temperature region of 299 K to 323 K. For 3.0 at.% Co substitution, $(\Delta S_M)_{max}$ was found to be 99.9 × 10^3 erg/cc (or 1.23 J/kg.K) with FWHM spread from 301 K to 327 K. From the above results, it is clear that for all the films FWHM of $\Delta S_M(T)$ curve lies around room temperature, and hence suitable for room temperature MCE application. It is also found that with small amounts of Fe/Co substitution in these films, the MCE can be enhanced. The impact of Fe substitution is more compared to Co with regards to enhancement of MCE in these films.

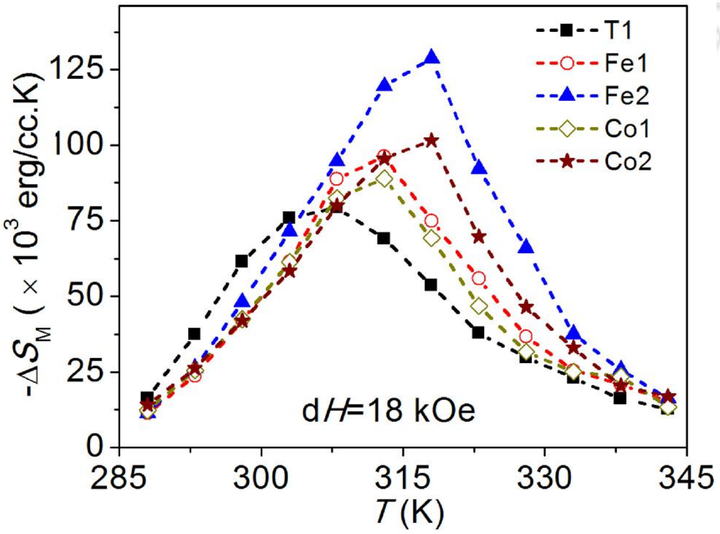

Figure 6.08: Temperature dependence of ΔS_M of all films obtained for dH of 18 kOe.

The other important parameter, viz., refrigeration capacity (RC) of these films, has been calculated using Eqn. 2.10 and the corresponding values are shown in Table 6.02. ΔS_{M} values obtained for these films near room temperature are high compared to those reported for Ni-Mn-Z films. For example, $(\Delta S_{\mathrm{M}})_{max}$~$1.14\times10^{3}$ erg/cc.K has been reported by Singh *et al.* [SING15] for Ni-Mn-In film for dH of 2 kOe across FOPT, $(\Delta S_{\mathrm{M}})_{max}$~8.8 J/kg.K at 353 K for dH of 90 kOe was found for epitaxial Ni-Mn-Co-In film on MgO (100) substrate around the metamagnetic martensitic transition [NIEM10], and $(\Delta S_{\mathrm{M}})_{max}$~ 94×10^{3} erg/cc.K was found for $Ni_{50.3}Mn_{36.9}Sb_{12.8}$ film at 297 K for dH of 20 kOe across FOPT [BARM15]. Actually, ΔS_{M} values estimated for the present films are comparable to bulk Ni-Mn-In alloys values. For example, (1) $(-\Delta S_{\mathrm{M}})_{max}$=2.3 J/kg.K for d$H$=30 kOe at 330 K was reported for $Mn_{50}Ni_{41}In_{9}$ melt-spun ribbons across SOFT [LIHF15], and (2) $(-\Delta S_{\mathrm{M}})_{max}$= 2.25 J/kg.K for d$H$ =50 kOe at 195 K was reported $Ni_{2.048}Mn_{1.312}In_{0.64}$ alloy across martensite T_{C} [PRAM16].

Figure 6.09 represents the variation of $(-\Delta S_{\mathrm{M}})_{\mathrm{max}}$ for dH up to 18 kOe for T1, Fe1, Fe2, Co1 and Co2 films. It is clear that for all the films, $(-\Delta S_{\mathrm{M}})_{\mathrm{max}}$ increased with increasing applied field (and hence with increasing dH). The variation of $(-\Delta S_{\mathrm{M}})_{\mathrm{max}}$ and RC with Fe/Co substitution for Mn in Ni-Mn-In film is shown in Figure 6.10. $(-\Delta S_{\mathrm{M}})_{\mathrm{max}}$ increases with increasing Fe/Co substitution and the variation is more for Fe substitution as compared to Co substitution. Similar behavior is seen for RC also as depicted in Figure 6.10. The nearly linear increase in $(-\Delta S_{\mathrm{M}})_{\mathrm{max}}$ and RC in this range of dH permits more control on the magnetic refrigeration process.

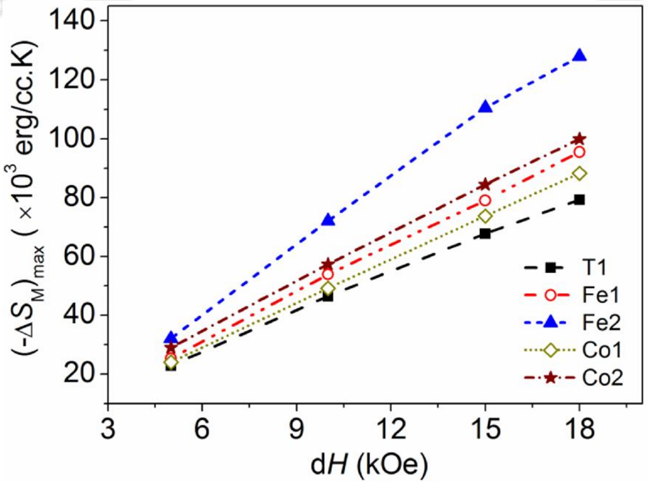

Figure 6.09: Variation of $(\Delta S_{M})_{\mathrm{max}}$ with applied field change (dH).

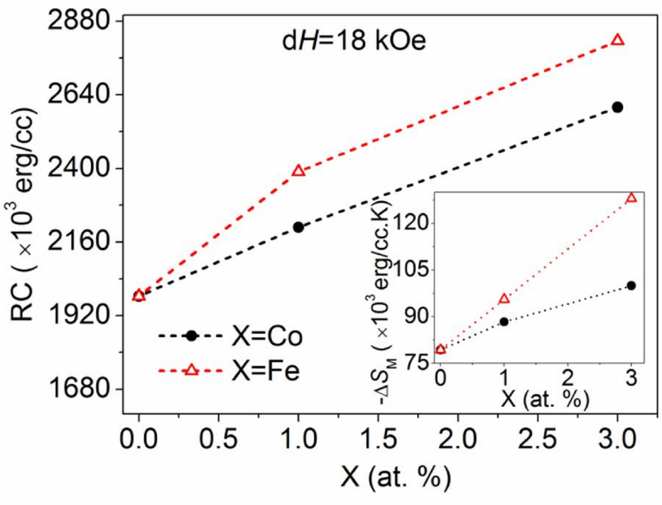

Figure 6.10: Variation of RC with Fe and Co at.%. Inset shows variation of ΔS_M with Fe and Co at.%.

Table 6.02. Magneto-caloric parameters of Ni-Mn-In and Ni-Mn-X-In (X=Fe, Co) films estimated for an applied field change (d*H*) of 18 kOe near T_C.

Film	T_C (±1) (K)	$(-\Delta S_M)_{max}$ (±0.4) ($\times10^3$ erg/cc.K)	RC (±6) ($\times10^3$ erg/cc)	$(-\Delta S_M)_{max}$ (±0.01)(J/kg.K)	RC (±0.1) (J/kg)
T1	309	79.3	1983	0.98	24.5
Fe1	316	95.5	2389	1.18	29.2
Fe2	317	127.9	2816	1.58	34.7
Co1	314	88.3	2208	1.09	27.4
Co2	315	99.9	2599	1.23	31.9

6.5 Magneto-dynamic properties

Room temperature FMR spectra of all the films were recorded at different polar angles (θ_H) ranging from applied magnetic field orientation along the film plane (θ_H =90°) to out-of-plane (θ_H =0°) directions using C-FMR technique described in chapter 2. Typical C-FMR spectra recorded at the X-band frequency of 9.44 GHz for T1 film at various polar angles are shown in Figure 6.11 as a typical example. The FMR signal is found to shift from higher field (for θ_H =0°) to lower field (for θ_H =90°) with change in polar angles, which signifies the presence of uniaxial anisotropy in the film. This behaviour is consistent with VSM analysis. The anisotropy constant (K_1) corresponding to the films has been evaluated by fitting H_r versus θ_H data to Eqn. 2.23.

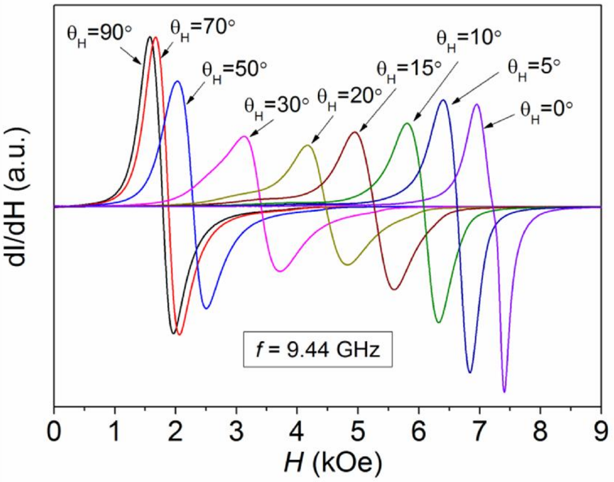

Figure 6.11: Typical FMR spectra (data of T1shown as example) for magnetic field orientations from parallel (θ_H =90^o) to perpendicular (θ_H =0^o) to field plane.

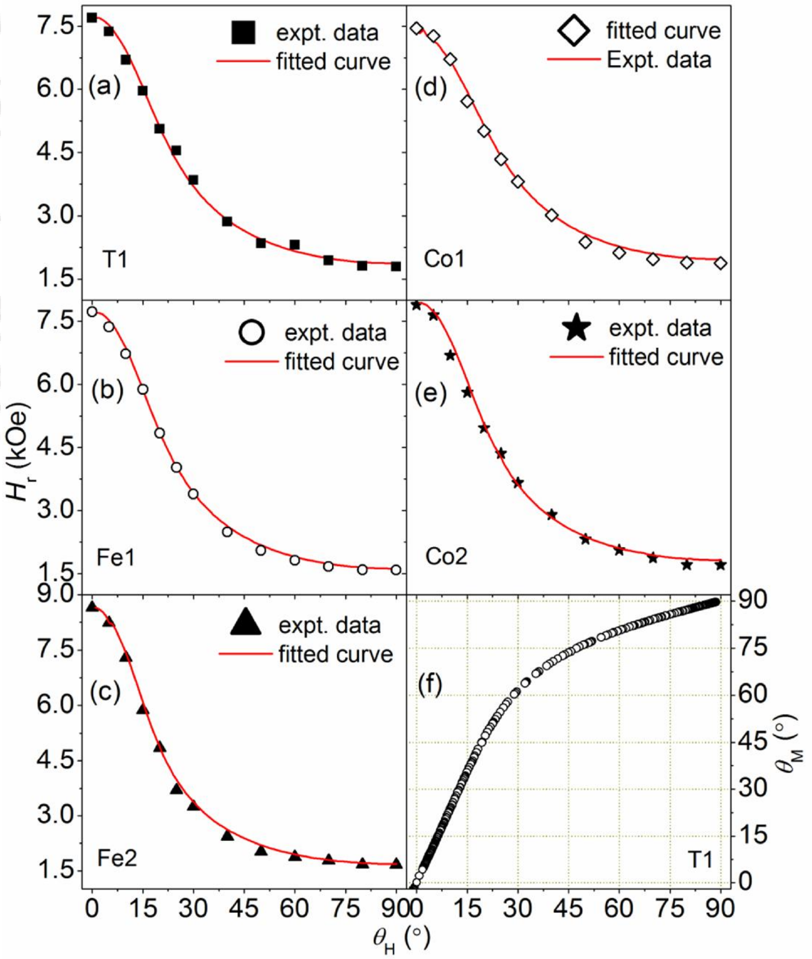

Figure 6.12: (a-e) Angular dependence (θ_H) of resonance field (H_r) at 9.44 GHz for all the films.(f) Typical θ_M vs. θ_H plot obtained for the films (T1 data shown as example).

Figure 6.12 (a-e) illustrate H_r variation as a function of θ_H for all films, where symbols represent experimental data points and the fitted curves are represented by continuous solid lines. As θ_H is decreased from 90° to 0°, H_r increases rapidly to a few kOe, confirming in-plane easy axis in the film as observed in magneto-static (VSM) measurements. The good fitting obtained for the experimental data is evident from the figure. Saturation magnetization (M_s) determined from VSM measurements was used to extract the value of anisotropy constant K_1 from evaluated from the $4\pi M_{\text{eff}}$ term by fitting. Estimated K_1 are tabulated in Table 6.03. Figure 6.12(f) represents the variation of equilibrium angle of magnetization (θ_M) with θ_H for T1 film. All films show similar behaviour. For all the films, the anisotropy value (K_1) found was of the order of $\sim 10^5$ erg/cc with a negative sign. Negative value of K_1 ensures in-plane magnetisation irrespective of the value of M_s of these films. During the analysis, the g values used for the films are also listed in Table 6.03. Best fitting was obtained for the given g values.

The damping of magnetization precession was analyzed from the broadening of the linewidth (ΔH) of the FMR spectra using Eqn. 2.25. ΔH versus θ_H data obtained from the out-of-plane FMR spectra recorded as a function of polar angle are depicted in Figure 6.13 as scattered points. It can be seen from Figure 6.13 that the numerically modeled curves yield a good fitting to the experimental data. The independent contributions to the total linewidth from different sources mentioned in Eqn. 2.25 are depicted in Figure 6.13(b-f) for all the films. The dimensionless Gilbert damping constant (α) for the films was found to be low (0.0080 ± 0.0002). The α value obtained in the present work is the lowest reported so far for any Ni-Mn-X-In films deposited on low cost Si substrate and similar to other Heusler alloy films like Ni-Mn-Sn film on MgO substrate (α = 0.0075) [DUBO11] and other Ni-Mn-Sn films discussed in previous chapters. A careful look at Figure 6.13 would reveal that with Fe substitution for Mn, ΔH increases with respect of the ternary film. On the other hand, upon Co substitution, ΔH decreases although the internal (Gilbert) damping constant (α) remains almost invariant in both the cases. To understand the role of various factors contributing to ΔH in a explicit manner, different contributions to ΔH have been individually plotted in Figure 6.13 (b-f). It is found that the major contributions to ΔH arise from the (1) internal contribution due to Gilbert damping (ΔH_α) and (2) external contributions due to both angle dependent 2-magnon scattering ($\Delta H_{2\text{-}mag}$) and angle independent constant broadening (ΔH_0).

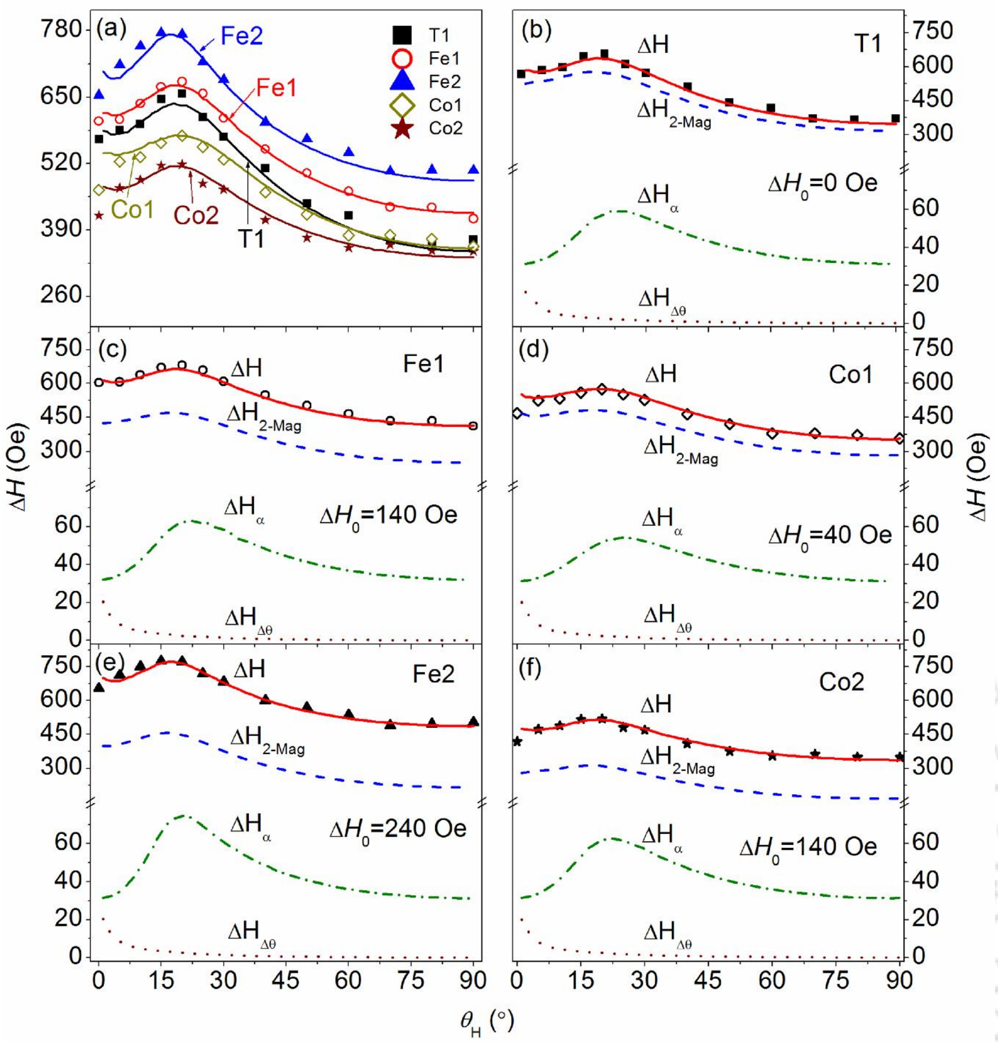

Figure 6.13: (a) Angular dependence (θ_H) of FMR linewidth (ΔH) recorded at 9.44 GHz for all the films. (b-f) Angular dependence of individual contributions ($\Delta H_{2\text{-}mag}$, ΔH_α and $\Delta H_{\Delta\theta}$) to total FMR linewidth ΔH. Angle independent ΔH_0 value is also given.

A detailed discussion about the origin of these contributions to damping has already been provided in the previous chapters. Hence, the role of these terms in linewidth broadening of these present films will only be discussed here. Figure 6.14 portrays the angular varation of ΔH_α and $\Delta H_{2\text{-}mag}$ terms for all the films. From the figure it is clear that the ΔH_α shows very small change with X element substitution. However, the $\Delta H_{2\text{-}mag}$ contribution reduces with X element substitution. The deviation in the curves near 20° is due to the change in dragging factor on account of slightly different variation in effective magnetization ($4\pi M_{\text{eff}}$) for each films. From the Figure 6.13, it can be seen that the major contributions to total linewidth for T1 film comes from 2-

magnon scattering ($\Delta H_{2\text{-}mag}$ is one order higher than ΔH_α at $\theta_\mathrm{H} = 90^\mathrm{o}$). ΔH_α amounts to ~9 % of ΔH for T1 film. With 1.1 at.% Fe substitution (in Fe1 film), ΔH increases although the data is flattered in nature as compared to T1 (i.e. variation of ΔH with angle is less as compared to T1). Since ΔH_α does not vary much, the hike in ΔH can be understood with the introduction of 140 Oe from the angle independent ΔH_0 term. Here, it should be noted that the $\Delta H_{2\text{-}mag}$ term decreased with 1.1 at.% Fe substitution (from ~318 Oe for T1 at $\theta_\mathrm{H} = 90^\mathrm{o}$ to ~253 Oe for Fe1 at $\theta_\mathrm{H} = 90^\mathrm{o}$). ΔH_α amounts to ~7.5 % of ΔH for Fe1 film. For 2.9 at.% Fe substitution (Fe2), ΔH value increases further. Here too, the increase is mainly governed by the increase in ΔH_0 term (240 Oe). The $\Delta H_{2\text{-}mag}$ term reduces further with 2.9 at.% Fe substitution (from ~318 Oe for T1 at $\theta_\mathrm{H} = 90^\mathrm{o}$ to ~216 Oe for Fe2 at $\theta_\mathrm{H} = 90^\mathrm{o}$). But the ΔH_α contribution to ΔH *is* reduced significantly (~6 %). However for Co substitution, the reverse effect is observed. With 1.0 at.% Co substitution (Co1), ΔH value decreases as compared to the T1 film. Only a small amount of ΔH_0 contribution (40 Oe) is found for this film. Hence, the decrease in ΔH for the film can be associated with the decrease in $\Delta H_{2\text{-}mag}$ contribution (from ~318 Oe for T1 to ~283 Oe at $\theta_\mathrm{H} = 90^\mathrm{o}$ for Co1 at $\theta_\mathrm{H} = 90^\mathrm{o}$). ΔH_α amounts to ~9 % of ΔH for Co1 film. 3.0 at.% Co substitution (Co2) results in the lowest ΔH value among all the films. Though the ΔH_0 contribution increased to 140 Oe for this film, the $\Delta H_{2\text{-}mag}$ contribution is significantly lower (from ~318 Oe for T1 at $\theta_\mathrm{H} = 90^\mathrm{o}$ to ~167 Oe for Co2 at $\theta_\mathrm{H} = 90^\mathrm{o}$), which reduces the overall ΔH value. ΔH_α contribution to ΔH remained unchanged at ~9% for the Co2 film as compared to the Co1 film.

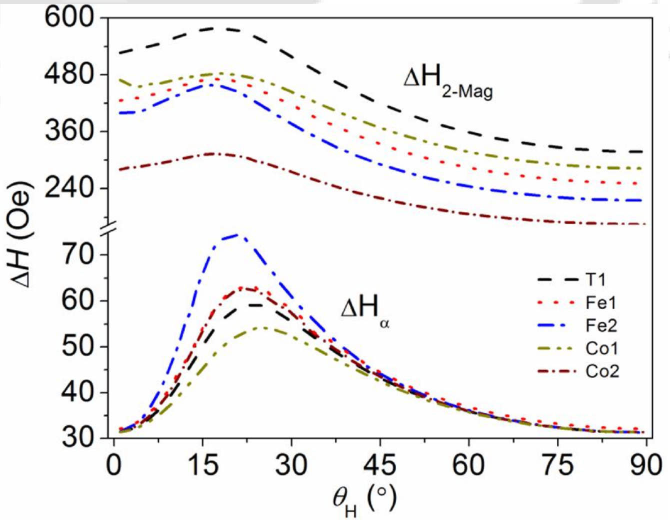

Figure 6.14: Angular dependence of individual contributions of $\Delta H_{2\text{-}mag}$ and ΔH_α to ΔH.

The above discussions show that small amounts of Fe/Co substitution (1-3 at.%) significantly affects the magneto-dynamic properties of austenite Ni-Mn-In, even though ~3 % Fe and Co substitution gives similar magneto-static behavior. The internal ΔH_α contribution related to Gilbert damping constant (α) also remains same for both the substitutions. But Co substitution reduces the overall ΔH which is desirable for application point of view. Hence, Co substitution in austenite Ni-Mn-In appears more appropriate for enhancing device related properties of the film. It is also evident from the above investigations that ΔH_α contribution to total linewidth ΔH is considerably small in these films which may be a limitation for their applications. However, this factor can be improved by improving film quality further. The frequency and angle independent linewidth term ΔH_0, which should be ideally zero, also contributes significantly to ΔH. Epitaxial growth films can reduce ΔH_0 significantly [DUBO11].Thus, the current study reveals the presence of low Gilbert damping constant (α) of 0.008 along with higher magnetic saturation, high perpendicular anisotropy and easy axis along film plane in the Ni-Mn-X-In films. This study also shows the critical factors contributing to the FMR linewidth and provides clues to control them.

Table 6.03: Magneto-dynamic parameters for Ni-Mn-In and Ni-Mn-X-In (X= Fe, Co) films

Alloy	ΔH (Oe) at $\theta_H = 90^o$	ΔH_0 (Oe)	$4\pi M_{eff}$ (±20) (Oe)	g	K_1 (±0.2) ($\times 10^5$ erg/cc)	α (±0.0002)
T1	369	0	4261	2.10	-1.8	0.0080
Fe1	410	140	4421	2.10	-1.5	0.0082
Fe2	505	240	5185	2.10	-2.0	0.0082
Co1	357	40	3855	2.10	-1.2	0.0080
Co2	346	140	4488	2.10	-1.0	0.0080

6.6 Summary

The current study on Ni-Mn-In and Ni-Mn-X-In (X=Fe,Co) films reveals several interesting properties for the first time. Some of the important results obtained are listed are listed below:

- Annealed films show room temperature stable $L2_1$ structure with room temperature ferromagnetism.
- As much as 120 emu/cc increase in magnetization is achieved when ~3 at.% Fe or Co is substituted for Mn in Ni-Mn-In alloy film.
- $(-\Delta S_M)_{max}$ in the vicinity of T_C increased from 79.3×10^3 erg/cc.K (0.98 J/kg.K) to 127.9×10^3 erg/cc.K (1.58 J/kg.K) for the film with 2.9 at.% Fe and 99.9×10^3 erg/cc.K (1.23 J/kg.K) for the film with 3.0 at.% Co, for dH of 18 kOe. These values are the highest achieved in Ni-Mn-In thin films and comparable to values obtained in bulk Ni-Mn-In alloys.
- FMR study of these films revealed for the first time low α (= 0.008), which did not show significant variation with substitution of Fe or Co. Co substitution decreases ΔH significantly.

Chapter 7

Mixed phase Ni-Mn-In and Ni-Mn-Fe-In thin films

In the previous chapter, austenite Ni-Mn-Fe-In films exhibiting high ΔS_M and large RC showed promise for use as magnetic refrigerants. These films also showed low Gilbert damping constant and high anisotropy and saturation magnetization. However the martensite phase of Ni-Mn-In alloys has not been explored yet. Considering several interesting properties exhibited by martensite Ni-Mn-Sn films, it would be interesting to study martensite Ni-Mn-In films. It is attempted to stabilize the martensite phase in Ni-Mn-In and Ni-Mn-Fe-In films and explore their structural and magnetic properties in this chapter.

7.1 Sample preparation and processing

Off-stoichiometric Ni-Mn-In and Ni-Mn-Fe-In films of 500 nm thickness were deposited on Si (100) substrate by DC magnetron sputtering from a 1 inch diameter $Ni_{50}Mn_{35}In_{15}$ alloy target of 1 mm thickness using the sputtering system displayed in Figure 2.05(a) in chapter 2. The working (Ar) gas pressure was maintained at 1.8 Pa and the electrical power applied on the magnetron gun was 35 W. Fe was introduced in the films by symmetrically placed 2 mm × 2 mm size Fe chips on the Ni-Mn-In target. It can be noticed that the target composition and sputtering parameters used in this study are different from the ones used to obtain the austenite films in the previous chapter. These were done to obtain films with structural characteristics quite different from the ones obtained in the previous chapter. The substrate holder was rotated at 15 rpm to ensure uniform film thickness. Before deposition, the sputtering chamber was evacuated to a base pressure of $<10^{-4}$ Pa. As-deposited ternary and quaternary films were annealed *ex situ* at 823 K and 973 K under residual Ar gas pressure of 10^{-3} Pa for 1 h and designated as NiMnIn_823 and NiMnIn_973, NiMnFeIn_823 and NiMnFeIn_973, respectively. To evaluate the effect of film thickness on the properties, Ni-Mn-Fe-In films of 250 nm, 800 nm and 1000 nm thickness were also deposited by only varying the deposition time while maintaining all other deposition conditions identical. All the Ni-Mn-Fe-In films of thickness 250 nm, 500 nm, 800 nm and 1000 nm are annealed *ex situ* at optimised temperature of 973 K for further studies. Uniformity in thickness of the films was confirmed with a surface profiler and the thickness was found to vary < 5 nm over the entire size of the films. Composition of the films was evaluated to be $Ni_{53.7}Mn_{29.5}In_{16.8}$ (500 nm), $Ni_{48.9}Mn_{29.5}Fe_{4.6}In_{17.0}$ (250 nm), $Ni_{48.5}Mn_{29.6}Fe_{4.8}In_{17.1}$ (500 nm), $Ni_{48.8}Mn_{29.6}Fe_{4.7}In_{16.9}$ (800 nm) and

$Ni_{48.6}Mn_{29.5}Fe_{4.9}In_{17.0}$ (1000 nm) using an energy dispersive X-ray spectroscopy unit attached to a field emission scanning electron microscope. The corresponding valence electron to atom (*e*/*a*) ratio of films are 7.94, 7.83, 7.82, 7.83 and 7.83, respectively.

7.2 Structure and morphology

Figure 7.01 shows the XRD patterns recorded for as-deposited and 823 K and 973 K annealed Ni-Mn-In and Ni-Mn-Fe-In films. The XRD pattern of as-deposited Ni-Mn-In film confirms the amorphous nature of the film like other films discussed in previous chapters. The amorphous nature is observed in all the as-deposited films. After the annealing treatment, the films show polycrystalline behaviour. Peaks in the XRD patterns of the 500 nm thick Ni-Mn-In film annealed at 823 K and 973 K correspond to reflections from the orthorhombic (311), (501), (341), (820) and (840) planes of the martensite phase. The XRD pattern of 500 nm thick Ni-Mn-Fe-In films annealed at 823 K exhibit orthorhombic martensite phase along with a weak (220) cubic peak of the austenite phase. On the other hand, the XRD pattern of the 973 K annealed film indicates the presence of reflections from (111), (200), (220) and (222) planes of cubic $L2_1$ austenite phase as well as the above mentioned reflections from the orthorhombic martensite phase planes. This shows the co-existence of orthorhombic martensite phase and cubic austenite phase at room temperature in the annealed Ni-Mn-Fe-In films. Moreover, presence of (111) and (200) super lattice peaks confirms $L2_1$ ordering with space group $Fm\bar{3}m$ in the austenite phase. A weak peak around $2\theta = 35°$ corresponding to (111) reflection from MnO phase is also observed in the annealed films. This is a consequence of minor surface oxidation of the films during annealing process, which could not be avoided. Ni-Mn-Fe-In films of other thicknesses annealed at 973 K also exhibit the mixed phase structure as shown in Figure 7.02. Though there are no reports on these alloy compositions in the literature, the presence of the mixed phase structure can be understood on the basis of the *e/a* ratio of the alloy compositions from the phase diagram [PLAN09]. The phase diagram indicates a martensite phase transition near room temperature in bulk samples with these *e*/*a* ratio values. It has been pointed out [AUGE12, MODA18b] that the first order structural phase transition may get broadened, resulting in coexistence of both martensite and austenite phases over a wide *e/a* range.

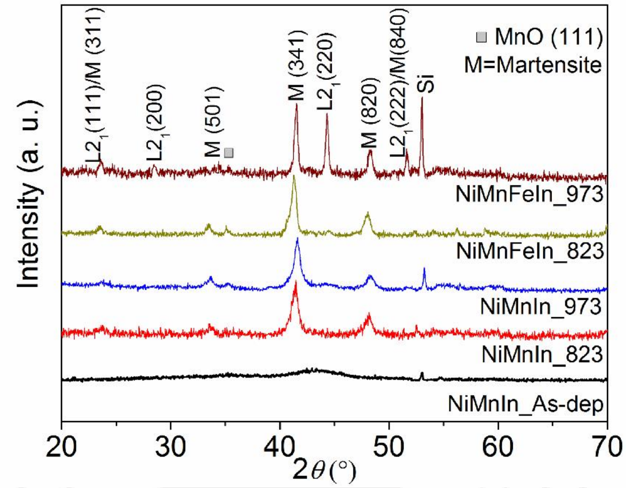

Figure 7.01: Room temperature XRD patterns of as-deposited, 823 K and 973 K annealed 500 nm thick Ni-Mn-In and Ni-Mn-Fe-In films.

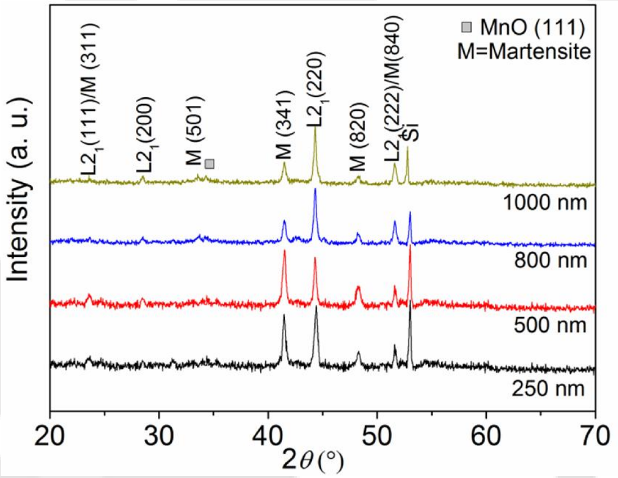

Figure 7.02: Room temperature XRD patterns of 973 K annealed Ni-Mn-Fe-In films of 250 nm, 500 nm, 800 nm and 1000 nm thickness.

Percentages of cubic austenite phase in 250 nm, 500 nm, 800 nm and 1000 nm quaternary films has been estimated to be 52 %, 41 %, 70 % and 69 %, respectively, by a simple method of comparing the area under the most intense austenite and martensite peaks in the XRD patterns shown in Figure 7.02. This preliminary analysis indicates that the austenite phase dominates in higher thickness quaternary films. The structural parameters of the cubic and orthorhombic phases in the thin film samples calculated from the XRD patterns using Eqns. 2.01 and 2.02 are listed in Table 7.01.

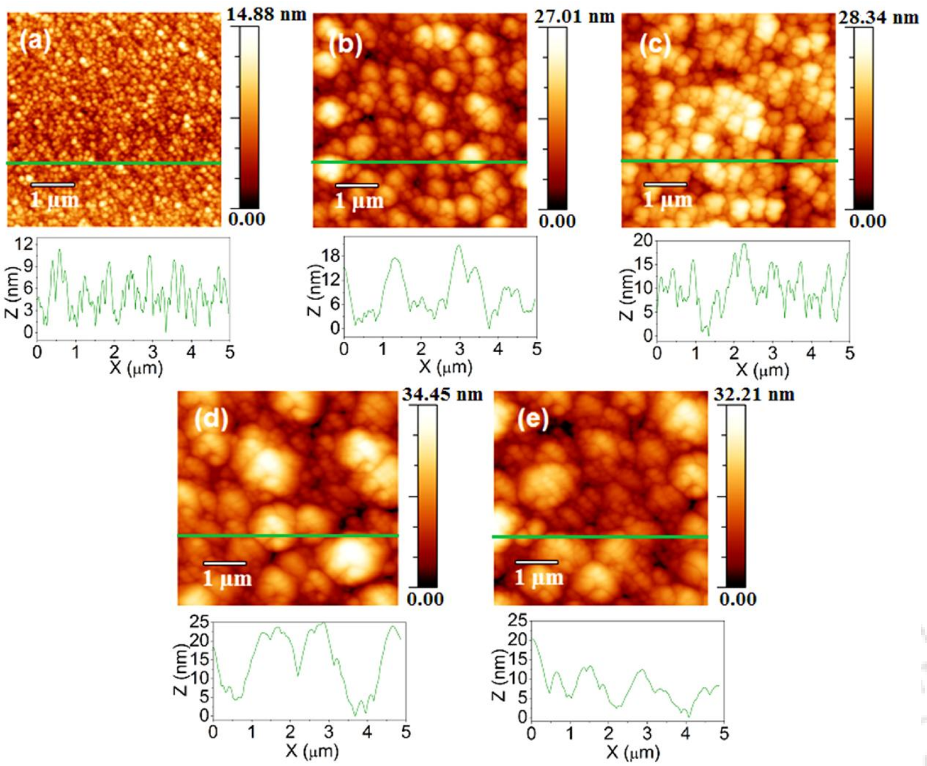

Figure 7.03: AFM images of (a) as-deposited (500 nm thick) and annealed Ni-Mn-Fe-In films of (b) 250 nm, (c) 500 nm, (d) 800 nm and (e) 1000 nm thickness.

Table 7.01: Composition and structural parameters for 973 K annealed Ni-Mn-In and Ni-Mn-Fe-In films

Film Type	Thickness (±5) (nm)	$L2_1$ %	M %	Cubic	Orthorhombic			$R_{av.}$ (nm)	$R_{r.m.s.}$ (nm)
				a (nm)	*a* (nm)	*b* (nm)	*c* (nm)		
Ni-Mn-In	500	0	100	-	1.625	1.037	0.614	-	-
Ni-Mn-Fe-In	250	58	42	0.577	1.618	1.034	0.605	3.5	4.4
Ni-Mn-Fe-In	500	41	59	0.577	1.618	1.031	0.612	3.6	4.5
Ni-Mn-Fe-In	800	70	30	0.577	1.618	1.034	0.605	3.9	4.8
Ni-Mn-Fe-In	1000	69	30	0.577	1.618	1.034	0.605	4.0	5.1

Figure 7.03(a-e) portray the atomic force microscope images of as-deposited and annealed Ni-Mn-Fe-In films captured at room temperature over a scan area of 5 µm × 5 µm. The average roughness ($R_{av.}$) and root mean square roughness ($R_{r.m.s}$) of as-deposited and 250 nm, 500 nm, 800 nm and 1000 nm annealed films are found to be

1.6 and 2.1, 3.5 and 4.4, 3.6 and 4.5, 3.9 and 4.8 and 4.0 and 5.1 nm, respectively. It is evident that upon annealing, the surface roughness of the films increases due to crystallization of the $L2_1$ and martensite phases.

7.3 Magneto-static properties

Isothermal variation of magnetic moment of 823 K and 973 K annealed 500 nm thick Ni-Mn-In and Ni-Mn-Fe-In films recorded as a function of applied field (*M-H* loops) at room temperature are shown in Figure 7.04. As-deposited amorphous film shows paramagnetic behaviour (*cf*. inset in Figure 7.04) which is in expected lines since spontaneous magnetism is observed only in crystalline Heusler alloys. Annealed films exhibited ferromagnetic behaviour which can be related to the crystalline nature of the films [VINO15]. Annealed Ni-Mn-In film is weakly magnetic with very low magnetic moment, which can be associated with its martensite structure. It is obvious from Figure 7.04 that the magnetic moment of Ni-Mn-In film increases slightly as the annealing temperature is increased from 823 K to 973 K which may be due to improvement in the crystallinity of the films at higher temperatures. With the substitution of Fe for (mostly) Ni, the annealed film structure changes to a dual phase structure and the presence of the cubic austenite phase induces significant spontaneous magnetization in the film.

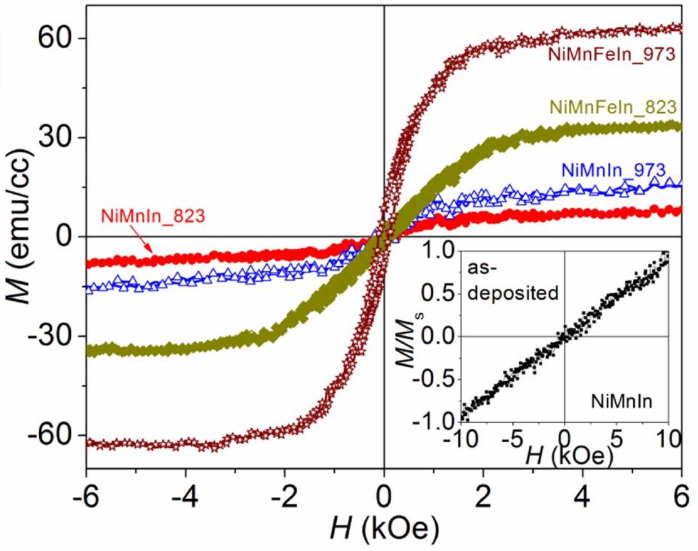

Figure 7.04: Room temperature in-plane *M-H* loops of annealed 500 nm thick Ni-Mn-In and Ni-Mn-Fe-In films. (Inset) Paramagnetic nature of as-deposited Ni-Mn-In film.

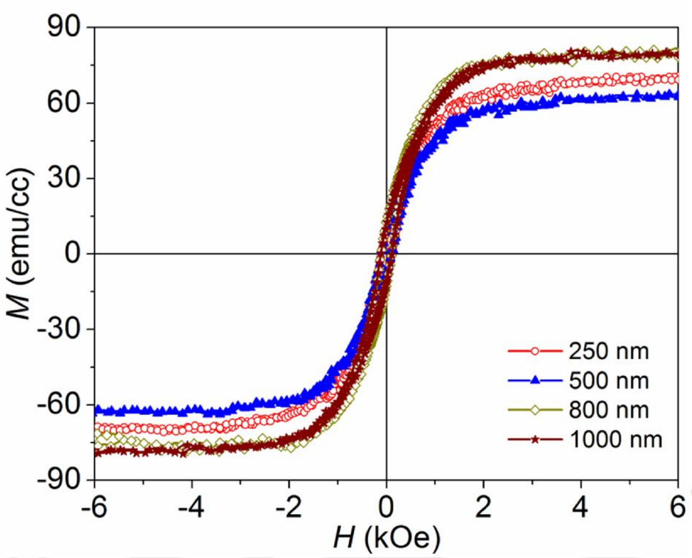

Figure 7.05: Room temperature *M-H* loops of 973 K annealed Ni-Mn-Fe-In films of thickness 250 nm, 500 nm, 800 nm and 1000 nm.

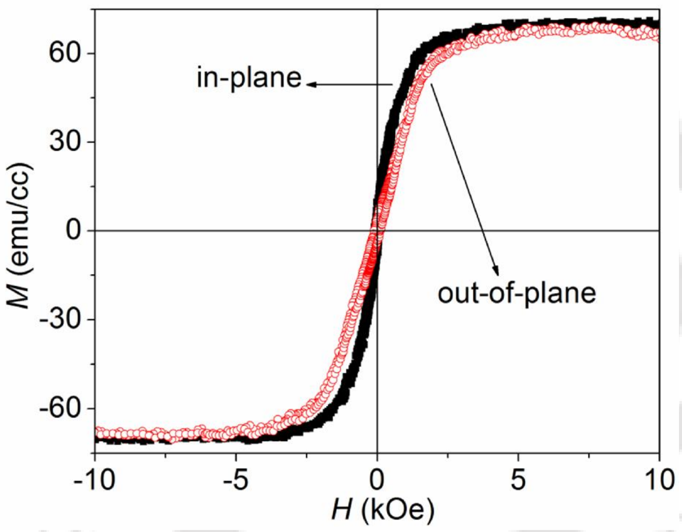

Figure 7.06: In-plane and out-of-plane *M-H* loops for 250 nm Ni-Mn-Fe-In film annealed at 973 K.

Careful look to *M-H* loop as shown in Figure 7.04 shows that Ni-Mn-Fe-In film annealed at 823 K shows significantly high magnetic moment which may be correlated with the introduction of Fe and formation of small amount of austenite phase (~ 10%). Ni-Mn-Fe-In films annealed at 973 K shows the highest magnetic moment and it is related with the austenite phase percentage (40-70 %) present in these mixed phase films. Figure 7.05 represents the *M-H* loops for 973 K annealed Ni-Mn-Fe-In thin films of different thickness. From the figure it is apparent that all the films are ferromagnetic at room temperature. Analysis of the phase percentage shows that in the 250 nm and 500 nm thick films, the cubic phase percentage is 58 % and 41 %, respectively which explains the decrease in magnetic moment of the 500 nm thick film. The lower austenite phase percentage in the 500 nm thick film might be due to improper annealing. Similarly, the 800 nm and 1000 nm thick Ni-Mn-Fe-In films have nearly 70% austenite phase (see Table 7.01), which clarifies the higher magnetic moment of these two films. The *M-H* loops recorded for in-plane and out-of-plane directions for 973 K annealed 250 nm thick Ni-Mn-Fe-In film is shown in Figure 7.06. The close similarity between the two curves signifies very low effective magnetic anisotropy in the film which also indicates that its magnetic property does not vary much when its orientation with the applied magnetic field is changed. This is a very interesting feature observed for the first time in Ni-Mn-Fe-In films.

Table 7.02: Magneto-static parameters of Ni-Mn-In and Ni-Mn-Fe-In films.

Film	Thickness (nm)	Annealing Temp. (K)	M_s (emu/cc)	T_C (K)
Ni-Mn-In	500	823	8	-
Ni-Mn-Fe-In	500	823	33	-
Ni-Mn-In	500	973	15	-
Ni-Mn-Fe-In	250	973	72	673
Ni-Mn-Fe-In	500	973	65	680
Ni-Mn-Fe-In	800	973	79	682
Ni-Mn-Fe-In	1000	973	80	683

Thermo magnetization (*M-T*) curves of the annealed 250 nm, 500 nm, 800 nm and 1000 nm thick Ni-Mn-Fe-In films have been recorded from room temperature to 800 K under the application of 1 kOe magnetic field. Figure 7.07 reveals that the films have high Curie temperature (T_C). It is also seen that with increase in thickness, the T_C does not vary much whereas the magnetic moment increases sharply for higher thickness films (*cf.* Table 7.02). The *M-T* curve for Ni-Mn-In film is not resolvable due to very low moment of the sample.

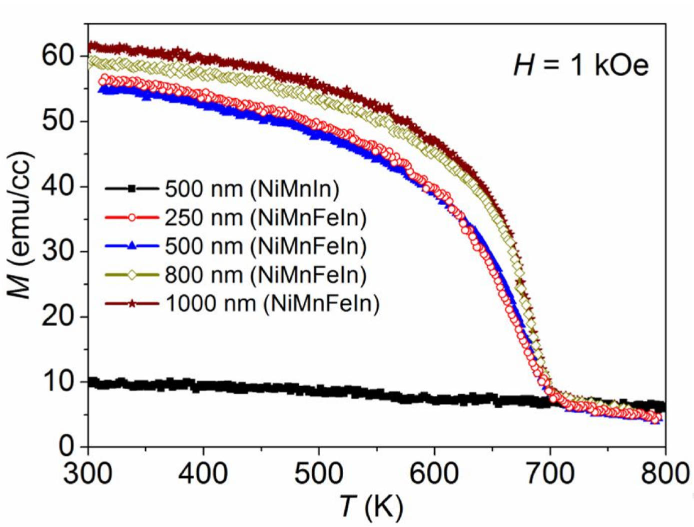

Figure 7.07: Thermo-magnetization (*M-T*) curves of 973 K annealed Ni-Mn-In and Ni-Mn-Fe-In films recorded with an applied magnetic field of 1 kOe.

7.4 Magneto-dynamic properties

FMR spectra were recorded for 973 K annealed Ni-Mn-Fe-In films at various angular positions of the films with respect to the magnetic field direction (θ_H) ranging from out-of-plane (0^o) to in-plane (90^o) orientations. Since Ni-Mn-In film is very weakly magnetic and the room temperature moment is very low, FMR spectra recorded were noisy and could not be analyzed with clarity. Hence, only the FMR spectra of 973 K annealed Ni-Mn-Fe-In films have been analyzed.

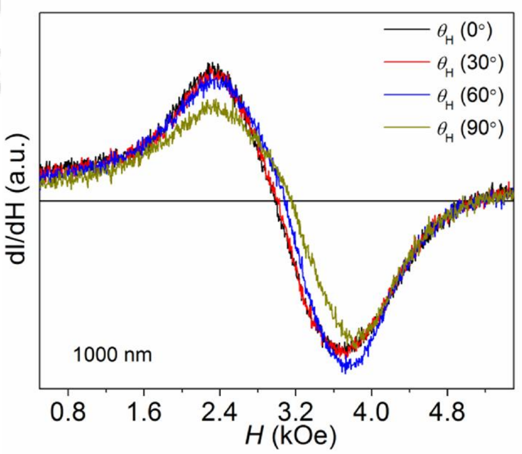

Figure 7.08: Room temperature FMR spectra of 973 K annealed 1000 nm thick Ni-Mn-Fe-In film recorded at different polar angles (θ_H) at microwave frequency of 9.44 GHz.

Typical spectra obtained for 973 K annealed 1000 nm Ni-Mn-Fe-In film are shown in Figure 7.08. From the figure, it is obvious that the resonance field (H_r) varies only by a few hundred Oe when the applied magnetic field is varied from in-plane to out-of-plane direction. This implies very low effective magnetic anisotropy in these films which is in accordance with nature of the *M-H* loops of the films. Similar behavior has also been observed for martensite Ni-Mn-Sn and Ni-Mn-Co-Sn films discussed in chapter 3 and 4. Variation of resonance field (H_r) as a function of θ_H for 973 K annealed Ni-Mn-Fe-In films of all thicknesses have been extracted from the FMR spectra, which are shown as scattered data points in Figure 7.09. The H_r versus θ_H data of all the films have been numerically fit to Eqn. 2.23 and the best fits are shown as solid lines in Figure 7.09. The numerically calculated values yielded a good fit to the experimental data.

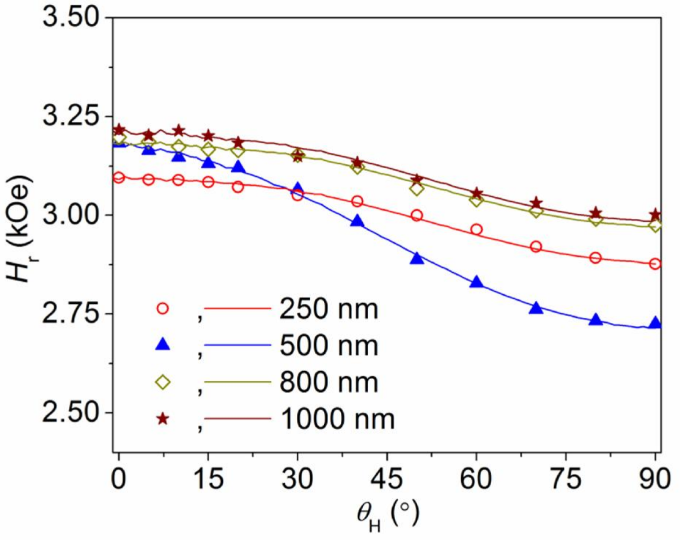

Figure 7.09: Polar angle (θ_H) variation of FMR resonance field (H_r) obtained at 9.44 GHz for 973 K annealed Ni-Mn-Fe-In films of different thicknesses.

The effective magnetization ($4\pi M_{\mathrm{eff}}$) was extracted from the analysis of H_r versus θ_H data and used in the linewidth analysis. The effective perpendicular anisotropy (K_1) was estimated from $4\pi M_{\mathrm{eff}}$ using M_s value determined from magneto-static (VSM) measurements and found to be ~10^4 erg/cc. These K_1 values (~10^4 erg/cc) are unusually low for Heusler alloy films which are usually of the order of 10^6 erg/cc [GOLU09, MODA17]. The low magnetic anisotropy of these films could be a consequence of the mixed phase structure, since it is known that poor crystallinity results in low anisotropy [MCHE00]. Very low magnetic anisotropy of these films results in magnetic properties which are almost independent of film orientation. Such films are expected to have a large number of stable states as compared to the two stable states in conventional magnetic films with high anisotropy. This unusual property may lead to possible applications in memory storage and logical devices in computer circuitry [JOHN58, KEFA70].

The magnetic relaxation dynamics in these mixed phase films was explored by fitting the ΔH data as a finction of θ_H to Eqn. 2.25. Figure 7.10 shows numerically estimated total linewidth as solid lines and the experimental data points as scattered points. It can be seen that the numerically modeled curves yielded a good fit to the experimental data. The Gilbert damping factor (α) has been extracted from Eqn. 2.25 and α value of 0.009 ± 0.001 has been obtained. It has to be pointed out that this study is the first of its kind on Ni-Mn-Fe-In films. The observed α value in the present Ni-Mn-Fe-In films can be compared with those reported for other Ni-Mn-based Heusler alloy films (~0.0075) in the literature [DUBO11] and as observed in previous chapters (~0.0070-0.0085). The slightly higher α obtained for these films as compared to other Ni-Mn-X-In(Sn) films might be due to the mixed phase structure of these films.

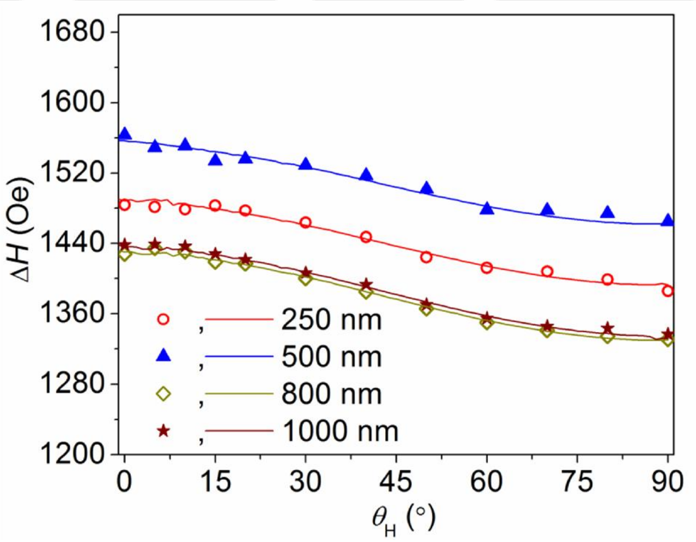

Figure 7.10: Polar angle (θ_H) variation of FMR resonance linewidth (ΔH) of 973 K annealed Ni-Mn-Fe-In films of different thicknesses acquired at 9.44 GHz.

Table 7.03: Magneto-dynamic properties of Ni-Mn-Fe-In films annealed at 973 K.

Film	g	$4\pi M_{\mathrm{eff}}$ (±5) (Oe)	K_1 (±0.2) (×10^4 erg/cc)	ΔH_0 (Oe)	α (±0.001)
250 nm	2.10	183	4.0	740	0.009
500 nm	2.10	157	3.0	800	0.009
800 nm	2.10	180	4.0	678	0.009
1000 nm	2.10	180	4.0	683	0.009

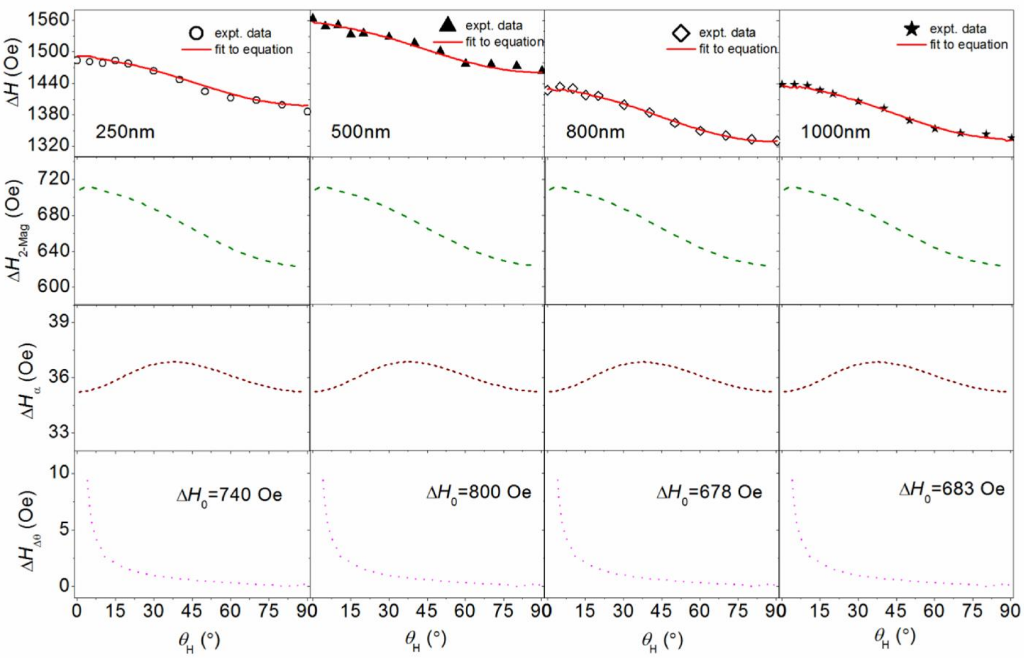

Figure 7.11: Angular dependence of individual contributions ($\Delta H_{2\text{-}mag}$, ΔH_{α} and $\Delta H_{\Delta\theta}$) to total FMR linewidth ΔH of 973 K annealed Ni-Mn-Fe-In films of different thicknesses.

The independent contributions of magnetic damping from different sources to the total FMR linewidth of all the Ni-Mn-Fe-In films are shown in Figure 7.11. From the figure it is clear that there is a large external contribution from the 2-magnon scattering ($\Delta H_{2\text{-mag}}$) and frequency independent inhomogeneity (ΔH_0) term (*c.f.* Figure 7.11). The same trend is observed for all the film thicknesses. The origin of this may be attributed to the high surface roughness induced due to the high temperature post annealing treatment and the presence of dual phase structure, which have resulted in more scattering centers in the films. From the linewidth analysis, it is also noticed that the linewidth of 500 nm thick Ni-Mn-Fe-In film is larger than 250 nm thick film which may be related to the lower percentage of $L2_1$ phase percentage in 500 nm Ni-Mn-Fe-In film. As the $L2_1$ phase percentage in 800 nm and 1000 nm Ni-Mn-Fe-In films are significantly high, the linewidth is narrower for these films. From the figure, it is also evident that the variation in total linewidth (ΔH) for these films is completely governed by the variation in ΔH_0 term. The value of α did not vary much among the films.

7.5 Summary

Structural, magneto-static and magneto-dynamic properties of $Ni_{53.7}Mn_{29.5}In_{16.8}$ and $Ni_{48.9}Mn_{29.5}Fe_{4.6}In_{17.0}$ films deposited on Si (100) substrate have been investigated in this chapter. Some of the exciting results found in this analysis are mentioned below.

- Ternary $Ni_{53.7}Mn_{29.5}In_{16.8}$ film with room temperature orthorhombic martensite phase has been obtained for the first time.
- Upon Fe substitution for Ni in the alloy film, mixed crystallographic phase (austenite cubic $L2_1$ and martensite) appear at room temperature.
- Magneto-static characterization confirmed the presence of room temperature ferromagnetism in annealed Fe substituted films with high Curie temperature (~683 K).
- Analysis of angular variation of FMR spectra revealed very low effective perpendicular magnetic anisotropy (~10^4 erg/cc) and moderately low Gilbert damping constant (α) of 0.009 ± 0.001 for the first time in Ni-Mn-Fe-In films.
- The unique combination of these magnetic properties indicates the possibility of using these films in isotropic magnetic storage devices.

Chapter 8

Conclusions and scope for future work

8.1 Conclusions

The main objective of this study was to explore various physical and functional properties of Ni-Mn-based thin films deposited on cost effective Si (100) substrate. Ternary Ni-Mn-Z (Z=Sn, In) alloy films of specific composition and the effect of fourth element such as nonmagnetic Cu and magnetic Fe and Co, substitution on structural and other functionally important parameters have been investigated. The chosen Ni-Mn-Z (Z=Sn,In) alloys are well investigated in bulk form and known to display martensite to austenite (M ↔ A) phase transition for specific compositions. Due to this unique feature, these alloys show several interesting properties like large MCE, EB, magneto-resistance etc. But, these alloys have not been well explored in their thin film form. So, the question, 'how these properties will change in reduced dimension?', remains unanswered. This work is primarily focused on exploring two different properties of these alloy films from two different application points of view, viz., MCE properties in terms of ΔS_M and RC for magnetic refrigerant application and magneto-dynamic properties in terms of damping parameters especially, α. for spintronic applications. Most of the results presented through these investigations are new which would be of interest not only from the fundamental view point of understanding the effect of thickness, composition, forth element substitution of magneto-static, magneto-caloric and magneto-dynamic properties of these alloy films but also from the application aspect. Some of the salient results obtained and conclusions drawn from the current thesis work are highlighted below:

Ternary $Ni_{48.14}Mn_{38.14}Sn_{13.72}$ alloy films of thickness from 250 nm to 1500 nm crystallized in austenite phase with high $L2_1$ order upon annealing at 823 K for 1 h. These austenite films exhibit ferromagnetic behavior with T_C close to room temperature without showing any signature of M ↔ A phase transition. Highest $(-\Delta S_M)_{max}$ of 65.3×10^3 erg/cc.K (0.81 J/kg.K) with RC of 451×10^3 erg/cc (5.6 J/kg) were obtained near room temperature for a field change of 12 kOe for the 250 nm thick film whereas the highest value of RC 845×10^3 erg/cc (10.5 J/kg) was achieved in 1500 nm film. Very low value of α (= 0.0070) was found for 500 nm film for the first time. Significant change is observed in properties with Cu, Fe, Co substitution in austenite Ni-Mn-Sn films. Small amounts of Fe (1.0 and 3.6 at.%) and Co (1.5 and 3.8 at.%) substitution modifies the M-H loop shape noticeably with increasing M_r/M_s ratio and decreasing H_c

with more of Fe/Co substitution. The effect on the magneto-static properties is more for Co substitution than Fe. But, in regard to MCE, Fe substitution enhances the $(-\Delta S_M)_{max}$ values comparably more than the other substituents. Moderately high $(-\Delta S_M)_{max}$ of 56.6 × 10^3 erg/cc (= 0.69 J/kg.K) and maximum RC of 2498 × 10^3 erg/cc (= 30.4 J/kg) were obtained for $Ni_{55.9}Mn_{33.4}Fe_{3.6}Sn_{7.4}$ film. Co substitution has a positive influence on the magneto-dynamic properties of Ni-Mn-Sn films. Very low value of α (= 0.007) was found for the first time in $Ni_{55.7}Mn_{33.0}Co_{3.8}Sn_{7.4}$ film together with perpendicular anisotropy and easy axis along film plane. Thus, small amounts of X (Cu, Fe, Co) element substitution in ternary austenite Ni-Mn-Sn alloy films improve their quality, although each element has its own influence on various properties. Hence, a proper choice of fourth element is required for enhancing a particular property of the ternary film.

$Ni_{53.4}Mn_{33.2}Sn_{13.4}$ films of different thicknesses (360 nm to 1000 nm) deposited under different deposition conditions exhibited for the first time room temperature martensite phase with a modulated 14M structure. Room temperature ferromagnetism is observed in these films with very high T_C (~560 - 570 K). A weak M ↔ A transition was observed in films of thickness > 500 nm when D > 90 nm, although the transition was spread over a wide temperature range. The MCE parameters of these films were very low. But these films showed very low K_1 (~10^4 erg/cc) with low α (~ 0.008) which may lead to possible applications in multistate memory storage and logical devices in computer circuitry. This unique property is observed for the first time in Ni-Mn- based alloy films. With Co substitution in martensite $Ni_{53.4}Mn_{33.2}Sn_{13.4}$ films, nearly 300 K increase in T_C is observed. Though these films also show room temperature martensite phase, the M ↔ A transition is swamped out in these films. A 3.8, 2.3, 1.7 and 1.6 fold increase in $(-\Delta S_M)_{max}$ is observed in these films as compared to $Ni_{53.4}Mn_{33.2}Sn_{13.4}$ films for 360 nm, 500 nm, 700 nm and 1000 nm films. Like the ternary film, the Co substituted films also possess low K_1 (~ 10^4 erg/cc) and α of 0.0085.

$Ni_{49.2}Mn_{39.7}In_{11.1}$ film of 500 nm thickness showed austenite phase with high $L2_1$ order upon annealing at 823 K for 1 h. This film did not reveal any signature of M ↔ A transition though it exhibited room temperature ferromagnetism. Moderately high $(-\Delta S_M)_{max}$ of 79.3 × 10^3 erg/cc.K (0.98 J/kg.K) with RC of 1983 × 10^3 erg/cc (24.5 J/kg) was observed for 18 kOe field change near room temperature for this film. Substitution of Fe/Co in small amounts (1 % and 3 %) improved its properties just as in the case of

Ni-Mn-Sn film. An increase in magnetization is observed with Fe/Co substitution and ~120 emu/cc increase in found for 3 at.% Fe/Co substitution. Like Ni-Mn-Sn films, here also Fe substitution has more effect on MCE properties than Co. Both Fe and Co enhance $(-\Delta S_M)_{max}$ and RC values of the films. Highest $(-\Delta S_M)_{max}$ of 127.9×10^3 erg/cc.K (1.58 J/kg.K) with RC of 2816×10^3 erg/cc (34.7 J/kg) was found for 2.9 at.% Fe substitution for 18 kOe field change. This is the highest value achieved in Ni-Mn-In thin films and comparable to values obtained in bulk Ni-Mn-In alloys across SOPT. FMR study on these films revealed that Co substitution is more suitable for improving the magneto-dynamic properties since it reduced ΔH more than Fe substitution. For the first time, low α (= 0.008) with moderate K_1 ($\sim 10^5$ erg/cc) is reported for Ni-Mn-In films.

Another set of $Ni_{53.7}Mn_{29.5}In_{16.8}$ films deposited from a different ternary target and annealed at 823 K and 973 K showed orthorhombic martensite phase with very low magnetization (~15 emu/cc). Upon Fe substitution (<5 at.%), the magnetization increases to ~ 65 emu/cc, with the formation of a mixed crystallographic phase (austenite cubic $L2_1$ and martensite). The cubic $L2_1$ phase has a dominant role in determining the magnetization of these dual phase films. FMR analysis revealed very low effective perpendicular magnetic anisotropy $\sim 10^4$ erg/cc smilar to martensite Ni-Mn-Sn films) and low Gilbert damping constant (α) of 0.009 ± 0.001 for the first time in Ni-Mn-Fe-In films.

8.2 Scope for future work

The present studies on ternary Ni-Mn-Z (Z = Sn, In) and quaternary Ni-Mn-X-Z (X = Cu, Fe, Co) Heusler alloy films sputter deposited on low cost Si (100) substrates reveal how the structural, magneto-static, magneto-caloric and magneto-dynamic properties of these alloy films could be tailored by atomic substitution and thickness variation. However, the questions pertaining to the M ↔ A transition could not be explored in these studies as a prominent signature of this transition was not observed in these films. It is however clear that the grain size of the films are crucial for observing this elusive transition. Hence, ways to improve the grain size of Ni-Mn-X films grown on Si (100) need to be explored such as use of underlayers, deposition of heated substrates, etc.

In the present work, a rigorous analysis on magneto-dynamic properties of these films has been done for the first time. The analysis revealed several new results which may be useful for future generation sensors and spintronic device applications. In order to realize these applications, the film quality has to be improved further so that the external contributions to the FMR linewidth can be reduced further. Preparing epitaxial or single crystal films would be good solutions for achieving better film quality. Magneto-dynamics, magneto-resistance and EB studies on multilayered structures made of these optimized film compositions are also suggested since these studies can reveal more applications for these films.

LFMA observed for the first time in Heusler alloy films have not be been investigated in this thesis. Focus on LFMA signal observed in Ni-Mn-X-Sn films may reveal several new insights on this poorly understood phenomenon. Moreover, a careful analysis on the LFMA signal in these films is required since these films are potential candidates for fabricating low magnetic field sensors in microwave frequency range.

References

[ACET11] Acet M., Mañosa L. and Planes A., Magnetic-Field-Induced Effects in Martensitic Heusler-Based Magnetic Shape Memory Alloys, Handb. Magn. Mater. 19, 231 (2011).

[ACHE03] Acher O., Queste S., Ledieu M., Barholz K-U. and Mattheis R. , Phys. Rev. B 68, 184414 (2003).

[AKKE17] Akkera H. S., Singh I. and Kaur D., J. Magn. Magn. Mater. 424, 194 (2017).

[AKSO09] Aksoy S., Acet M., Deen P. P., Mañosa L. and Planes A. ,Phys. Rev. B 79, 212401 (2009).

[ALIE10] Aliev A. M., Batdalov A. B., Kamilov I. K., Koledov V. V., Shavrov V. G., Buchelnikov V. D., Garci´a J., Prida V. M. and Hernando B., Appl. Phys. Lett. 97, 212505 (2010).

[ANIN01] An introduction to the program fullprof 2000 (Version July 2001).

[ANNA11] Annadurai A., Manivel Raja M., Prabahar K., Kumar A., Kannan M. D. and Jayakumar S ,J. Magn. Magn. Mater. 323, 2797 (2011).

[ARIA99] Arias R., Mills D. L., Phys. Rev. B. 60, 7395 (1999).

[AUGE12] Auge A., Teichert N., Meinert M., Reiss G., Hütten A., Yüzüak E., Dincer I., Elerman Y., Ennen I. and Schattschneider P., Phys. Rev. B 85, 214118 (2012).

[AYDO16] Aydogdu Y., Turabi A. S., Kok M., Aydogdu A., Yakinci Z. D., Aksan M. A., Yakinci M. E. and Karaca H. E. , J. Alloys Compd. 683, 339 (2016).

[BACO71] Bacon G. E., Plant J. S., J. Phys. F: Met. Phys. 1, 524 (1971).

[BALK07] Balke B., Wurmehl S., Fecher G. H., Felser C., Maria C., Alves M., Bernardi F., J. Morais, Appl. Phy. Lett. 90, 172501 (2007).

[BANE12] Banerjee S. and Tyagi A. K., Functional materials?: preparation, processing and applications, Elsevier (2012).

[BARI11] Barik S. K., Krishnamoorthi C. and Mahendiran R., J. Magn. Magn. Mater. 323, 1015 (2011).

[BARM15] Barman R. and Kaur D.,Vacuum 120, 22 (2015).

[BAZA64] Bazarov I. P., Thermodynamics, Oxford, New York, Pergamon Press (1964).

[BEHL13] Behler A., Teichert N., Dutta B., Waske A., Hickel T., Auge A., Hutten A. and Eckert J., AIP Adv. 3, 122112 (2013).

[BELM15] Belmeguenai M., Tuzcuoglu H., Gabor M., Petrisor T., Tiusan C., Berling D., Zighem F. and Mourad Chérif S., J. Magn. Magn. Mater. 373, 140 (2015).

[BERN12] Bernard D., Cristian P., Ursula E., Dimitri Houssameddine L B-P and R S, Spin polarised magnetic device, U. S. Patent 8279666 B2 (2012).

[BHAT87] Bhat S. V., Ganguly P., Ramakrishnan T. V. and Rao C. N. R. ,J. Phys. C Solid State Phys. 20, L559 (1987).

[BHOB07] Bhobe P. A., Priolkar K. R. and Nigam A. K., Appl. Phys. Lett. 91, 242503 (2007).

[BING09] Bingham N. S., Phan M. H., Srikanth H., Torija M. A. and Leighton C., J. Appl Phys. 106, 023909 (2009).

[BOUR12] Bouroushian M. and Kosanovic T. , Cryst. Struct. Theory Appl. 1, 35 (2012).

[BRAD34] Bradley A. J., Rodgers J. W. , Proc. Roy. Soc. London. A 144, 340 (1934).

[BROW02] Brown P. J.,Crangle J.,Kanomata T., Matsumoto M.,Neumann K.-U.,Ouladdiaf B. and Ziebeck K. R. A., J. Phys.: Condens. Matter 14, 10159 (2002).

[BROW06] Brown P. J., Gandy A. P., Ishida K., Kainuma R., Kanomata T., Neumann K. -U., Oikawa K., Ouladdiaf B. and Ziebeck K. R. A., J. Phys. Condens. Matter 18, 2249 (2006).

[BROW76] Brown G. V. , J. Appl. Phys. 47, 3673 (1976).

[BUCH08] Buchelnikov V. D., Entel P., Taskaev S. V., Sokolovskiy V. V., Hucht A., Ogura M., Akai H., Gruner M. E. and Nayak S. K. , Phys. Rev. B 78, 184427 (2008).

[BUCH11] Buchelnikov V. D. and Sokolovskiy V. V. , Phys. Met. Metallogr. 112, 633 (2011).

[CAST51] Castelliz L. , Monatsh. Chem. 82, 1059 (1951).

[CAST52] Castelliz L., Monatsh. Chem. 83, 1314 (1952).

[CHEN07] Chen Y. –C., Hung D. –S., Yao Y. –D., Lee S. –F., Ji H. –P. and Yu C. , J. Appl. Phys. 101, 09C104 (2007).

[CHEN13] Chen S. and Ren Z., Mater. Today 16, 387 (2013)

[CHEN15] Chen X., Naik V. B., Mahendiran R. and Ramanujan R. V., J. Alloys Comp. 618, 187 (2015).

[CHER99] Chernenko V. A., Scripta Mater. 40, 523 (1999).

[CHOI15] Choi J. H. and Iniewski K., High-speed devices and circuits with THz applications, CRC Press, Taylor & Francis Group (2015).

[CONG10] Cong D. Y., Roth S., Pötschke M., Hürrich C., Schultz L., Appl. Phys. Lett. 97, 21908 (2010).

[CROU15] Crouïgneau G., Porcar L., Courtois P., Pairis S., Mossang E., Eyraud E. and Bourgault D. , J. Appl. Phys. 117, 035302 (2015).

[CULL01] Cullity B. D., Stock S. R., Elements of X-ray diffraction, 3rd edn, Pearson Eduaction, Boston (2001).

[CZAJ16] Czaja P., Chulist R., Szczerba M. J., Przewoznik J., Olejnik E., Chrobak A., Maziarz W. and Cesari E. ,J. Appl. Phys. 119, 165102 (2016).

[CZIC06] Czichos H., Saito T., Smith L., Handbook of Materials Measurements methods, Springer, Berlin (2006).

[DASR11] Das R., Sarma S., Perumal A. and Srinivasan A., J. Appl. Phys. 109, 07A901 (2011).

[DASR13a] Das R., Saravanan P., Arvindha Babu D., Perumal A. and Srinivasan A., J. Magn. Magn. Mater. 344, 152 (2013).

[DASR13b] Das R., Ph.D. Thesis entitled "Study of phase transitions and magneto-caloric effect in Ni-Mn-X (X = Ga, Sn, In) ferromagnetic shape memory alloys", Department of Physics, Indian Institute of Technology Guwahati (2013).

[DIEN12] Dieny B. , Papusoi C. , Ebels U. ,Houssameddine D. ,Buda-Prejbeanu L. ,Sousa R., "Spin Polarised Magnetic Device"US Patent, US8279666 (2012).

[DUBO11] Dubowik J., Zaleski K., Glowinski H. and Goscianska I. , Phys. Rev. B 84, 184438 (2011).

[DUBO12a] Dubowik J., Ehresmann A., Kakazei G. and Bunyaev S. A. ,Acta Phys. Pol. A 121, 1121 (2012).

[DUBO12b] Dubowik J., Zaleski K., Goscianska I., Glowinski H. and Ehresmann A. ,Appl. Phys. Lett. 100, 162403 (2012).

[DUBE12] Dubenko I., Samanta T., Kumar Pathak A., Kazakov A., Prudnikov V., Stadler S., Granovsky A., Zhukov A. and Ali N. ,J. Magn. Magn. Mater. 324, 3530 (2012).

[DUJZ07] Du J., Zheng Q., Ren W. J., Feng W. J., Liu X. G. and Zhang Z. D., J. Phys. D: Appl. Phys. 40, 5523 (2007).

[DULE71] Dulebohn, "Tracer controlled machining by electrically induced erosion", U.S. Patent 3,614,372 (1971).

[DUNA11] Dunand D. C. and Mullner P., Adv. Mater. 23, 216 (2011).

[DURA18] Duran A., J. Supercond. Nov. Magn. (2018). DOI: 10.1007/s10948-018-4686-8.

[DURR15] Dürrenfeld P., Gerhard F., Chico J., Dumas R. K., Ranjbar M., Bergman A., Bergqvist L., Delin A., Gould C., Molenkamp L. W. and Åkerman J. , Phys. Rev. B 92, 214424 (2015).

[DUTO16] Dutoit C. –E., Dolocan V. O., Kuzmin M., Michez L., Petit M., Le Thanh V., Pigeau B. and Bertaina S. , J. Phys. D. Appl. Phys. 49, 45001 (2016).

[FANY13] Fan Y., Smith K. J., Lüpke G., Hanbicki A. T., Goswami R., Li C. H.,Zhao H. B. and Jonker B. T., Nature Nanotech. 8, 438 (2013).

[FELS16] Felser C. and Hirohata A., Heusler alloys: properties, growth, applications (2016).

[FENG09] Feng W. J., Du J., Li B., Hu W. J., Zhang Z. D., Li X. H. and Deng Y. F., J. Phys. D: Appl. Phys. 42, 152003 (2009).

[FENG11] Fenga W.J., Zuo L., Li Y.B., Wang Y. D., Gao M. and Fang G. L., Mat. Sci. Eng. B 176, 621 (2011).

[FONE59] Foner S., Rev. Sci. Instrum. 30, 548 (1959).

[FUJI00] Fujita A., Fukamichi K., Gejima F., Kainuma R. and Ishida K., Appl. Phys. Lett. 77, 3054 (2000).

[GALA05] Galanakis I. and Dederichs P. H., Half-metallic alloys?: fundamentals and applications, Springer (2005).

[GAOB09a] Gao B., Hu F. X., Shen J., Wang J., Sun J. R. and Shen B. G., J. Magn. Magn. Mater. 321, 2571 (2009).

[GAOB09b] Gao B., Shen J., Hu F. X., Wang J., Sun J. R. and Shen B. G., Appl. Phys. A 97, 443 (2009).

[GAOY03] Gao Y., Niu H. and Chen C. Q., Chem. Phys. Lett. 367, 141 (2003).

[GEBE09] Gebert A., Roth S., Oswald S. and Schultz L. , Corros. Sci. 51, 1163 (2009).

[GHOS13] Ghosh A. and Mandal K., J. All. Comp. 579, 295 (2013).

[GHOS14] Ghosh A. and Mandal K. , Phys. Procedia 54, 10 (2014).

[GIAU33] Giauque W. .F and MacDougall D. P., Phys. Rev. 43, 768 (1933).

[GILB04] Gilbert T. L., IEEE Trans. Magn. 40, 3443 (2004).

[GILB55] Gilbert T. L. , Phys. Rev. 100, 1243 (1955).

[GILL09] Gillessen M., Dronskowski R., J. Comput. Chem. 30, 1290 (2009).

[GILL10] Gillessen M., Dronskowski R., J. Comput. Chem. 31, 612 (2010).

[GOLO12] Golosovsky M., Monod P., Muduli P. K. and Budhani R. C. ,Phys. Rev. B 85, 184418 (2012).

[GOLU09] Golub V. O., Reddy K. M., Chernenko V., Müllner P., Punnoose A., Ohtsuka M., Mullner P., Punnoose A. and Ohtsuka M., J. Appl. Phys. 105, 2013 (2009).

[GOLU17] Golub V. O., Lvov V. A., Aseguinolaza I., Salyuk O., Popadiuk D., Kharlan Y., Kakazei G. N., Araujo J. P., Barandiaran J. M. and Chernenko V. A. , Phys. Rev. B 95, 24422 (2017).

[GRAF09] Graf T., Casper F., Winterlik J., Balke B., Fecher G. H., Felser C., Anorg Z., Allg. Chem. 635, 976 (2009).

[GRAF11] Graf T., Felser C., and Parkin S. S. P., Prog. Solid State Chem. 39, 1 (2011).

[GROO83] Groot R. A. de, Mueller F. M., Engen P. G. van, Buschow K. H. J., Phys. Rev. Lett. 50, 2024 (1983).

[GSCH08] Gschneidner Jr. K. A. and Pecharsky V. K., Int. J. Refrig. 31, 945 (2008).

[GUOX14] Guo X., Xi L. ,Li Y. , Han X. , Li D., Wang Z. , Zuo Y. , Appl. Phys. Lett. 105, 72411 (2014).

[GUPT15] Gupta K. N. and Gupta N. , Magnetic Materials: Types and Applications, chapter 12 in Advanced Electrical and Electronics Materials, Hoboken (ed.), John Wiley & Sons Inc.,pp. 423–448. (2015).

[GURE96] Gurevich A. G. and Melkov G. A., Magnetization Oscillations and Waves, CRC Press, Boca Raton (1996).

[GUTF11] Gutfleisch O. , Willard M. A. , Brück E. , Chen C. H. , Sankar S. G. , and Liu J. P. , Adv. Mater. 23, 821 (2011).

[HANZ06] Han Z. D., Wang D. H., Zhang C. L., Tang S. L., Gu B. X. and Du Y. W., Appl. Phys. Lett. 89, 182507 (2006).

[HANZ07] Han Z. D., Wang D. H., Zhang C. L., Xuan H. C., Gu B. X. and Du Y. W., Appl. Phys. Lett. 90, 042507 (2007).

[HANZ08] Han Z. D., Wang D. H., Zhang C. L., Xuan H. C., Zhang J. R., Gu B. X., and Du Y. W., J. Appl. Phys. 104, 053906 (2008).

[HANZ10] Han Z., Wang D., Qian B., Feng J., Jiang X. and Du Y., Jpn. J. Appl. Phys. 49, 10211 (2010).

[HARW11] Harward I. , O'Keevan T. , Hutchison A., Zagorodnii V., Celinski Z., Rev. Sci. Instrum. 82, 95115 (2011).

[HECK74] Heck C. , Magnetic materials and their applications. Butterworth & Co. Pub. Ltd, (1974).

[HEUS03] Heusler F. , Verh. Dtsch. Phys. Ges. 5, 219 (1903).

[HEUS34] Heusler O., Ann. Phys. 411, 155 (1934).

[HORC07] Horcas I., Fernandez R. , Gomez-Rodriguez J. M. , Colchero J. , Gomez-Herrero J. and Baro A. M., Rev. Sci. Instrum. 78, 013705 (2007).

[HORN04] Horne M., Strange P., Temmerman W.M., Szotek Z., Svane A., Winter H., J. Phys.: Condens. Matt. 16, 5061 (2004).

[HTTP1] http://nptel.ac.in/courses/115103039/module16/lec39/4.html

[HTTP2] https://www.nanoscience.com/technology/sem-technology/sample-electron-interaction/

[HTTP3] https://en.wikipedia.org/wiki/Energy-dispersive_X-ray_spectroscopy

[HTTP4] https://www.nts.com/services/testing/electrical/sem-eds-analysis/

[HUMM98] Hummel R. E., Understanding materials science?: history, properties, applications, Springer (1998).

[HUSA16] Husain S., Akansel S., Kumar A., Svedlindh P. and Chaudhary S., Sci. Rep. 6, 28692 (2016).

[IMAN06] Imano Y., Omori T., Oikawa K., Sutou Y., Kainuma R. and Ishida K., Mater. Sci. Eng. A 438–440, 970 (2006).

[ISOG15] Isogami S., Kawai T. and Futamoto M., Mater. Trans. 57, 1489 (2015).

[JETT12] Jetta N., Ozdemir N., Rios S., Bufford D., Karaman I. and Zhang X., Thin Solid Films 520, 3433 (2012)

[JIAN17] Jiang S., Sun L., Yin Y., Fu Y., Luo C., Zhai Y. and Zhai H. , AIP Adv. 7, 56029 (2017).

[JING15] Jing C., Yu L., Zheng D., Liao P., Cao Y., Liang J., Li Z., Kang B. and Zhang J., Prog. Nat. Sci. Mater. Int. 25, 117 (2015).

[JINX02] Jin X., Marioni M., Bono D., Allen S.M., O'Handley R.C. and Hsu T.Y., J. Appl.Phys. 91, 8222 (2002).

[JOHN58] John S. E., John C. L. and Robert S. S., Isotropic thin magnetic film, US Patent, US3047423A (1958).

[JOHN96] Johnson M. T., Bloemen P. J. H., den Broeder F. J. A., De Vries J. J., Reports Prog. Phys. 59, 1409 (1996).

[JUZA48] Juza R., Hund F. , Z Anorg Allg Chem 257, 1 (1948).

[JUZA68] Juza R., Dethlefsen W., Seidel H. and Benda K. V., Anorg. und Allg. Chemie 356, 253 (1968).

[KAIN06] Kainuma R., Imano Y., Ito W., Sutou Y., Morito H., Okamoto S., Kitakami O., Oikawa K., Fujita A., Kanomata T. and Ishida K.,Nature 439, 957 (2006).

[KAIN07] Kainuma R., Oikawa K., Ito W., Sutou Y., Kanomata T., Ishida K., Planes A., Ishida K., Fujita A., Kanomata T. and Ishida K., J. Appl. Phys. 101, 53919 (2007).

[KAND07] Kandpal H. C., Ksenofontov V., Wojcik M., Seshadri R., Felser C., J. Phys. D: Appl. Phys. 40, 1587 (2007).

[KAUF06] Kaufmann M. D., "Magnetization Dynamics in All-optical Pump-probe Experiments: Spin-wave Modes and Spin-current Damping," Ph.D Thesis, Georg-AugustUniversität, Göttingen, Germany (2006).

[KAZA11] Kazakov A. P., Prudnikov V. N., Granovsky A. B., Zhukov A. P., Gonzalez J., Dubenko I., Pathak A. K., Stadler S., and Ali N., Appl. Phys. Lett. 98, 131911 (2011).

[KEFA70] Kefalas John H., Multiple state memory, U. S. Patent, US3707706A (1970).

[KHAN07a] Khan M., Ali N. and Stadler S., J. Appl. Phys. 101, 053919 (2007).

[KHAN07b] Khan M., Dubenko I., Stadler S. and Ali N., J. Appl. Phys. 102, 113914 (2007).

[KITA10] Kitanovski A. and Egolf P. W., Int. J. Refrig. 33, 449 (2010).

[KITT05] Kittel C., Introduction to solid state physics, Wiley, New York (2005).

[KLAE13] Klaer P., Herper H. C., Entel P., Niemann R., Schultz L., Fahler S. and Elmers H. J., Phys. Rev. B 88, 174414 (2013).

[KRAR03] Krar S., Gill A., Exploring Advanced Manufacturing Technologies, Industrial Press Inc (2003).

[KREN05a] Krenke T., Duman E., Acet M., Wassermann E. F., Moya X., Ma˜nosa L. and Planes A., Nat. Mater. 4, 450 (2005).

[KREN05b] Krenke T, Acet M, Wassermann E F, Moya X, Mañosa L and Planes A , Phys. Rev. B 72, 014412 (2005).

[KREN07a] Krenke T., Duman E., Acet M., Wassermann E. F., Moya X., Mañosa L., Planes A., Suard E. and Ouladdiaf B., Phys. Rev. B 75, 104414 (2007).

[KREN07b] Krenke T., Moya X., Aksoy S., Acet M., Entel P., Mañosa L., Planes A., Elerman Y., Yücel A. and Wassermann E. F.,J. Magn. Magn. Mater. 310, 2788 (2007).

[KRIV07] Krivosik P., Mo N., Kalarickal S., Patton C. E., J. Appl. Phys. 101, 83901 (2007).

[KUAN08] Kuanr B. K., Maat S., Chandrashekariaih S., Veerakumar V., Camley R. E. and Celinski Z., J. Appl. Phys. 103, 07C107 (2008).

[KUND17] Kundu A., Gruner M. E., Siewert M., Hucht A., Entel P. and Ghosh S. ,Phys. Rev. B 96, 064107 (2017).

[KURE13] Kurebayashi H., Skinner T. D., Khazen K., Olejník K., Fang D., Ciccarelli C., Campion R. P., Gallagher B. L., Fleet L., Hirohata A. and Ferguson A. J. ,Appl. Phys. Lett. 102, 62415 (2013) .

[LAND35] Landau L. D. and Lifshitz E. M., Phys. Z. Sowietunion 8, 153 (1935).

[LAZP11] Lázpita P., Barandiarán J. M., Gutiérrez J., Feuchtwanger J., Chernenko V. A. and Richard M. L., New J. Phys. 13, 033039 (2011)

[LEEH08] Lee H. , Wen L. , Pathak M. , Janssen P. , LeClair P. ,Alexander C. , Mewes C. K. A., Mewes T. , J. Phys. D. Appl. Phys. 41 ,215001 (2008).

[LIHF15] Li H., Feng S., Ren J., Zhai Q., Fu J., Luo Z. and Zheng H. ,J. Magn. Magn. Mater. 391, 17,(2015).

[LIND09] Lindner J., Barsukov I., Raeder C., Hassel C., Posth O., Meckenstock R., Landeros P. and Mills D. L., Phys. Rev. B 80, 224421 (2009).

[LIZJ07] Li Z., Jing C., Chen J., Yuan S., Cao S. and Zhang, J Appl. Phys. Lett. 91, 112505 (2007).

[MACH13] Machavarapu R. and Jakob G., Appl. Phys. Lett. 102, 232406 (2013).

[MAKS15] Maksymov I. S.,Kostylev M., Phys. E Low-Dimensional Syst. Nanostructures. 69, 253 (2015).

[MALY09] Malygin G., Tech. Phys. 54, 1782 (2009). (check)

[MANO10] Mañosa L., González-Alonso D., Planes A., Bonnot E., Barrio M., Tamarit J. -L., Aksoy S. and Acet M., Nat. Mater. 9, 478 (2010).

[MCEL94] McElfresh, M., Fundamentals of Magnetism and Magnetic Measurements, Quantum Design (1994).

[MCHE00] McHenry M E and Laughlin D E ,Acta Mater. 48, 223 (2000).

[MEIK56] Meiklejohn W. H. and Bean C. P., Phys. Rev. 102, 1413 (1956).

[MILT02] Miltat A. T. J. and Albuquerque G., Spin dynamics in confined magnetic structures I, Springer, Berlin, Heidelberg (2002).

[MIUR04] Miura Y., Nagao K., Shirai M., Phys. Rev. B 69, 144413 (2004).

[MIZU02] Mizukami S., Ando Y. and Miyazaki T.,Phys. Rev. B 66, 104413 (2002).

[MODA16] Modak R., Samantaray B., Mandal P., and Srinivasan A., Appl. Phys. A 122, 252 (2016).

[MODA17] Modak R., Samantaray B., Mandal P. and Srinivasan A., J. Alloys Compd. 692, 529 (2017).

[MODA18a] Modak. R., Samantaray B., Mandal P., Srinivasu V. V. and Srinivasan A., AIP Conf. Proc. 1953, 120006 (2018).

[MODA18b] Modak R., Raja M. M. and Srinivasan A., J. Magn. Magn. Mater. 448, 146 (2018).

[MONT05] Montiel H., Alvarez G., Betancourt I., Zamorano R. and Valenzuela R. ,Appl. Phys. Lett. 86, 072503 (2005).

[MONT06] Montiel H., Alvarez G., Gutierrez M. P., Zamorano R. and Valenzuela R. ,IEEE Trans. Magn. 42, 3380 (2006).

[MUTH10] Muthu S. E., Rao N. V. R., Raja M. M., Kumar D. M. R., Radheep D. M. and Arumugam S., J. Phys. D. Appl. Phys. 43, 425002 (2010).

[NAKA13] Nakayama H. ,Althammer M. ,Chen Y. -T. , Uchida K. , Kajiwara Y. , Kikuchi D. ,Ohtani T. , Geprgs S. , Opel M. , Takahashi S. , Gross R. , Bauer G. E. W. , Goennenwein S. T. B., and Saitoh E. , Phys. Rev. Lett. 110, 206601 (2013).

[NALW02] Nalwa H. S., Handbook of thin film materials, Academic Press (2002).

[NAYA09] Nayak A. K., Suresh K. G. and Nigam A. K., J. Phys. D. Appl. Phys. 42, 35009 (2009).

[NIEM10] Niemann R., Heczko O., Schultz L. and Fähler S., Appl. Phys. Lett. 97, 222507 (2010).

[NISH78] Nishiyama Z., Martensitic transformation, Academic Press, New York, (1978).

[NODA76] Noda Y. and Ishikawa Y., J. Phys. Soc. Japan 40, 690 (1976).

[NOWO50] Nowotny H. and Bachmayer K.,Chemie 81, 488 (1950).

[NOWO51] Nowotny H. and Glatzl B., Monatsh. 82, 720 (1951).

[OHAN00] O'Handley R.C, Modern Magnetic Materials Principles and Applications, Wiley, New York (2000).

[OHRI92] Ohring M., Materials Science of Thin Films, Academic Press, London (1992).

[ONER07] Oner Y., Kamer O., Alveroglu E., Acet M. and Krenke T., J. Alloys Compd. 429, 64 (2007).

[ONER12] Öner Y. ,J. Appl. Phys. 111, 07E111 (2012).

[OOGA06] Oogane M., Wakitani T., Yakata S., Yilgin R., Ando Y., Sakuma A., and Miyazaki T., Jpn. J. Appl. Phys. 45, 3889 (2006).

[OTSU98] Otsuka K. and Wayman C. M., Shape Memory Materials, Cambridge University Press, UK (1998).

[PAND17] Pandey S., Quetz A., Aryal A., Dubenko I., Mazumdar D., Stadler S. and Ali N. ,Magnetochemistry 3, 3 (2017).

[PATH08] Pathak A. K., Khan M., Dubenko I., Stadler S. and Ali N., J. Phys. D: Appl. Phys. 41, 202004 (2008).

[PATH09a] Pathak A. K., Khan M., Gautam B. R., Stadler S., Dubenko I. and Ali N., J. Magn. Magn. Mater. 321, 963 (2009).

[PATH09b] Pathak A. K., Dubenko I., Stadler S. and Ali N., IEEE Trans. Magn. 45, 3855 (2009).

[PATH10] Pathak A. K., Dubenko I., Pueblo C., Stadler S. and Ali N., J. Appl. Phys. 107, 09A907 (2010).

[PATT6a] Patton C. E., J. Appl. Phys. 39, 3060 (1968).

[PECH01] Pecharsky V. K. and Gschneidner K. A. ,J. Appl. Phys. 90, 4614 (2001)

[PECH99] Pecharsky V. K. and Gschneidner K. A. , J. Appl. Phys. 86, 565 (1999)

[PHAN07] Phan M. H., Yu S. C., J. Magn. Magn. Mater. 308, 325 (2007).

[PHAN12] Phan T. L., Zhang P., Dan N. H., Yen N. H., Thanh P. T., ThanhT. D., Phan M. H. and Yu S. C., Appl. Phys. Lett. 101, 212403 (2012).

[PICO04] Picozzi S., Continenza A., Freeman A. J., Phys. Rev. B 69, 094423 (2004).

[PIER97] Pierre J., Skolozdra R. V., Tobola J., Kaprzyk S., Hordequin C., Kouacou M. A., Karla I., Currat R. and Leli´evre-Berna E., J. Alloys Comp. 262-263, 101 (1997).

[PLAN09] Planes A., Mañosa L. and Acet M. , J. Phys. Condens. Matter 21, 233201 (2009).

[PONS00] Pons J., Chernenko V. A., Santamarta R. and Cesari E., Acta. Mater. 48, 3027 (2000).

[PONS08] Pons J., Cesari E., Segu´I. C., Masdeu F., Santamarta R., Mater. Sci. Eng. A 481–482, 57 (2008).

[PORC12] Porcar L., Bourgault D. and Courtois P., Appl. Phys. Lett. 100, 152405 (2012).

[PRAM16] Pramanick S., Dutta P., Chatterjee S., Giri S. and Majumdar S. ,J. Magn. Magn. Mater. 405, 270 (2016).

[PRIO11] Priolkar K. R., Lobo D. N., Bhobe P. A., Emura S. and Nigam A .K. , Europhysics Lett. 94, 38006 (2011).

[PRIO13] Priolkar K. R., Bhobe P.A., Lobo D. N., D'Souza S. W., Barman S. R., Chakrabarti A. and Emura S. , Phys. Rev. B 87, 144412 (2013).

[QIND06] Qin Q. D., Zhao Y. G., Cong P. J., Liang Y. H., Zhou W. J., J. Alloys Compd. 420 ,121 (2006).

[RAFI15] Rafique M., Study of the Magnetoelectric Properties of Multiferroic Thin Films and Composites for Device Applications.Ph.D. thesis, COMSATS Institute of Information Technology Islamabad-Pakistan (2015).

[RANJ06] Ranjan R., Banik S., Barman S. R., Kumar U., Mukhopadhyay P. K. and Pandey D. , Phys. Rev. B 74, 224443 (2006).

[RANK09] Ranke P. J. von, Oliveira N. A. de, Alho B. P., Plaza E. J. R., Sousa V. S. R. de, Caron L. and Reis M. S., J. Phys.: Condens. Matter 21, 056004 (2009).

[ROBE79] Robertson J. H., Acta Crystallogr. Sect. A. 35, 350 (1979).

[RODR01] Rodríguez-Carvajal J., IUCr Newsletter 26, 12 (2001).

[RODR93] Rodríguez-Carvajal J., Phys. B Condens. Matter 192, 55 (1993).

[ROTH54] Rothery W. H., Adv. in Physics 3, 149 (1954).

[ROYT98] Roytburd A., Kim T., Su Q., Slutsker J. and Wuttig M., Acta Mater. 46, 5095 (1998).(check)

[SAMA15] Samantaray B., Singh A. K., Perumal A., Ranganathan R., Mandal P. and Ranganathan R. , AIP Adv. 5, 067157 (2015).

[SASI04] Sasioglu E., Sandratskii L. M. and Bruno P. , Phys. Rev. B 70, 24427 (2004).

[SASI08] Sasioglu E., Sandratskii L. M. and Bruno P. , Phys. Rev. B 77, 64417 (2008).

[SATO13] Sato R., Magneto resistive effect element with a magnetic film generating spin fluctuation of conduction electrons, U. S. Patent 8411394 B2 (2013).

[SCHE06] Scheck C., Cheng L., and Bailey W. E., Appl. Phys. Lett. 88, 252510 (2006).

[SESH02] Seshan K., Handbook of Thin-film Deposition Processes and Techniques: Principles, Methods, Equipment, and Applications, Noyes publication, New York (2002).

[SHAR07a] Sharma V. K., Chattopadhyay M. K., Kumar R., Ganguli T., Tiwari P. and Roy S. B., J. Phys.: Condens. Matter 19, 496207 (2007).

[SHAR07b] Sharma V. K., Chattopadhyay M. K. and Roy S. B., J. Phys. D: Appl. Phys. 40, 1869 (2007).

[SHAW13] Shaw J. M. , Nembach H. T., and Silva T. J., Phys. Rev. B 87, 54416 (2013).

[SHUR00] Shur M. and Fjeldly T. A., Silicon and beyond?: advanced device models and circuit simulators, World Scientific(2000).

[SIHU07] Sihues M. D., Durante-Rincón C. A. , Fermin J. R. , J. Magn. Magn. Mater. 316, e462 (2007).

[SING14] Singh K., Singh S. K. and Kaur D., J. Appl. Phys. 116, 114103 (2014).

[SING15] Singh K. and Kaur D. ,Sensors Actuators A Phys. 236, 247 (2015).

[SLAU02] Slaughter J. , Savtchenko L. , Goronkin H. , Korkin A. , Multi-state magnetoresistance random access cell with improved memory storage density, US Patent, US20040012994A1 (2002).

[SMIT56] Smith D. O, Rev. Sci. Instrum. 27, 261(1956).

[SOKO12] Sokolovskiy V. V., Buchelnikov V. D., Zagrebin M. A., Entel P., Sahoo S. and Ogura M., Phys. Rev. B 86, 134418 (2012).

[SOKO13] Sokolov A., Zhang L., Dubenko I., Samanta T., Stadler S. and Ali N., Appl. Phys. Lett. 102, 072407 (2013).

[SOKO17] Sokolovskiy V. V., Sokolovskaya Y. A., Zagrebin M. A., Buchelnikov V. D. and Zayak A. T. ,J. Magn. Magn. Mater. (2017) DOI: 10.1016/j.jmmm.2017.11.055.

[SOZI13] Sozinov A., Lanska N., Soroka A. and Zou W., Appl. Phys. Lett. 102, 21902 (2013).

[SPAR64] Sparks M., Ferromagnetic relaxation theory, McGraw-Hill, New York, 1964.

[SRIV11] Srivastava V., Song Y., Bhatti K., James R. D., Adv. Energy Mater. 1, 97 (2011).

[SRIV12] Srivastava V. and Bhatti K. P., Solid State Phenom. 189, 189 (2012).

[SUHL55] Suhl H., Phys. Rev. 97, 555 (1955).

[SURE11] Suresh Kumar V. and Mahendiran R., J Appl. Phys. 109, 023903 (2011).

[SUTO04] Sutou Y., Imano Y., Koeda N., Omori T., Kainuma R., Ishida K., Oikawa K., Appl. Phys. Lett. 85, 4358 (2004).

[SVOB04] Svoboda J., Magnetic Technique for the Treatment of Materials, Kluwer Academic Publishers, Dordrecht (2004).

[SWAL62] Swalin R. A., Thermodynamics of Solids, John Wiley & Sons, New York (1962).

[SZYT89] Szytula A., Ptasiewicz-Bak H., Leciejewicz J., J. Magn. Magn. Mater. 80, 195 (1989).

[TAJI77] Tajima K., Ishikawa Y., Webster P. J., Stringfellow M. W., Tocchetti D., and Zeabeck K. R. A., J. Phys. Soc. Japan 43, 483 (1977).

[TAKA09] Takamura Y., Nakane R., Sugahara S., J. Appl. Phys. 105, 07B109 (2009).

[TANC17] Tan C., Tai Z., Zhang K., Tian X. and Cai W. ,Sci. Rep. 7, 43387 (2017).

[TEGU02] Tegus O., Brück E., Zhang L., Dagula, Buschow K. H. J. and de Boer F. R., Physica B 319, 174 (2002).

[TEIC15a] Teichert N., Boehnke A., Behler A., Weise B., Waske A. and Hütten A., Appl. Phys. Lett. 106, 192401 (2015).

[TEIC15b] Teichert N., Auge A., Yüzüak E., Dincer I., Elerman Y., Krumme B., Wende H., Yildirim O., Potzger K. and Hütten A. ,Acta Mater. 86, 279 (2015).

[TISH03] Tishin A. M. and Spichkin Y. I., The Magnetocaloric Effect and its Applications, IOP, Bristol (2003).

[TISH99] Tishin A. M., Handbook of Magnetic Materials, North Holland, Amsterdam, (1999).

[TITO12] Titov I., Acet M., Farle M., González-Alonso D., Mañosa L., Planes A. and Krenke T.,J. Appl. Phys. 112, 73914 (2012)

[TITO14] Titov I., Ph.D. Thesis entitled "Influence of magnetism on the martensitic transition and related magnetocaloric effect in NiMn-based Heusler alloys", Department of Physics, University of Duisburg-Essen (2014).

[TOBO00] Tobola J. and Pierre J., J. Alloys Comp. 296, 243 (2000).

[TOBO03] Tobola J., Kaprzyk S., and Pecheur P., Phys. St. Sol. (b) 236, 531 (2003).

[TOBO98] Tobola J., Pierre J., Kaprzyk S., Skolozdra R.V., Kouacou M.A., J. Phys. Condens. Matter 10,1013 (1998).

[TODD94] Todd Robert H., Allen Dell K., Alting L., Manufacturing Processes Reference Guide. Industrial Press Inc (1994). ISBN 0-8311-3049-0.

[TRIT01] Tritt T. M., Recent trends in thermoelectric materials research II, Academic Press(2001).

[TRUD10] Trudel S., Gaier O., Hamrle J., and Hillebrands B., J. Phys. D: Appl. Phys. 43, 193001 (2010).

[TURA16] Turabi A. S., Lázpita P., Sasmaz M., Karaca H. E. and Chernenko V. A. , J. Phys. D. Appl. Phys. 49, 205002 (2016).

[UBAL17] Uba L., Bonda A., Uba S., Bekenov L. V. and Antonov V. N., J. Phys. Condens. Matter 29, 275801 (2017).

[VINO15] Vinodh Kumar S., Singh R. K., Seenithurai S., Bysakh S., Manivel Raja M. and Mahendran M. ,Mater. Res. Bull. 61, 95 (2015).

[VISH10a] Vishoni R. and Kaur D., Surf. Coat. Tech. 204, 3773 (2010).

[VISH10b] Vishoni R. and Kaur D., J. Appl. Phys. 107, 103907 (2010).

[VISH11] Vishnoi R., Singhal R. and Kaur D., J. Nanoparticle Res. 13, 3975 (2011).

[VOLK11] Volkerts J. P., Magnetic thin films?: properties, performance, and applications, Nova Science Publishers (2011).

[VONO74] Vonsovskii S. V., Magnetism, Israel Program Sci. Translations, Jerusalem (1974).

[WAGE94] Wagendristel A., Wang Y., An Introduction to Physics and Technology of Thin Films, World Scientific, Singapore, 1994.

[WANG01] Wang Z. M., Ni G., Xu Q. Y., Sang H. and Du Y. W., J. Magn. Magn.Mater. 234, 371 (2001).

[WARB81] Warburg E., Annalen der Physik, 249,141, (1881)

[WATA76] Watanabe K., Trans. Jpn. Inst. Met. 17, 220 (1976).

[WEBS01] Webster P. J., Ziebeck K. R. A., and Neumann K.-U.,Magnetic Properties of Metals, Landolt-B¨ornstein, New Series, Group III, Vol. 32/c, ed by H. P. J. Wijn, Springer, Berlin (2001).

[WEBS69] Webster P. J., Contemp. Phys. 10, 559 (1969).

[WEBS73] Webster P. J., Ziebeck K. R. A., J Phys. Chem. Solids 34, 1647 (1973).

[WEBS88] Webster P. J. and Ziebeck K. R. A., Alloys and Compounds of d-Elements with Main Group Elements, Part 2, edited by H. P. J. Wijn, Landolt-Bornstein, New Series, Group III, Vol. 19/c, Springer, Berlin, (1988).

[WILL53] Williamson G . and Hall W . , Acta Metall. 1, 22 (1953).

[WINZ04] Winzek B., Schmitz S., Rumpf H., Sterzl T., Hassdorf R., Thienhaus S., Feydt J., Moske M., and Quandt E., Mat. Sci. Eng. A 378, 40 (2004).(check)

[XUYX18] Xu Y., Xu C., Yang D., Zhang R., Huang X., Jiang Y., Yu G. and Pan L. , J. Alloys Compd. 739, 77 (2018).

[YEMK10] Ye M., Kimura A., Miura Y., Shirai M., Cui Y. T., Shimada K., Namatame H., Taniguchi M., Ueda S., Kobayashi K., Kainuma R., Shishido T., Fukushima K. and Kanomata T. ,Phys. Rev. Lett. 104, 1 (2010).

[YILG07] Yilgin R., Oogane M., Ando Y. and Miyazaki T. ,J. Magn. Magn. Mater. 310, 2322 (2007).

[YUSL06] Yu S., Liu Z., Liu G., Chen J. and Cao Z., Wu G. H., Zhang B. and Zhang X. X., Appl. Phys. Lett. 89, 162503 (2006).

[YUSY07a] Yu S. Y., Ma L., Liu G. D., Liu Z. H., Chen J. L., Cao Z. X., Wu G. H., Zhang B. and Zhang X. X., Appl. Phys. Lett. 90, 242501 (2007).

[YUSY07b] Yu S. Y., Cao Z. X., Ma L., Liu G. D., Chen J. L., Wu G. H., Zhang B. and Zhang X. X., Appl. Phys. Lett. 91 102507 (2007).

[YUZU13] Yüzüak E., Dincer I., Elerman Y., Auge A., Teichert N. and Hütten A., Appl. Phys. Lett. 103, 222403 (2013).

[ZHAN04] Zhang Y. Q. and Zhang Z. D., J. Alloys Comp. 365, 35 (2004).

[ZHAN16] Zhang X., Qian M., Miao S., Su R., Liu Y., Geng L. and Sun J., J. Alloys Compd. 656, 154 (2016)

[ZHUK16] Zhukov A., Novel functional magnetic materials: fundamentals and applications (2016)

[ZIEB01] Ziebeck K. R. A., Neumann K. U., Magnetic Properties of Metals. Landolt-Börnstein, New Series, Group III, vol 32/c, ed. by H.R.J. Wijn, Springer, Berlin (2001).

[ZUTI04] Žutic I, Fabian J. and Das Sarma S., Rev. Mod. Phys. 76, 323 (2004).

Publications

LIST OF PUBLICATIONS ORIGINATING FROM THE THESIS WORK

In Journals:

[1]. Significant room temperature magneto-caloric effect in Ni-Mn-Sn thin films
Rajkumar Modak, B. Deka, M. Manivel Raja and A. Srinivasan
Advanced Science Letters **22** (2016) 26-29.
DOI: 10.1166/asl.2016.6794

[2]. Low Gilbert damping and in-plane magnetic anisotropy in Ni-Mn-Sn thin film with high $L2_1$ order
Rajkumar Modak, B. Samantaray, P. Mandal and A. Srinivasan
Applied Physics A **122** (2016) 252.
DOI: 10.1007/s00339-016-9765-8

[3]. Thickness dependent structural, magnetic and magneto-dynamic properties of Mn rich Ni-Mn-Sn films
Rajkumar Modak, B. Samantaray, P. Mandal and A. Srinivasan
Journal of Alloys and Compounds **692** (2017) 529-534.
DOI: 10.1016/j.jallcom.2016.09.036

[4]. Enhanced magneto-caloric effect upon Co substitution in Ni-Mn-Sn thin films
Rajkumar Modak, M. Manivel Raja and A. Srinivasan
Journal of Magnetism and Magnetic Materials **448** (2018) 146-152.
DOI: 10.1016/j.jmmm.2017.06.063

[5]. Structural, magneto-static and magneto-dynamic properties of Fe substituted Ni-Mn-In films
Rajkumar Modak, M. Manivel Raja and V. V. Srinivasu and A. Srinivasan
Thin Solid Films **653** (2018) 384-389.
DOI: 10.1016/j.tsf.2018.03.067

[6]. Effect of Cu/Fe/Co substitution on static and dynamic magnetic properties of Ni-Mn-Sn alloy thin films
Rajkumar Modak, V. V. Srinivasu and A. Srinivasan
Journal of Magnetism and Magnetic Materials **464** (2018) 50-55.
DOI: 10.1016/j.jmmm.2018.05.050

[7]. Enhanced magneto-static and magneto-dynamic properties in Fe/Co substituted Ni-Mn-In alloy films
Rajkumar Modak and Ananthakrishnan Srinivasan
IEEE Transactions on Magnetics **54** (2018) 6100405.
DOI: 10.1109/TMAG.2018.2847417

[8]. New aspects of microwave absorption in ferromagnetic Ni-Mn-Sn thin films
A. Srinivasan, **Rajkumar Modak**, C. Swapna and V. V. Srinivasu
Acta Physica Polonica A **134** (2018) 178-181.
DOI: 10.12693/APhysPolA.134.178

[9]. Enhanced magneto-caloric effect upon fourth element (Cu, Fe, Co) substitution in Ni-Mn-Sn thin films
Rajkumar Modak, M. Manivel Raja and A Srinivasan
Applied Physics A **125** (2019) 57.
DOI: 10.1007/s00339-018-2340-8

[10]. Enhanced room temperature magneto-caloric effect upon Fe/Co substitution in Ni-Mn-In films
Rajkumar Modak and Ananthakrishnan Srinivasan
Journal of Applied Physics **(Under review).**

In Conference Proceedings:

[1]. Structural and magnetic properties of Ni-Mn-Sn thin films
Rajkumar Modak, B. Deka, A.K. Singh, A. Gayen, A. Perumal, M. Manivel Raja and A. Srinivasan
AIP Conference Proceedings **1665** (2015) 080072.
DOI: 10.1063/1.4917976

[2]. Comparison of field swept ferromagnetic resonance methods – A case study using Ni-Mn-Sn films
Rajkumar Modak, B. Samantaray, P. Mandal, V. V. Srinivasu and A. Srinivasan
AIP Conference Proceedings **1953** (2018) 120006.
DOI: 10.1063/1.5033071

LIST OF PUBLICATIONS WHICH ARE NOT PART OF THIS THESIS WORK

In Journals:

[1]. Effect of atomic disorder on magnetization and half-metallic character of Cr_2CoGa alloy
B. Deka, **Rajkumar Modak**, P. Paul and A. Srinivasan
Journal of Magnetism and Magnetic Materials **418** (2016) 107-111.
DOI: 10.1016/j.jmmm.2016.01.064

In Conference Proceedings:

[1]. Structural and optical properties of electrospun MoO_3 nanowires
Arnab Kumar Das, **Rajkumar Modak** and Ananthakrishnan Srinivasan
AIP Conference Proceedings **1953** (2018) 030021.
DOI: 10.1063/1.5032356